# Vortex Fiber Nulling for Exoplanet Observations

Thesis by
Daniel Echeverri

In Partial Fulfillment of the Requirements for the
Degree of
Doctor of Philosophy in Physics


CALIFORNIA INSTITUTE OF TECHNOLOGY
Pasadena, California

2024
Defended January 19, 2024

Daniel Echeverri
ORCID: 0000-0002-1583-2040

# ACKNOWLEDGEMENTS

My completion of this PhD was only possible through the mentorship, guidance, love, and support of countless people who, not only in the past six years but from the very start, propelled me towards this milestone. It would be impossible to name and acknowledge everyone along the way, so here are just a few.

First, thank you, Dimitri, for going above and beyond to give me an academic home. You single-handedly kept me in this field and on this path when you welcomed me into your group; I wouldn't be here without the postbacc and guidance you gave me to get into grad school. Since then, you have continued to serve as a patient advisor, mentor, and friend. By constantly sending me to conferences and connecting me with collaborators, you have also helped me build a wide network and community that I can lean on for the rest of my career. In a similar vein, thank you to my undergraduate advisor, Jeremy Kasdin. You took an opportunity on an inexperienced freshman, introduced me to coronagraphy, and inspired me to pursue a field I had never heard of before. Your continued guidance and encouragement are invaluable.

During my tenure at Caltech, I was fortunate to have other fantastic mentors, including Nem and Gary. Through your guidance I always had a support structure with which I knew I could never fail. Together, you two trained me as an experimentalist and patiently explained, simulated, and re-explained the fundamentals of optics that I lacked. Further, thank you to the postdocs who filled in the gaps along the way: Jason, Ashley, JB, Max, Pradip, Ji, and others.

To my labmates, Jerry, Yinzi, Katelyn, Jackie, Ben, and especially Niyati and Jorge: thank you for being there to keep the office, lab, and research fun. Here's to the many Settebello pizzas and board game nights that ultimately fueled much of what you'll read in this Thesis. I also deeply appreciate the conversations we had during conferences about the field, life, and everything in between. To the Caltech admins, particularly Judy, Nam, and Mika, thank you for helping me navigate the requirements of the degree in the face of unexpected challenges, and for putting up with my many last minute requests. You made my PhD so much easier through your support. Beyond campus, thank you to all the collaborators who helped me along the way, especially the KPIC team and the Keck folks. Jacques, Eduardo, Peter, Sylvain, Paul, and many others, you taught me so much about what it takes to build

and run an instrument, and made me feel welcome and at home while on-island.

Of course, I wouldn't be where I am now without the many, many friends who made things fun, kept me motivated, and made me who I am today. To my school friends, Tobi, Mac, and Tiff, thank you for sticking with me and continuing to support me more than 15 years later, despite my apparent inability to text on a regular basis. To my college friends and roommates, the MAEs, Fabian, Yon, Pat, Leea, and all the others who made Princeton the second home that it was: thank you. From 3AM song and dance breaks during problem sets, to Charter Fridays, and of course late night chats and bike rides to de-stress, you helped me through the academic rigors, making college fun while also putting up with my wildest years. Outside of Princeton, thank you, Cyndia, Luke, and the others from my summer at JPL, for exploring the mountains, deserts, and beaches of California to inspire me to move out West. With such wonderful friendships already, I was fortunate to make another core group of incredible friends in Grad School. You've been there from the first week of this PhD, dancing ridiculously to Game of Thrones, going on ski trips, and flooding hot tubs at weekend cabin getaways. To the few I was lucky enough to live with, Karen, Catherine, Josh, and Dom, thank you for making a third home with me in LA, even if that home no longer has a bar on the first floor or impromptu staircase Olympics. To Ty, who was by my side for most of this PhD, despite a pandemic and hours of driving between LA and SLO: I could not have come this far without your love and support; thank you.

Finally, I'd like to thank my family. To my parents, I recognize the sacrifices and challenges you endured, known and unknown to me, to make everything possible for me and my sisters. Thank you for encouraging me to explore my curiosities, teaching me to never settle for less, and encouraging me to shoot for the stars. To my sisters, my original cheerleaders and advocates, thank you for putting up with all my chaos when I was younger. You served as incredible role models, paving the way both in school and in life to show me what was possible. I love you and appreciate everything you've done for me.

# ABSTRACT

As of December 11, 2023, there are just over 5555 confirmed exoplanet detections. Of these exoplanets, only around 200 have been spectroscopically characterized. Spectra are crucial since they provide unique insights into the physical and chemical properties of exoplanets, their atmospheres, and their formation history. Few exoplanet spectra have been obtained because the prevailing spectroscopic techniques, transit spectroscopy and direct imaging, access different physical separations around a star and leave a gap in coverage from about 1 to 10 AU. This gap coincides with the peak of the giant planet occurrence rate such that there is an important population of exoplanets whose spectra cannot be readily obtained with the prevailing techniques. Interferometry can unlock access to these exoplanets and provide spectra for them.

Exoplanet interferometry has seen waves of interest in the past. However new developments, such as the first interferometric detections, have stoked a revived interest. Though VLTI/GRAVITY and other multi-aperture, long-baseline instruments currently dominate the field, there is a push to develop simpler interferometric architectures. Cross-aperture techniques are of particular interest as they can be readily implemented on existing and future direct imaging instruments with few-to-no modifications. Such single-telescope interferometers and nullers can reach well-within the inner working angle of conventional coronagraphs, but require significantly less infrastructure and investment than their long-baseline counterparts.

This thesis presents vortex fiber nulling (VFN), a new cross-aperture technique for detecting and spectroscopically characterizing exoplanets at separations less than one diffraction beamwidth ($\lesssim 1\ \lambda/D$). VFN utilizes the full collecting area of a telescope to efficiently observe within the inner working angle of conventional coronagraphs. The first chapters of this thesis develop the VFN concept and how it can be readily implemented on existing and future instruments. Subsequent chapters present the laboratory demonstrations used to validate the technique and test its limits. Finally, the last chapters cover the design and deployment of a VFN mode to the KPIC instrument at the Keck Telescope. This includes a glimpse into VFN's capabilities with the first direct detection and spectroscopic characterization of three M dwarf companions previously known only from radial velocity and astrometry. This thesis therefore follows the development of VFN from a concept in 2018 to an operating mode with confirmed detections in 2023.

# PUBLISHED CONTENT AND CONTRIBUTIONS

Echeverri, D., J. W. Xuan, J. D. Monnier, et al. (Apr. 2024). "Vortex Fiber Nulling for Exoplanet Observations: First Direct Detection of M Dwarf Companions around HIP 21543, HIP 94666, and HIP 50319". In: *The Astrophysical Journal Letters* 965.2, L15, p. L15. DOI: 10.3847/2041-8213/ad3619. arXiv: 2403.17295 [astro-ph.EP].

My Role: I set requirements for target selection and simulated the observations to verify that the companions would be detectable. I then analyzed the VFN data and prepared the manuscript.

Echeverri, D., J. W. Xuan, N. Jovanovic, J.-R. Delorme, et al. (2023). "First light of the vortex fiber nulling mode on the Keck planet imager and characterizer". In: *Techniques and Instrumentation for Detection of Exoplanets XI*. Ed. by G. J. Ruane. Vol. 12680. International Society for Optics and Photonics. SPIE, p. 126800M. DOI: 10.1117/12.2677656. URL: https://doi.org/10.1117/12.2677656.

My Role: same as the JATIS version of this paper, listed below.

Echeverri, D., J. W. Xuan, N. Jovanovic, G. Ruane, et al. (July 2023). "Vortex fiber nulling for exoplanet observations: implementation and first light". In: *Journal of Astronomical Telescopes, Instruments, and Systems* 9, 035002, p. 035002. DOI: 10.1117/1.JATIS.9.3.035002. arXiv: 2309.06514 [astro-ph.IM]. URL: https://doi.org/10.1117/1.JATIS.9.3.035002.

My Role: I led the design of the new mode, helped assemble it in the lab, and then helped install and commission it at the telescope. I prepared and performed the experiments, reduced and analyzed the results, and executed the SNR simulations. I also prepared the manuscript.

Echeverri, D., G. Ruane, N. Jovanovic, J.-R. Delorme, et al. (Sept. 2021). "Broadband vortex fiber nulling: high-dispersion exoplanet science at the diffraction limit". In: *Techniques and Instrumentation for Detection of Exoplanets X*. Ed. by S. B. Shaklan and G. J. Ruane. Vol. 11823. Society of Photo-Optical Instrumentation Engineers (SPIE) Conference Series, 118230A, 118230A. DOI: 10.1117/12.2597160. arXiv: 2210.15910 [astro-ph.EP].

My Role: I designed and performed the laboratory experiments, executed the simulations, and prepared the manuscript.

Echeverri, D., G. Ruane, B. Calvin, et al. (Dec. 2020). "Detecting and characterizing close-in exoplanets with vortex fiber nulling". In: *Optical and Infrared Interferometry and Imaging VII*. Ed. by P. G. Tuthill, A. Mérand, and S. Sallum. Vol. 11446. Society of Photo-Optical Instrumentation Engineers (SPIE) Conference Series, 1144619, p. 1144619. DOI: 10.1117/12.2563142. arXiv: 2012.04239 [astro-ph.IM].

My Role: I designed and performed the visible-wavelength experiments, assisted

with the K band experiments, and designed the new testbed presented. I also prepared the manuscript.

Echeverri, D., G. Ruane, N. Jovanovic, T. Hayama, et al. (Sept. 2019). "The vortex fiber nulling mode of the Keck Planet Imager and Characterizer (KPIC)". In: *Society of Photo-Optical Instrumentation Engineers (SPIE) Conference Series*. Vol. 11117. Society of Photo-Optical Instrumentation Engineers (SPIE) Conference Series, 111170V, p. 111170V. DOI: 10.1117/12.2528529. arXiv: 1909.03538 [astro-ph.IM].
My Role: I designed and performed the laboratory experiments, led the design of the KPIC VFN mode, and executed the performance simulations presented. I also prepared the manuscript.

Echeverri, D., G. Ruane, N. Jovanovic, D. Mawet, et al. (May 2019). "Vortex fiber nulling for exoplanet observations I. Experimental demonstration in monochromatic light". In: *Optics Letters* 44.9, p. 2204. DOI: 10.1364/OL.44.002204. arXiv: 1811.02083 [astro-ph.IM].
My Role: I executed the experiments and led the manuscript preparation.

# TABLE OF CONTENTS

Acknowledgements . . . iii
Abstract . . . v
Published Content and Contributions . . . vi
Table of Contents . . . vii
List of Illustrations . . . x
List of Tables . . . xiii
Nomenclature . . . xiv
Chapter I: Introduction . . . 1
1.1 Indirect Methods for Exoplanet Detection . . . 2
1.2 Major Findings from Indirect Methods . . . 5
1.3 Spectral Characterization . . . 8
1.4 Methods for Spectroscopy . . . 12
1.5 Interferometry and Nulling . . . 19
1.6 Summary and Overview of Thesis . . . 29
Chapter II: VFN Concept . . . 47
2.1 Single-Mode Fibers . . . 47
2.2 Fiber Coupling . . . 49
2.3 The Direct Spectroscopy Case . . . 53
2.4 A Primer on Fiber Nulling . . . 56
2.5 Vortex Fiber Nulling . . . 59
2.6 Limitations . . . 63
2.7 Further Considerations . . . 70
Chapter III: Proof of Concept . . . 77
*Article* Vortex Fiber Nulling for Exoplanet Observations: Experimental Demonstration in Monochromatic Light . . . 77
3.1 Abstract . . . 77
3.2 Introduction . . . 78
3.3 Experimental Setup . . . 80
3.4 Procedure . . . 81
3.5 Results . . . 81
3.6 Discussion . . . 83
3.7 Conclusions . . . 85
Chapter IV: Laboratory Demonstrations . . . 88
4.1 Monochromatic Experiments . . . 89
4.2 Broadband Experiments . . . 92
4.3 The Polychromatic Reflective Testbed (PoRT) . . . 98
Chapter V: The KPIC VFN Mode . . . 106
*Article Excerpt* The Vortex Fiber Nulling Mode of the Keck Planet Imager and Characterizer (KPIC) . . . 106

5.1 Introduction . . . 107
5.2 The KPIC VFN Mode . . . 107
5.3 Predicted On-Sky VFN Performance . . . 110
*Supplemental Work* . . . 114
5.4 Comment on Tip-Tilt Magnitude . . . 114
5.5 Effect of On-Sky Wavefront Residuals . . . 114
5.6 Preliminary KPIC Vortex Characterization . . . 117
5.7 KPIC VFN Laboratory Integration . . . 119
Chapter VI: KPIC VFN First Light . . . 127
*Article* Vortex Fiber Nulling for Exoplanet Observations: Implementation and First Light . . . 127
6.1 Abstract . . . 127
6.2 Introduction . . . 128
6.3 The Vortex Fiber Nulling Concept . . . 130
6.4 A VFN Mode for KPIC . . . 133
6.5 On-Sky Commissioning . . . 139
6.6 Analysis . . . 143
6.7 Next Steps . . . 149
6.8 Conclusion . . . 152
*Supplemental Work* . . . 153
6.9 KPIC VFN Versus DS Mode . . . 153
Chapter VII: KPIC VFN Detections . . . 165
*Article* Vortex Fiber Nulling for Exoplanet Observations: First Direct Detection of M Dwarf Companions around HIP 21543, HIP 94666, and HIP 50319 . . . 165
7.1 Introduction . . . 166
7.2 Targets . . . 167
7.3 Observations and Data Analysis . . . 170
7.4 Results and Discussion . . . 172
7.5 Conclusion . . . 176
*Supplemental Work* . . . 179
7.6 Extended Results . . . 179
7.7 Note About Target Selection . . . 184
Chapter VIII: KPIC VFN Upgrades . . . 194
8.1 Scalar VFN . . . 194
8.2 Vector Vortex Mask Specifications . . . 199
8.3 Atmospheric Dispersion Corrector . . . 209
8.4 Pointing Control . . . 215
Chapter IX: Summary and Perspectives . . . 231
9.1 Summary . . . 231
9.2 Perspectives . . . 233

# LIST OF ILLUSTRATIONS


*Number* *Page*

1.1 The photoevaporation gap. . . . . 7
1.2 1-10 AU peak in giant planet occurrence rate. . . . . 8
1.3 Exoplanet atmosphere at varying resolutions. . . . . 9
1.4 Abundance ratios in protoplanetary disks. . . . . 10
1.5 Exoplanets with measured spectra. . . . . 18
1.6 Fringe basics in interferometry. . . . . 20
1.7 Bracewell nulling concept. . . . . 21
2.1 Gaussian approximation for fiber mode. . . . . 49
2.2 Airy PSF coupling and MFD scaling for an SM2000 fiber. . . . . 51
2.3 Direct spectroscopy coupling versus fiber offset. . . . . 52
2.4 Fiber nulling architecture with two sub-apertures. . . . . 57
2.5 Fiber nulling architecture with a phase knife. . . . . 58
2.6 Charge 1 and charge 2 vortex phase. . . . . 60
2.7 Charge 1 and charge 2 coupling on circular aperture. . . . . 61
2.8 VFN sensitivity to angular offset errors. . . . . 64
2.9 VFN coupling maps in the presence of trefoil. . . . . 66
2.10 VFN null sensitivity to wavefront aberrations. . . . . 67
2.11 VFN performance on various telescope apertures. . . . . 71
2.12 Line profiles for VFN on various telescope apertures. . . . . 73
3.1 Schematic and diagram of a VFN system, along with off-axis coupling efficiency for charge 1. . . . . 79
3.2 Theoretical versus measured PSFs and coupling maps for first VFN laboratory experiments. . . . . 82
3.3 Linear scans of VFN coupling in first VFN laboratory experiments . . 83
4.1 Schematic and picture of the transmissive VFN testbed at Caltech . . 90
4.2 Simulated and measured monochromatic VFN coupling map, and average radial profiles, from improved laboratory experiments . . . . 91
4.3 Schematic and picture of the transmissive VFN testbed with circular polarizers for broadband experiments. . . . . 93
4.4 On- and off-axis coupling efficiency, along with radial profile and coupling map, for polycrhomatic VFN laboratory experiments. . . . . 96

4.5 CAD model and picture of the PoRT testbed at Caltech. . . . . 99
4.6 Coupling map and line profiles of the DAFN laboratory experiments using the PoRT testbed. . . . . 101
4.7 Coupling maps for the PLN laboratory experiments using the PoRT testbed. . . . . 102
5.1 Diagram of the planned KPIC VFN mode, along with comparison between DS and VFN mode observing scheme. . . . . 108
5.2 Charge 2 K band vortex masks planned for KPIC VFN mode. . . . . 109
5.3 PyWFS wavefront and jitter residuals measured on-sky on June 2019, used for KPIC VFN performance predictions. . . . . 111
5.4 KPIC VFN charge 1 and charge 2 performance prediction simulations using on-sky PyWFS residuals. . . . . 113
5.5 Approximate relationship between on-sky RMS wavefront residuals and corresponding KPIC VFN null depth. . . . . 115
5.6 KPIC VFN vortex mask as-mounted, along with resulting laboratory versus simulated PSF. . . . . 118
5.7 Laboratory validation of the KPIC VFN mode prior to deployment. Pupil images, coupling maps, and average radial profiles for charge 1 and charge 2 masks. . . . . 121
6.1 Charge 1 and charge 2 vortex phase, diagram of a VFN system, and theoretical coupling efficiency. . . . . 132
6.2 Diagram of the deployed KPIC VFN mode. . . . . 134
6.3 Coupling maps and line profile of the KPIC VFN mode measured in-situ on the NIRSPEC detector. . . . . 138
6.4 On- and off-axis end-to-end throughput for the KPIC VFN mode, measured on-sky during commissioning. . . . . 142
6.5 KPIC VFN predicted sensitivity from measured on-sky throughput during commissioning. . . . . 148
6.6 KPIC VFN versus DS mode SNR. . . . . 154
7.1 HIP 21543 spectrum from 2023 October VFN observations . . . . . 171
7.2 VFN CCF and CHARA detection plots for three detected M dwarf companions . . . . . 174
7.3 Posterior distribution and ACF of residuals for HIP 21543 . . . . . 180
7.4 Posterior distribution and ACF of residuals for HIP 94666 . . . . . 181
7.5 Posterior distribution and ACF of residuals for HIP 50319 . . . . . 182
8.1 Coupling maps for scalar VFN charge 1 . . . . . 196

8.2 Uncorrected null performance with a scalar charge 1 mask . . . . . 197
8.3 Parameters for an optical wedge to correct dispersion in scalar VFN. . 197
8.4 Samples of spot defect simulations for vortex requirements. . . . . 202
8.5 Sensitivity to spot defects in vortex mask. . . . . 203
8.6 Ghosts from pupil-plane vector vortex mask. . . . . 205
8.7 Null contribution from dispersion. . . . . 211
8.8 Spectrally-resolved null contributions from DAR, tip-tilt jitter, and wavefront residuals. . . . . 212
8.9 Spectrally-resolved companion coupling with DAR. . . . . 214
8.10 PSD from original KPIC tracking system. . . . . 217
8.11 Step response for the KPIC FAM. . . . . 220
8.12 Preliminary timing diagram for original tracking control. . . . . 221
8.13 Extended open-loop PSD for tracking system. . . . . 224
8.14 Block diagram of new KPIC tracking control. . . . . 225
8.15 Transfer function for KPIC feedback assist. . . . . 226
8.16 On-sky PSD for the new KPIC tracking control system. . . . . 228
8.17 On-sky PSD for the new KPIC tracking control system – overlaid. . . 228
9.1 Predicted yield from VFN on HISPEC. . . . . 235

# LIST OF TABLES

*Number* *Page*

2.1 Coefficients for VFN Zernike Sensitivity . . . . . 68
2.2 Optimal parameters for pupil plane and focal plane VFN . . . . . 72
3.1 Contributions from wavefront error to measured laboratory null depth. 84
4.1 Summary of best VFN laboratory demonstrations . . . . . 98
5.1 Null and peak coupling of the KPIC VFN mode in the laboratory. . . 122
6.1 Observations for VFN Commissioning . . . . . 141
6.2 Values for SNR calculation in Fig. 6.5 . . . . . 148
7.1 Targets and Observations . . . . . 169
7.2 Fitted Parameters from VFN . . . . . 173
7.3 Fitted Parameters from CHARA . . . . . 173
8.1 Contributions from vortex mask to KPIC charge 1 null . . . . . 208
8.2 VFN performance without an ADC . . . . . 210
8.3 ADC requirements from jitter and wavefront residuals . . . . . 212

# NOMENCLATURE

**1D, 2D, 3D.** one-dimension(al), two-dimension(al), three-dimension(al).

**ADC.** atmospheric dispersion compensator.

**ADI.** angular differential imaging.

**AO.** adaptive optics.

**AR.** anti-reflection.

**CHARA.** Georgia State University Center for High Angular Resolution Astronomy.

**DAFN.** dual aperture fiber nuller.

**DAR.** differential atmospheric refraction.

**DM.** deformable mirror.

**DS.** direct spectroscopy.

**EFC.** electric field conjugation.

**ELT.** Extremely Large Telescope.

**FAM.** fiber alignment mirror.

**FEU.** fiber extraction unit.

**FIU.** fiber injection unit.

**HDC.** high dispersion coronagraphy.

**HWO.** Habitable Worlds Observatory (NASA Mission).

**IWA.** inner working angle.

**K band.** Astronomical band spanning roughly 2.0 to 2.4 $\mu$m in KPIC.

**KPIC.** Keck Planet Imager and Characterizer.

**LBT(I).** Large Binocular Telescope (Interferometer).

**LCP.** Liquid Crystal Polymer.

**MFD.** mode field diameter.

**NCPA.** non-common path aberration(s).

**NIRSPEC.** Near Infrared Spectrograph (Keck II Telescope).

**NRM.** non-redundant masking.

**OAP.** off-axis parabolic mirror.

**P-V.** peak-to-valley.

**PFN.** Palomar Fiber Nuller (Palomar Observatory).

**PLN.** photonic lantern nuller.

**PSD.** power spectral density.

**PSF.** point spread function.

**PyWFS.** pyramid wavefront sensor.

**RDI.** reference differential imaging.

**RMS.** root-mean-square.

**RV.** radial velocity.

**SAM.** sparse aperture masking.

**SB9.** Ninth Catalog of Spectroscopic Binaries.

**SHWFS.** Shack-Hartmann wavefront sensor.

**SMF.** single-mode fiber.

**SNR.** signal-to-noise ratio.

**TPF-I.** Terrestrial Planet Finder - Interferometer (NASA Mission).

**VFN.** vortex fiber null(ing/er).

**VLT(I).** Very Large Telescope (Interferometer).

**WDS.** Washington Double Star Catalog.

**WFE.** wavefront error.

**WFR.** wavefront residuals, usually after AO correction.

*Chapter 1*

# INTRODUCTION

The quest to unravel the mysteries of our cosmic origin has long captivated human curiosity. At its heart lie fundamental questions about where we come from, how we got here, and whether we are alone. As with all scientists, astronomers are tasked with taking such profound and awe-inspiring concepts and reducing them to tractable and readily quantifiable measurements from which fragments of an answer can be derived. The search for our origin thus raises new questions about the formation of our solar system and its planets. However, a generally-applicable answer must extend beyond our own solar system and requires a broader investigation into other planetary systems. In fact, by comparing our system to others, we gain insight into its formation and what makes it, and the Earth, special. This naturally leads to the study of exoplanets: planets that orbit stars other than the Sun.

Many have speculated for centuries about the existence of exoplanets in the first place. Giordano Bruno in the $16^{\text{th}}$ century is often said to be one of the first to promote the idea of planets around other stars. Arguments can nevertheless be made about earlier concepts by philosophers and thinkers of almost every culture regarding the existence of other "worlds" or the the uniqueness of our own planets. Beyond speculation, obtaining explicit evidence of exoplanets was a seemingly impossible task. With the advent of telescopes, an intuitive way to search for exoplanets was to try to observe their light directly, the same way we see stars and other cosmic objects. However, exoplanets are much dimmer than their stars, such that they are generally lost behind the blinding glare of their host. Trying to image an exoplanet is often compared to trying to distinguish the light from a firefly flying next to a lighthouse from thousands of miles away. Direct observation was thus not possible for a long time, and indirect methods proved to be a more fruitful way to detect exoplanets. That is, by observing the effect of an exoplanet on its host star one can infer its presence and a wealth of additional information. Though this thesis will focus on a specific direct method of observation, it is important to first understand the indirect methods as they represent a vital part of the field and provide much of our current understanding about exoplanets. Moreover, there are significant benefits to leveraging the complementary nature of the data obtained from the various techniques.

## 1.1 Indirect Methods for Exoplanet Detection

There are four major indirect methods that have yielded a plethora of exoplanet detections: radial velocity (RV), transit photometry, astrometry, and gravitational microlensing. Combined, these techniques account for more than 5488 of the 5557 confirmed exoplanets as of December 11, 2023 (R. L. Akeson et al., 2013)[1]. Each method operates in a distinct way, with its own strengths, weaknesses, and biases, leading to different measurables and insights.

### Microlensing

Gravitational microlensing is distinct from the other three techniques since it observes the increase in flux from a different, distant star as the host star passes in front of it. The foreground star's gravitational field bends the light from the background star, thereby acting like a lens and producing a distinctive flux curve over a relatively brief period of time. The planet's lesser mass causes a small momentary deviation in this curve which can be measured and reveals the planet's existence. This technique has led to 204 confirmed detections, including several detections of "rogue" planets (planets that are not bound to a host star). The NASA Roman Space Telescope is primed to drastically increase the statistics available from this technique by providing thousands of new microlensing detections. However, the nature of this method is such that observations are fleeting and cannot be repeated to obtain additional information about the exoplanet.

### Radial Velocity

The RV technique changes the narrative by observing the exoplanet's host star rather than a background source. In the same way that the gravitational pull from the star causes the planet to orbit, the planet causes the star to wobble with a periodic motion around their combined center of mass. This reflex motion leads to a Doppler shift in the star's spectrum that can be directly translated to a shift in the star's velocity along the line of sight from Earth, known as the radial velocity. The semi-amplitude of the velocity shift, $K_{\mathrm{RV}}$, is a measure of the variation within half an orbital period and is given by

$$K_{\mathrm{RV}} = \left(\frac{2\pi G}{P}\right)^{1/3} \frac{M_p \sin i}{(M_\star)^{2/3}} \frac{1}{\sqrt{(1-e^2)}}, \tag{1.1}$$

where $P$ is the period of the signal, $M_p$ and $M_\star$ are the planet and star mass, respectively, $i$ is the orbital inclination relative to the line of sight, and $e$ is the

[1] NASA exoplanet archive: `https://exoplanetarchive.ipac.caltech.edu/`

eccentricity. A detection is thus made by meticulously tracking the star's RV with high resolution spectroscopy and searching for periodic signals that would indicate the presence of an exoplanet. Equation 1.1 reveals a bias in this technique since higher-mass planets on shorter periods introduce stronger signals. RV detections are also implicitly biased towards older, more mature stars whose spectra are more stable and ammenable to precise measurements. The RV technique has nevertheless proven exceptionally effective, with 1071 confirmed detections so far, including the first detection of an exoplanet around a main-sequence star (Mayor et al., 1995). These detections provide insight into the planet's orbital parameters, like the period and eccentricity. They also provide a lower limit on the planet mass, though they cannot constrain the precise value due the degeneracy with the orbital inclination ($M_p \sin i$). The RV method continues to improve with increasingly stable spectrographs and refined methods for calibrating systematics that are pushing to lower-mass and younger systems.

**Astrometry**

The astrometry technique also relies on the host star's periodic wobble. However, rather than measuring the doppler shift in star's spectrum, astrometry makes precise measurements of the star's position in the sky. The wobble is seen as a deviation from the roughly-linear proper motion that a star traces through the sky relative to much more distant, and relatively non-moving background stars. The projected angular orbit of the star due to the planet is generally miniscule and therefore challenging to measure. Assuming a circular orbit, the semi-amplitude of the angular deviation, $\Delta\theta$, is given by

$$\Delta\theta = 954.3 \frac{M_p/M_{\rm Jup}}{M_\star/M_\odot} \frac{a/{\rm AU}}{d/{\rm pc}}, \tag{1.2}$$

where $\Delta\theta$ is in $\mu$as, $M_\odot$ and $M_\odot$ are the mass of Jupiter and the Sun, respectively, $a$ is the semi-major axis of the planet's orbit, and $d$ is the distance to the system. Thus, once a noticeable wobble is detected, it can be used to unambiguously determine the mass and orbital parameters of the planet, including the inclination and eccentricity. As with the equation for the RV semi-amplitude, Eq. 1.2 shows a bias towards massive planets. However, it is also biased towards nearby systems with exoplanets on wide orbits. The challenges in this technique have limited the number of confirmed detection to just 3 so far. Astrometry has nevertheless been successfully used to follow-up on detections by other techniques to constrain the orbital parameters and mass of the exoplanets. Moreover, the ESA Gaia mission (Gaia Collaboration et al., 2016) promises to revolutionize this technique. Among

its many science goals, Gaia aims to measure the position of over 1.8 Billion stars over the course of 10 years with a precision down to 20 $\mu$as or less for bright stars. This will allow Gaia to detect hundreds, if not thousands, of new exoplanets and is already proving incredibly useful in guiding the selection of stars to target with other techniques (Kervella et al., 2019; Brandt, 2021; De Rosa et al., 2023).

**Transit Photometry**

The final indirect method for detection is transit photometry. This relies on a chance alignment between the host star and the exoplanet along the line of sight so that when the planet passes in front of the star, or "transits," it blocks part of the starlight. An observer can therefore measure the star's brightness over time and search for dips. Unlike the microlensing phenomenon, transits are periodic and can be measured each time the planet completes an orbit. The depth of the transit, meaning how much the starlight is dimmed, is set by the ratio of the radius of star, $R_\star$, and the planet, $R_p$. Assuming a uniform stellar disk, the depth is

$$\Delta F = \left(\frac{R_p}{R_\star}\right)^2. \tag{1.3}$$

The interval between subsequent transits directly gives the orbital period. Meanwhile, the orbital inclination is measured from the duration of the transit. In this way, the transit technique provides the planet's radius and orbit. However, detections are biased towards larger planets that provide a larger transit depth. There is also an implicit bias against active stars with spots, since the spots reduce the transit depth and affect the timing accuracy. Additionally, the probability that a planet transits its star is approximately given by

$$P \approx \frac{R_\star}{a}. \tag{1.4}$$

This limits the orbital separations accessed by this techinque since the chances of a transit decrease significantly as the semi-major axis increases. For example, the Earth only has a 1:200 chance of being observed via transit from another star. Despite the odds, the transit photometry method has been the most prolific so far, with 4146 confirmed detections. This is in large part due to the NASA Kepler mission which revolutionized the technique the same way that Gaia promises to do for astrometry. Over the course of its extended nine year lifetime, Kepler surveyed more than 500,000 stars in a small patch of sky known as the Kepler field, and produced more than 2700 confirmed exoplanets. An additional note to the transit technique is that it can detect more than just the planets that transit their star; the

precision in the transit timing is such that small variations in the orbital period can be measured. These variations point to additional planets perturbing the first one's orbit. This sub-method of detection is known as transit timing variation and has led to an additional 28 confirmed detections which are of particular interest since they are explicitly in multi-planet systems.

## 1.2 Major Findings from Indirect Methods

The results so far from these techniques have led to several profound insights into exoplanets. The first and most obvious conclusion is that exoplanets are ubiquitous and widely diverse. The sheer number of detections in only 30 years makes this clear. Planets have been detected around all types of stars from pulsars (Wolszczan et al., 1992), to M-dwarfs (Anglada-Escudé et al., 2016), to G-type stars like our own Sun (Jenkins et al., 2015), as well as in multi-star systems (Doyle et al., 2011), and even free-floating without a host star at all (Sumi et al., 2011). Additionally, mass measurements show that planets span a wide range from a fraction of the Earth's mass (Agol et al., 2021) up to $\sim$13 $M_{\rm Jup}$ (Khandelwal et al., 2023). The upper cutoff here is set only by the definition of a planet, which must not cross the deuterium burning limit where fusion begins (Lecavelier des Etangs and Lissauer, 2022; Spiegel et al., 2011).

An early finding from the indirect methods was that there is a large population of giant ($\gtrsim$1 $M_{\rm Jup}$) planets at very small separations ($\lesssim$10 day periods). These "hot Jupiters" were unexpected and challenged our understanding of planet formation, which was originally based on our own solar system where planets are neatly arranged so that small planets are nearby and larger planets are further out. Their existence therefore raised immediate questions about their formation, leading to a few possibilities. One is in-situ formation through either gravitational instabilities or core accretion. The former is generally ruled out by thermal and dynamical constraints (Rafikov, 2005), but the latter is possible (Batygin et al., 2016). Another solution to the hot Jupiter conundrum is that the planets formed further from the star, where the disk provides plenty of gas and volatile elements to source from, and then they migrated inward to their final position. Different migrations theories thus evolved, including interactions with the protoplanetary disk leading to cavities and spirals that coerce the planet towards the star, or alternatively interactions with other forming planets and planetesimals that scatter the Jupiters inward. Any such theory must reconcile with results from observations and hence must explain the planets' final mass, position, and eccentricity. Fortney et al. (2021) provide a great review

on hot Jupiters, what we know about them, and the subsequent theories that have evolved from further observations of this surprising class of objects.

The categorization of planets from mass and separation was thus a useful tool from the start. As detection techniques matured, and transit observations provided radius measurements, they were combined with the mass measurements to obtain densities. These enabled further distinction of exoplanets by their bulk composition into gas giants, Neptune-like icy giants, and smaller rocky planets. Each of these categories leaves plenty of room for further diversity. For example, a surprisingly large number of terrestrial planets at small separations proved to have very large radii but relatively low mass, indicating a rocky core and an inflated atmosphere. Combining densities with separation measurements, predictions could be made about the material in the planet; a terrestrial planet at the appropriate distance from its star could have a bulk temperature that would support liquid water. In this way, we can group planets into categories of primarily silicate worlds, or water worlds, or super-heated gaseous behemoths, and much more. Many planets had no analogues to planets in our solar system, providing new samples against which theories can be tested.

With categories defined and a large sample size obtained, demographic-level studies ensued. Occurrence rates were a natural way to assess the importance of different categories and to search for trends within them. For example, one key trend is that stars with higher metallicity are more likely to host exoplanets (Fischer et al., 2005; Osborn et al., 2020), implying a relationship between planet formation and the type of readily-available material in the source disk.

One of the most significant findings from occurrence measurements is that sub-Neptunes and super-Earths are the most common outcomes of planet formation at short orbits. Figure 1.1, reproduced here from Fulton and Petigura (2018), shows the occurrence rate of planets in <100 day orbits as a function of planet radius. They found that planets with radii <4 $R_{\rm Earth}$ are an order of magnitude more common than their giant counterparts at these separations. The bimodal shape of the distribution is especially noteworthy. It indicates that there are two distinct populations of planets: sub-Neptunes ($\sim$2$-$4 $R_{\rm Earth}$) and super-Earths ($\sim$1$-$1.6 $R_{\rm Earth}$). The gap in occurrence between the two encodes details about the formation mechanism, such as the fundamental role that photoevaporation can play in the retention or loss of atmospheres for small planets (Owen et al., 2013). Interestingly, our solar system has no analogues for either of these types of planets despite their prevalence elsewhere.

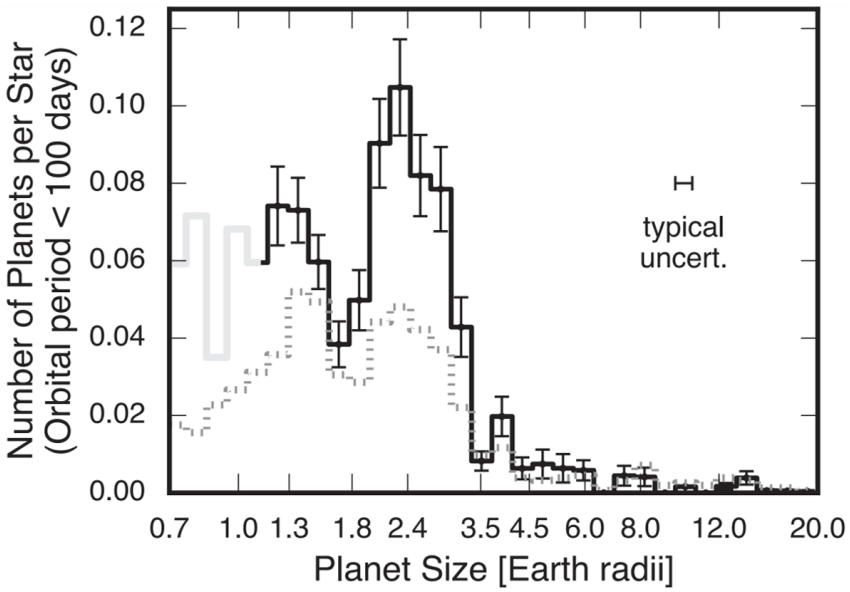


Figure 1.1: Distribution of close-in planet sizes. The solid line shows the number of planets per star with orbital periods less than 100 days as a function of planet size. A deep trough in the radius distribution separates two populations of planets with $R$>1.7 $R_{\rm Earth}$ and $R$<1.7 $R_{\rm Earth}$. As a point of reference, the dotted line shows the size distribution of detected planets, before completeness corrections are made arbitrarily scaled for visual comparison - Figure and caption adapted from Fulton and Petigura (2018), showing evidence of the photoevaporation gap.

Another major finding is in the occurrence rate for giant planets beyond 0.3 AU. Figure 1.2, reproduced here from Fulton, Rosenthal, et al. (2021), shows that there is a pronounced peak in the giant planet occurrence rate between 1 and 10 AU. This was determined by combining 30 years' worth of surveys and accounting for completeness in the observations. Giant planets are thus 4 times more likely to be found at these key separations than within 1 AU, and two times more likely than beyond 10 AU. The sharp increase around 1 AU seems to correlate with the snow line where water condenses into ice around typical stars. Such a correlation could indicate that increased solid material enhances giant planet creation, and could have implications on migration models. The increased occurrence from 1-10 AU is of particular interest to this thesis since it motivates new techniques, like vortex fiber nulling, that can target giant planets where they are most likely to orbit (see Sec. 1.4).

The findings mentioned in this section are just a glimpse of select highlights from the indirect methods so far. Imminent improvements provided by Gaia and other recent or upcoming indirect detection instruments (Pepe et al., 2021; Szentgyorgyi et al., 2018) promise to further grow the exoplanet census and expand our understanding.

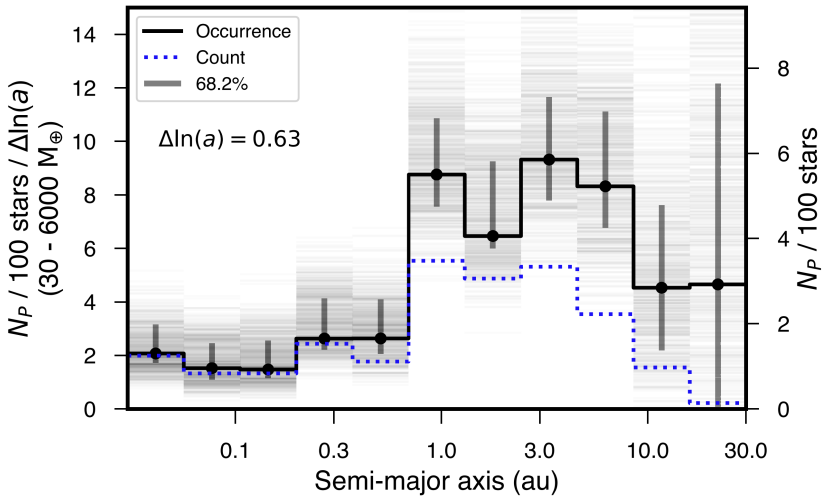


Figure 1.2: Nonparametric occurrence rates for semi-major axes of 0.03–30 AU for planets with minimum masses from 30–6000 $M \sin i$, assuming uniform occurrence across $\ln(M \sin i)$. The dashed blue line represents a planet count in each semi-major axis bin without correcting for completeness, bold lines and dots show the maximum posterior values for the Poisson likelihood model, vertical lines represent 15.9%–84.1% confidence intervals (except for the last bin, which shows 0–68.2%), and transparent steps show draws from the occurrence posterior. We see a clear enhancement around 1–10 AU, and a tentative fall-off beyond that range - Figure and caption adapted from Fulton, Rosenthal, et al. (2021).

### 1.3 Spectral Characterization

Indirect methods have therefore built our understanding of planet demographics, including how common different types of planets are and their bulk properties. From these we have gained insights into planet formation and migration mechanisms. However, there remain glaring holes in our knowledge, some of which can only be addressed by observing the spectra of the planets themselves. A spectrally-resolved view provides a new window through which to analyze exoplanets and also holds promising avenues for improving the sensitivity of exoplanet detections.

A planet's spectrum encodes a great deal of information about the physical, chemical, and possible biological processes that shaped its history (Birkby, 2018). The planet's atmosphere in particular leaves a distinct signature on the observed light, and can only be characterized through spectroscopy. However, the wavelength sampling, or resolution ($R = \lambda/\Delta\lambda$), of the spectrum can either reveal the details or hide them depending on the discernible features. Figure 1.3, reproduced from Birkby (2018), shows a modeled atmospheric spectrum of a hot Jupiter containing $H_2O$ and CO. The spectral lines are completely blended together at the lowest resolutions such that

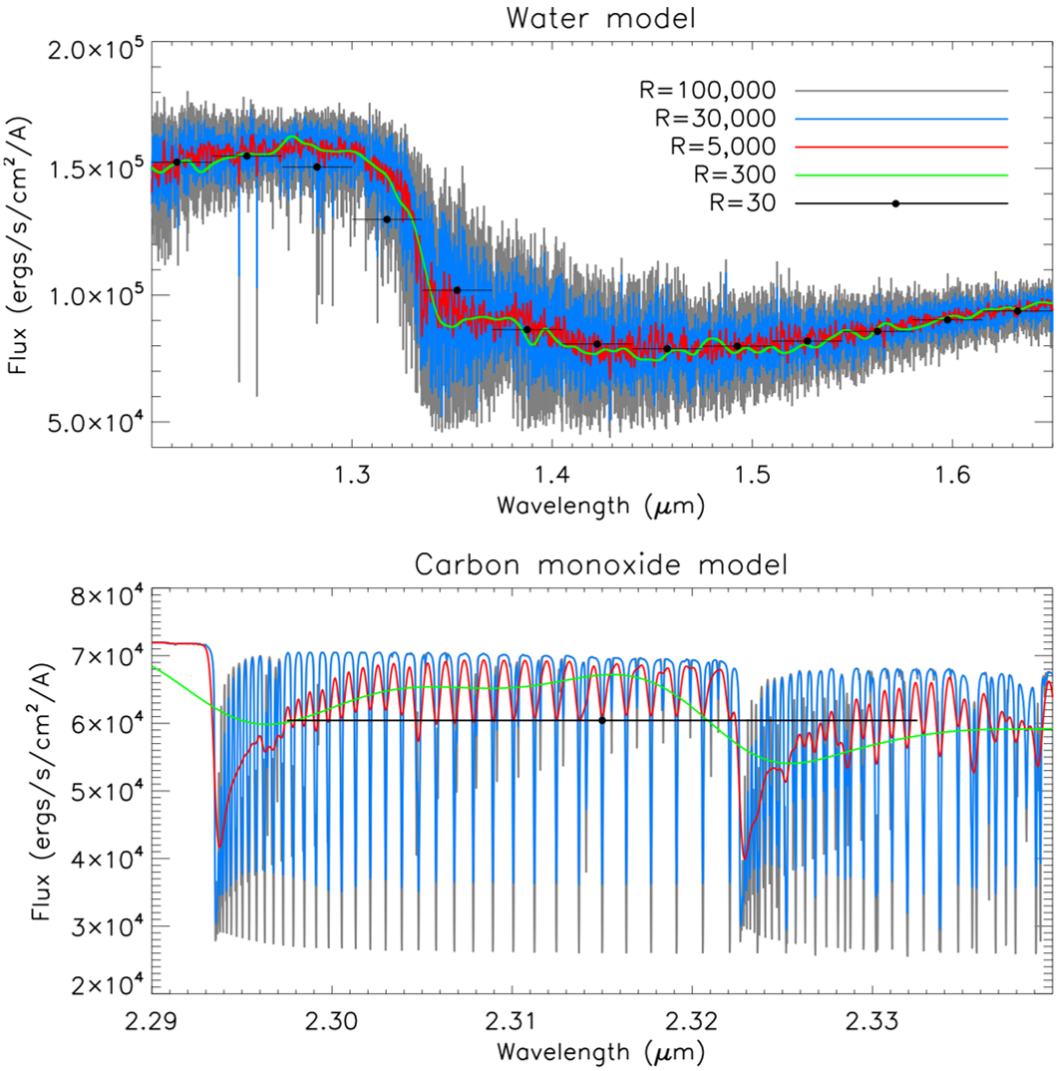


Figure 1.3: The effect of decreasing spectral resolution. The two panels show different wavelength regions of a model hot Jupiter atmosphere containing water and carbon monoxide. Note the difference in the x-axis scale. The model has been convolved to different spectral resolutions. Note how many individual CO lines are lost between a resolution of $R$=100, 000 and $R$=300. The shallower lines disappear more quickly, but some of the stronger CO lines remain even at $R$=5, 000, albeit much reduced in line depth. Each line that is detected with the high-resolution technique increases the total planet signal-to-noise by a factor of $\sqrt{N_{\rm lines}}$ - Figure and caption adapted from Birkby (2018).

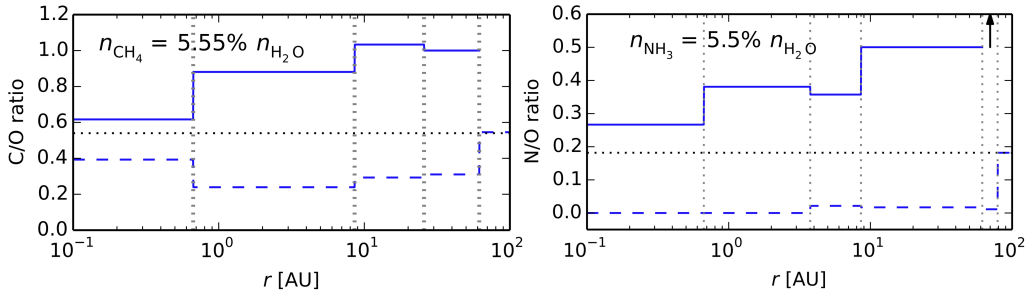


Figure 1.4: Abundance ratios is protoplanetary disks. Left: C/O ratio in gas (solid lines) and dust (dashed lines) as a function of semi-major axis in a static disk, assuming the median observed $CH_4$ abundance. Estimates assume that the CO ices are in pure form. The veritcal dotted lines mark the snowline locations of the main C and O carriers. Right: Same as left but for N/O ratio, assuming the median observed $NH_3$ anundance and that the CO and $N_2$ ices are in pure form - Figure and caption adapted from Piso et al. (2016).

an observation only shows the underlying continuum shape of the spectrum. This can help determine the spectral type of the exoplanet. However, as the resolution improves, the bandhead and individual spectral lines start to be resolved. At the highest resolutions, the lines are deep and readily distinguished from each other, and the shapes of different lines can be determined. This unlocks significantly more information, making high spectral resolution observations invaluable to exoplanet science.

With resolved spectral lines, it is possible to determine the chemical composition of an exoplanet's atmosphere since each molecule produces a unique set of lines that are distinguishable at high resolution. Measurements of the presence and quantity of $H_2O$, $CO_2$, CO, $NH_3$, and other molecules can then be used to determine the abundance of individual elements and yield ratios thereof, such as C/O and N/O. These ratios are valuable in themselves since they provide insight into the atmosphere. However, they can also be used as tracers of the exoplanet's origin within the protoplanetary disk that spawned it. Öberg et al. (2011) and Piso et al. (2016) showed that the elemental ratios vary within a protoplanetary disk due to the snowlines, or boundaries where different molecules condense out of their gaseous form. This is shown in Fig. 1.4 for C/O and N/O, reproduced from the Piso et al. (2016) paper. As an exoplanet forms, it will pull from the available materials in the disk and thus its abundance ratios reflect the ratios of the location where it formed. With high-enough spectral resolution it is possible to differentiate

between different isotopologues and hence get abundance ratios at the isotope level, such as Deuterium/Hydrogen or $^{13}C/^{12}C$. This can provide further granularity on the origin of an exoplanet within the disk as well as the formation pathway that the exoplanet may have taken (Mollière et al., 2019). Abundance measurements provided by spectra can therefore tell us about the formation and migration history of exoplanets, helping resolve open questions between different theories derived from indirect methods.

Beyond atmospheric composition, spectroscopy can inform on dynamic processes from the exoplanet. For example, with resolved spectral lines, it is possible to measure the broadening introduced by spin as part of the planet's atmosphere gets red shifted and another part gets blue shifted (Snellen, Brandl, et al., 2014). This measurement of the length of a day on a planet has significant implications on formation history. As a planet cools down, it tends to spin-up due to conservation of angular momentum. However, interactions with the host-star's gravity, such a tidal locking for close-in exoplanets, can dampen the rotational velocity. Other mechanisms can also set the terminal rotation rate. Magnetic braking introduced by a coupling of the exoplanet's magnetic field to the circumplanetary disk can absorb some of the angular momentum and reduce the rotation rate (Batygin, 2018). With high-enough spectral resolution, measurements can go beyond spin to Doppler imaging, which generates spatially-resolved maps of the planet's atmosphere and cloud coverage (Crossfield et al., 2014). Even though the exoplanet itself remains unresolved in such observations, this converts the planet atmosphere from a one-dimensional composition model to a churning 2 or 3D body with different atmospheric layers and gradients. Insight into the presence of clouds and their distribution feeds back into the atmospheric models that are used for retrievals and hence helps provide more accurate abundance and other measurements as well.

Exoplanet spectroscopy can also strengthen the information provided by indirect measurements. For example, in the same way that the host-star's radial velocity is measured in the RV method, direct observations can measure the exoplanet's own radial velocity. This provides additional information about the planet's orbit and can help constrain orbital parameters and obtain the planet's true mass (Schwarz et al., 2016; Lecavelier des Etangs and Vidal-Madjar, 2016; Xuan et al., 2023). Beyond the science value, the Doppler shift in an exoplanet's lines has technological applications as well. The exoplanet and star will generally have different RV shifts during a given observation, and this can be used to disentangle the star's spectrum

from that of the exoplanet. For exoplanets with short orbits, the RV can change within a few hours, such that the shift would be measurable over the course of an observation. The exoplanet's spectral lines can then be distinguished from that of the host star or from the Earth's atmosphere (tellurics) since the latter will remain mostly fixed in the instrument's reference frame whereas the exoplanet lines will be shifting over the course of the observation. This is just one element of high dispersion coronagraphy (HDC), which will be expanded upon in the following section after some of the challenges in obtaining spectra have been introduced.

Many of the applications and utilities for high resolution spectroscopy mentioned here focus on giant planets. This is partially because giant planets are easier to detect, as explained in the next section. However, understanding giant planets is of crucial importance more broadly since their gravity has massive impacts on their stellar system as a whole and especially on other planets in the system. Giant planets shape the orbits of other planets and can shape the protoplanetary disk itself. They therefore move and possibly drain the material from which other planets draw during their own formation. Giant planets can also launch material at other planets; looking at our own solar system, it is believed that Jupiter's gravity bombarded the Earth in a period known as the Late Heavy Bombardment with icy comets that may have provided much of the water we now have (Gomes et al., 2005). It is reasonable to expect that the same thing is happening in other systems. Thus building an understanding of giant planets also helps build an understanding of smaller planets.

Looking forward, the techniques being developed, tested, and optimized on giant planets will inform and be directly applicable to smaller planets in the future as engineering capabilities improve. For example, abundance ratios and composition measurements of super-Earths and sub-Neptunes can help explain how these two populations of planets differ and the paths that they followed in their formation. Eventually, high resolution spectroscopy of exoplanets may verify the presence of molecules in exoplanet atmospheres that point to biological processes. Such "biosignatures" would revolutionize our understanding of life, how it develops, and how it evolves. However, such capabilities are predicated on sensitive molecular detections that require testing and validation with less challenging exoplanets.

### 1.4 Methods for Spectroscopy

There are two prevailing techniques for obtaining spectra from exoplanets. The first, more widely applied so far, is transit spectroscopy. This builds on the transit pho-

tometry method but measures the transit depth at different wavelengths to measure the spectrum. The second prevailing technique is direct imaging, which spatially resolves the exoplanet from its host star to sample photons from the planet directly.

**Transit Spectroscopy**

As a planet transits in front of its host star, the bulk of its core blocks out some of the starlight. However, some light passes through the exoplanet's atmosphere, which preferentially filters specific wavelengths depending on the chemical composition of the atmosphere. Spectra taken during the transit therefore show different transit depths at each wavelength, providing the opacity as a function of wavelength and therefore the exoplanet's transmission spectrum. For this reason, this is known as transmission spectroscopy. Another related form of spectroscopy observes the exoplanet as it passes behind (i.e., is eclipsed) by its host star. Shortly before the the eclipse, the measured signal contains light form both the star and exoplanet. Once the planet passes behind the star, its signal is blocked and hence only the star's spectrum is measured. Through careful calibration and subtraction of the pre- and post-eclipse spectra, the planet's emission spectrum can be obtained.

Given the sensitivity of transit observations, and the multitude of transiting exoplanets, this technique has been extremely successful; transit spectra have been obtained for more than 130 exoplanets so far[2]. These spectra are crucial to our understanding of atmospheres for close-in exoplanets. CO, $H_2O$, $CH_4$, $CO_2$ and other molecules have been detected in hot Jupiters and warm Neptunes (Brogi and Line, 2019; Snellen, de Kok, de Mooij, et al., 2010; Tinetti et al., 2007; Swain, Vasisht, et al., 2008; Swain, Tinetti, et al., 2009). Wind patterns, both day-to-night side and vertical, have also been detected (Brogi, de Kok, et al., 2016; Seidel et al., 2020; Snellen, de Kok, de Mooij, et al., 2010). Similarly, detections have been made of the condensation of volatile species like iron as they pass through the exoplanet's cooler night side (Ehrenreich et al., 2020). Combined, these results provide deep insights into the 3D nature of atmospheres and the dynamical processes within them, that can then be used to test different atmospheric and cloud models (Miller-Ricci Kempton et al., 2012; Zhang et al., 2017; Harada et al., 2021; Flowers et al., 2019; Beltz et al., 2021). This is only a sample of the findings and impact from transit spectroscopy.

[2]Based on the NASA Exoplanet Archive's Atmospheric Spectroscopy Table

**Direct Imaging**

The second prevailing method capable of providing exoplanet spectra is direct imaging. This is the "intuitive" technique alluded to at the very beginning the chapter, where light from the exoplanet is observed directly in the same way that other cosmic objects are observed. As mentioned earlier, the challenge is that the light from an exoplanet is many orders of magnitude fainter than that from its host star, such that the planet photons are drowned out in the flood of starlight; giant self-luminous exoplanets are generally $10^{-3}$–$10^{-5}$ times fainter than their host star in the near-infrared while terrestrial planets are significantly fainter. The holy grail of exoplanet imaging, an Earth-like planet around a Sun-like star, would be at a flux ratio of $10^{-10}$ in the visible.

High-contrast imaging instruments use coronagraphs to address this challenge. The coronagraph suppresses starlight while allowing planet light to efficiently pass through the instrument. There are many coronagraph designs but they generally converge to have an optic that preferentially manipulates the starlight in one plane and then a downstream optic that rejects the light in a subsequent plane. The classic Lyot coronagraph, for example, uses an opaque spot to block the core of a star's image in a focal plane. This diffracts light to the edges of the aperture in the subsequent pupil plane, where a Lyot Stop slightly smaller than the geometric pupil blocks the edges of the beam, thereby preventing the starlight from propagating to the final focal plane. Though originally invented to observe the solar corona (Lyot, 1939), the design similarly allows the off-axis exoplanet light to pass unobstructed by the focal plane mask, thereby mitigating the starlight while making an exoplanet visible. Coronaraphs can use both phase and amplitude effects in the focal or pupil plane to achieve the desired starlight rejection, and there are now a plethora of different designs. Some options include: vortex coronagraphs that place a phase screw in the focal plane (Mawet et al., 2005; Foo et al., 2005; Ruane et al., 2018), shaped pupil coronagraphs which block parts of the pupil to modify the amplitude (Kasdin et al., 2003; Currie, Kasdin, et al., 2018), and phase-induced amplitude apodization coronagraphs that use phase to provide similar amplitude modulation (Guyon, 2003).

Coronagraph designs can attain deep starlight rejection but they all assume a specific input light, generally a flat wavefront at the pupil. Aberrations from the atmosphere and within the optical train deviate the starlight from this ideal, introducing wavefront errors that allow starlight to leak through the coronagraph. Adaptive optic (AO)

systems mitigate this effect by measuring and correcting the wavefront (Babcock, 1953; Wizinowich et al., 2000; Rousset et al., 2003). While the effects of AO in other fields of astronomy are striking, bringing blurry and crowded fields into sharp focus, AO is fundamental to achieving viable starlight rejection with coronagraphs through the Earth's turbulent atmosphere. However, even with the best AO correction provided by modern systems, coronagraphic images are still plagued by residual wavefront errors that lead to "speckles." These spot-like concentrations of starlight can mimic the signal from an exoplanet, thereby contaminating the image plane and limiting the detection capabilities (Racine et al., 1999). Coronagraphs are being designed to be more robust to wavefront errors, and different observing and analysis strategies have been developed to help distinguish speckles from exoplanets. For example, angular differential imaging (ADI) leverages the natural field rotation introduced as a star moves in the sky during an observation (Marois, Lafrenière, et al., 2006). During post-processing, the images can be de-rotated and stacked such that the quasi-static speckles are smeared in the final image while the planet is fixed relative to the star. Another example is reference-star differential imaging (RDI) where images on various reference stars are stacked and then subtracted from the images on the target star, thereby removing the quasi-static speckles that are consistent across all the frames (Lafrenière et al., 2009).

Some of the challenges of direct imaging can also be tackled with high-dispersion coronagraphy (HDC). This idea combines the starlight rejection capabilities of high-contrast imaging with the spectral discrimination capabilities of high-resolution spectroscopy (Snellen, de Kok, Birkby, et al., 2015; Kawahara et al., 2014; J. Wang, Mawet, Ruane, et al., 2017). Beyond enabling a detailed spectral characterization of exoplanets (see Sec. 1.3), the high resolution spectra in HDC provide several benefits that can be exploited to improve the sensitivity and detection capabilities of exoplanet imagers. At high spectral resolution, the host star's spectrum is distinctly different from the exoplanet's due to their different temperatures, molecular composition, radial velocity, and more. For example, the previous section covered how the Doppler shift can be used to disentangle the two spectra. The spectrum of the exoplanet is also distinct from the low-frequency spectral signature of a speckle, such that HDC can mitigate the effect of quasi-static speckles in observations (Sparks et al., 2002). These differences effectively amount to a post-processing gain where the strength of a detection is improved by leveraging the distinctive features in the spectra. The magnitude of this gain depends on many aspects of the spectra, such as the number of resolved spectral lines and the line depth (Birkby, 2018). A recent

demonstration with medium resolution spectra from the James Web Space Telescope (JWST) showed a gain of $10^2-10^3$ with HDC compared to other post-processing techniques (Ruffio et al., 2023).

As with the other exoplanet detection methods, direct imaging has biases that make it better at detecting certain types of planets. One such bias is towards young giant planets, since planets generally cool down with age such that younger planets are hotter and hence brighter. This improves the relative flux ratio compared to the central host star and reduces the impact of residual starlight. For this reason, direct imaging surveys often target young stars whose exoplanets are still hot and bright from formation. Additionally, direct imaging is particularly biased towards exoplanets on wide orbits. The intensity of residual diffracted light from the host star decreases with separation in the focal plane. This means that an exoplanet observed further from its star faces less residual starlight than an exoplanet observed at a smaller separation. Taken altogether, these biases mean that current direct imaging instruments are primarily sensitive to giant planets at wide separations from young stars. This demographic is conveniently complementary to the population of exoplanets observable with other techniques.

According to the NASA Exoplanet Archive, 69 exoplanets have been detected via direct imaging as of December 11 2023. The HR 8799 system is a prototypical direct imaging discovery with four giant exoplanets of $\sim$7$-$10 $M_{\rm Jup}$ orbiting between 15 and 70 AU from the host star (Marois, Macintosh, et al., 2008; Marois, Zuckerman, et al., 2010). These planets have been extensively characterized with spectroscopy (J. J. Wang, Ruffio, et al., 2021; Doelman et al., 2022; Oppenheimer et al., 2013), and as some of the first wide-orbit exoplanets to have their spectra taken, they revealed distinct differences from other similar-mass objects. For example, they show little to no $CH_4$ absorption, suggesting disequilibrium chemistry (J. Wang, Mawet, Fortney, et al., 2018), and appear to extend the L/T transition to redder and lower luminosities (Bowler et al., 2010). Other exemplar exoplanets from direct imaging include $\beta$ Pic b, a $\sim$9 $M_{\rm Jup}$ exoplanet on a edge-on 9 AU orbit that was the first exoplanet to have its spin measured (Lagrange, Gratadour, et al., 2009; Snellen, Brandl, et al., 2014), and 51 Eri b (Macintosh, Graham, Barman, et al., 2015) which competes with PDS 70 b and c for the title of lowest mass directly imaged exoplanet (J. J. Wang, Ginzburg, et al., 2020). Currie, Biller, et al. (2023) provide a great up-to-date review of exoplanet direct imaging and related spectroscopy.

Looking forward, several major developments promise to improve the capabilities and sensitivity of high-contrast imaging systems. Upgrades to extreme AO systems should reduce residual post-coronagraphic starlight in images by a factor of 10 to 100 on current telescopes in the coming years (Males et al., 2020; Guyon et al., 2020). The move to extremely large telescopes will increase the surface area and hence the number of available photons by $\sim$10$\times$ over the largest current telescopes, and will push to planets at smaller separations. The Roman Coronagraphic Instrument, slated to launch in the mid 2020's, will demonstrate wavefront sensing and control with deformable mirrors in space for the first time, suppressing starlight down to $\leq 10^{-8}$ of its raw flux (Shi et al., 2017; Seo et al., 2018). Looking even further, the Astro 2020 Decadal Review recommended a dedicated high-contrast imaging mission to launch in the 2040's. Known as the Habitable Worlds Observatory (HWO), this mission has a goal of detecting and characterizing $\sim$25 habitable Earth-like exoplanets (National Academies of Sciences, Engineering, and Medicine, 2021).

**A Gap in Coverage**

Transit spectroscopy and direct imaging have therefore had great success in spectrally characterizing exoplanets so far, and both hold promising prospects for the future. However, these two techniques are limited in the exoplanets that they can characterize. Transit spectroscopy relies on a chance alignment between an exoplanet and its host star. This means that the probability that a planet can be observed in transit rapidly diminishes with increasing orbital separation (see Eq. 1.4). Thus, transit spectroscopy is only sensitive to exoplanets on short orbits. Meanwhile, direct imaging is sensitive to exoplanets on wide orbits. Though coronagraphs can efficiently suppress starlight over a large region around the star, they have an inner working angle (IWA) within which they begin to suppress the planet as well. Once the coronagraph suppresses the already-faint planet light, the exoplanet's signal becomes lost in the stellar glare and detector noise. The IWA is conventionally defined as the point where the coronagraph's throughput for the planet is 50% of its maximum at wide separations. Current coronagraphic instruments have an IWA of $\sim$2$-$3 $\lambda/D$ within which detection is nearly impossible (where $\lambda$ is the wavelength and $D$ is the telescope diameter) (Macintosh, Graham, Ingraham, et al., 2014; Beuzit et al., 2019). This IWA conspires with the decreasing transit probability to create a region of orbital separations that cannot be readily characterized.

Figure 1.5 shows the known exoplanets with measured spectra plotted by semi-major axis and planet mass (where the mass can also be the "minimum" mass $M_p \sin i$

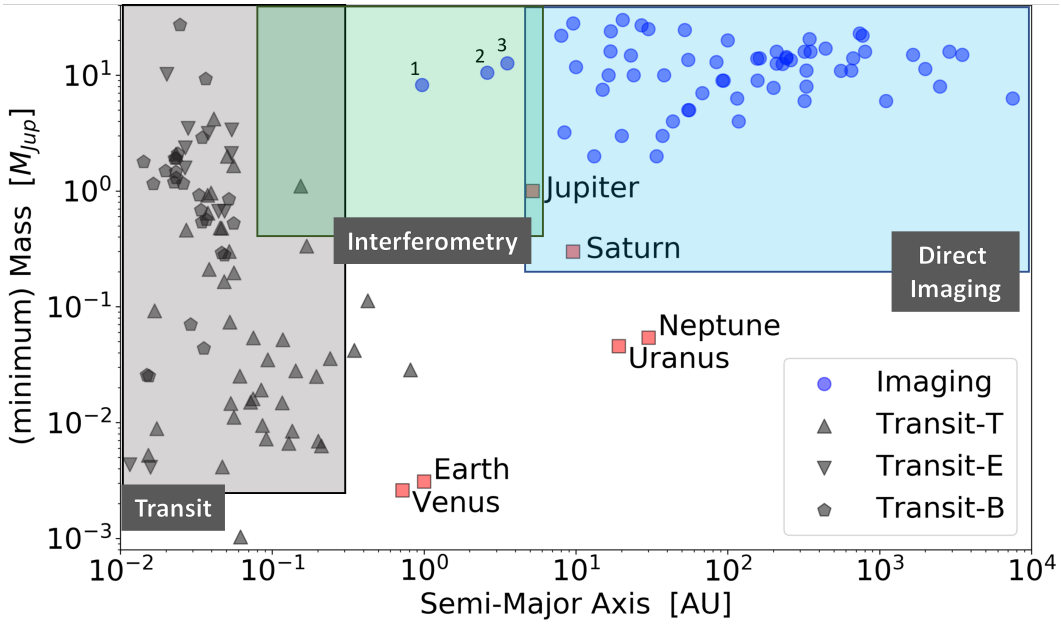


Figure 1.5: Exoplanets with measured spectra plotted by orbit semi-major axis and planet mass. Planets observed via transit spectroscopy are in grey. Upward pointing triangles show planets with transmission spectra, downward pointing are for emission spectra, and pentagons are for planets with both transmission and emission spectra. Directly imaged planets are shown as blue circles. The boxed regions roughly represent the limits of each technique. The three numbered imaging planets within the interferometry region are briefly discussed in the relevant paragraph in this section. The data for this plot was take from the NASA Exoplanet Archive's Planetary Systems and Atmospheric Spectroscopy tables. Note that planets with spectra but no listed orbital separation or mass are omitted from the plot.

when the true mass is unknown). The figure was made using data from the Planetary Systems and Atmospheric Spectroscopy tables available on the NASA Exoplanet Archive. This assumes that spectra have been obtained for all directly imaged exoplanets, which is a fair assumption since all current direct imaging instruments can at least obtain photometry in different spectral bands. Planets with transit spectra are shown in grey while planets with imaging spectra are in blue. Note that some planets are omitted from the plot because they do not have a known semi-major axis or mass. The grey box denotes the approximate domain spanned by the transit technique, based on where the bulk of the data points lie. The blue box denotes the imaging domain in the near-infrared for current telescopes; the left bound is set at 4.5 AU based on a 2 $\lambda/D$ IWA at $\lambda$=2.0 $\mu$m and $D$=10 m for a star at 50 pc.

There is a clear gap in the figure from about 0.3 AU to 4.5 AU where neither transit nor direct imaging can efficiently obtain exoplanet spectra. Unfortunately, this gap

largely coincides with the peak of the giant planet occurrence rate, which spans 1-10 AU (see Sec. 1.2 and Fig. 1.2).

The three blue points within 4.5 AU are noteworthy as outliers for the direct imaging technique. The point labeled 1 is a brown dwarf binary whose low flux ratio ($\sim 1/10$) and close proximity (10 pc) enabled JWST to detect it despite the small orbital separation (Calissendorff et al., 2023). Point 2 is also a brown dwarf binary, with a similarly favorable flux ratio of $\sim 1/7$ and at 25 pc, detected from the ground using the Keck AO system (Liu et al., 2011). The final point, 3, is of particular interest to this thesis since it is a $\sim$13 $M_{\mathrm{Jup}}$ companion to an F5V-type star at 40 pc with a flux ratio of $10^{-4}$, but detected with the VLTI/GRAVITY instrument (Hinkley, Lacour, et al., 2023). This makes it an interferometric detection, as opposed to a typical direct imaging detection. Interferometry is a third technique capable of obtaining exoplanet spectra at significant flux ratios and targeting exoplanets in the gap between transit and direct imaging; its domain is shown in green in Fig 1.5. The vortex fiber nulling technique at the core of this thesis is a novel implementation of interferometry.

## 1.5 Interferometry and Nulling

Interferometry is a detection technique that, like direct imaging, can capture the light directly from exoplanets themselves. As its name suggests, interferometry works through constructive and/or destructive interference of the incoming light. This makes it sensitive to minute differences in the input signal, providing access to small angular separations. The sensitivity is precise enough that one of the earliest applications was for measuring stellar radii (Michelson et al., 1921), and since then it has been used to resolve spots and convection patches on stellar surfaces (Paladini et al., 2018; Roettenbacher, Monnier, Korhonen, et al., 2016). Interferometry can therefore access exoplanets at small and intermediate separations, including those that are inaccessible to transit spectroscopy and direct imaging (see Fig. 1.5). Thus, interferometric instruments enable the spectroscopic characterization of giant planets where they are most likely to occur. Even as high-contrast imaging instruments move to shorter wavelengths, where the IWA decreases by a factor of ~4 (e.g., from 2000 nm to 500 nm), interferometry will have its place. An exoplanet detected at the inner edge of the coronagraph in short wavelengths will disappear behind the IWA at longer wavelengths, such that it cannot be characterized in the near-infrared with the same setup. Interferometric observations in the near-infrared can then supplement the coronagraph's detection to provide spectra over a wider region.

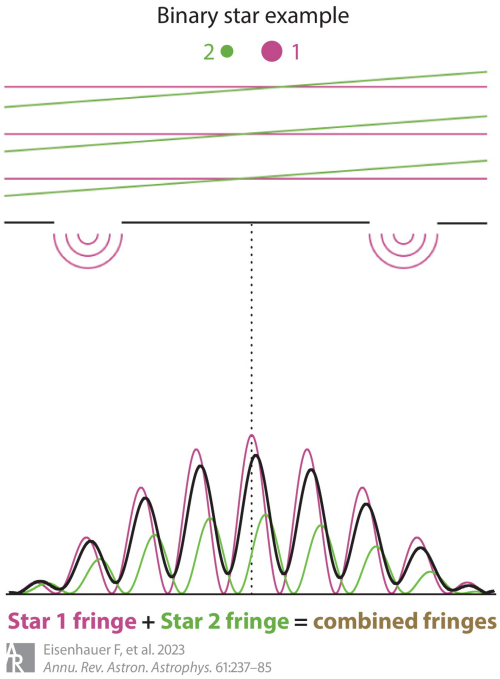


Figure 1.6: Young's two-slit experiment illustrates the basics of optical interferometry. Each part of a distant source (red+green) creates its own fringe that incoherently adds together (black). - Figure and caption adapted from Eisenhauer, Monnier, et al. (2023).

Interferometry generally works by combining plane waves to create a distinctive sinusoidal interference pattern, or "fringe," similar to that from Young's double-slit experiment. As shown in Fig. 1.6, each point in the field creates fringes with a unique phase and intensity based on the position and brightness at that location. The fringes from different points in the field combine incoherently to generate an interferogram whose amplitude and phase uniquely encode information about the source. Since each point generates a sine wave, the intensity distribution of the imaged field can be determined with a Fourier Transform. This standard implementation, relying on constructive interference, is already extremely capable, though it does not suppress the glare of the starlight. An alternative implementation specifically geared towards exoplanet detection was proposed by R. N. Bracewell in a 1978 paper that stated, "a way to enhance the planet over the star is to place an interference null on the star" (Bracewell, 1978). A more detailed explanation of the so-called "nulling" interferometer was further developed in two subsequent papers (Bracewell and MacPhie, 1979; MacPhie et al., 1979). This original Bracewell nuller thus combines the light from two symmetric telescope apertures but with a $\pi$ phase shift between

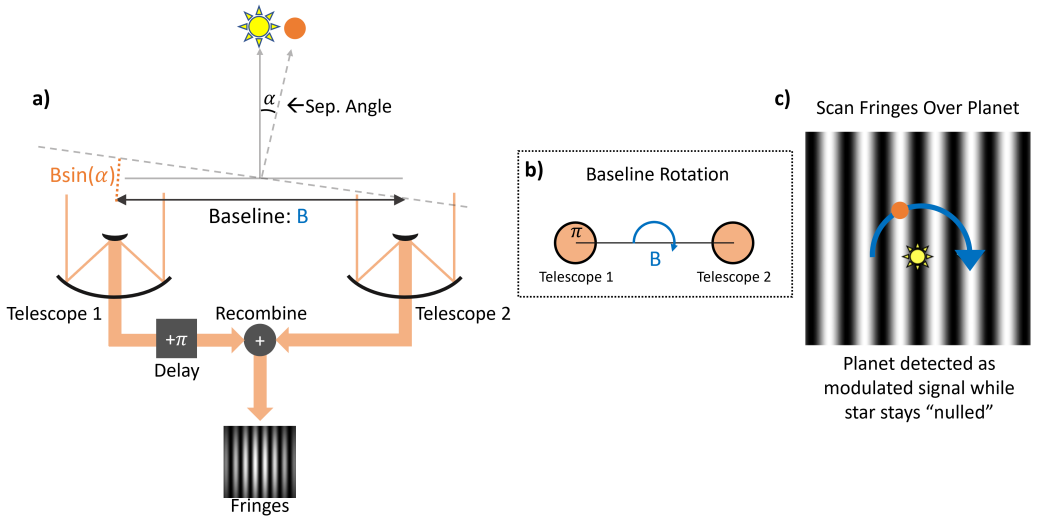


Figure 1.7: Bracewell nulling concept. (a) The light from two symmetric telescope apertures separated by a baseline $B$ is combined with a $\pi$ phase shift between the two to create interference fringes. Both telescopes are pointed at a host star with an exoplanet at a separation angle $\alpha$. The optical path delay for the off-axis planet light between the two telescopes is approximately $B\sin(\alpha)$. (b) The baseline between the two telescopes is rotated, or alternatively, the field rotates around the baseline. (c) This causes the bright fringes to scan over the planet resulting in a modulation of the planet signal. The host star stays centered on the on-axis dark fringe, thereby nulling the starlight.

the two. The result is an on-axis destructive interference fringe and periodic off-axis constructive bright fringes, as shown in Fig. 1.7(a). By aligning the star with the dark on-axis fringe, its light is rejected while the light from an off-axis planet is passed with the intensity of the bright fringe that it lands on.

At the heart of nulling is the destructive interference of plane waves from a source. The wave from each aperture can be described by

$$U_j(\lambda) = A_j(\lambda)e^{i\frac{2\pi}{\lambda}d_j + i\phi_j}, \tag{1.5}$$

where $A_j$ is the amplitude for each wave, $d_j$ is the optical path delay, and $\phi_j$ is the phase shift. In the classical Bracewell design, two apertures and hence two waves are used. Assuming that the two apertures are such that the waves have equal intensity, then $A_1^2 = A_2^2 = A^2 = I_0$. When the two waves are interfered, the transmitted intensity of the resulting light is

$$I(\lambda) = |U_1(\lambda) + U_2(\lambda)|^2 = 2I_0(\lambda)\left[1 + \cos\left(\frac{2\pi}{\lambda}(d_1 - d_2) + (\phi_1(\lambda) - \phi_2(\lambda))\right)\right]. \tag{1.6}$$

Setting telescope 2 as the reference point, then $d_2 = 0$ and $d_1 \approx B\alpha$ for small off-axis angles (see Fig. 1.7(a)). Here, $B$ is the baseline, or the separation between the two telescopes, and $\alpha$ is angular separation to the second source point. A $\pi$ phase shift is purposely introduced between the two apertures such that $\phi_1(\lambda) - \phi_2(\lambda) = \pi$ for a properly-phased nuller. With these values and some trigonometric identities, Eq. 1.6 simplifies to

$$I(\lambda) = 4I_0(\lambda) \sin^2\left(\frac{\pi\alpha B}{\lambda}\right). \tag{1.7}$$

This $\propto \sin^2(\pi\alpha/\Phi)$ relationship, where $\Phi = \lambda/B$ is the fringe period, is the key relationship from Bracewell's original proposal. The resulting fringe pattern, shown in Fig. 1.7, can be thought of as a "transmission map" projected onto the sky. Light from points in different parts of the field are transmitted with an efficiency set by the intensity of the fringe that lies over them. The on-axis star has $\alpha = 0$, thereby overlapping with the central dark fringe, such that $I = 0$ and its light is suppressed. Meanwhile the exoplanet rests off-axis, overlapping with some bright part of a fringe. Its transmittance is generally non-zero, with peak efficiency occurring when it lies at the peak of a fringe, at a separation of $\alpha = \lambda/2B$ along the axis perpendicular to the fringes. Bracewell took this a step further by introducing a baseline rotation, shown in Fig. 1.7(b,c), at a specific frequency so that the fringes also rotate and are scanned over the exoplanet. While the star's image remains fixed on the central dark fringe, the planet signal is modulated at a known frequency that can be distinguished from other variations arising from phase or other errors. Note that with a spectrally-resolved signal of sufficient resolution, the planet could be disentangled from the star spectroscopically with the HDC technique rather than photometrically with baseline rotation. In the HDC case, the nuller serves to reduce the perceived flux ratio between the two sources. However, increasing the resolution for a conventional nuller can pose additional challenges not covered here but that complicate a spectral-only detection.

The quality of starlight rejection can be quantified by the "null" depth

$$N = \frac{I_{\text{min}}}{I_{\text{max}}}, \tag{1.8}$$

where $I_{\text{min}}$ is the residual stellar intensity after *destructive* interference and $I_{\text{max}}$ is the intensity with *constructive* interference (i.e., the intensity of the total starlight collected by the cumulative aperture area). This is analogous to the contrast provided by a coronagraph, which is the ratio of the intensity of the residual starlight with the coronagraph versus the peak intensity of the stellar image without the coronagraph.

A deeper null indicates less residual starlight on the detector and hence a more favorable observation for the exoplanet. A point-like star would be completely nulled such that $I_{\min} = 0$ and therefore $N = 0$. However, with the spatial resolution of an interferometer, the star's true finite angular size causes a non-zero amount of starlight leakage as the star's limbs start to overlap with the bright fringes. This is known as the geometric stellar leakage, and for a uniform stellar disk it is given by

$$N_{\mathrm{gl}} = \frac{\pi^2}{4}\left(\frac{B\theta_\star}{\lambda}\right)^2, \tag{1.9}$$

where $\theta_\star$ is the angular radius of the star (Absil et al., 2006). In a well-pointed rotating nuller, the bias from this leakage is constant for a uniform star and hence can be removed from the observation, but the photon noise contribution remains a source of error. Another similar source of null degradation is introduced by exozodiacal dust, which acts as an extended source of light overlapping several bright fringes in the interferometer (Defrère, Absil, den Hartog, et al., 2010; Absil et al., 2006). This was a significant concern in early nulling development as the occurrence and magnitude of exozodii were unknown. However, surveys performed by major first-generation nullers have shown that exozodii will generally not be a concern in exoplanet surveys (Ertel et al., 2020; Mennesson, Millan-Gabet, et al., 2014). A different type of error, not due to a resolved extended source, arises from an imperfect phase shift. A phase error can be expressed as, $\Delta\phi(\lambda) = \pi + \epsilon(\lambda)$, where $\epsilon(\lambda)$ is the wavelength-dependent phase error. The average residual stellar intensity over a $\Delta\lambda$ bandwidth is then

$$I_{\min} = \int_{\Delta\lambda} I(\lambda)d\lambda = 2I_0 \int_{\Delta\lambda} \left[1 + \cos(\pi + \epsilon(\lambda))\right] d\lambda, \tag{1.10}$$

where a flat input spectrum is assumed such that $I(\lambda) = I_0$ at all wavelengths. Recognizing that $1 + \cos(\pi + \epsilon(\lambda)) = 2\sin^2(\epsilon(\lambda)/2)$, and assuming that $\epsilon$ is small, the average null contribution across the band from phase errors is thus

$$N_{\mathrm{pe}} = \frac{I_{\min}}{I_{\max}} = \frac{\int_{\Delta\lambda} \epsilon(\lambda)^2 d\lambda}{4\Delta\lambda} = \frac{\sigma^2}{4}, \tag{1.11}$$

where $\sigma^2$ is the variance of the phase error over the band. As with the geometric leakage term, this phase error term adds a bias, increasing the null floor and the photon noise level. Unlike the $N_{\mathrm{gl}}$, the bias will vary with the turbulence of the atmosphere and is harder to calibrate out, though statistical methods have been developed to tackle this issue (Hanot et al., 2011; Mennesson, Defrère, et al., 2016). However, the photon noise from the increased stellar light remains as an error source.

Interferometric techniques rapidly grew in popularity at the turn of the century, with several major projects coming online around that time. These included the Keck Interferometer (Colavita, R. Akeson, et al., 2003; Colavita, Wizinowich, et al., 2013), the Center for High Angular Resolution Astronomy (CHARA array - ten Brummelaar et al., 2005), the Large Binocular Telescope Interferometer (LBTI - Hinz et al., 2016; Defrère, Hinz, Mennesson, et al., 2016), and the Very Large Telescope Interferometer (VLTI - Schöller, 2007). Due to the stringent requirements on wavefront error, which scales with the wavelength, and the promise of lower-contrast requirements, these projects have have generally operated in the near- and mid-infrared. Dedicated nulling space missions in the mid-infrared were proposed in the early 2000's; the Darwin mission (Fridlund, 2000; Kaltenegger et al., 2005) and Terrestrial Planet Finder - Interferometer (TPF-I) mission (Beichman et al., 1999; Lawson and Dooley, 2005; Lawson, Lay, et al., 2007) both received great interest. These mission concepts led to feasibility studies like GENIE (Absil et al., 2006; Gondoin et al., 2008), which eventually stalled, along with others on the Keck Interferometer Nuller and LBTI nuller which resulted in the aforementioned conclusions about the effect of exozodii on nulling observations. The initial space concepts were ultimately cancelled due to technical challenges and other funding priorities. However, renewed interest is mounting with the European Space Agency's Large Interferometer for Exoplanets (LIFE) mission, which is a nulling concept that may detect 25-45 rocky exoplanets within the habitable zone of their host stars (Quanz et al., 2022). The renewed interest builds on growing interferometric successes in recent years from the VLTI/GRAVITY instrument (Eisenhauer, Perrin, et al., 2008; GRAVITY Collaboration, Abuter, et al., 2017) and the nulling promise of the upcoming VLTI/NOTT instrument (Defrère, Absil, Berger, et al., 2018; Laugier et al., 2023; Defrère, Bigioli, et al., 2022).

**Cross-Aperture Interferometry and Nulling**

The instruments mentioned above rely on multiple telescopes, and hence are generally referred to as "long-baseline" interferometers. These instruments show great promise and have led to significant results (included below), but they require large infrastructure investments that make implementation challenging and expensive. To make interferometry more readily available, cross-aperture techniques have been developed where the interference is performed across the aperture of a single telescope. Such interferometers are generally simpler to implement and can leverage existing infrastructure at most observatories. One of the key trade-offs is the de-

creased baseline length, limiting the angular resolution. However, cross-aperture nullers can still access exoplanets at $<\lambda/4D$, reaching significantly smaller separations than conventional coronagraphs (Serabyn, Ruane, et al., 2022; Serabyn, Mennesson, Martin, et al., 2019; Serabyn, Mennesson, and Martin, 2020).

Sparse aperture masking (SAM) was one of the first cross-aperture techniques, and is implemented by dividing the light from a single telescope's primary mirror into sub-apertures that are then interfered (Tuthill, Monnier, et al., 2000; Tuthill, J. Lloyd, et al., 2006). The related non-redundant masking (NRM) technique constrains the positions of the sub-apertures to only include non-redundant baselines, as the name suggests. Thus, SAM/NRM only requires a binary pupil mask that either transmits or blocks sections of the primary aperture. The sections can be judiciously selected to achieve the desired angular resolution and sky coverage. The downside is that a significant part of the aperture must be obstructed to avoid creating redundant baselines. This greatly reduces the overall throughput for the instrument. Given the relative simplicity in implementation, SAM/NRM has been tested at Keck (Tuthill, Monnier, et al., 2000) and the VLT (Lacour et al., 2011; Cheetham et al., 2016), in the LBTI (Defrère, Hinz, Skemer, et al., 2015), in the Gemini Planet Imager (Greenbaum et al., 2019), and even on JWST (Artigau et al., 2014).

An alternative cross-aperture approach is kernel phase, which treats any image as the result of interference within the telescope aperture. In this way, interferometric information, namely closure phases, can be extracted from the image even if redundant baselines are present (Martinache, 2010). This provides two key benefits. The first is that it works on a filled aperture, meaning that the full collecting area of the telescope can be used. This significantly increases the throughput of the observations. The second is that since kernel phase relies only on post-processing methods, it can be broadly applied to many instruments without requiring modification or additional hardware. The major requirement is a high-quality image with high Strehl, which can be provided by space-based telescopes or by modern extreme AO systems. Thus, kernel phase has been demonstrated on archival Hubble Space Telescope data (Pope, Martinache, et al., 2013), as well as at the Palomar Telescope (Pope, Tuthill, et al., 2016), at the VLT (Kammerer, Ireland, et al., 2019), at Keck (Wallace et al., 2020), and on JWST (Kammerer, Cooper, et al., 2023).

One of the challenges in increasing the sub-aperture sizes and hence the throughput in SAM/NRM from the ground is the turbulence of the atmosphere. As a sub-aperture grows, the phase variations within it increase, reducing the quality of the interference pattern. However, if the light from each sub-aperture is injected into a single mode fiber (SMF), then the fiber acts as a spatial and phase filter which removes the variations between the different baselines. The output from the fibers can then be interfered to obtain the same result as SAM/NRM but with larger sub-apertures (Perrin et al., 2006). Additionally, the fibers can be selectively combined to effectively re-map the pupil and generate non-redundant baselines. This was first demonstrated at the Lick Observatory (Huby et al., 2012). Another demonstration is underway in the Subaru Coronagraphic Extreme Adaptive Optics (SCExAO) instrument (Jovanovic et al., 2015). The new interferometric module, called the Fibered Imager foR a Single Telescope (FIRST), currently provides $R = 300$ spectra but is being upgraded to provide $R = 4000$ (Vievard et al., 2023). A key benefit of this technique is that its fibered output makes it readily adaptable to new integrated optics architectures. For example, fibers can be fed to a photonic device that remaps and combines the various baselines, including a $\pi$ phase shift for nulling if desired. The phasing can then be easily performed and maintained within the photonic device, simplifying the implementation and compacting the overall footprint. Other similar concepts are also being tested, such as the GLINT (Guided-Light Interferometric Nulling Technology) module which is also a part of SCExAO (Martinod et al., 2021).

With SMFs in mind, another cross-aperture technique becomes apparent: the fiber itself can be used as the beam recombination element. In this way, the mode selective properties of the fiber (covered in Sec. 2.2) help mitigate pointing and wavefront errors. Sub-apertures can then be placed across the telescope pupil and the resulting image is focused onto the fiber tip. The output of the fiber is a single intensity measurement which is the sum of the transmission map projected onto the sky. As with the original Bracewell nuller, the baseline is then rotated in this technique to scan the fringes around the star. This encodes the presence of a faint companion as a distinct sinusoidal intensity modulation in the output of the fiber. Some of the key principles behind fiber nulling will be covered in more detail in the next chapter. The first demonstration of this kind of fiber nulling was with the Palomar Fiber Nuller which combined two symmetric sub-apertures with a $\pi$ phase shift across the 200 inch Hale Telescope (PFN - Mennesson, Haguenauer, et al., 2006; Martin et al., 2008; Mennesson, Hanot, et al., 2010). The PFN demonstration

was also the first time that instrumental baseline rotation for interferometry was demonstrated; previous techniques all relied on sky rotation. Alternative designs for fiber nulling have since been developed, such as increasing the number of and phase between sub-apertures. However, when combining the light into an SMF, the full telescope aperture can be utilized so long as the phase across the aperture results in an on-axis image that will not couple into the fiber (Serabyn, Ruane, et al., 2022). This increases the overall throughput and leads to the vortex fiber nulling (VFN) technique that is the focus of this thesis.

Therefore, several cross-aperture techniques exist and new ones are actively being developed and tested. These techniques can be readily implemented on existing and future direct imaging instruments, leveraging the extant architecture needed for coronagraphy. The interferometric modes on these instruments complement the coronagraph and promise to bridge the gap to transit spectroscopy.

**Highlighted Science Results**

Due to the challenges involved, few exoplanets have been detected with interferometry. However, this is rapidly changing, with multiple detections coming from the GRAVITY instrument alone. The first detection was a major milestone in multiple regards. The GRAVITY team not only detected the iconic HR 8799 e planet, but also provided $R \sim 500$ spectra in K band that were used to confirm the spectral type as well as derive temperature and surface gravity measurements that in turn led to radii and mass estimates (GRAVITY Collaboration, Lacour, et al., 2019). The astrometric precision provided by the ∼100 m baseline was a full order of magnitude more precise than that provided by previous direct imaging observations. This allowed GRAVITY constrained the exoplanet's orbit, revealing that the HR 8799 system is not entirely co-planar. Additionally, the spectra were obtained at a high signal-to-noise ratio (SNR) of 5 per spectral channel, indicating that the instrument is sensitive to planets with a K band magnitude up to 19 and at a flux ratio up to $2.5 \times 10^{-4}$ at separations greater than 100 mas. Since then, GRAVITY also detected and spectroscopically characterized $\beta$ Pic b (GRAVITY Collaboration, Nowak, et al., 2020; Lagrange, Rubini, et al., 2020) and $\beta$ Pic c (Nowak et al., 2020), making the latter the first direct observation of an exoplanet originally discovered with the radial velocity technique. The astrometry on the b planet revealed a high mass, and the spectra show a low C/O ratio, which suggest that the planet formed through core accretion. Adding another pair of detections to their already-impressive record, GRAVITY also detected both protoplanets around PDS 70 and provided $R \sim 500$

spectra on each one (J. J. Wang, Vigan, et al., 2021). Finally, in 2023 the GRAVITY instrument detected HD 206893 c, an exoplanet that was previously only hinted-at by RV observations and Gaia astrometry (Hinkley, Lacour, et al., 2023); this is the planet labeled 3 in Fig. 1.5. The detection is particularly noteworthy as the spectra reveal that the planet is $\sim$ 12.7 $M_{\rm Jup}$ but is unambiguously undergoing deuterium burning, and the outer companion to the host star is a 28 $M_{\rm Jup}$ brown dwarf. This makes the HD 206893 system an ideal testing ground for theories defining the distinction between brown dwarf and planetary mass objects.

In terms of exoplanet detections, long-baseline interferometry definitively dominates so far, with GRAVITY leading the way. However, other instruments are pushing to fainter companions as well. The CHARA array has published detections of companions up to 270 to 370 times fainter than their primary star (Roettenbacher, Monnier, Fekel, et al., 2015; Roettenbacher, Monnier, Henry, et al., 2015). This 370 corresponds to a difference in magnitude between the companion and the primary of $\Delta$Mag$\sim$6.5. Prior to the GRAVITY results, these were the highest contrast confirmed companion detections that were published from long-baseline interferometry. In terms of cross-aperture interferometry, SAM/NRM has some of the best confirmed detections so far. Hinkley, Kraus, et al. (2015) detected 7 low-mass companions between 74 and 254 mas ($\sim$1$-$2 $\lambda/D$) and pushing up to a $\Delta$Mag of 6. The companions detected in that work definitively occupy the brown dwarf desert, a region around stars where intermediate mass ratio ($\lesssim$0.1) objects are particularly scarce (Kouwenhoven et al., 2007; Kraus et al., 2008). The detections therefore provide crucial insight into this rare population. Other notable confirmed SAM/NRM detections include GJ 802 (J. P. Lloyd et al., 2006; Ireland et al., 2008), HD 142527 (Biller et al., 2012; Greenbaum et al., 2019), and HR 2690 (Greenbaum et al., 2019). The JWST NRM mode also had its first results, with a $\Delta$Mag$\sim$4.5 detection of AB Dor (Sivaramakrishnan et al., 2023). Key highlights from kernel phase are the aforementioned HST (Pope, Martinache, et al., 2013) and JWST (Kammerer, Cooper, et al., 2023) results, and the detection of $\alpha$ Oph at a $\Delta$Mag$\sim$3.5 (Pope, Tuthill, et al., 2016).

From fiber nulling, the only results available so far are those from the PFN. Serabyn, Mennesson, Martin, et al. (2019) reported the detection of $\eta$ Peg B at a $\Delta$Mag = 5. However, in that same work, they determined that the null floor of about $4.8\times10^{-4}$ was set by the geometric leakage from the host star. This null value gave a corresponding host star diameter of $3.66^{+0.56}_{-0.68}$ mas, which is consistent with the accepted

value of $3.22 \pm 0.07$ measured from long-baseline interferometry. In this way, the authors demonstrated that cross-aperture nulling is capable of reaching on-sky null depths $<10^{-3}$ and is sensitive enough to measure large stellar diameters. Earlier results from the PFN also demonstrated a new statistical null self-calibration method (Hanot et al., 2011), placed constraints on the presence of hot exozodiacal dust and companions around Vega (Mennesson, Serabyn, et al., 2011), and detected hot dust around AB Aur (Kühn et al., 2015).

## 1.6 Summary and Overview of Thesis

Close to 99% of all confirmed exoplanets so far have been detected through indirect means. Therefore, these indirect results form the foundation of our understanding about exoplanets. From them, we have learned that exoplanets are not only ubiquitous but also incredibly diverse. The extensive catalog of indirectly-detected exoplanets provides insights into demographics, occurrence rates, formation mechanisms, and more. However, certain properties of exoplanets can only be assessed through spectral characterization, meaning that certain aspects of planet formation remain obscured. A planet's spectrum holds information about the physical, chemical, dynamical, and possible biological processes that have shaped its history. This includes measurements of atmospheric composition, abundance ratios, cloud coverage, spin rates, and more. Direct imaging and transit spectroscopy are the predominant methods for obtaining exoplanet spectra, but they each access different physical separations around a star. Combining the coverage from these two techniques, there is still a gap from about 1 to 10 AU where exoplanets cannot be efficiently characterized. Unfortunately, this gap coincides with the peak of the giant planet occurrence rate as determined by decades of RV surveys.

Interferometry is an additional method for detecting and characterizing exoplanets, and is capable of providing spectra for planets at intermediate separations. This includes the population of giant planets that would otherwise remain inaccessible for spectroscopy. Recent developments in long-baseline instrumentation have highlighted the capabilities of interferometry. Since the first interferometric detection of an exoplanet in 2019, an additional 5 planets have been detected this way, all with simultaneous $R\sim500$ spectra. This includes a new exoplanet that was previously only hinted-at by indirect methods. Building on this momentum, there is now a resurgence in interferometric and nulling methods.

*Cross-aperture techniques are of particular interest as they can be readily implemented on existing and future direct imaging instruments with few-to-no modifications required. Such single-telescope interferometers and nullers can reach well-within the inner working angle of conventional coronagraphs but require significantly less infrastructure and investment than long-baseline techniques.*

This thesis therefore presents a new cross-aperture nulling technique called vortex fiber nulling (VFN) that builds on the demonstrated heritage of the PFN instrument. However, rather than employing a sub-aperture mask, VFN utilizes a vortex phase mask to unlock access to the full collecting area of the primary mirror. By accessing separations $\lesssim 1\lambda/D$, VFN is complementary to conventional coronagraphy and can detect and spectrally characterize exoplanets in the gap between transit and direct imaging.

**Remaining Chapters**

This thesis follows the development of VFN from a concept in 2018 to an operating mode at a major telescope with three confirmed companion detections in 2023. This chapter, Chapter 1, provided much of the background and motivation for VFN as summarized above. Chapter 2 dives into the VFN concept itself. This covers the principles behind fiber coupling, leading to the nulling effect and then presenting the considerations and trades related to VFN. Chapter 3 serves as a proof of concept to encourage further work by presenting the first laboratory demonstration of VFN in monochromatic light. Chapter 4 builds on those preliminary results with additional laboratory demonstrations that achieved better monochromatic and polychromatic performance. That chapter serves to validate that the VFN performance, both in terms of null and off-axis coupling, is sufficient for on-sky operation. With VFN validated in the laboratory, Chapter 5 introduces the first on-sky VFN demonstrator to be included as an observing mode in the Keck Planet Imager and Characterizer (KPIC) instrument. This includes an overview of the KPIC VFN design followed by a simulations to predict the on-sky performance. The chapter then closes out with a laboratory characterization of the as-built instrument prior to deployment.

Chapter 6 presents the first-light results from the KPIC VFN mode. It covers the instrument design along with validation tests performed with the as-built and as-installed instrument in-situ at the telescope. It also shows the commissioning results, leading to on-sky throughput measurements that are used to determine SNR and sensitivity predictions for the instrument mode. Chapter 7 then presents the

first companion detections from the KPIC VFN mode. This includes two confident detections at a ΔMag~5 and a tentative detection of a companion with ΔMag~6.6. These detections by VFN represent the first time any of the three companions were directly detected, as the targets were previously only known from RV and/or astrometry observations. The VFN spectra were used to determine the companion temperature and RV, and to constrain their spin.

Chapter 8 then covers planned upgrades to the KPIC VFN instrument which will allow the instrument to access even smaller separations and will approximately double the companion throughput. Finally, Chapter 9 concludes by reviewing the key points from previous chapters and providing a perspective on the capabilities of putative VFN modes on future instruments at Keck, the Thirty Meter Telescope, and on the HWO mission.

## References

Absil, O. et al. (Mar. 2006). "Performance study of ground-based infrared Bracewell interferometers. Application to the detection of exozodiacal dust disks with GENIE". In: *Astronomy & Astrophysics* 448.2, pp. 787–800. DOI: 10.1051/0004-6361:20053516. arXiv: astro-ph/0511223 [astro-ph].

Agol, E. et al. (Feb. 2021). "Refining the Transit-timing and Photometric Analysis of TRAPPIST-1: Masses, Radii, Densities, Dynamics, and Ephemerides". In: *The Planetary Science Journal* 2.1, 1, p. 1. DOI: 10.3847/PSJ/abd022. arXiv: 2010.01074 [astro-ph.EP].

Akeson, R. L. et al. (Aug. 2013). "The NASA Exoplanet Archive: Data and Tools for Exoplanet Research". In: *Publ. Astron. Soc. Pac.* 125.930, p. 989. DOI: 10.1086/672273. arXiv: 1307.2944 [astro-ph.IM].

Anglada-Escudé, G. et al. (Aug. 2016). "A terrestrial planet candidate in a temperate orbit around Proxima Centauri". In: *Nature* 536.7617, pp. 437–440. DOI: 10.1038/nature19106. arXiv: 1609.03449 [astro-ph.EP].

Artigau, É. et al. (Aug. 2014). "NIRISS aperture masking interferometry: an overview of science opportunities". In: *Space Telescopes and Instrumentation 2014: Optical, Infrared, and Millimeter Wave*. Ed. by J. Oschmann Jacobus M. et al. Vol. 9143. Society of Photo-Optical Instrumentation Engineers (SPIE) Conference Series, 914340, p. 914340. DOI: 10.1117/12.2055191. arXiv: 1406.6882 [astro-ph.IM].

Babcock, H. W. (Oct. 1953). "The Possibility of Compensating Astronomical Seeing". In: *Publications of the Astronomical Society of the Pacific* 65.386, p. 229. DOI: 10.1086/126606.

Batygin, K. (Apr. 2018). "On the Terminal Rotation Rates of Giant Planets". In: *The Astronomical Journal* 155.4, 178, p. 178. DOI: 10.3847/1538-3881/aab54e. arXiv: 1803.07106 [astro-ph.EP].

Batygin, K., P. H. Bodenheimer, and G. P. Laughlin (Oct. 2016). "In Situ Formation and Dynamical Evolution of Hot Jupiter Systems". In: *The Astrophysical Journal* 829.2, 114, p. 114. DOI: 10.3847/0004-637X/829/2/114. arXiv: 1511.09157 [astro-ph.EP].

Beichman, C. A., N. J. Woolf, and C. A. Lindensmith (1999). *The Terrestrial Planet Finder (TPF) : a NASA Origins Program to search for habitable planets*.

Beltz, H. et al. (Jan. 2021). "A Significant Increase in Detection of High-resolution Emission Spectra Using a Three-dimensional Atmospheric Model of a Hot Jupiter". In: *The Astronomical Journal* 161.1, 1, p. 1. DOI: 10.3847/1538-3881/abb67b. arXiv: 2009.09030 [astro-ph.EP].

Beuzit, J.-L. et al. (Nov. 2019). "SPHERE: the exoplanet imager for the Very Large Telescope". In: *Astronomy and Astrophysics* 631, A155, A155. DOI: 10.1051/0004-6361/201935251. arXiv: 1902.04080 [astro-ph.IM].

Biller, B. et al. (July 2012). "A Likely Close-in Low-mass Stellar Companion to the Transitional Disk Star HD 142527". In: *The Astrophysical Journal Letters* 753.2, L38, p. L38. DOI: 10.1088/2041-8205/753/2/L38. arXiv: 1206.2654 [astro-ph.SR].

Birkby, J. L. (2018). "Spectroscopic Direct Detection of Exoplanets". In: *Handbook of Exoplanets*. Ed. by H. J. Deeg and J. A. Belmonte. Cham: Springer International Publishing, pp. 1485–1508. ISBN: 978-3-319-55333-7. DOI: 10.1007/978-3-319-55333-7_16. URL: https://doi.org/10.1007/978-3-319-55333-7_16.

Bowler, B. P. et al. (Nov. 2010). "Near-infrared Spectroscopy of the Extrasolar Planet HR 8799 b". In: *The Astrophysical Journal* 723.1, pp. 850–868. DOI: 10.1088/0004-637X/723/1/850. arXiv: 1008.4582 [astro-ph.EP].

Bracewell, R. N. (1978). "Detecting nonsolar planets by spinning infrared interferometer". In: *Nature* 274, p. 780. DOI: 10.1038/274780a0.

Bracewell, R. N. and R. H. MacPhie (1979). "Searching for nonsolar planets". In: *Icarus* 38, pp. 136–147. DOI: 10.1016/0019-1035(79)90093-9.

Brandt, T. D. (June 2021). "The Hipparcos-Gaia Catalog of Accelerations: Gaia EDR3 Edition". In: *The Astrophysical Journal Supplement Series* 254.2, 42, p. 42. DOI: 10.3847/1538-4365/abf93c. arXiv: 2105.11662 [astro-ph.GA].

Brogi, M., R. J. de Kok, et al. (Feb. 2016). "Rotation and Winds of Exoplanet HD 189733 b Measured with High-dispersion Transmission Spectroscopy". In: *The Astrophysical Journal* 817.2, 106, p. 106. DOI: 10.3847/0004-637X/817/2/106. arXiv: 1512.05175 [astro-ph.EP].

Brogi, M. and M. R. Line (Mar. 2019). "Retrieving Temperatures and Abundances of Exoplanet Atmospheres with High-resolution Cross-correlation Spectroscopy". In: *The Astornomical Journal* 157.3, 114, p. 114. DOI: 10.3847/1538-3881/aaffd3. arXiv: 1811.01681 [astro-ph.EP].

Calissendorff, P. et al. (Apr. 2023). "JWST/NIRCam Discovery of the First Y+Y Brown Dwarf Binary: WISE J033605.05-014350.4". In: *The Astrophysical Journal Letters* 947.2, L30, p. L30. DOI: 10.3847/2041-8213/acc86d. arXiv: 2303.16923 [astro-ph.SR].

Cheetham, A. C. et al. (Aug. 2016). "Sparse aperture masking with SPHERE". In: *Optical and Infrared Interferometry and Imaging V*. Ed. by F. Malbet, M. J. Creech-Eakman, and P. G. Tuthill. Vol. 9907. Society of Photo-Optical Instrumentation Engineers (SPIE) Conference Series, 99072T, 99072T. DOI: 10.1117/12.2231983.

Colavita, M. M., R. Akeson, et al. (Aug. 2003). "Observations of DG Tauri with the Keck Interferometer". In: *The Astrophysical Journal Letters* 592.2, pp. L83–L86. DOI: 10.1086/377704. arXiv: astro-ph/0307051 [astro-ph].

Colavita, M. M., P. Wizinowich, et al. (Oct. 2013). "The Keck Interferometer". In: *Publications of the Astronomical Society of the Pacific* 125.932, p. 1226. DOI: 10.1086/673475.

Crossfield, I. J. M. et al. (Jan. 2014). "A global cloud map of the nearest known brown dwarf". In: *Nature* 505.7485, pp. 654–656. DOI: 10.1038/nature12955. arXiv: 1401.8145 [astro-ph.EP].

Currie, T., B. Biller, et al. (July 2023). "Direct Imaging and Spectroscopy of Extrasolar Planets". In: *Protostars and Planets VII*. Ed. by S. Inutsuka et al. Vol. 534. Astronomical Society of the Pacific Conference Series, p. 799. DOI: 10.48550/arXiv.2205.05696. arXiv: 2205.05696 [astro-ph.EP].

Currie, T., N. J. Kasdin, et al. (Apr. 2018). "Laboratory and On-sky Validation of the Shaped Pupil Coronagraph's Sensitivity to Low-order Aberrations With Active Wavefront Control". In: *Publications of the Astronomical Society of the Pacific* 130.986, p. 044505. DOI: 10.1088/1538-3873/aaab41. arXiv: 1801.09760 [astro-ph.IM].

De Rosa, R. J. et al. (Apr. 2023). "Direct imaging discovery of a super-Jovian around the young Sun-like star AF Leporis". In: *Astronomy and Astrophysics* 672, A94, A94. DOI: 10.1051/0004-6361/202345877. arXiv: 2302.06332 [astro-ph.EP].

Defrère, D., O. Absil, J.-P. Berger, et al. (Dec. 2018). "The path towards high-contrast imaging with the VLTI: the Hi-5 project". In: *Experimental Astronomy* 46.3, pp. 475–495. DOI: 10.1007/s10686-018-9593-2. arXiv: 1801.04148 [astro-ph.IM].

Defrère, D., O. Absil, R. den Hartog, et al. (Jan. 2010). "Nulling interferometry: impact of exozodiacal clouds on the performance of future life-finding space missions". In: *Astronomy & Astrophysics* 509, A9, A9. DOI: 10.1051/0004-6361/200912973. arXiv: 0910.3486 [astro-ph.IM].

Defrère, D., P. M. Hinz, B. Mennesson, et al. (June 2016). "Nulling Data Reduction and On-sky Performance of the Large Binocular Telescope Interferometer". In: *The Astrophysical Journal* 824.2, 66, p. 66. DOI: 10.3847/0004-637X/824/2/66. arXiv: 1601.06866 [astro-ph.EP].

Defrère, D., P. M. Hinz, A. Skemer, et al. (Sept. 2015). "Exoplanet science with the LBTI: instrument status and plans". In: *Techniques and Instrumentation for Detection of Exoplanets VII*. Ed. by S. Shaklan. Vol. 9605. Society of Photo-Optical Instrumentation Engineers (SPIE) Conference Series, 96051G, 96051G. DOI: 10.1117/12.2188912. arXiv: 1509.01299 [astro-ph.IM].

Defrère, D., A. Bigioli, et al. (2022). "L-band nulling interferometry at the VLTI with Asgard/Hi-5: status and plans". In: *Optical and Infrared Interferometry and Imaging VIII*. Ed. by A. Mérand, S. Sallum, and J. Sanchez-Bermudez. Vol. 12183. International Society for Optics and Photonics. SPIE, 121830H. DOI: 10.1117/12.2627953. URL: https://doi.org/10.1117/12.2627953.

Doelman, D. S. et al. (May 2022). "L-band Integral Field Spectroscopy of the HR 8799 Planetary System". In: *The Astronomical Journal* 163.5, 217, p. 217. DOI: 10.3847/1538-3881/ac5d52. arXiv: 2203.08165 [astro-ph.EP].

Doyle, L. R. et al. (Sept. 2011). "Kepler-16: A Transiting Circumbinary Planet". In: *Science* 333.6049, p. 1602. DOI: 10.1126/science.1210923. arXiv: 1109.3432 [astro-ph.EP].

Ehrenreich, D. et al. (Apr. 2020). "Nightside condensation of iron in an ultrahot giant exoplanet". In: *Nature* 580.7805, pp. 597–601. DOI: 10.1038/s41586-020-2107-1. arXiv: 2003.05528 [astro-ph.EP].

Eisenhauer, F., G. Perrin, et al. (Jan. 2008). "GRAVITY: The AO-Assisted, Two-Object Beam-Combiner Instrument for the VLTI". In: *The Power of Optical/IR Interferometry: Recent Scientific Results and 2nd Generation*. Ed. by A. Richichi et al., p. 431. DOI: 10.1007/978-3-540-74256-2_50.

Eisenhauer, F., J. D. Monnier, and O. Pfuhl (Aug. 2023). "Advances in Optical/Infrared Interferometry". In: *Annual Review of Astronomy and Astrophysics* 61, pp. 237–285. DOI: 10.1146/annurev-astro-121622-045019. arXiv: 2303.00453 [astro-ph.IM].

Ertel, S. et al. (Apr. 2020). "The HOSTS Survey for Exozodiacal Dust: Observational Results from the Complete Survey". In: *The Astronomical Journal* 159.4, 177, p. 177. DOI: 10.3847/1538-3881/ab7817. arXiv: 2003.03499 [astro-ph.SR].

Fischer, D. A. and J. Valenti (Apr. 2005). "The Planet-Metallicity Correlation". In: *The Astrophysical Journal* 622.2, pp. 1102–1117. DOI: 10.1086/428383.

Flowers, E. et al. (May 2019). “The High-resolution Transmission Spectrum of HD 189733b Interpreted with Atmospheric Doppler Shifts from Three-dimensional General Circulation Models”. In: *The Astronomical Journal* 157.5, 209, p. 209. DOI: 10.3847/1538-3881/ab164c. arXiv: 1810.06099 [astro-ph.EP].

Foo, G., D. M. Palacios, and G. A. Swartzlander (2005). “Optical vortex coronagraph”. In: *Opt. Lett.* 30, pp. 3308–3310. DOI: 10.1364/OL.30.003308.

Fortney, J. J., R. I. Dawson, and T. D. Komacek (2021). “Hot Jupiters: Origins, Structure, Atmospheres”. In: *Journal of Geophysical Research: Planets* 126.3. e2020JE006629 2020JE006629, e2020JE006629. DOI: https://doi.org/10.1029/2020JE006629. eprint: https://agupubs.onlinelibrary.wiley.com/doi/pdf/10.1029/2020JE006629. URL: https://agupubs.onlinelibrary.wiley.com/doi/abs/10.1029/2020JE006629.

Fridlund, C. V. M. (Jan. 2000). “Darwin - the Infrared Space Interferometer”. In: *Darwin and Astronomy : the Infrared Space Interferometer*. Ed. by B. Schürmann. Vol. 451. ESA Special Publication, p. 11.

Fulton, B. J. and E. A. Petigura (Dec. 2018). “The California-Kepler Survey. VII. Precise Planet Radii Leveraging Gaia DR2 Reveal the Stellar Mass Dependence of the Planet Radius Gap”. In: *The Astronomical Journal* 156.6, 264, p. 264. DOI: 10.3847/1538-3881/aae828. arXiv: 1805.01453 [astro-ph.EP].

Fulton, B. J., L. J. Rosenthal, et al. (July 2021). “California Legacy Survey. II. Occurrence of Giant Planets beyond the Ice Line”. In: *The Astrophysical Journal Supplement Series* 255.1, 14, p. 14. DOI: 10.3847/1538-4365/abfcc1. arXiv: 2105.11584 [astro-ph.EP].

Gaia Collaboration et al. (Nov. 2016). “The Gaia mission”. In: *Astronomy and Astrophysics* 595, A1, A1. DOI: 10.1051/0004-6361/201629272. arXiv: 1609.04153 [astro-ph.IM].

Gomes, R. et al. (May 2005). “Origin of the cataclysmic Late Heavy Bombardment period of the terrestrial planets”. In: *Nature* 435.7041, pp. 466–469. DOI: 10.1038/nature03676.

Gondoin, P. et al. (Jan. 2008). “GENIE: a Ground-Based European Nulling Instrument at ESO Very Large Telescope Interferometer”. In: *The Power of Optical/IR Interferometry: Recent Scientific Results and 2nd Generation*. Ed. by A. Richichi et al., p. 445. DOI: 10.1007/978-3-540-74256-2_51.

GRAVITY Collaboration, R. Abuter, et al. (June 2017). “First light for GRAVITY: Phase referencing optical interferometry for the Very Large Telescope Interferometer”. In: *Astronomy and Astrophysics* 602, A94, A94. DOI: 10.1051/0004-6361/201730838. arXiv: 1705.02345 [astro-ph.IM].

GRAVITY Collaboration, S. Lacour, et al. (Mar. 2019). “First direct detection of an exoplanet by optical interferometry. Astrometry and K-band spectroscopy of HR 8799 e”. In: *Astronomy & Astrophysics* 623, L11, p. L11. DOI: 10.1051/0004-6361/201935253. arXiv: 1903.11903 [astro-ph.EP].

GRAVITY Collaboration, M. Nowak, et al. (Jan. 2020). "Peering into the formation history of $\beta$ Pictoris b with VLTI/GRAVITY long-baseline interferometry". In: *Astronomy & Astrophysics* 633, A110, A110. DOI: 10.1051/0004-6361/201936898. arXiv: 1912.04651 [astro-ph.EP].

Greenbaum, A. Z. et al. (June 2019). "Performance of the Gemini Planet Imager Non-redundant Mask and Spectroscopy of Two Close-separation Binaries: HR 2690 and HD 142527". In: *The Astronomical Journal* 157.6, 249, p. 249. DOI: 10.3847/1538-3881/ab17db. arXiv: 1904.09006 [astro-ph.IM].

Guyon, O. (June 2003). "Phase-induced amplitude apodization of telescope pupils for extrasolar terrestrial planet imaging". In: *Astronomy & Astrophysics* 404, pp. 379–387. DOI: 10.1051/0004-6361:20030457. arXiv: astro-ph/0301190 [astro-ph].

Guyon, O. et al. (Dec. 2020). "Validating advanced wavefront control techniques on the SCExAO testbed/instrument". In: *Adaptive Optics Systems VII*. Ed. by L. Schreiber, D. Schmidt, and E. Vernet. Vol. 11448. Society of Photo-Optical Instrumentation Engineers (SPIE) Conference Series, 114481Z, 114481Z. DOI: 10.1117/12.2562723.

Hanot, C. et al. (Mar. 2011). "Improving Interferometric Null Depth Measurements using Statistical Distributions: Theory and First Results with the Palomar Fiber Nuller". In: *The Astrophysical Journal* 729.2, 110, p. 110. DOI: 10.1088/0004-637X/729/2/110. arXiv: 1103.4719 [astro-ph.IM].

Harada, C. K. et al. (Mar. 2021). "Signatures of Clouds in Hot Jupiter Atmospheres: Modeled High-resolution Emission Spectra from 3D General Circulation Models". In: *The Astrophysical Journal* 909.1, 85, p. 85. DOI: 10.3847/1538-4357/abdc22. arXiv: 1912.02268 [astro-ph.EP].

Hinkley, S., S. Lacour, et al. (Mar. 2023). "Direct discovery of the inner exoplanet in the HD 206893 system. Evidence for deuterium burning in a planetary-mass companion". In: *Astronomy & Astrophysics* 671, L5, p. L5. DOI: 10.1051/0004-6361/202244727. arXiv: 2208.04867 [astro-ph.EP].

Hinkley, S., A. L. Kraus, et al. (June 2015). "Discovery of Seven Companions to Intermediate-mass Stars with Extreme Mass Ratios in the Scorpius-Centaurus Association". In: *The Astrophysical Journal Letters* 806.1, L9, p. L9. DOI: 10.1088/2041-8205/806/1/L9. arXiv: 1505.03858 [astro-ph.EP].

Hinz, P. M. et al. (Aug. 2016). "Overview of LBTI: a multipurpose facility for high spatial resolution observations". In: *Optical and Infrared Interferometry and Imaging V*. Ed. by F. Malbet, M. J. Creech-Eakman, and P. G. Tuthill. Vol. 9907. Society of Photo-Optical Instrumentation Engineers (SPIE) Conference Series, 990704, p. 990704. DOI: 10.1117/12.2233795.

Huby, E. et al. (May 2012). "FIRST, a fibered aperture masking instrument. I. First on-sky test results". In: *Astronomy & Astrophysics* 541, A55, A55. DOI: 10.1051/0004-6361/201118517. arXiv: 1203.5075 [astro-ph.IM].

Ireland, M. J. et al. (May 2008). "Dynamical Mass of GJ 802B: A Brown Dwarf in a Triple System". In: *The Astrophysical Journal* 678.1, p. 463. DOI: 10.1086/529578. URL: https://dx.doi.org/10.1086/529578.

Jenkins, J. M. et al. (Aug. 2015). "Discovery and Validation of Kepler-452b: A 1.6 $R_{\rm earth}$ Super Earth Exoplanet in the Habitable Zone of a G2 Star". In: *The Astronomical Journal* 150.2, 56, p. 56. DOI: 10.1088/0004-6256/150/2/56. arXiv: 1507.06723 [astro-ph.EP].

Jovanovic, N. et al. (Sept. 2015). "The Subaru Coronagraphic Extreme Adaptive Optics System: Enabling High-Contrast Imaging on Solar-System Scales". In: *Publications of the Astronomical Society of the Pacific* 127.955, p. 890. DOI: 10.1086/682989. arXiv: 1507.00017 [astro-ph.IM].

Kaltenegger, L. and M. Fridlund (Jan. 2005). "The Darwin mission: Search for extra-solar planets". In: *Advances in Space Research* 36.6, pp. 1114–1122. DOI: 10.1016/j.asr.2005.05.061.

Kammerer, J., R. A. Cooper, et al. (Jan. 2023). "The Near Infrared Imager and Slitless Spectrograph for JWST. V. Kernel Phase Imaging and Data Analysis". In: *Publications of the Astronomical Society of the Pacific* 135.1043, 014502, p. 014502. DOI: 10.1088/1538-3873/ac9a74. arXiv: 2210.17528 [astro-ph.IM].

Kammerer, J., M. J. Ireland, et al. (June 2019). "Kernel phase imaging with VLT/NACO: high-contrast detection of new candidate low-mass stellar companions at the diffraction limit". In: *Monthly Notices of the Royal Astronomical Society* 486.1, pp. 639–654. DOI: 10.1093/mnras/stz882. arXiv: 1903.11252 [astro-ph.EP].

Kasdin, N. J. et al. (Jan. 2003). "Extrasolar Planet Finding via Optimal Apodized-Pupil and Shaped-Pupil Coronagraphs". In: *The Astrophysical Journal* 582.2, pp. 1147–1161. DOI: 10.1086/344751.

Kawahara, H. and T. Hirano (Sept. 2014). "Characterizing Earth-like Planets Using a Combination of High-Dispersion Spectroscopy and High-Contrast Instruments: Doppler-shifted Water and Oxygen Lines". In: *arXiv e-prints*, arXiv:1409.5740, arXiv:1409.5740. DOI: 10.48550/arXiv.1409.5740. arXiv: 1409.5740 [astro-ph.EP].

Kervella, P. et al. (Mar. 2019). "Stellar and substellar companions of nearby stars from Gaia DR2. Binarity from proper motion anomaly". In: *Astronomy and Astrophysics* 623, A72, A72. DOI: 10.1051/0004-6361/201834371. arXiv: 1811.08902 [astro-ph.SR].

Khandelwal, A. et al. (Apr. 2023). "Discovery of a massive giant planet with extreme density around the sub-giant star TOI-4603". In: *Astronomy and Astrophysics* 672, L7, p. L7. DOI: 10.1051/0004-6361/202245608. arXiv: 2303.11841 [astro-ph.EP].

Kouwenhoven, M. B. N., A. G. A. Brown, and L. Kaper (Mar. 2007). "A brown dwarf desert for intermediate mass stars in Scorpius OB2?" In: *Astronomy & Astrophysics* 464.2, pp. 581–599. DOI: 10.1051/0004-6361:20054396. arXiv: astro-ph/0611903 [astro-ph].

Kraus, A. L. et al. (May 2008). "Mapping the Shores of the Brown Dwarf Desert. I. Upper Scorpius". In: *The Astrophysical Journal* 679.1, pp. 762–782. DOI: 10.1086/587435. arXiv: 0801.2387 [astro-ph].

Kühn, J. et al. (Feb. 2015). "Exploring Intermediate (5-40 au) Scales around AB Aurigae with the Palomar Fiber Nuller". In: *The Astrophysical Journal* 800.1, 55, p. 55. DOI: 10.1088/0004-637X/800/1/55. arXiv: 1502.03626 [astro-ph.SR].

Lacour, S. et al. (Aug. 2011). "Sparse aperture masking at the VLT. I. Faint companion detection limits for the two debris disk stars HD 92945 and HD 141569". In: *Astronomy & Astrophysics* 532, A72, A72. DOI: 10.1051/0004-6361/201116712. arXiv: 1107.1426 [astro-ph.IM].

Lafrenière, D. et al. (Apr. 2009). "HST/NICMOS Detection of HR 8799 b in 1998". In: *The Astrophysical Journal Letters* 694.2, pp. L148–L152. DOI: 10.1088/0004-637X/694/2/L148. arXiv: 0902.3247 [astro-ph.EP].

Lagrange, A. M., D. Gratadour, et al. (Jan. 2009). "A probable giant planet imaged in the $\beta$ Pictoris disk. VLT/NaCo deep L'-band imaging". In: *Astronomy & Astrophysics* 493.2, pp. L21–L25. DOI: 10.1051/0004-6361:200811325. arXiv: 0811.3583 [astro-ph].

Lagrange, A. M., P. Rubini, et al. (Oct. 2020). "Unveiling the $\beta$ Pictoris system, coupling high contrast imaging, interferometric, and radial velocity data". In: *Astronomy & Astrophysics* 642, A18, A18. DOI: 10.1051/0004-6361/202038823.

Laugier, R. et al. (Mar. 2023). "Asgard/NOTT: L-band nulling interferometry at the VLTI. I. Simulating the expected high-contrast performance". In: *Astronomy & Astrophysics* 671, A110, A110. DOI: 10.1051/0004-6361/202244351. arXiv: 2211.09548 [astro-ph.IM].

Lawson, P. R. and J. A. Dooley (June 2005). *Technology Plan for the Terrestrial Planet Finder Interferometer*. Technical Report, JPL-Publ-05-5.

Lawson, P. R., O. P. Lay, et al. (Mar. 2007). *Terrestrial Planet Finder Interferometer Science Working Group Report*. NASA STI/Recon Technical Report N.

Lecavelier des Etangs, A. and J. J. Lissauer (June 2022). "The IAU working definition of an exoplanet". In: *New Astronomy Reviews* 94, 101641, p. 101641. DOI: 10.1016/j.newar.2022.101641. arXiv: 2203.09520 [astro-ph.IM].

Lecavelier des Etangs, A. and A. Vidal-Madjar (Apr. 2016). "The orbit of beta Pictoris b as a transiting planet". In: *Astronomy and Astrophysics* 588, A60, A60. DOI: 10.1051/0004-6361/201527631. arXiv: 1602.04683 [astro-ph.EP].

Liu, M. C. et al. (Oct. 2011). "CFBDSIR J1458+1013B: A Very Cold (>T10) Brown Dwarf in a Binary System". In: *The Astrophysical Journal* 740.2, 108, p. 108. DOI: 10.1088/0004-637X/740/2/108. arXiv: 1103.0014 [astro-ph.SR].

Lloyd, J. P. et al. (Oct. 2006). "Direct Detection of the Brown Dwarf GJ 802B with Adaptive Optics Masking Interferometry". In: *The Asrophysical Journal* 650.2, pp. L131–L134. DOI: 10.1086/508771. arXiv: astro-ph/0607516 [astro-ph].

Lyot, B. (June 1939). "The study of the solar corona and prominences without eclipses (George Darwin Lecture, 1939)". In: *Monthly Notices of the Royal Astronomical Society* 99, p. 580. DOI: 10.1093/mnras/99.8.580.

Macintosh, B., J. R. Graham, T. Barman, et al. (2015). "Discovery and spectroscopy of the young Jovian planet 51 Eri b with the Gemini Planet Imager". In: *Science* 350.6256, pp. 64–67.

Macintosh, B., J. R. Graham, P. Ingraham, et al. (Sept. 2014). "First light of the Gemini Planet Imager". In: *Proceedings of the National Academy of Science* 111.35, pp. 12661–12666. DOI: 10.1073/pnas.1304215111. arXiv: 1403.7520 [astro-ph.EP].

MacPhie, R. H. and R. N. Bracewell (Jan. 1979). "An Orbiting Infrared Interferometer to Search for Nonsolar Planets". In: *Instrumentation in Astronomy III*. Ed. by D. L. Crawford. Vol. 172. Society of Photo-Optical Instrumentation Engineers (SPIE) Conference Series, p. 271. DOI: 10.1117/12.957091.

Males, J. R. et al. (Dec. 2020). "MagAO-X first light". In: *Society of Photo-Optical Instrumentation Engineers (SPIE) Conference Series*. Vol. 11448. Society of Photo-Optical Instrumentation Engineers (SPIE) Conference Series, 114484L, p. 114484L. DOI: 10.1117/12.2561682.

Marois, C., D. Lafrenière, et al. (Apr. 2006). "Angular Differential Imaging: A Powerful High-Contrast Imaging Technique". In: *The Astrophysical Journal* 641.1, pp. 556–564. DOI: 10.1086/500401. arXiv: astro-ph/0512335 [astro-ph].

Marois, C., B. Macintosh, et al. (Nov. 2008). "Direct Imaging of Multiple Planets Orbiting the Star HR 8799". In: *Science* 322.5906, p. 1348. DOI: 10.1126/science.1166585. arXiv: 0811.2606 [astro-ph].

Marois, C., B. Zuckerman, et al. (Dec. 2010). "Images of a fourth planet orbiting HR 8799". In: *Nature* 468.7327, pp. 1080–1083. DOI: 10.1038/nature09684. arXiv: 1011.4918 [astro-ph.EP].

Martin, S. et al. (July 2008). "The development and applications of a ground-based fiber nulling coronagraph". In: *Optical and Infrared Interferometry*. Ed. by M. Schöller, W. C. Danchi, and F. Delplancke. Vol. 7013. Proc. SPIE, 70131Y, 70131Y. DOI: 10.1117/12.789484.

Martinache, F. (Nov. 2010). "Kernel Phase in Fizeau Interferometry". In: *The Astrophysical Journal* 724.1, pp. 464–469. DOI: 10.1088/0004-637X/724/1/464. arXiv: 1009.3933 [astro-ph.IM].

Martinod, M.-A. et al. (Jan. 2021). "Scalable photonic-based nulling interferometry with the dispersed multi-baseline GLINT instrument". In: *Nature Communications* 12, 2465, p. 2465. DOI: 10.1038/s41467-021-22769-x.

Mawet, D. et al. (Nov. 2005). "Annular Groove Phase Mask Coronagraph". In: *The Astrophysical Journal* 633.2, pp. 1191–1200. DOI: 10.1086/462409.

Mayor, M. and D. Queloz (Nov. 1995). "A Jupiter-mass companion to a solar-type star". In: *Nature* 378.6555, pp. 355–359. DOI: 10.1038/378355a0.

Mennesson, B., P. Haguenauer, et al. (June 2006). "Deep broad-band infrared nulling using a single-mode fiber beam combiner and baseline rotation". In: *SPIE*. Ed. by J. D. Monnier, M. Schöller, and W. C. Danchi. Vol. 6268. Proc. SPIE, 626830, p. 626830. DOI: 10.1117/12.672157.

Mennesson, B., C. Hanot, et al. (July 2010). "High contrast stellar observations within the diffraction limit at the Palomar Hale telescope". In: *Ground-based and Airborne Instrumentation for Astronomy III*. Ed. by I. S. McLean, S. K. Ramsay, and H. Takami. Vol. 7735. Proc. SPIE, 773511, p. 773511. DOI: 10.1117/12.857633.

Mennesson, B., R. Millan-Gabet, et al. (Dec. 2014). "Constraining the Exozodiacal Luminosity Function of Main-sequence Stars: Complete Results from the Keck Nuller Mid-infrared Surveys". In: *The Astrophysical Journal* 797.2, 119, p. 119. DOI: 10.1088/0004-637X/797/2/119.

Mennesson, B., E. Serabyn, et al. (July 2011). "New Constraints on Companions and Dust within a Few AU of Vega". In: *Astrophys. J.* 736.1, 14, p. 14. DOI: 10.1088/0004-637X/736/1/14.

Mennesson, B., D. Defrère, et al. (Aug. 2016). "Making high-accuracy null depth measurements for the LBTI exozodi survey". In: *Optical and Infrared Interferometry and Imaging V*. Ed. by F. Malbet, M. J. Creech-Eakman, and P. G. Tuthill. Vol. 9907. Society of Photo-Optical Instrumentation Engineers (SPIE) Conference Series, 99070X, p. 99070X. DOI: 10.1117/12.2231839.

Michelson, A. A. and F. G. Pease (May 1921). "Measurement of the Diameter of $\alpha$ Orionis with the Interferometer." In: *The Astrophysical Journal* 53, pp. 249–259. DOI: 10.1086/142603.

Miller-Ricci Kempton, E. and E. Rauscher (June 2012). "Constraining High-speed Winds in Exoplanet Atmospheres through Observations of Anomalous Doppler Shifts during Transit". In: *The Astrophysical Journal* 751.2, 117, p. 117. DOI: 10.1088/0004-637X/751/2/117. arXiv: 1109.2270 [astro-ph.EP].

Mollière, P. and I. A. G. Snellen (Feb. 2019). "Detecting isotopologues in exoplanet atmospheres using ground-based high-dispersion spectroscopy". In: *Astronomy and Astrophysics* 622, A139, A139. DOI: 10.1051/0004-6361/201834169. arXiv: 1809.01156 [astro-ph.EP].

National Academies of Sciences, Engineering, and Medicine (2021). *Pathways to Discovery in Astronomy and Astrophysics for the 2020s*. The National Academies Press. ISBN: 978-0-309-46586-1. DOI: 10.17226/26141.

Nowak, M. et al. (Oct. 2020). "Direct confirmation of the radial-velocity planet $\beta$ Pictoris c". In: *Astronomy & Astrophysics* 642, L2, p. L2. DOI: 10.1051/0004-6361/202039039. arXiv: 2010.04442 [astro-ph.EP].

Öberg, K. I., R. Murray-Clay, and E. A. Bergin (Dec. 2011). "The Effects of Snowlines on C/O in Planetary Atmospheres". In: *The Astrophysical Journal Letters* 743.1, L16, p. L16. DOI: 10.1088/2041-8205/743/1/L16. arXiv: 1110.5567 [astro-ph.GA].

Oppenheimer, B. R. et al. (May 2013). "Reconnaissance of the HR 8799 Exosolar System. I. Near-infrared Spectroscopy". In: *The Astrophysical Journal* 768.1, 24, p. 24. DOI: 10.1088/0004-637X/768/1/24. arXiv: 1303.2627 [astro-ph.EP].

Osborn, A. and D. Bayliss (Jan. 2020). "Investigating the planet-metallicity correlation for hot Jupiters". In: *Monthly Notices of the Royal Astronomical Society* 491.3, pp. 4481–4487. DOI: 10.1093/mnras/stz3207. arXiv: 1911.05830 [astro-ph.EP].

Owen, J. E. and Y. Wu (Oct. 2013). "Kepler Planets: A Tale of Evaporation". In: *The Astrophysical Journal* 775.2, 105, p. 105. DOI: 10.1088/0004-637X/775/2/105. arXiv: 1303.3899 [astro-ph.EP].

Paladini, C. et al. (Jan. 2018). "Large granulation cells on the surface of the giant star $\pi^1$ Gruis". In: *Nature* 553.7688, pp. 310–312. DOI: 10.1038/nature25001.

Pepe, F. et al. (Jan. 2021). "ESPRESSO at VLT. On-sky performance and first results". In: *Astronomy & Astrophysics* 645, A96, A96. DOI: 10.1051/0004-6361/202038306. arXiv: 2010.00316 [astro-ph.IM].

Perrin, G. et al. (Dec. 2006). "High dynamic range imaging by pupil single-mode filtering and remapping". In: *Monthly Notices of the Royal Astronomical Society* 373.2, pp. 747–751. DOI: 10.1111/j.1365-2966.2006.11063.x. arXiv: astro-ph/0609362 [astro-ph].

Piso, A.-M. A., J. Pegues, and K. I. Öberg (Dec. 2016). "The Role of Ice Compositions for Snowlines and the C/N/O Ratios in Active Disks". In: *The Astrophysical Journal* 833.2, 203, p. 203. DOI: 10.3847/1538-4357/833/2/203. arXiv: 1611.00741 [astro-ph.EP].

Pope, B., F. Martinache, and P. Tuthill (Apr. 2013). "Dancing in the Dark: New Brown Dwarf Binaries from Kernel Phase Interferometry". In: *The Astrophysical Journal* 767.2, 110, p. 110. DOI: 10.1088/0004-637X/767/2/110. arXiv: 1302.6682 [astro-ph.SR].

Pope, B., P. Tuthill, et al. (Jan. 2016). "The Palomar kernel-phase experiment: testing kernel phase interferometry for ground-based astronomical observations". In: *Monthly Notices of the Royal Astronomical Society* 455.2, pp. 1647–1653. DOI: 10.1093/mnras/stv2442. arXiv: 1510.06406 [astro-ph.IM].

Quanz, S. P. et al. (Aug. 2022). "Large Interferometer For Exoplanets (LIFE). I. Improved exoplanet detection yield estimates for a large mid-infrared space-interferometer mission". In: *Astronomy & Astrophysics* 664, A21, A21. DOI: 10.1051/0004-6361/202140366. arXiv: 2101.07500 [astro-ph.EP].

Racine, R. et al. (May 1999). "Speckle Noise and the Detection of Faint Companions". In: *Publications of the Astronomical Society of the Pacific* 111.759, pp. 587–594. DOI: 10.1086/316367.

Rafikov, R. R. (Mar. 2005). "Can Giant Planets Form by Direct Gravitational Instability?" In: *The Astrophysical Journal Letters* 621.1, pp. L69–L72. DOI: 10.1086/428899. arXiv: astro-ph/0406469 [astro-ph].

Roettenbacher, R. M., J. D. Monnier, H. Korhonen, et al. (May 2016). "No Sun-like dynamo on the active star $\zeta$ Andromedae from starspot asymmetry". In: *Nature* 533.7602, pp. 217–220. DOI: 10.1038/nature17444. arXiv: 1709.10107 [astro-ph.SR].

Roettenbacher, R. M., J. D. Monnier, F. C. Fekel, et al. (Aug. 2015). "Detecting the Companions and Ellipsoidal Variations of RS CVn Primaries. II. o Draconis, a Candidate for Recent Low-mass Companion Ingestion". In: *The Astrophysical Journal* 809.2, 159, p. 159. DOI: 10.1088/0004-637X/809/2/159. arXiv: 1507.03601 [astro-ph.SR].

Roettenbacher, R. M., J. D. Monnier, G. W. Henry, et al. (July 2015). "Detecting the Companions and Ellipsoidal Variations of RS CVn Primaries. I. $\sigma$ Geminorum". In: *The Astrophysical Journal* 807.1, 23, p. 23. DOI: 10.1088/0004-637X/807/1/23. arXiv: 1504.06628 [astro-ph.SR].

Rousset, G. et al. (Feb. 2003). "NAOS, the first AO system of the VLT: on-sky performance". In: *Adaptive Optical System Technologies II*. Ed. by P. L. Wizinowich and D. Bonaccini. Vol. 4839. Society of Photo-Optical Instrumentation Engineers (SPIE) Conference Series, pp. 140–149. DOI: 10.1117/12.459332.

Ruane, G. et al. (Jan. 2018). "Vortex coronagraphs for the Habitable Exoplanet Imaging Mission concept: theoretical performance and telescope requirements". In: *Journal of Astronomical Telescopes, Instruments, and Systems* 4, 015004, p. 015004. DOI: 10.1117/1.JATIS.4.1.015004. arXiv: 1803.03909 [astro-ph.IM].

Ruffio, J.-B. et al. (Oct. 2023). "JWST-TST High Contrast: Achieving direct spectroscopy of faint substellar companions next to bright stars with the NIRSpec IFU". In: *arXiv e-prints*, arXiv:2310.09902, arXiv:2310.09902. DOI: 10.48550/arXiv.2310.09902. arXiv: 2310.09902 [astro-ph.EP].

Schöller, M. (Oct. 2007). "The Very Large Telescope Interferometer: Current facility and prospects". In: *New Astronomy Reviews* 51.8-9, pp. 628–638. DOI: 10.1016/j.newar.2007.06.008.

Schwarz, H. et al. (Sept. 2016). "The slow spin of the young substellar companion GQ Lupi b and its orbital configuration". In: *Astronomy and Astrophysics* 593, A74, A74. DOI: 10.1051/0004-6361/201628908. arXiv: 1607.00012 [astro-ph.EP].

Seidel, J. V. et al. (Jan. 2020). "Wind of change: retrieving exoplanet atmospheric winds from high-resolution spectroscopy". In: *Astronomy and Astrophysics* 633, A86, A86. DOI: 10.1051/0004-6361/201936892. arXiv: 1912.02787 [astro-ph.EP].

Seo, B.-J. et al. (Aug. 2018). "Hybrid lyot coronagraph for WFIRST: high contrast testbed demonstration in flight-like low flux environment". In: *Space Telescopes and Instrumentation 2018: Optical, Infrared, and Millimeter Wave*. Ed. by M. Lystrup et al. Vol. 10698. Society of Photo-Optical Instrumentation Engineers (SPIE) Conference Series, 106982P, 106982P. DOI: 10.1117/12.2314358.

Serabyn, E., B. Mennesson, S. Martin, et al. (Oct. 2019). "Nulling at short wavelengths: theoretical performance constraints and a demonstration of faint companion detection inside the diffraction limit with a rotating-baseline interferometer". In: *Mon. Notices Royal Astron. Soc.* 489.1, pp. 1291–1303. DOI: 10.1093/mnras/stz2163. arXiv: 1908.05977 [astro-ph.IM].

Serabyn, E., G. Ruane, and D. Echeverri (Aug. 2022). "Observing inside the coronagraphic regime with optimized single-mode nulling interferometry". In: *Space Telescopes and Instrumentation 2022: Optical, Infrared, and Millimeter Wave*. Ed. by L. E. Coyle, S. Matsuura, and M. D. Perrin. Vol. 12180. Society of Photo-Optical Instrumentation Engineers (SPIE) Conference Series, 121800N, 121800N. DOI: 10.1117/12.2630589. arXiv: 2210.09412 [astro-ph.IM].

Serabyn, E., B. Mennesson, and S. Martin (Dec. 2020). "Observing inside the coronagraphic regime with nulling interferometry". In: *Society of Photo-Optical Instrumentation Engineers (SPIE) Conference Series*. Vol. 11446. Society of Photo-Optical Instrumentation Engineers (SPIE) Conference Series, 114461K, 114461K. DOI: 10.1117/12.2562947.

Shi, F. et al. (Sept. 2017). "Dynamic testbed demonstration of WFIRST coronagraph low order wavefront sensing and control (LOWFS/C)". In: *Society of Photo-Optical Instrumentation Engineers (SPIE) Conference Series*. Ed. by S. Shaklan. Vol. 10400. Society of Photo-Optical Instrumentation Engineers (SPIE) Conference Series, 104000D, p. 104000D. DOI: 10.1117/12.2274887.

Sivaramakrishnan, A. et al. (Mar. 2023). *NIRISS Commissioning Results: NIS-019 NRM Performance (NGAS CAR-703, APT 1093)*.

Snellen, I. A. G., R. J. de Kok, J. L. Birkby, et al. (Apr. 2015). "Combining high-dispersion spectroscopy with high contrast imaging: Probing rocky planets around our nearest neighbors". In: *Astronomy & Astrophysics* 576, A59, A59. DOI: 10.1051/0004-6361/201425018. arXiv: 1503.01136 [astro-ph.EP].

Snellen, I. A. G., B. R. Brandl, et al. (May 2014). "Fast spin of the young extrasolar planet $\beta$ Pictoris b". In: *Nature* 509.7498, pp. 63–65. DOI: 10.1038/nature13253.

Snellen, I. A. G., R. J. de Kok, E. J. W. de Mooij, et al. (June 2010). "The orbital motion, absolute mass and high-altitude winds of exoplanet HD209458b". In: *Nature* 465.7301, pp. 1049–1051. DOI: 10.1038/nature09111. arXiv: 1006.4364 [astro-ph.EP].

Sparks, W. B. and H. C. Ford (Oct. 2002). "Imaging Spectroscopy for Extrasolar Planet Detection". In: *The Astrophysical Journal* 578.1, pp. 543–564. DOI: 10.1086/342401. arXiv: astro-ph/0209078 [astro-ph].

Spiegel, D. S., A. Burrows, and J. A. Milsom (Jan. 2011). "The Deuterium-burning Mass Limit for Brown Dwarfs and Giant Planets". In: *The Astrophysical Journal* 727.1, 57, p. 57. DOI: 10.1088/0004-637X/727/1/57. arXiv: 1008.5150 [astro-ph.EP].

Sumi, T. et al. (May 2011). "Unbound or distant planetary mass population detected by gravitational microlensing". In: *Nature* 473.7347, pp. 349–352. DOI: 10.1038/nature10092. arXiv: 1105.3544 [astro-ph.EP].

Swain, M. R., G. Tinetti, et al. (Oct. 2009). "Water, Methane, and Carbon Dioxide Present in the Dayside Spectrum of the Exoplanet HD 209458b". In: *The Astrophysical Journal* 704.2, pp. 1616–1621. DOI: 10.1088/0004-637X/704/2/1616. arXiv: 0908.4010 [astro-ph.EP].

Swain, M. R., G. Vasisht, and G. Tinetti (Mar. 2008). "The presence of methane in the atmosphere of an extrasolar planet". In: *Nature* 452.7185, pp. 329–331. DOI: 10.1038/nature06823.

Szentgyorgyi, A. et al. (July 2018). "The GMT-consortium large earth finder (G-CLEF): an optical echelle spectrograph for the Giant Magellan Telescope (GMT)". In: *Ground-based and Airborne Instrumentation for Astronomy VII*. Ed. by C. J. Evans, L. Simard, and H. Takami. Vol. 10702. Society of Photo-Optical Instrumentation Engineers (SPIE) Conference Series, 107021R, 107021R. DOI: 10.1117/12.2313539.

ten Brummelaar, T. A. et al. (July 2005). "First Results from the CHARA Array. II. A Description of the Instrument". In: *The Astrophysical Journal* 628.1, pp. 453–465. DOI: 10.1086/430729. arXiv: astro-ph/0504082 [astro-ph].

Tinetti, G. et al. (July 2007). "Water vapour in the atmosphere of a transiting extrasolar planet". In: *Nature* 448.7150, pp. 169–171. DOI: 10.1038/nature06002.

Tuthill, P., J. D. Monnier, et al. (Apr. 2000). "Michelson Interferometry with the Keck I Telescope". In: *Publications of the Astronomical Society of the Pacific* 112.770, pp. 555–565. DOI: 10.1086/316550. arXiv: astro-ph/0003146 [astro-ph].

Tuthill, P., J. Lloyd, et al. (June 2006). "Sparse-aperture adaptive optics". In: *Society of Photo-Optical Instrumentation Engineers (SPIE) Conference Series*. Ed. by B. L. Ellerbroek and D. Bonaccini Calia. Vol. 6272. Society of Photo-Optical Instrumentation Engineers (SPIE) Conference Series, 62723A, 62723A. DOI: 10.1117/12.672342.

Vievard, S. et al. (Oct. 2023). "Photonic spectro-interferometry with SCExAO/FIRST at the Subaru Telescope: towards H$\alpha$ imaging of protoplanets". In: *Society of Photo-Optical Instrumentation Engineers (SPIE) Conference Series*. Vol. 12680. Society of Photo-Optical Instrumentation Engineers (SPIE) Conference Series, 126800H, 126800H. DOI: 10.1117/12.2676319.

Wallace, A. L. et al. (Oct. 2020). "High-resolution survey for planetary companions to young stars in the Taurus molecular cloud". In: *Monthly Notices of the Royal Astronomical Society* 498.1, pp. 1382–1396. DOI: 10.1093/mnras/staa2434. arXiv: 2008.06065 [astro-ph.EP].

Wang, J. J., A. Vigan, et al. (Mar. 2021). "Constraining the Nature of the PDS 70 Protoplanets with VLTI/GRAVITY". In: *The Astronomical Journal* 161.3, 148, p. 148. DOI: 10.3847/1538-3881/abdb2d. arXiv: 2101.04187 [astro-ph.EP].

Wang, J. J., S. Ginzburg, et al. (June 2020). "Keck/NIRC2 L'-band Imaging of Jovian-mass Accreting Protoplanets around PDS 70". In: *The Astronomical Journal* 159.6, 263, p. 263. DOI: 10.3847/1538-3881/ab8aef. arXiv: 2004.09597 [astro-ph.EP].

Wang, J. J., J.-B. Ruffio, et al. (Oct. 2021). "Detection and Bulk Properties of the HR 8799 Planets with High-resolution Spectroscopy". In: *The Astronomical Journal* 162.4, 148, p. 148. DOI: 10.3847/1538-3881/ac1349. arXiv: 2107.06949 [astro-ph.EP].

Wang, J., D. Mawet, J. J. Fortney, et al. (Dec. 2018). "Detecting Water in the Atmosphere of HR 8799 c with L-band High-dispersion Spectroscopy Aided by Adaptive Optics". In: *The Astronomical Journal* 156.6, 272, p. 272. DOI: 10.3847/1538-3881/aae47b. arXiv: 1809.09080 [astro-ph.EP].

Wang, J., D. Mawet, G. Ruane, et al. (Apr. 2017). "Observing Exoplanets with High Dispersion Coronagraphy. I. The Scientific Potential of Current and Next-generation Large Ground and Space Telescopes". In: *The Astronomical Journal* 153.4, 183, p. 183. DOI: 10.3847/1538-3881/aa6474. arXiv: 1703.00582 [astro-ph.EP].

Wizinowich, P. et al. (2000). “First Light Adaptive Optics Images from the Keck II Telescope: A New Era of High Angular Resolution Imagery”. In: *Publications of the Astronomical Society of the Pacific* 112, pp. 315–319. DOI: 10.1086/316543.

Wolszczan, A. and D. A. Frail (Jan. 1992). “A planetary system around the millisecond pulsar PSR1257 + 12”. In: *Nature* 355.6356, pp. 145–147. DOI: 10.1038/355145a0.

Xuan, J. W. et al. (Dec. 2023). “Validation of elemental and isotopic abundances in late-M spectral types with the benchmark HIP 55507 AB system”. In: *arXiv e-prints*, arXiv:2312.02297, arXiv:2312.02297. DOI: 10.48550/arXiv.2312.02297. arXiv: 2312.02297 [astro-ph.SR].

Zhang, J., E. M. .-. Kempton, and E. Rauscher (Dec. 2017). “Constraining Hot Jupiter Atmospheric Structure and Dynamics through Doppler-shifted Emission Spectra”. In: *The Astrophysical Journal* 851.2, 84, p. 84. DOI: 10.3847/1538-4357/aa9891. arXiv: 1711.02684 [astro-ph.EP].

*Chapter 2*

# VFN CONCEPT

This chapter presents the VFN concept as a new single-telescope technique for detecting and spectroscopically characterizing exoplanets within the inner working angle of conventional coronagraphs. The chapter starts with the fundamental principles of single mode fibers and fiber coupling, before proceeding to the theory of how VFN can hypothetically achieve complete starlight rejection. It then covers design considerations, limitations, and key benefits of VFN.

This chapter is based on and expands upon the work by Garreth Ruane, who first proposed the VFN concept. It therefore draws heavily on the original VFN paper (Ruane, J. Wang, et al., 2018), the subsequent design considerations paper (Ruane, Echeverri, et al., 2019), and personal communications with Ruane.

---

## 2.1 Single-Mode Fibers

An optical fiber is a waveguide where light traveling inside is bound and shaped by the index of refraction profile in the guide material. There are many designs for optical fibers but the simplest are step-index, where the cross-section is split into two concentric circular regions, each with a uniform index of refraction. The inner region is referred to as the "core," extending to a radius of $a_{\text{core}}$, and the outer region is the "cladding," which theoretically extends to infinity but in practice is simply much larger than the core. For an ideal step-index fiber (Jeunhomme, 1989), the refractive indices can be expressed as

$$n(r) = \begin{cases} n_{\text{core}} & r \leq a_{\text{core}} \\ n_{\text{clad}} & r > a_{\text{clad}} \end{cases}, \tag{2.1}$$

where $r$ is the radial distance from the center, and $n_{\text{clad}} < n_{\text{core}}$. The propagation of light through such a fiber is discretized into distinct modes defined by the properties of the fiber and the input field. Guided modes, the ones that survive with low losses along the length of the fiber, are primarily bound to the core region and exponentially decay in amplitude in the cladding. Other modes are either rejected by the fiber or are quickly radiated out through the cladding. Depending on the core diameter,

indices of refraction, and wavelength of light, the fiber can support multiple guided modes or a single mode. For VFN, we are interested in the single-mode fiber (SMF) case, which occurs when the normalized frequency parameter,

$$V = \frac{2\pi}{\lambda} a_{\text{core}} \sqrt{n_{\text{core}}^2 - n_{\text{clad}}^2}, \tag{2.2}$$

is less than the critical value $V_c = 2.405$. The $\sqrt{n_{\text{core}}^2 - n_{\text{clad}}^2}$ term is also known as the numerical aperture (NA) and roughly defines the range of input angles over which light can enter the fiber and be guided. For a given fiber (i.e., fixed core radius and refractive indices), Eq. 2.2 and the critical value give a "cutoff" wavelength,

$$\lambda_c = \frac{V}{V_c}\lambda = \frac{2\pi}{V_c} a_{\text{core}} \text{NA}, \tag{2.3}$$

defining the shortest wavelength for which the fiber is single moded.

The field for the single mode, or fundamental mode, can be expressed as

$$\Psi(r) = \psi_0 \begin{cases} \frac{J_0(Ur/a_{\text{core}})}{J_0(U)} & r \leq a_{\text{core}} \\ \frac{K_0(Wr/a_{\text{core}})}{K_0(U)} & r > a_{\text{core}} \end{cases}, \tag{2.4}$$

where $U$ and $W$ are constants fulfilling $U^2 + W^2 = V^2$ and

$$\frac{J_0(U)}{UJ_1(U)} = \frac{K_0(W)}{WK_1(W)}. \tag{2.5}$$

In these equations, $J_{\text{n}}$ denotes the Bessel function of the first kind of order n and similarly $K_{\text{n}}$ the modified Bessel function of the second kind. Note that since this mode is transversely polarized with linear polarization, it is often denoted as the $\text{LP}_{01}$ mode. We can approximate this fundamental mode with the Gaussian

$$\Psi(r) \approx \sqrt{\frac{2}{\pi\omega^2}} \exp\left(-(\frac{r}{\omega})^2\right), \tag{2.6}$$

where $2\omega$ is the mode field diameter (MFD), which varies with wavelength. The MFD can be approximated by

$$\text{MFD} = 2a_{\text{core}} \left(0.65 + 0.434(\frac{\lambda}{\lambda_c})^{3/2} + 0.01419(\frac{\lambda}{\lambda_c})^6\right) \tag{2.7}$$

to better than 1% accuracy for $0.8 < \lambda/\lambda_c < 2$ (Jeunhomme, 1989).

There are other Gaussian approximations but the one chosen here sets the Gaussian so that it yields the highest coupled power for the true mode (Marcuse, 1977; Jeunhomme, 1989). Figure 2.1 shows the profile for the true Bessel fiber mode, per Eq. 2.4, along with the Gaussian approximation. The mode is shown at 2.2 $\mu$m ($\lambda/\lambda_c = 1.21$) wavelength for a representative Thorlabs SM2000 fiber with $a_{\text{core}} = 5.5$ $\mu$m and indices $n_{\text{core}} = 1.4436$ and $n_{\text{clad}} = 1.4381$.

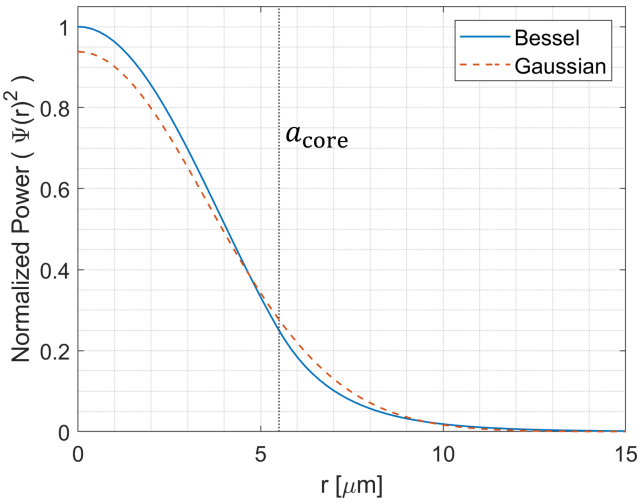


Figure 2.1: Normalized power profile of the fundamental mode in an SMF using the true form (solid blue line) and the Gaussian approximation (dashed orange line). This assumes a Thorlabs SM2000 fiber and $\lambda = 2.2\mu$m ($\lambda/\lambda_c = 1.21$).

## 2.2 Fiber Coupling

For our direct imaging applications, the light from the telescope is injected into the SMF by placing the fiber in the focal plane and imaging the desired object onto the fiber tip. Fibers only accept and transmit fields that match the guided modes, so for an SMF, the part of the field matching the fundamental mode will be coupled. The coupling efficiency, $\eta$, provides the fraction of the total power incident on the fiber that is accepted into the transmitted mode. It is determined by the square magnitude of the overlap integral between the incident field, $E(\mathbf{r})$, and the fiber mode, $\Psi(\mathbf{r})$,:

$$\eta = \left| \int E(\mathbf{r})\Psi(\mathbf{r}) dA \right|^2 . \tag{2.8}$$

Here $\mathbf{r} = (r, \theta)$ are the polar coordinates in the fiber plane. In this formulation, we have assumed for simplicity that the electric field and fundamental mode are normalized such that

$$\int |E(\mathbf{r})|^2 dA = 1 \qquad \text{and} \qquad \int |\Psi(\mathbf{r})|^2 dA = 1. \tag{2.9}$$

If they are not normalized accordingly, then Eq. 2.8 needs to be divided by the power in each term (i.e., the result of the integrals in Eq. 2.9). The fundamental mode as expressed in Eq. 2.6 meets the normalization requirement. The electric field depends on the telescope aperture and the wavefront error. For now, consider an evenly illuminated, unobstructed circular aperture with a flat wavefront at the pupil.

In the image plane, where the SMF is located, such a field leads to a point-spread function (PSF) known as the Airy diffraction pattern:

$$f_0(y) = \frac{ka^2}{f}\frac{J_1(y)}{y}, \tag{2.10}$$

where $a$ is the pupil radius, $f$ is the focal length of the imaging optic, $y = kar/f$, and $k = 2\pi/\lambda$. An additional normalization of $1/(a\sqrt{\pi})$ must be applied to meet the requirement from Eq. 2.9. With this PSF, the overlap integral becomes

$$\int E(\mathbf{r})\Psi(\mathbf{r})dA = \frac{2\sqrt{2}}{a\omega}\int f_0(y)e^{-(r/\omega)^2}rdr$$

$$= \frac{2\sqrt{2}}{\omega}\int_0^\infty J_1(kar/f)e^{-(r/\omega)^2}dr = \frac{\sqrt{2}}{\pi q/4}\left(1 - e^{-(\pi q/4)^2}\right), \tag{2.11}$$

where $q = 2ka\omega/(\pi f)$. We thus get the coupling efficiency for an Airy PSF aligned to the center of a SMF as the square magnitude of the overlap integral:

$$\eta = \frac{2}{(\pi q/4)^2}\left(1 - e^{-(\pi q/4)^2}\right)^2. \tag{2.12}$$

Equation 2.12 is plotted in Fig. 2.2(a) as a function of $q$ in the solid blue curve. Note that by collecting terms in $q$, and recognizing that F#=$f/D$ where $D = 2a$ is the aperture diameter, we get

$$q = \frac{\text{MFD}}{\lambda \text{F\#}}. \tag{2.13}$$

From this equation, it becomes clear that $q$ is the relative size of the fiber mode to the spot size of the PSF (the Airy disk in this case). The figure thus shows that for a given MFD, and therefore a given fiber, there is an optimal F# that sets the spot size to maximize the on-axis coupling efficiency. Later chapters refer to an F# mismatch in some experiments; that mismatch is due to an incorrect F# for the fiber, thereby yielding a sub-optimal $q$ value. The maximum coupling efficiency for an unaberrated Airy PSF occurs at $q = 1.41$ with a peak efficiency of 81% assuming the Gaussian fiber mode approximation. Figure 2.2(a) also shows in dashed orange the coupling efficiency computed from a numerical simulation using the real fiber mode (Eq. 2.4), assuming $\lambda = 2.2$ $\mu$m ($\lambda/\lambda_c = 1.21$) and the SM2000 fiber parameters. The Bessel solution is in good agreement with the Gaussian solution, yielding a peak efficiency of 77% also at $q = 1.41$. In the remainder of this thesis, we will generally use the Gaussian approximation for the fiber mode unless otherwise stated. This is consistent with previous publications on SMFs in astronomical applications (Shaklan et al., 1988; Jovanovic et al., 2017; J. Wang and Jurgenson, 2020).

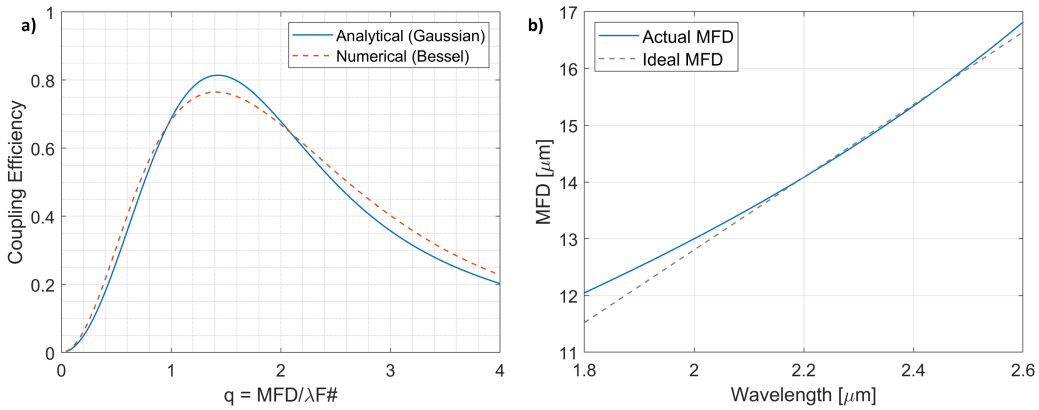


Figure 2.2: Key parameters for coupling into single mode fibers. (a) Coupling efficiency, $\eta$, versus the $q$ parameter assuming an Airy PSF. The solid blue curve shows the analytical solution from Eq. 2.12 which assumes a Gaussian fiber mode. The dashed orange curve is from a numerical simulation using the true mode from Eq. 2.4 at $\lambda = 2.2$ $\mu$m. The $q$ parameter is the ratio between the mode field diameter and the Airy spot size. (b) Scaling of MFD with wavelength according to Eq. 2.7 in solid blue, alongside the ideal MFD for maximum coupling at each wavelength in dashed grey. The ideal MFD is set by the assumed F# = 4.54, which gives $q = 1.41$ at $\lambda = 2.2$ $\mu$m. Both plots use the properties of a Thorlabs SM2000 fiber.

Since the $q$ value is wavelength-dependent, the F# for optimal coupling changes with wavelength for a given fiber. This has implications for the broadband capabilities of SMFs. However, the MFD for a fiber is also wavelength-dependent and scales similarly to the spot size. Thus, we can set the F# to give maximum coupling at one wavelength and then rely on the MFD scaling to ensure good coupling elsewhere. Figure 2.2(b) shows the MFD versus wavelength according to Eq. 2.7, along with the ideal MFD for maximum coupling at each wavelength assuming an F# of 4.54. This F# provides the ideal $q = 1.41$ at 2.2 $\mu$m assuming an SM2000 fiber. The two curves grow at roughly the same rate, indicating that $q$ remains roughly constant over the plotted region. This enables injection with >80% efficiency for a 36% fractional bandwidth spanning a much wider region than the astronomical K band.

The analysis so far has only considered the coupling efficiency for an on-axis point source, but the efficiency changes with the position of the PSF relative to the fiber. The peak coupling occurs on-axis since the Airy core is well-matched to the fiber mode. As the PSF shifts off-axis, the match worsens. Figure 2.3(a) shows the coupling efficiency as a function of the relative offset between the fiber and the PSF. As expected, the solid blue curve for the Airy PSF peaks at ~80% and then drops

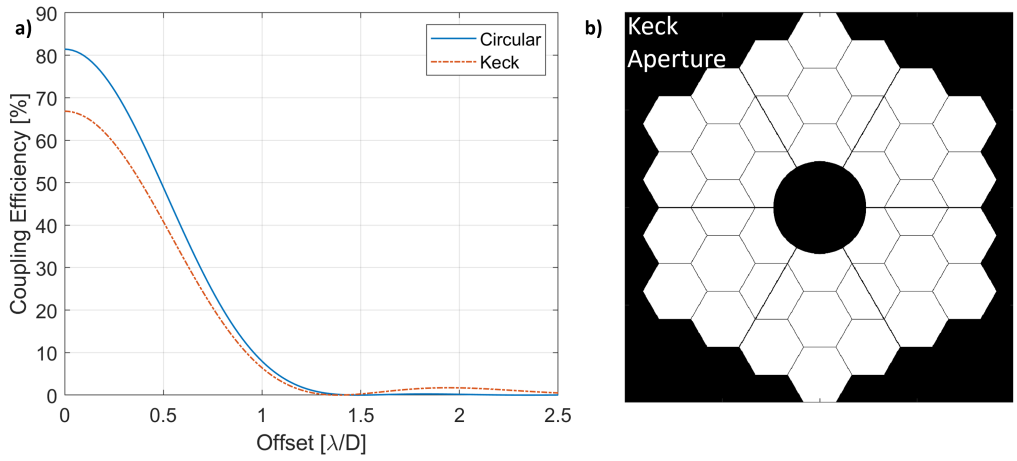


Figure 2.3: Direct spectroscopy coupling. (a) Coupling efficiency as a function of the relative offset between the fiber and the incident PSF. The solid blue curve is for the Airy PSF resulting from an unobstructed circular aperture while the orange dash-dotted curve is for the Keck aperture shown in plot (b).

off as the offset increases. In practice, this means that the coupling efficiency is sensitive to the pointing accuracy: a misalignment of 0.2 $\lambda/D$ drops the coupling by 6%. By 0.6 $\lambda/D$, the coupling is half of its peak value.

Equation 2.8 can be used to compute the coupling for any incident field by modifying $E(\mathbf{r})$ accordingly. We can thus asses the coupling efficiency on realistic telescope apertures that have central obscurations, secondary support structures ("spiders"), segment gaps, and other diffractive features that cast light away from the core of the PSF. Consider the Keck Telescope aperture shown in Fig. 2.3(b) as an example. The orange dash-dotted curve in plot (a) shows that the peak coupling is 67%. This occurs for $q = 1.45$, validating that the optimal $q$ value does not change much for most common apertures (Ruane, Echeverri, et al., 2019). As with the circular aperture, the coupling efficiency drops with separation, reaching a minimum at $\sim$1.4 $\lambda/D$. The Keck aperture has a more-noticeable increase in coupling from 1.5 to 2.5 $\lambda/D$ than a circular aperture due to the enhanced first diffraction ring from the central obstruction. This increase is small though, and the coupling approaches zero shortly thereafter. There are ways to modify the incident light through beam-shaping optics to improve the on-axis (i.e., no-offset) coupling into an SMF even in the presence of central obstructions (Jovanovic et al., 2017; Calvin et al., 2021). Though these are generally not addressed in this thesis, they show great promise for VFN (Ruane, Echeverri, et al., 2019), and are a route for further investigation and improvement.

In the same way that different telescope apertures affect the coupling efficiency, wavefront aberrations also deform and affect the PSF, reducing the coupling efficiency (Shaklan et al., 1988; Jovanovic et al., 2017). For ground-based observations, atmospheric turbulence is the dominant source of wavefront error assuming that quasi-static aberrations inside the instrument can be removed through calibration. The goal of an adaptive optics (AO) system is to reduce the atmospheric wavefront aberrations and generally gather the light back into the core of the PSF. A common metric for AO performance is the Strehl ratio, which measures the peak intensity in the system PSF compared to the zero-wavefront error case. High Strehl indicates better AO performance and more power in the core. The coupling efficiency is thus directly correlated with the Strehl ratio (Jovanovic et al., 2017). Furthermore, averaged over the integration time for a frame in an observation, wavefront aberrations tend to broaden the PSF such that they not only reduce the peak coupling efficiency, but also widen the curves shown in Fig. 2.3(a). This has implications for exoplanet observations as addressed in the next section.

## 2.3 The Direct Spectroscopy Case

Having covered the fundamentals of single-mode fibers and fiber coupling, we can consider the astronomy application. Exoplanet direct characterization strives to minimize the starlight and maximize the planet light. Looking at the curves in Fig. 2.3(a), this happens naturally when the fiber is aligned to the planet position in the focal plane. In this case, the planet will sit at the peak of the curve while the star will land off-axis and couple into the fiber with reduced efficiency; the larger the planet-star separation, the better the starlight rejection. This observing strategy is referred to as direct spectroscopy (DS) since the planet is aligned directly to the fiber. DS has now been employed by multiple direct imaging instruments and instrument concepts (Delorme et al., 2021; Vigan et al., 2023; Kotani et al., 2020; Mawet, Fitzgerald, et al., 2022).

Employing SMFs for direct imaging presents several notable advantages beyond their inherent starlight rejection capabilities. One significant benefit is the ease with which they can be routed to a spectrograph for detailed characterization. In conventional setups, where the spectrograph is affixed to the optical train and moves with the telescope during observations, issues such as thermal fluctuations and mechanical drifts can compromise measurement stability. However, with SMFs making the connection between the telescope and the science detector, the spectrograph can be strategically located in a controlled environment within the facility, mitigating

the effect of external factors on measurement precision. The single-mode output of these fibers represents another key advantage. Characterized by the Gaussian-like fundamental mode, this output ensures that wavefront aberrations and pointing errors before the fiber are encoded solely as variations in the transmitted power. When this light is projected onto the spectrograph's detector, the linespread function maintains a constant form and position, changing only in intensity with variation in the front-end conditions. This, coupled with the enhanced stability from relocating the science detector, significantly improves the stability of the wavelength calibration and the accuracy of the resulting spectra. Additionally, connecting the SMF to a spectrograph easily enables high dispersion coronagraphy. As explained in Sec. 1.4, HDC leverages the different spectral features between a star and an exoplanet to disentangle the light from each one. This acts as an additional post-processing gain of up to several orders of magnitude, closing the contrast gap between the star and planet. The highly-stable output of an SMF lends itself naturally to this application.

SMFs also reduce the amount of background signal during observations by collecting light from a smaller solid angle on the sky. For near- and mid-infrared applications, a further reduction can be achieved by placing the fiber's output end within the cold volume around the detector. This prevents thermal emission from a warm fiber tip. While the background signal can ideally be subtracted through measurements during the observation, or by assuming it is constant and measuring it preemptively during calibrations, the extra light still introduces increased photon noise which cannot be removed and degrades the sensitivity. Therefore, a reduction in background signal can significantly improve observations, especially when targeting companions around fainter stars.

The fiber in DS observations picks out a small spatial region in the focal plane with a specific spatial frequency and phase. This makes it particularly well-suited for speckle nulling techniques (Bottom et al., 2016). When applied to SMF observations, the goal of speckle nulling is not necessarily to reduce the intensity but rather to modify the electric field of the speckle over the fiber so that it is rejected by the fiber mode. This ultimately comes down to Eq. 2.8, and finding a solution for $E(\mathbf{r})$ that minimizes the coupled power for the speckle. For example, consider a quasi-static speckle of starlight introduced by wavefront error, that manifests as a roughly Gaussian blob coinciding with the planet position. One way to cancel the blob is to apply a sinusoidal pattern with a specific phase, amplitude, and frequency to create another speckle that destructively interferes with the first or that modi-

fies the field to be rejected by the fiber. This can successfully reduce the coupled starlight (Mawet, Ruane, et al., 2017). However, such solutions need to be carefully considered to avoid inadvertently affecting the planet coupling. In a pathological case, one could apply a phase that kills the starlight over the fiber but also casts much of the planet light away from the fiber core. A recent on-sky demonstration showed an improvement of 3× in starlight rejection with negligible effect on the companion PSF (Xin et al., 2023). It is also possible to adapt the commonly-used electric field conjugation (EFC) technique to operate on the coupling efficiency equation for improved starlight rejection (Llop-Sayson et al., 2019; Liberman et al., 2023). These techniques could allow DS observations to reach deeper contrasts at smaller separations.

The direct spectroscopy technique has led to several key findings in recent years. Focusing on the results of the Keck Planet Imager and Characterizer (KPIC) instrument alone, which was deployed in 2018 and has already detected 29 substellar companions, there are plenty of results to highlight. J. J. Wang et al. (2021) detected all four known exoplanets to HR 8799 and reported the first spin measurements for them. These results: provided the first high spectral resolution ($R$>10,000) detection of the b, d, and e planets, yielded CO and $H_2O$ measurements, and gave a higher-confidence (2× better SNR) detection of HR 8799 c while using 3.5× less exposure time than the previous NIRSPAO detection. The detection of HR 8799 e at 385 mas (~8 $\lambda/D$) is particularly noteworthy since it had previously never been detected at either medium nor high spectral resolution, thereby demonstrating the power of HDC with single-mode fibers. J. Wang, Kolecki, et al. (2022) demonstrated another aspect of the DS capabilities through the detection of elemental abundances (C and O) in the benchmark brown dwarf HR 7672 B. They found that the brown dwarf had abundances consistent with that of its primary star, thereby adding only the third benchmark brown dwarf with this characteristic, and providing a key comparison point for understanding the origin of substellar companions. Moreover, DS also unlocks a potential path for detecting moons around exoplanets. An "exomoon" induces a wobble in the planet's orbit which can be detected as a corresponding Doppler shift in the planet's spectral lines, much the same way that the shift in host star lines indicates a planet in RV observations. Ruffio et al. (2023) showed that the current RV sensitivity from direct spectroscopy of exoplanets with the KPIC instrument is sufficient for detecting exomoons with a 1-4% mass ratio around brown-dwarfs. Such detections would not only provide a new class of objects to study but would inform on planet formation mechanisms and outcomes.

Despite the significant advantages and capabilities of the DS technique, there are limitations to consider. One limitation is that the throughput for common telescope apertures is less than that on an ideal circular, unobstructed aperture. For example, rather than reaching 81%, the Keck aperture limits DS observations to a maximum coupling of 67% under ideal conditions (see Fig. 2.3). This represents a ~33% loss in throughput compared to conventional imaging techniques (assuming the coronagraph uses the full telescope aperture, which is not always the case). However, with modern AO systems that reach high Strehl and hence can provide close to ideal coupling, this is a relatively small cost to pay given the many benefits that DS provides. The throughput hit is therefore a minor limitation and challenging detections can still be made, as evidenced by the results in the previous paragraph. A more crucial constraint is the prerequisite for accurate knowledge of the exoplanet's position relative to the star prior to DS observations. The exoplanet is usually too faint to see with the fast tracking cameras used for pointing control, so the fiber is aligned by tracking on the host star and offsetting to the planet position. However, recall that a misalignment of only 0.6 $\lambda/D$ cuts the coupling efficiency in half; this corresponds to ~28 mas on-sky for the Keck Telescope at 2.2 $\mu$m. Thus, if the planet position is not known to better than a fraction of $\lambda/D$, the throughput can drop significantly, down to effectively 0% for errors greater than 1 $\lambda/D$. This implicitly limits DS observations to only follow-up on known exoplanets, rather than performing search campaigns for new companions.

Direct spectroscopy observations are also limited in the separations that they can observe. Though the SMF rejects some amount of starlight anytime the star is not on-axis, the rejection worsens with decreasing separation. At separations $\lesssim 1\ \lambda/D$, the fiber overlaps with the core of the stellar PSF and the starlight rejection is minor. This is especially true on a stellar PSF that has been broadened by residual atmospheric aberrations, as described towards the end of the previous section. Speckle nulling techniques may help but at such small separations, they significantly degrade the planet PSF and therefore decreasing the throughput.

## 2.4 A Primer on Fiber Nulling

As with conventional direct imaging, the starlight rejection in fiber-based observations at small separations can be improved through nulling interferometry. So-called fiber nulling follows similar principles to what was presented at the beginning of Sec. 1.5; namely that the star is aligned to an on-axis null so that its light is rejected while the light from an off-axis exoplanet is transmitted. However, the nulling con-

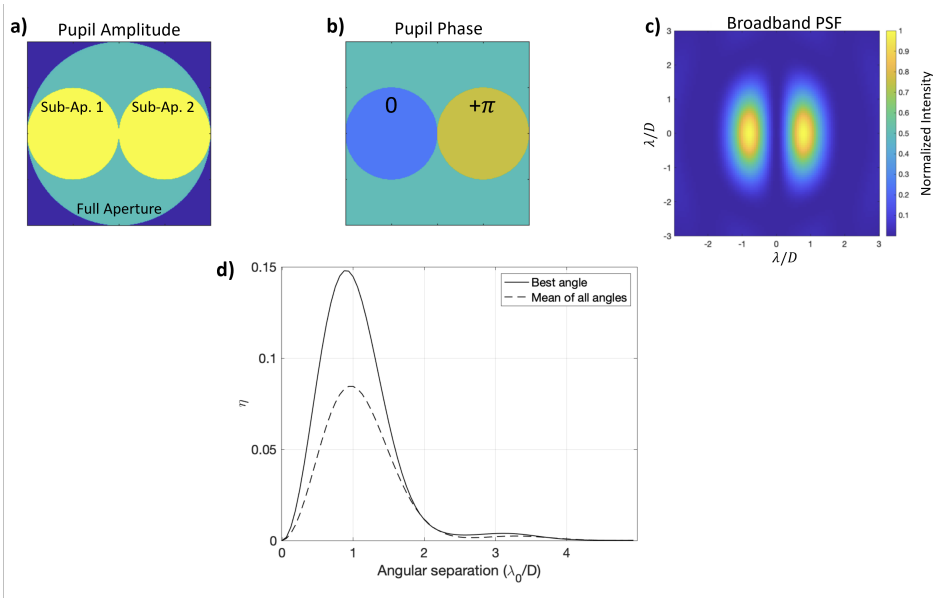


Figure 2.4: Architecture for two sub-aperture nulling. Pupil amplitude (a) and phase (b), as well as the resultant focal-plane PSF for a pair of maximal sup-apertures. (d) The radial efficiency for these sub-apertures. - Figure and caption adapted from Serabyn, Ruane, et al. (2022).

dition into an SMF is slightly different than with classical nullers since the fiber acts as a natural mode-filtering element. The requirement with a fiber is therefore that Eq. 2.8 go to zero on-axis but compute to non-zero for off-axis points. This boils down to modifying the system PSF so that the electric field for an on-axis point is orthogonal to the field accepted by the fiber.

The Palomar Fiber Nuller (PFN), introduced in the cross-aperture part of Sec. 1.5, is one option for fiber nulling. Like the original Bracewell nuller, the PFN destructively interferes two sub-apertures to create an interference pattern with a central null resting over the star. This is shown in Fig. 2.4, where the top row has the pupil amplitude and phase for a PFN-like system along with the corresponding focal plane intensity for a point source. The fiber is aligned to the on-axis null so that the starlight is rejected from coupling into the fiber. Off-axis points along the line orthogonal to the fringe pattern couple into the fiber with the efficiency shown in the lower plot of Fig. 2.4. Since the aperture mask blocks part of the pupil, the coupling efficiency as reported in the plot is normalized to the total light incident on the primary mirror. This accounts for losses from the mask and the fiber to provide the throughput for both elements needed to implement this nulling architecture. The peak coupling is 15% at $\sim 1\ \lambda/D$. However, this peak only occurs along the axis

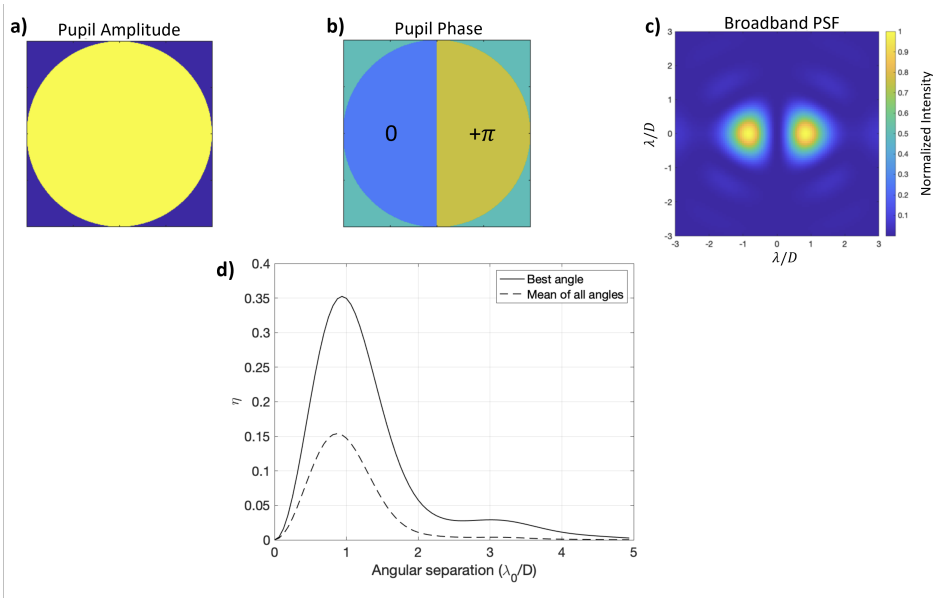


Figure 2.5: Architecture for phase knife nulling. Pupil amplitude (a) and phase (b), as well as the resultant focal-plane PSF for a $\pi$ phase step across the aperture centerline. (d) The resultant radial efficiency. - Figure and caption adapted from Serabyn, Ruane, et al. (2022).

perpendicular to the fringe pattern. So if the planet is at a different position angle, it will couple into the fiber with lower efficiency even if it is 1 $\lambda/D$ from the star. The PFN is just one option in a much larger family of pupil phase solutions that lead to on-axis fiber nulls and off-axis planet coupling. Serabyn, Ruane, et al. (2022) did a study of various pupil phase and amplitude solutions and found that another promising option is to extend the sub-apertures to each fill half of the plane. In this scenario, half of the pupil is shifted in phase by $\pi$ relative to the other half. This solution is referred to as the phase knife and is shown in Fig. 2.5 in a similar format to the earlier PFN plot. The phase knife also generates an on-axis null but it achieves higher overall throughput since it utilizes the full telescope aperture. The peak coupling of just over 35% occurs at around 1 $\lambda/D$. The phase knife provided the highest throughput out of the all the options considered in the study. Hence, when an exoplanet's position angle relative to the star is known, the phase knife may be the most promising option, though the sensitivity to wavefront error and pointing for this architecture still need to be considered.

An interesting finding from the study was that the azimuthal coverage in the focal plane can be increased by placing multiple sub-apertures radially along the pupil with a uniform incremental phase between them. As the number of sub-aperture

tiling the pupil increases, the region of peak coupling wraps azimuthally around the star, converging towards a ring of high coupling efficiency at ~1 $\lambda/D$. In the limit of an infinite number of sub-apertures completely tiling the pupil, each with infinitesimal area, this design approaches a spiral phase ramp, known as a vortex phase, and yields the VFN architecture. Though the peak coupling efficiency is lower than that of the phase knife, the complete azimuthal coverage provided by VFN enables it to efficiently search for exoplanets within ~2 $\lambda/D$ all around the star. The phase knife and other similar architectures would require observations at various orientations to sample the same area.

## 2.5 Vortex Fiber Nulling

VFN achieves its nulling effect by adding an azimuthally-increasing phase ramp to the light incident on the fiber. This ramp, known as a vortex phase, is a standard tool for conventional coronagraph designs (Mawet, Riaud, et al., 2005; Swartzlander, 2009). In a coronagraph, the vortex is placed in a focal plane to diffract the on-axis starlight to the edges of the pupil where it can be blocked by a pupil stop so that it does not propagate to subsequent image planes. For VFN the vortex serves a slightly different purpose. It is used to impart a phase pattern that is orthogonal to the fundamental mode of the fiber, not to selectively diffract the starlight. As such, the vortex phase in VFN can be applied at a focal or pupil plane while still producing the desired nulling effect. The following text and the majority of this thesis assumes the vortex is in a pupil as this has several advantages, briefly covered in Sec. 2.7, and the pupil implementation is what has been demonstrated in the lab and on-sky.

The ideal vortex phase is described by $\exp(il\theta)$, where $l$ is an integer known as the topological charge (Beijersbergen et al., 1994; Swartzlander, 2001). The charge defines the number of times the phase wraps over the unit circle; for charge 1, the phase goes from 0 to $2\pi$ once while for charge 2, the phase reaches $2\pi$ at 180° and then $4\pi$ at 360°. The phases for both charge 1 and 2 vortices are shown in Fig. 2.6. When a vortex phase is applied to an evenly-illuminated circular pupil with a flat wavefront, the field in a subsequent focal plane is given by the $l$th-order Hankel transform (Ruane, 2016):

$$h(\mathbf{r}) = (-i)^l e^{(il\theta)} \frac{k}{f} \int_0^a J_l(k\rho r/f)\, \rho d\rho. \tag{2.14}$$

The result of this transform, and hence the on-axis PSF, can be expressed as

$$E(\mathbf{r}) = f(r) e^{(il\theta)}, \tag{2.15}$$

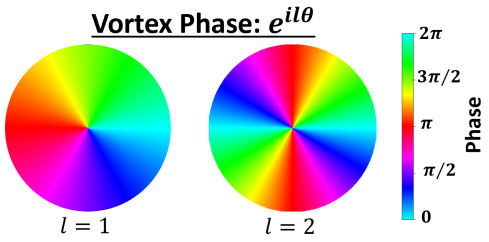


Figure 2.6: Phase for a charge $l = 1$ and $l = 2$ vortex.

where $f(r)$ is a function on the radial coordinate only. As before, Eq. 2.8 provides the coupling efficiency into the fiber given the incident electric field (Eq. 2.15). With this PSF, and assuming the fiber is also on-axis, the overlap integral becomes

$$\int f(r)e^{(il\theta)}\Psi(r)\, r dr d\theta = \int_0^\infty f(r)\Psi(r)\, r dr \int_0^{2\pi} e^{(il\theta)}\, d\theta. \tag{2.16}$$

The integral has been split into radial and azimuthal terms given that $\Psi(r)$ and $f(r)$ rely only on $r$, while $\exp(il\theta)$ relies only $\theta$. The azimuthal term integrated over the full 0 to $2\pi$ bounds of the unit circle computes to zero for any non-zero integer $l$:

$$\int_0^{2\pi} e^{(il\theta)} d\theta = \begin{cases} 2\pi & l = 0 \\ 0 & l \neq 0 \end{cases}. \tag{2.17}$$

This makes the full overlap integral go to zero such that the coupling into a SMF is zero when the fiber is aligned to a PSF with an integer vortex phase. In this way, VFN achieves a perfect null for any on-axis point source. The star's image can then be aligned to the fiber and thus starlight is completely rejected.

The VFN coupling efficiency for an off-axis source is, nevertheless, non-zero. This is because a PSF that lands off-center on the fiber has an electric field whose vortex phase is not axially symmetric over the fiber mode, and hence the overlap integral does not go to zero. The left column in Fig. 2.7 shows the two-dimensional coupling efficiency maps for VFN with a charge $l = 1$ and $l = 2$ vortex. This is generated by computing the overlap integral for a PSF at each point in the field, assuming that the fiber is aligned to the optical axis. The brightness at each location in the map can therefore be interpreted as the amount of light that couples into the fiber for a point source situated at that location in the field. This is akin to the transmission map for a classical nuller (see Sec. 1.5), where the brightness encodes the intensity of the light that is accepted from each point in the map. As such, the VFN coupling map,

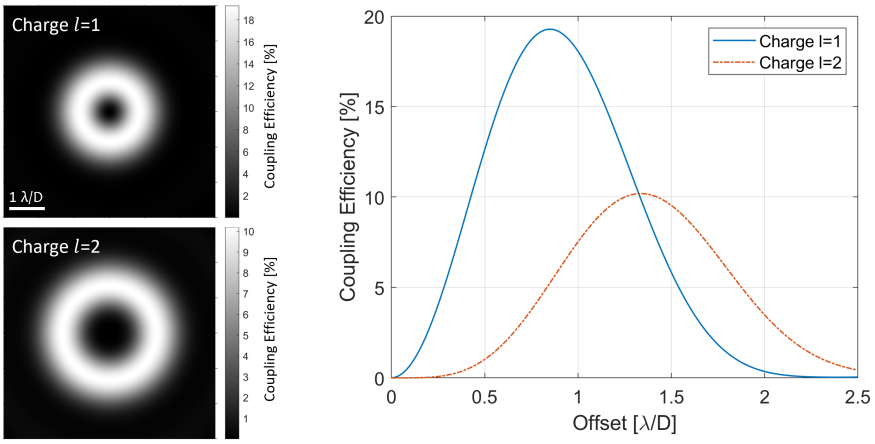


Figure 2.7: Charge 1 and 2 coupling on a circular aperture. Left column: Two-dimensional coupling maps for VFN with a charge 1 (top) and charge 2 (bottom) vortex phase. The maps each span a 6×6 $\lambda/D$ field of view. Note the difference in colorbars, as the charge 1 map goes from 0 to 20% while charge 2 goes from 0 to 10%. Right plot: azimuthally-averaged coupling efficiency for each charge.

sometimes referred to as the "donut," can be thought of as a bright interferometric fringe with a central null point. For a circular aperture, the fringe is fully symmetric around the null. The right plot in Fig. 2.7 shows the azimuthal average for each of the two maps. The peak coupling with charge 1 is ~20% at 0.85 $\lambda/D$ and with charge 2 it is ~10% at 1.35 $\lambda/D$. Note that the radius of the bright fringe increases as the vortex charge increases, but this comes at the expense of decreased coupling efficiency. Higher vortex charges are therefore possible but with diminishing returns. For example, charge 3 has a peak of 6.5% at 1.8 $\lambda/D$ and charge 4 has a peak <5% at 2.2 $\lambda/D$. This thesis, and the bulk of the published VFN work, focuses on implementations with charge 1 and 2 vortices.

The circular symmetry of the VFN fringe is a key characteristic that allows it to efficiently search for new planets around a star. With DS observations, one would need to raster-scan the fiber over the field to cover the same area. Such a procedure would achieve higher coupling at each individual fiber location but overall lower efficiency due to the increased total observation time (ref Sec. 6.9). Similarly, the phase knife achieves higher coupling within its two-lobed transmission map but it would require field rotation to sample all angles around the star. VFN has lower peak coupling but can scan the full annulus around the star at once, improving the total observing efficiency.

With VFN's symmetric, annular fringe, a detection is not made through baseline rotation as done in many other nullers. Bracewell's original concept used the intensity modulation introduced by scanning the fringes over planet to extract the planet signal from that of the star. This is also how the PFN operated. The same could be achieved with VFN by breaking the annular fringe into an azimuthally-varying form using crossed linear polarizers. A detection would then be made by rotating one of the polarizers to scan the X-like fringe pattern over the planet (Serabyn, Mennesson, et al., 2020). However, that implementation would cut the effective throughput in half due to the polarization filtering. Rather than detecting the exoplanet photometrically, the VFN concept can leverage the power of the HDC technique to make a spectral detection. The light from the SMF output in VFN is primarily a combination of planet light, post-nulling residual starlight (see Sec. 2.6), and background light. At medium- to high-resolution, the spectrum from each of these terms is different such that they can be distinguished from each other. In practice, one way to do this is through forward modeling, as was done for the detections in Chapter 7. The SMF in VFN observations is thus generally routed to a spectrograph, as done for DS observations. In this way, a VFN observation not only serves to detect the exoplanet but also to simultaneously characterize it. Note that in the laboratory and other experiments presented in later chapters, a photometer rather than a spectrograph was used as a simple way to demonstrate the nulling effect and validate the coupling efficiency. These photometric results are nevertheless applicable to the spectral detection technique as long as they hold in broadband, as demonstrated, so that spectroscopy can be performed.

**SNR and Integration Time**

The effectiveness of the VFN technique can be quantified using the signal-to-noise ratio (SNR) of a detection. Ruane, J. Wang, et al. (2018) presented this calculation in detail, and the text below follows that derivation. The calculation is again applied in Sec. 6.6, though the formulation in that later section is slightly different than what is expressed here. For that section, $\eta$, $T$, and $q$ are combined into one $T$ term, and $\Phi$ is directly defined over the spectral channel width.

The SNR in an observation is given by

$$\mathrm{SNR} = \frac{S_p}{\sqrt{S_s + S_p + S_b + \mathrm{RN}}}, \tag{2.18}$$

where $S_p$, $S_s$, and $S_b$ are the planet, star, and background signal, respectively, while RN is the square of the read noise from the detector. The signal from the planet and

the star can be expressed as

$$S_{p,s} = \eta_{p,s}\Phi_{p,s}\tau\Delta\lambda AqT. \tag{2.19}$$

In this equation $\eta_{p,s}$ is the coupling efficiency for the planet or star as computed by Eq. 2.8. $\Phi_{p,s}$ is the photon flux at the primary mirror from the planet or star, in units of photons per unit area per unit time per unit wavelength. $\tau$ is the integration time, $A$ is the collecting area of the telescope, and $q$ is the quantum efficiency of the detector. Assuming that the planet and background signals, as well as the read noise, are significantly smaller than the signal from the residual starlight, the observation is said to be photon-noise limited. In this case, the SNR per spectral channel is

$$\mathrm{SNR} = \frac{S_p}{\sqrt{S_s}} = \frac{\eta_p}{\sqrt{\eta_s}}\sqrt{\frac{\epsilon^2\Phi_s\tau\lambda AqT}{R}}, \tag{2.20}$$

where $R = \lambda/\Delta\lambda$ is the spectral resolution at the desired wavelength, and $\epsilon = \Phi_p/\Phi_s$ is the photometric flux ratio between the planet and the star. Setting a goal SNR per spectral channel for a detection, we can then determine the necessary integration time as

$$\tau = \frac{\eta_s}{\eta_p^2}\left[\frac{(\mathrm{SNR})^2 R}{\epsilon^2\Phi_s\lambda AqT}\right] = \frac{\eta_s}{\eta_p^2}\tau_0. \tag{2.21}$$

$\tau_0$ is therefore a constant for a given observation, and is driven by the goal SNR and the flux ratio of the desired star-planet system. VFN serves to reduce the requisite integration time for a detection by reducing the amount of residual starlight (minimizing $\eta_s$) while passing as much planet light as possible (maximizing $\eta_p$). Note that the improvement in integration time is directly proportional to the null and inversely proportional to the square of the planet coupling, such that the requisite integration time is more sensitive to changes in planet coupling than star coupling.

## 2.6 Limitations

As with any coronagraphic or interferometric technique, VFN is sensitive to various types of error that can lead to increased starlight coupling. Since these errors worsen $\eta_s$, they in turn increase the integration time required for a given SNR. In this section, we briefly list some of the dominant sources of error, and provide an approximation of the $\eta_s$ relationship for each of them. These $\eta_s$ terms can then be combined as

$$\eta_s = \eta_{\mathrm{jit}} + \eta_{\mathrm{gl}} + \eta_{\mathrm{wfe}} + \eta_{\mathrm{vvl}} + \dots, \tag{2.22}$$

and used in Eq. 2.21 to determine their effect on an observation.

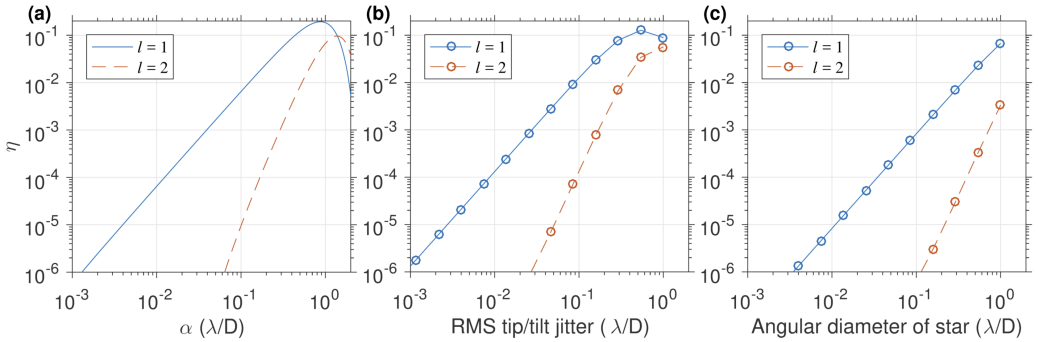


Figure 2.8: Coupling efficiency of (a) a point source as a function of angular offset from the optical axis and the fraction of starlight that couples into the fiber versus (b) tip/tilt jitter and (c) the size of the star. These values are calculated via a numerical simulations of the optical system with tip-tilt errors introduced in a Monte Carlo fashion. - Figure and caption adapted from Ruane, Echeverri, et al. (2019).

### Pointing Sensitivity

Nullers are generally very sensitive to pointing accuracy since the star must be well-aligned to the dark fringe to ensure it is properly rejected. In VFN, the vortex charge determines the relationship; a charge 1 vortex has a second-order dependence while charge 2 has a fourth order dependence. This means that VFN with charge 2 is more robust to pointing errors but that comes at the expense of reduced off-axis coupling and a decreased sensitivity to companions at small separations. Figure 2.8(a) shows the coupling efficiency for each charge at small separations in log scale to reveal the second- and fourth-order dependence.

In practice, VFN should be performed behind an AO system which can keep the star's image aligned to the fiber on average. However, the AO system cannot completely correct pointing errors such that residuals at high-frequency, known as tip-tilt jitter, shift the star around the null point and cause it to partially couple into the fiber. These residuals will generally take the form of a normal distribution characterized by a standard deviation, $\sigma_{\text{jit}}$. Assuming that the jitter residuals from the AO system are mean-zero (keeping the star aligned to the fiber), then the standard deviation is the same as the root-mean-square (RMS) of the distribution; later chapters will often report the jitter magnitude in RMS. Figure 2.8(b) shows the time-averaged null depth in the presence of jitter. This is computed from numerical simulations where tip-tilt errors are injected in a Monte Carlo fashion, sampling from a mean-zero normal distribution with the desired standard deviation. The plot validates that the

contribution to the null depth from residual jitter can be approximated as

$$\eta_{\text{jit}} \approx \left(\sigma_{\text{jit}} \frac{D}{\lambda}\right)^{2l}, \tag{2.23}$$

where $\sigma_{\text{jit}}$ is in radians, $D$ and $\lambda$ are the telescope diameter and the operating wavelength as usual, and $l$ is the vortex charge.

**Geometric Leakage**

Similarly, the finite angular size of the stellar disk causes some of its light to come in at an off-axis angle and couple into the fiber. The resulting null contribution can be computed in a similar fashion to the jitter but modeling the star as a uniform disk. The result is shown in Fig. 2.8(c). A power-law fit to the curves yields

$$\eta_{\text{gl}} \approx \left(\frac{2\theta_\star}{\gamma} \frac{D}{\lambda}\right)^{2l}, \qquad \gamma = \begin{cases} 3.5 & l = 1 \\ 4.2 & l = 2 \end{cases}. \tag{2.24}$$

In this equation, $\theta_\star$ is the angular radius of the star in radians and $\gamma$ is a coefficient for the fit that depends on the vortex charge. This equation is analogous, and unsurprisingly very similar, to Eq. 1.9 for the geometric leakage in a classical two-aperture nuller. Note that the plot in Fig. 2.8(c) is shown with the x-axis as the angular diameter of the star, rather than its radius; the equation here is written with respect to the radius to match the expression for the classical nuller.

**Wavefront Aberrations**

Wavefront aberrations have two effects on the coupling efficiency for VFN. The first is that they deform the bright coupling fringe so that it is no longer a symmetric annular ring but rather has different regions of increased or decreased coupling efficiency locally. Figure 2.9 shows this effect with the Zernike trefoil aberration as an example. The symmetry remains roughly unchanged until about 0.05 waves RMS, corresponding to 110 nm RMS for $\lambda = 2.2$ $\mu$m. Even when the coupling efficiency loses its symmetry, some regions experience lower coupling while others experience higher coupling. This means that the azimuthally-averaged peak coupling only goes down by a small amount for moderate levels of wavefront error; for charge 1, the average peak is 19.2% with no wavefront error and 18.1% with 0.05 waves RMS of trefoil. Charge 2 goes from 10.2% to 9.5% in the same scenarios. Other aberrations have similar effects on the bright fringe, though the asymmetries that are introduced are different for each case. Furthermore, since the wavefront residual from an AO

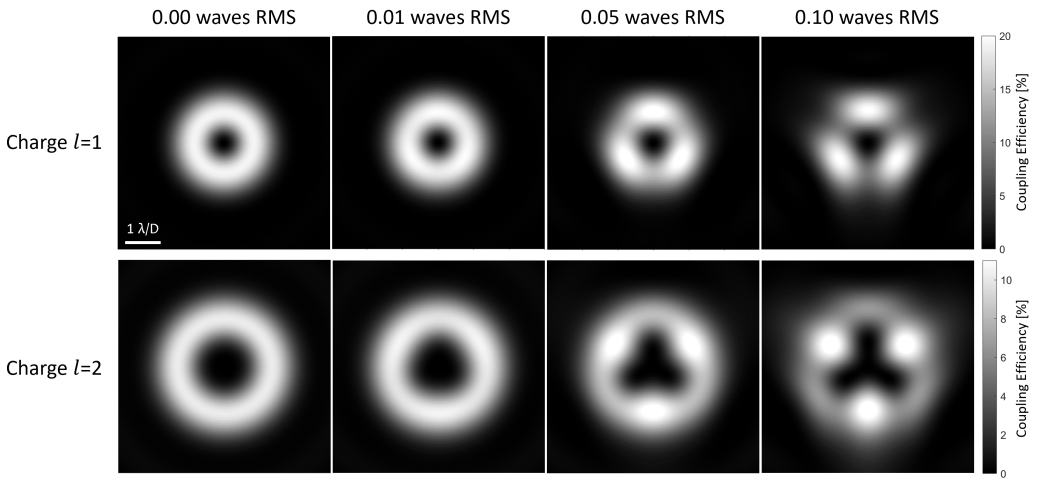


Figure 2.9: Coupling efficiency maps for charge 1 (top row) and charge 2 (bottom row) VFN in the presence of varying amounts of trefoil from 0.00 to 0.10 waves RMS (0 to 220 nm RMS at $\lambda = 2.2$ $\mu$m). The case with zero wavefront error shows a fully symmetric annular fringe which starts to separate into lobes as the error increases. All maps span a 6×6 $\lambda/D$ field of view. Note the change in colorbars between charge 1 and 2 and that some of the high-coupling regions in the right maps are saturated in the colormap.

system are generally mean-zero, assuming non-common-path aberrations are well-calibrated, there should be no bias towards some magnitude of aberration. As such, though at some instance in time, the aberrations may cause reduced coupling over the planet, at some other time, they will cause increased coupling. Section 5.3 provides a detailed simulation of the effect of wavefront error on the average VFN coupling. The results there show how the presence of realistic on-sky residuals from the Keck AO system only degrades the peak charge 1 coupling from about 19% to 14% averaged over the observation.

The second effect of wavefront error on the coupling in VFN is to degrade the on-axis null point. This increases $\eta_s$ and hence increases the amount of starlight coupled into the fiber. However, Ruane, Echeverri, et al. (2019) showed that the null is only sensitive to specific aberrations, depending on the vortex charge. This sensitivity is easily delineated in the Zernike basis based on the azimuthal index of the aberrations. The Zernikes are generally expressed as $Z_n^m(r, \theta)$, where $m$ is the azimuthal index. With this in mind, VFN with charge $l = 1$ has a second-order dependence on aberrations with $m = \pm 1$, corresponding to tip,tilt, and coma. Meanwhile, charge $l = 2$ has a dominant second-order dependence on aberrations

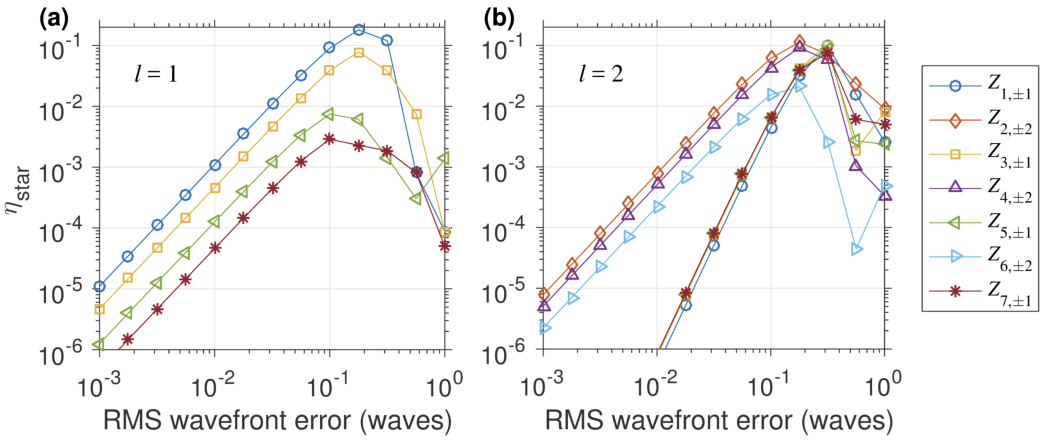


Figure 2.10: Null sensitivity to low-order aberrations for charges (a) $l = 1$ and (b) $l = 2$ assuming the star is a point source and the pupil is circular. The modes that appear in (a) have azimuthal index $m = \pm 1$ (i.e., tip, tilt, and all orders of coma) and the null depth follows a second-order power law. The same modes appear in (b) with a fourth-order power law, while the null depth has a second-order sensitivity to modes with azimuthal index $m = \pm 2$ (i.e., all orders of astigmatism). Terms with $m \neq \pm 1$ or $m \neq \pm 2$ are omitted because they do not contribute to the null depth in either case. - Figure and caption adapted from Ruane, Echeverri, et al. (2019).

with $m = \pm 2$, corresponding to astigmatism, and a less impactful fourth-order dependence on the $m = \pm 1$ terms. Figure 2.10 shows the on-axis coupling efficiency for charge 1, plot (a), and 2, plot (b), as a function of RMS wavefront error for the various Zernikes. Note that Zernikes with other azimuthal index values ($m \neq 1$ or $m \neq 2$) do not have any impact on the null in VFN and are not shown in the plots. This also means that all of the trefoil cases shown in Fig. 2.9 still yield a complete null ($\eta_s = 0$), as trefoil does not affect the on-axis coupling for either vortex charge.

Fitting a power law to the second-order terms in Fig. 2.10 provides a set of coefficients $b_{nm}$ that can be used to determine the null contribution from each Zernike aberration as

$$\eta_{nm} = (b_{nm}\omega_{nm})^2, \tag{2.25}$$

where $\omega_{nm}$ is the RMS wavefront error in the given aberration. Table 2.1 provides the coefficients for the first 100 low-order Zernike aberrations. Note that this table only includes the terms with a second-order dependence and the coefficients were computed through numerical simulation assuming a circular unobstructed aperture; the coefficients may be different on other apertures. With these coefficients, the wavefront in a system can be decomposed into Zernike aberrations and the corresponding null contribution from wavefront error can be determined. Assuming

that the wavefront error is small ($\omega_{nm} << 1$) such that fourth-order terms can be neglected, then the null contribution is well-estimated by

$$\eta_{\text{wfe}} \approx \sum_{nm} (b_{nm}\omega_{nm})^2. \tag{2.26}$$

This estimation was done for the experiment presented in Chapter 3 and successfully recovered the measured null depth.

Table 2.1: Coefficients for VFN Zernike Sensitivity

| Noll Index | $n$ | $m$ | $b_{nm}$ | Noll Index | $n$ | $m$ | $b_{nm}$ |
|---|---|---|---|---|---|---|---|
| Charge 1 | | | | Charge 2 | | | |
| 2,3 | 1 | ±1 | 3.33 | 5,6 | 2 | ±2 | 2.80 |
| 7,8 | 3 | ±1 | 2.15 | 12,13 | 4 | ±2 | 2.23 |
| 16,17 | 5 | ±1 | 1.12 | 23,24 | 6 | ±2 | 1.50 |
| 29,30 | 7 | ±1 | 0.67 | 38,39 | 8 | ±2 | 1.03 |
| 46,47 | 9 | ±1 | 0.47 | 57,58 | 10 | ±2 | 0.77 |
| 67,68 | 11 | ±1 | 0.34 | 80,81 | 12 | ±2 | 0.59 |

NOTE- Only the coefficients corresponding to second-order power laws are shown; charge 2 VFN has additional fourth-order sensitivities with their own coefficients. The reported $b_{nm}$ values are computed for a circular unobstructed aperture, and may be different on other apertures.

**Vector Vortex Leakage**

The vortex phase is usually generated using a dedicated vortex mask that is inserted into the optical path. These masks take many different forms but their implementation generally falls into two categories: scalar and vectorial. Scalar vortex masks apply the requisite phase through longitudinal phase delay, while vector masks rely on a geometric phase shift. Section 8.1 presents a detailed explanation of VFN when using a scalar vortex mask. However, the most common masks used in direct imaging are vector masks. All of the laboratory and on-sky experiments reported in this thesis have used vector masks as well.

Vector vortex masks act as a half-wave plate with a spatially-varying fast axis. This means that the applied phase is polarization-dependent, and can be expressed with

a Jones matrix, $\mathbf{M}_{\circlearrowleft}$. In the circular polarization basis, the matrix is

$$\mathbf{M}_{\circlearrowleft} = c_V \begin{bmatrix} 0 & e^{il\theta} \\ e^{-il\theta} & 0 \end{bmatrix} + c_L \begin{bmatrix} 1 & 0 \\ 0 & 1 \end{bmatrix}, \tag{2.27}$$

where the basis vectors are the right- and left-hand circularly polarized field components, and $c_V$ and $c_L$ are wavelength-dependent coefficients set by the mask (Ruane, Echeverri, et al., 2019). An ideal vortex mask has $c_L = 0$ such that all of the incident light exits the optic with the vortex phase, though conjugate phase ramps are applied to the light in each polarization state. Regardless of the phase ramp direction, all the light takes the requisite $\exp \pm il\theta$ form and the overlap integral still computes to zero for on-axis point sources.

However, actual vector vortex masks have wavelength dependent retardance errors, $\epsilon_L(\lambda)$, that introduce the second term in the vortex Jones matrix. This term causes a fraction of the incident light to pass through the vortex without acquiring the vortex phase. That light, referred to as the zero-order leakage, propagates to the focal plane, appears as a normal Airy PSF, and therefore couples into the fiber. The power in the fraction of light that sees this term is given by $|c_L|^2 \approx \epsilon_L(\lambda)^2/4$. The corresponding contribution to the null floor is thus

$$\eta_{\mathrm{vvl}} \approx |c_L|^2 \eta_0 = \frac{\epsilon_L(\lambda)^2}{4} \eta_0, \tag{2.28}$$

where $\eta_0$ is the coupling efficiency into the fiber for the non-vortex PSF; from Sec. 2.2, we know that $\eta_0$ is ~80% for a circlar unobstructed aperture and ~67% for the Keck aperture.

The vector vortex leakage was the limiting term for the null depth in some of the experiments presented in later Chapters. We also leverage the wavelength-dependence of this term for tracking purposes. In the science band, the PSF from the vortex mask as seen by the tracking camera is a ring that is difficult to centroid on, especially in the presence of wavefront errors. However, if the vortex mask has a larger retardance error in the tracking band, then the resulting PSF is a combination of the Airy PSF with the vortex PSF. This provides a central peak that can be used for centroiding to identify the star on the tracking camera and steer its PSF to center on the fiber. This is described in more detail in Secs. 6.4 and 8.4. However, note that minimizing the $c_L$ term in the science band should still be the highest priority when procuring a mask so that the null contribution is small; the tracking benefit is simply a useful side-effect in the out-of-band light.

**Dispersion**

Chromatic dispersion, such as that introduced by differential atmopsheric refraction (DAR) or from an optical wedge, can also reduce the quality of the VFN null. Dispersion causes a wavelength-dependent shift in the PSF in the focal plane such that the fiber can only be aligned to the star's image at a single wavelength. Thus, other wavelengths effectively experience a tilt which reduces their null depth. For charge 2 vortex operations, dispersion is not a significant effect. However, for charge 1 it is a larger issue due to the increased coupling at small separations. The effect of dispersion is covered in significantly more detail in Sec. 8.3.

## 2.7 Further Considerations

The previous sections considered a single design for VFN: an implementation with the vortex in the pupil and a circular unobstructed aperture. This serves to cover the core concepts needed for developing the technique and understanding its limitations. However, a major benefit of VFN is that it achieves similar performance across different telescope apertures and regardless of whether the vortex phase is applied in a pupil plane or a focal plane. This makes it readily applicable to different instrument architectures at different telescopes.

A simple case to consider is that of a circular aperture with a central obscuration. In this case, a more general form of Eqs. 2.16 and 2.17 shows that the null condition for VFN is still met. This is because the first integral is still separable such that the radial term and its bounds change but the azimuthal term remains the same and hence computes to zero. To demonstrate the performance with other pupil shapes, Ruane, Echeverri, et al. (2019) simulated VFN on the apertures of three major telescopes: Keck, TMT (the Thirty Meter Telescope), and GMT (the Giant Magellan Telescope). These apertures are shown in the top row of Fig. 2.11 alongside the baseline unobstructed circular aperture. The simulations revealed that the on-axis coupling is zero regardless of the aperture shape such that a star would be nulled with VFN on any of these telescopes. Furthermore, the corresponding 2D coupling maps for charge 1 and 2 are shown for each aperture in plots (a)-(d) of the figure. The maps are all very similar, reflecting the fact that the off-axis coupling is only marginally affected. The main effect on the map is that apertures with distinct flat edges (i.e., Keck and GMT) show a weak azimuthal modulation.

In that analysis, additional simulations were also carried out to test the VFN performance with the vortex mask in a focal plane rather than in the pupil plane. These

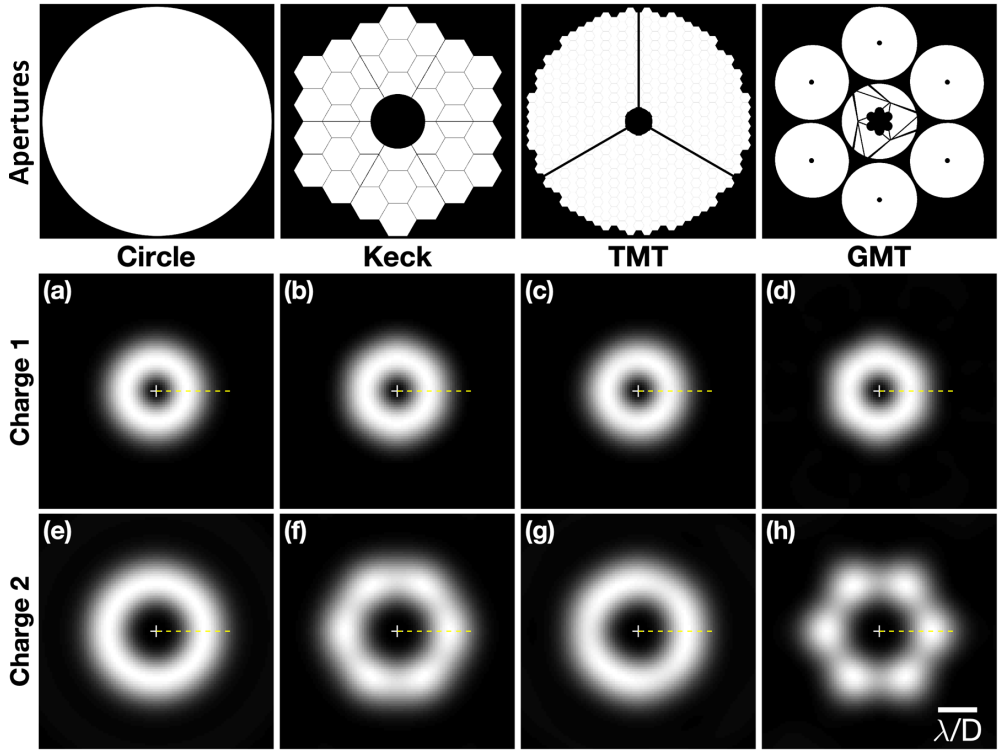


Figure 2.11: VFN performance on various telescope apertures. Top Row, left to right: Pupil shapes for a circular aperture, the Keck Telescopes, the Thirty Meter Telescope (TMT), and the Giant Magellan Telescope (GMT). Middle and bottom rows: 2D coupling maps over a 6×6 $\lambda/D$ square for each pupil (columns) and charge (rows). Figure 2.12 shows a horizontal line profile starting from the origin as indicated by the dashed yellow line. - Figure and caption adapted from Ruane, Echeverri, et al. (2019)

showed that the nulling effect and the off-axis coupling are very similar with either implementation. In fact, the original VFN concept paper used a charge 1 vortex in the focal plane (Ruane, J. Wang, et al., 2018). The primary difference between focal and pupil VFN is that the spot size over the fiber needs to be changed to achieve the same off-axis coupling efficiency. This amounts to a different $q$ value from Eq. 2.13 depending on the architecture. Table 2.2 lists the $q_{\text{opt}}$ value that maximizes the peak off-axis coupling efficiency ($\eta_{\text{peak}}$), along with the angular separation where it occurs ($\alpha_{\text{peak}}$), for each architecture considered in the study. This covers vortex charges 1 and 2, as well as the no-vortex case, and the pupil and focal plane implementations on all four apertures mentioned above.

Table 2.2: Optimal parameters for pupil plane and focal plane VFN

| | | Pupil plane VFN | | | Focal plane VFN | | |
|---|---|---|---|---|---|---|---|
| Pupil | $l$ | $q_{\text{opt}}$ | $\alpha_{\text{peak}}$ $(\lambda/D)$ | $\eta_{\text{peak}}$ (%) | $q_{\text{opt}}$ | $\alpha_{\text{peak}}$ $(\lambda/D)$ | $\eta_{\text{peak}}$ (%) |
| Circ | 0 | 1.4 | 0.0 | 82 | - | - | - |
| | 1 | 1.4 | 0.85 | 19 | 2.5 | 0.84 | 20 |
| | 2 | 1.3 | 1.3 | 10 | 3.6 | 1.3 | 10 |
| Keck | 0 | 1.5 | 0.0 | 67 | - | - | - |
| | 1 | 1.4 | 0.90 | 18 | 2.6 | 0.90 | 19 |
| | 2 | 1.4 | 1.5 | 11 | 3.8 | 1.5 | 11 |
| TMT | 0 | 1.4 | 0.0 | 76 | - | - | - |
| | 1 | 1.4 | 0.87 | 19 | 2.5 | 0.87 | 20 |
| | 2 | 1.3 | 1.4 | 9.6 | 3.6 | 1.4 | 9.9 |
| GMT | 0 | 1.5 | 0.0 | 62 | - | - | - |
| | 1 | 1.4 | 0.88 | 15 | 2.6 | 0.87 | 16 |
| | 2 | 1.3 | 1.5 | 10 | 3.6 | 1.4 | 10 |

NOTE- $l$ is the charge of the vortex mask, $q_{\text{opt}}$ is the value of $q = \text{MFD}/(\lambda\, F\#)$ that maximizes the peak coupling efficiency (i.e., $\eta_{\text{peak}}$), $\alpha_{\text{peak}}$ is the angular separation at $\eta_{\text{peak}}$, and $D$ is the circumscribed pupil diameter. - Table and caption adapted from Ruane, Echeverri, et al. (2019)

The table reveals the key takeaways from this section. First, the pupil plane implementation of VFN has the same $q$ value regardless of the vortex charge, and this same $q$ value also yields the highest coupling efficiency for DS observations. Thus, an instrument can be designed with a single F# for fiber injection that will work across all SMF-based observing modes. Conversely, a VFN mode can be added to an existing DS instrument without changing the fiber injection unit; only a vortex mask needs to be added in the pupil plane. The second takeaway is that VFN still works with the vortex in a focal plane. However, this architecture requires a fiber injection unit capable of changing the system F# between observing modes. The final takeaway is exemplified by Fig. 2.12, which shows a crosscut of the coupling maps for each architecture on the four apertures considered here. The coupling curves are all nearly identical, even for the GMT aperture which poses a significant design challenge for conventional coronagraphs. Therefore, regardless of the architecture, VFN is flexible and can be readily implemented.

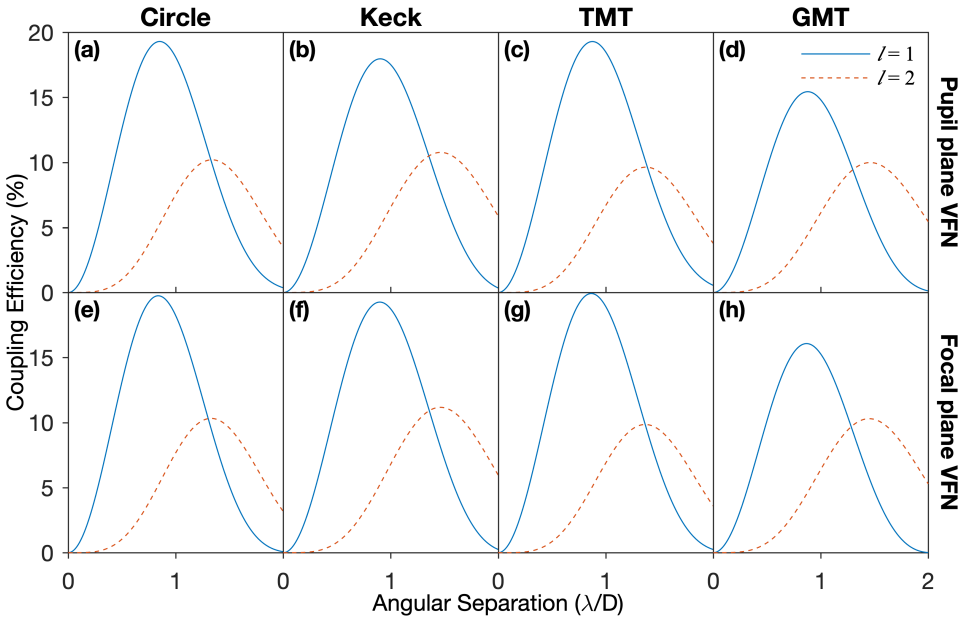


Figure 2.12: Coupling efficiency, $\eta$, for a point source versus its angular separation from the optical axis. These curves are calculated assuming the optimal value of $q$ (see Table 2.2). Results are shown with the vortex mask placed in (a)-(d) the pupil and (e)-(h) the focal plane. - Figure and caption adapted from Ruane, Echeverri, et al. (2019).

## References

Beijersbergen, M. W. et al. (1994). "Helical-wavefront laser beams produced with a spiral phaseplate". In: *Opt. Commun.* 112, pp. 321–327. DOI: 10.1016/0030-4018(94)90638-6.

Bottom, M. et al. (July 2016). "Speckle nulling wavefront control for Palomar and Keck". In: *Adaptive Optics Systems V*. Ed. by E. Marchetti, L. M. Close, and J.-P. Véran. Vol. 9909. Society of Photo-Optical Instrumentation Engineers (SPIE) Conference Series, 990955, p. 990955. DOI: 10.1117/12.2233025.

Calvin, B. et al. (Feb. 2021). "Enhancing Direct Exoplanet Spectroscopy with Apodizing and Beam Shaping Optics". In: *Publications of the Astronomical Society of the Pacific* 133.1020, 024503, p. 024503. DOI: 10.1088/1538-3873/abdace. arXiv: 2102.11499 [astro-ph.IM].

Delorme, J.-R. et al. (July 2021). "Keck Planet Imager and Characterizer: a dedicated single-mode fiber injection unit for high-resolution exoplanet spectroscopy". In: *Journal of Astronomical Telescopes, Instruments, and Systems* 7, 035006, p. 035006. DOI: 10.1117/1.JATIS.7.3.035006. arXiv: 2107.12556 [astro-ph.IM].

Jeunhomme, L. B. (1989). *Single-Mode Fiber Optics: Principles and Applications*. 2nd ed. New York: Marcel Dekker. ISBN: 978-0824781705.

Jovanovic, N. et al. (Aug. 2017). "Efficient injection from large telescopes into single-mode fibres: Enabling the era of ultra-precision astronomy". In: *Astronomy and Astrophysics* 604, A122, A122. DOI: 10.1051/0004-6361/201630351. arXiv: 1706.08821 [astro-ph.IM].

Kotani, T. et al. (Dec. 2020). "Extremely high-contrast, high spectral resolution spectrometer REACH for the Subaru Telescope". In: *Adaptive Optics Systems VII*. Ed. by L. Schreiber, D. Schmidt, and E. Vernet. Vol. 11448. Society of Photo-Optical Instrumentation Engineers (SPIE) Conference Series, 1144878, p. 1144878. DOI: 10.1117/12.2561755.

Liberman, J. et al. (Oct. 2023). "Implicit electric field conjugation for improved starlight rejection through a single-mode fiber". In: *Society of Photo-Optical Instrumentation Engineers (SPIE) Conference Series*. Vol. 12680. Society of Photo-Optical Instrumentation Engineers (SPIE) Conference Series, 126802D, p. 126802D. DOI: 10.1117/12.2677532.

Llop-Sayson, J. et al. (Jan. 2019). "Demonstration of an electric field conjugation algorithm for improved starlight rejection through a single mode optical fiber". In: *Journal of Astronomical Telescopes, Instruments, and Systems* 5, 019004, p. 019004. DOI: 10.1117/1.JATIS.5.1.019004. arXiv: 1903.11162 [astro-ph.IM].

Marcuse, D. (May 1977). "Loss Analysis of Single-Mode Fiber Splices". In: *AT T Technical Journal* 56, pp. 703–718.

Mawet, D., P. Riaud, et al. (Nov. 2005). "Annular Groove Phase Mask Coronagraph". In: *The Astrophysical Journal* 633.2, pp. 1191–1200. DOI: 10.1086/462409.

Mawet, D., G. Ruane, et al. (2017). "Observing Exoplanets with High-dispersion Coronagraphy. II. Demonstration of an Active Single-mode Fiber Injection Unit". In: *Astrophys. J.* 838.2, p. 92. DOI: 10.3847/1538-4357/aa647f.

Mawet, D., M. P. Fitzgerald, et al. (Aug. 2022). "Fiber-fed high-resolution infrared spectroscopy at the diffraction limit with Keck-HISPEC and TMT-MODHIS: status update". In: *Ground-based and Airborne Instrumentation for Astronomy IX*. Ed. by C. J. Evans, J. J. Bryant, and K. Motohara. Vol. 12184. Society of Photo-Optical Instrumentation Engineers (SPIE) Conference Series, 121841R, 121841R. DOI: 10.1117/12.2630142.

Ruane, G. (2016). "Optimal Phase Masks for High Contrast Imaging Applications". PhD thesis. Rochester Institute of Technology.

Ruane, G., D. Echeverri, et al. (Sept. 2019). "Vortex fiber nulling for exoplanet observations: conceptual design, theoretical performance, and initial scientific yield predictions". In: *Society of Photo-Optical Instrumentation Engineers (SPIE) Conference Series*. Vol. 11117. Society of Photo-Optical Instrumentation Engineers (SPIE) Conference Series, 1111716, p. 1111716. DOI: 10.1117/12.2528555. arXiv: 1908.09780 [astro-ph.IM].

Ruane, G., J. Wang, et al. (Nov. 2018). "Efficient Spectroscopy of Exoplanets at Small Angular Separations with Vortex Fiber Nulling". In: *Astrophysical Journal* 867.2, 143, p. 143. DOI: 10.3847/1538-4357/aae262. arXiv: 1809.06483 [astro-ph.IM].

Ruffio, J.-B. et al. (Mar. 2023). "Detecting Exomoons from Radial Velocity Measurements of Self-luminous Planets: Application to Observations of HR 7672 B and Future Prospects". In: *The Astronomical Journal* 165.3, 113, p. 113. DOI: 10.3847/1538-3881/acb34a. arXiv: 2301.04206 [astro-ph.EP].

Serabyn, E., G. Ruane, and D. Echeverri (Aug. 2022). "Observing inside the coronagraphic regime with optimized single-mode nulling interferometry". In: *Space Telescopes and Instrumentation 2022: Optical, Infrared, and Millimeter Wave*. Ed. by L. E. Coyle, S. Matsuura, and M. D. Perrin. Vol. 12180. Society of Photo-Optical Instrumentation Engineers (SPIE) Conference Series, 121800N, 121800N. DOI: 10.1117/12.2630589. arXiv: 2210.09412 [astro-ph.IM].

Serabyn, E., B. Mennesson, and S. Martin (Dec. 2020). "Observing inside the coronagraphic regime with nulling interferometry". In: *Society of Photo-Optical Instrumentation Engineers (SPIE) Conference Series*. Vol. 11446. Society of Photo-Optical Instrumentation Engineers (SPIE) Conference Series, 114461K, 114461K. DOI: 10.1117/12.2562947.

Shaklan, S. and F. Roddier (1988). "Coupling starlight into single-mode fiber optics". In: *Appl. Opt.* 27.11, pp. 2334–2338. DOI: 10.1364/AO.27.002334.

Swartzlander, G. A. (2001). "Peering into darkness with a vortex spatial filter". In: *Opt. Lett.* 26.8, pp. 497–499. DOI: 10.1364/OL.26.000497.

– (Sept. 2009). "The optical vortex coronagraph". In: *Journal of Optics A: Pure and Applied Optics* 11.9, 094022, p. 094022. DOI: 10.1088/1464-4258/11/9/094022.

Vigan, A. et al. (Sept. 2023). "First light of VLT/HiRISE: High-resolution spectroscopy of young giant exoplanets". In: *arXiv e-prints*, arXiv:2309.12390, arXiv:2309.12390. DOI: 10.48550/arXiv.2309.12390. arXiv: 2309.12390 [astro-ph.IM].

Wang, J. J. et al. (Oct. 2021). "Detection and Bulk Properties of the HR 8799 Planets with High-resolution Spectroscopy". In: *The Astronomical Journal* 162.4, 148, p. 148. DOI: 10.3847/1538-3881/ac1349. arXiv: 2107.06949 [astro-ph.EP].

Wang, J. and C. Jurgenson (Nov. 2020). "Exoplanet Sciences with Nulling Interferometers and a Single-mode Fiber-fed Spectrograph". In: *The Astronomical Journal* 160.5, 210, p. 210. DOI: 10.3847/1538-3881/abb5a3. arXiv: 2007.15529 [astro-ph.IM].

Wang, J., J. R. Kolecki, et al. (Apr. 2022). "Retrieving the C and O Abundances of HR 7672 AB: A Solar-type Primary Star with a Benchmark Brown Dwarf". In: *The Astronomical Journal* 163.4, 189, p. 189. DOI: 10.3847/1538-3881/ac56e2. arXiv: 2202.02477 [astro-ph.EP].

Xin, Y. et al. (July 2023). “On-sky speckle nulling through a single-mode fiber with the Keck Planet Imager and Characterizer”. In: *Journal of Astronomical Telescopes, Instruments, and Systems* 9, 035001, p. 035001. DOI: 10.1117/1.JATIS.9.3.035001. arXiv: 2307.11893 [astro-ph.IM].

*Chapter 3*

# PROOF OF CONCEPT

This chapter is a reproduction of my first VFN paper, demonstrating the concept in the laboratory for the first time. It showed a null of $6{\times}10^{-5}$ and average peak coupling of 12% in monochromatic visible light with a commercially available, off-the-shelf monochromatic charge 1 vortex mask. The achieved null depth was readily explained by the measured wavefront error in the optical bench and the limited peak coupling was explained by the focal ratio used for the final coupling lens. Though later chapters present better laboratory performance, this paper validated the core elements of VFN to prove that the concept was sound and that we understood the limitations of our implementation.

---

## Vortex Fiber Nulling for Exoplanet Observations: Experimental Demonstration in Monochromatic Light

Echeverri, D. et al. (May 2019). "Vortex fiber nulling for exoplanet observations I. Experimental demonstration in monochromatic light". In: *Optics Letters* 44.9, p. 2204. DOI: 10.1364/OL.44.002204. arXiv: 1811.02083 [astro-ph.IM].

### 3.1 Abstract

Vortex fiber nulling is a method for spectroscopically characterizing exoplanets at small angular separations, $\lesssim 1\lambda/D$, from their host star. The starlight is suppressed by creating an optical vortex in the system point spread function, which prevents the stellar field from coupling into the fundamental mode of a single-mode optical fiber. Light from the planet, on the other hand, couples into the fiber and is routed to a spectrograph. Using a prototype vortex fiber nuller (VFN) designed for monochromatic light, we demonstrate coupling fractions of $6 \times 10^{-5}$ and $> 0.1$ for the star and planet, respectively.

## 3.2 Introduction

Detecting spectral signs of life in the atmospheres of exoplanets is a premier goal of modern astronomy. While future large-aperture space telescopes with coronagraphs may enable the direct imaging and spectroscopy of Earth-like exoplanets orbiting stars similar to our sun (see e.g., Ruane, Mawet, et al., 2018), the next-generation of ground-based telescopes with adaptive optics will focus on planets in the habitable zone of cooler M dwarf stars, such as the known planets Proxima Centauri b (Anglada-Escudé et al., 2016) and Ross 128 b (Bonfils et al., 2017). The number of planets expected to be detected and spectroscopically characterized with both space-based and ground-based facilities is, however, limited by the inner working angles of their respective high contrast imaging systems. Improving sensitivity at smaller angular separations provides access to many more potential targets whose planet-to-star flux ratios are made favorable by their close proximity to their host star. Accessing smaller separations also increases the maximum wavelength at which these exoplanets can be observed.

We present an experimental demonstration of an optical system known as a vortex fiber nuller (VFN - Ruane, Wang, et al., 2018) that allows for the spectral characterization of exoplanets at angular separations less than the Rayleigh criterion; i.e., $<1.22\ \lambda/D$, where $\lambda$ is the wavelength and $D$ is the telescope diameter. Figure 3.1(a) illustrates a VFN with a vortex phase mask (Beijersbergen et al., 1994) placed in a pupil plane to impart a phase pattern of the form $\exp(\pm il\theta)$, as in Swartzlander (2001), where $l$ is an integer known as the charge. This prevents the starlight from coupling into a single-mode fiber (SMF) which is actively aligned with the star's geometric image in the focal plane. The stellar point spread function (PSF) is rejected by the SMF because its complex field is orthogonal to the fiber's fundamental mode. For an arbitrary point source, the fraction of light that couples into the fiber as a function of its angular separation from the optical axis, $\alpha$, is

$$\eta(\alpha) = \frac{\left|\int \Psi(\mathbf{r}) f(\mathbf{r};\alpha) dA\right|^2}{\int |\Psi(\mathbf{r})|^2 dA \int |f(\mathbf{r};\alpha)|^2 dA}, \tag{3.1}$$

where $\Psi(\mathbf{r})$ is the fiber mode and $f(\mathbf{r};\alpha)$ is the field in the final image plane (Shaklan et al., 1988). $dA$ is the differential area and $\mathbf{r} = (r, \theta)$ are polar coordinates in the $(x, y)$ plane. For common SMFs, the fundamental mode can be approximated as a Gaussian with the functional form $\Psi(r) = \exp[-(2r/D_f)^2]$, where $D_f$ is the mode field diameter. Any stellar field of the form $f(\mathbf{r};0) = f_r(r)\exp(\pm il\theta)$ leads to $\eta(0) = \eta_{\text{star}} = 0$. However, light from a point source (e.g., a planet) at an angular

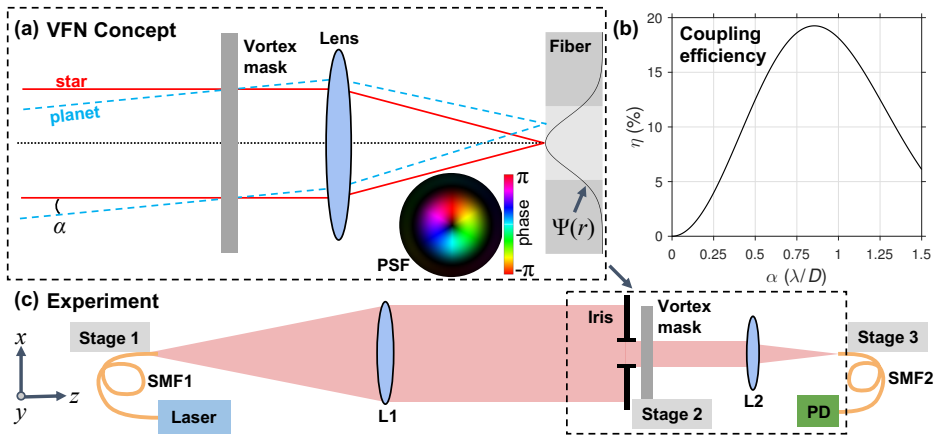


Figure 3.1: (a) Schematic of a vortex fiber nuller (VFN). Light from the star (red rays) and planet (blue rays) passes through a vortex mask with complex transmittance $\exp(\pm il\theta)$. The image of the star is aligned to a single-mode fiber on the optical axis with fundamental mode, $\Psi(r)$, whereas the planet image is slightly off-axis. Each has a characteristically donut-shaped point spread function (PSF) and phase proportional to the azimuthal angle; the inset shows the simulated phase and PSF. (b) The coupling efficiency, $\eta$, evaluated for any point at angular separation $\alpha$, assuming the star is at $\alpha = 0$. (c) Diagram of the prototype VFN demonstrated here. Light from a fiber-coupled laser is launched by SMF1 and collimated by lens L1 (focal length $f = 200$ mm) to evenly illuminate an iris defining the pupil. The beam passes through a liquid crystal vector vortex mask directly behind the iris and is focused by lens L2 ($f = 11$ mm) onto SMF2. We measure the coupled power using photodiode PD. Stages 1 and 3 have five-axes while stage 2 is a two-axis stage. Linear actuators provide computer control of the $x$ and $y$ directions for the vortex mask and $x$, $y$, and $z$ for SMF2.

separation $\alpha$ will couple into the fiber with the efficiency shown in Fig. 3.1(b). The maximum theoretical coupling efficiency in this arrangement, $\eta = 19\%$, is achieved at $\alpha = 0.86\ \lambda/D$ with $D_f = 1.4\ \lambda F\#$, where $F\#$ is the focal ratio of the lens. In practice, the single-mode fiber is routed to a spectrograph which is used to separate the starlight as well as measure and analyze spectral signatures in the planet light (Wang et al., 2017).

Vortex fiber nulling is akin to traditional nulling interferometry (Bracewell, 1978; Haguenauer et al., 2006), but makes use of the full telescope aperture. The key advantages are (1) the extremely small inner working angle, (2) the rotational symmetry of the coupling function, allowing for spectral follow up of planets when the azimuthal orientation of their orbits are uncertain, and (3) the theoretically wavelength-independent nulling of starlight across astronomically relevant bandwidths ($\Delta\lambda/\lambda \approx 0.2$). Here, we demonstrate the predicted nulling effect in the

laboratory using a prototype system designed for monochromatic light.

### 3.3 Experimental Setup

Figure 3.1(c) shows a diagram of the experimental optical layout. Light from a SMF-coupled laser diode operating at $\lambda = 635$ nm is collimated by a 200 mm focal length lens (L1) and evenly illuminates a 3.6 mm diameter iris. A charge $l$=1, liquid crystal vector vortex mask (Thorlabs WPV10L-633) immediately after the iris applies the desired phase pattern to the incoming beam in the pupil plane. Computer-controlled linear actuators (Zaber X-NA08A25) on stage 2 provide fine transverse alignment ($< 1$ $\mu$m repeatability) of the vortex mask in the $x$ and $y$ directions.

The vortex mask is a half wave plate with a spatially-variant fast axis angle, $\chi = l\theta/2$. The transmitted complex field is $E_{R,L} = \exp(\pm i2\chi)E_{L,R}$, where $E_R$ and $E_L$ are the right and left circularly polarized components, respectively (Marrucci et al., 2006). The two output components have conjugate vortex phases of the form $\exp(\pm il\theta)$ and a polarization state that is orthogonal to the input. The monochromatic mask in use is optimized to provide the half wave retardance, and thus the vortex phase, at a single wavelength.

An 11 mm focal length aspheric lens (L2) focuses the beam onto the detection fiber (SMF2) centered on the optical axis and connected to a variable-gain silicon photodiode (PD; Femto OE-200-SI). The path lengths between the iris, vortex, and L2 are 5 and 35 mm respectively, set by the size of their mounts. SMF1 and SMF2 are both SM600 fibers with $D_f = 3.6{-}5.3$ $\mu$m and a measured single-mode cutoff wavelength of <550 nm. Each is fixed to a 5-axis stage (stages 1 and 3; degrees of freedom: $x$, $y$, $z$, tip, and tilt). Computer-controlled piezo actuators (Thorlabs PE4) on stage 3 position SMF2 to an accuracy of 10 nm (15 $\mu$m travel) in the $x$, $y$, and $z$ directions.

We used a Shack-Hartmann wavefront sensor (ImagineOptic HASO4-Broadband) to minimize the static aberrations during alignment. The total wavefront error, through both lenses and with the vortex mask in the beam but offset so as not to create a singularity in the phase, was 7.3 nm RMS ($\sim \lambda/100$).

We determined the maximum coupling efficiency by translating the vortex mask such that the beam passed through a region far from the phase singularity and then co-aligning SMF1 and SMF2. In this configuration, the coupling efficiency was 56% which is in close agreement with the theoretical value of 57% expected from our $F$#=3.1 system assuming an optimal $F$# of 5 provided that the SMF2 mode-

field diameter is 4.45 $\mu m$ (manufacturer specification is 3.6-5.3 $\mu m$). We attribute 0.4% of the coupling losses to the measured wavefront error. Improved coupling efficiency is possible by matching the $F\#$ with the ideal value given the true fiber mode diameter and using a custom lens.

### 3.4 Procedure

The objective of the experimental procedure was (1) to demonstrate that light from an on-axis, unresolved source is rejected by SMF2 and (2) to show that light from an off-axis source couples into SMF2 with the predicted efficiency. Since the system PSF is shift-invariant, we can simulate a planet by translating SMF1 or SMF2 in the $(x, y)$ plane; both are equivalent barring a magnification factor. Thus, for convenience and to maintain low wavefront error, we opted to measure the coupling efficiency as a function of the position of SMF2 using highly-accurate piezo actuators.

To ensure that aberrations were minimized, we removed stage 3 and SMF2 and took images of the PSF with a CMOS detector (Thorlabs DCC1545M) with and without the vortex mask. Then, with stage 3 and SMF2 back in place, we performed several two-dimensional raster scans of SMF2 in a 7×7 $\mu$m square, adjusting the position of the vortex mask between each scan until we minimized the coupling for the simulated star, $\eta_{\text{star}}$.

At each SMF2 position, we checked that the power measured by the PD was above the predetermined noise floor and then averaged 100 measurements before moving SMF2 to the next location. Once each full 2D scan was completed, we inserted a calibrated power meter (Thorlabs PM100D, S120C) in front of SMF2 and measured the total power in the beam to normalize the signal at the output. Finally, we determined the bias signal of the PD by blocking the light source and subtracted the bias from our measurements. To obtain $\eta$, we normalized the measured power by the total power accounting for the transmission of SMF2, including the Fresnel reflections at both ends (3.46% per facet) as well as propagation losses (0.34% per meter).

### 3.5 Results

Figure 3.2 shows images of the PSF at the plane of SMF2 (Figure 3.2(a-d)) and the two-dimensional coupling maps obtained by scanning SMF2 in the $(x, y)$ plane. The PSF image with the beam passing through the edge of the vortex mask (Fig. 3.2(b)) resembles an Airy pattern (Fig. 3.2(a)) validating that the collimated beam evenly illuminates the iris. The PSF with the vortex centered on the iris (Fig. 3.2(d))

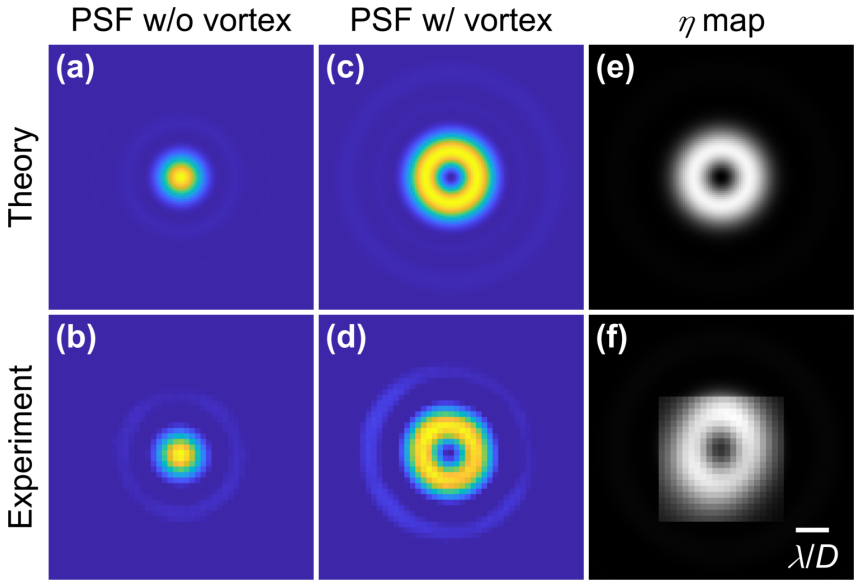


Figure 3.2: PSFs (a)-(b) without and (c)-(d) with the vortex mask centered on the pupil. (e)-(f) Coupling efficiency, or "$\eta$ map," as a function of the position of SMF2, equivalent to the source, with respect to the optical axis (0.35 $\mu$m step size). The theoretical predictions match well with our experimental results. The PSF images and coupling map have six samples per $\lambda F\#$.

appears annular in shape as predicted (Fig. 3.2(c)). The ideal coupling efficiency as a function of the 2D position of SMF2 (see Fig. 3.2(e)) is a donut shape with the radial profile in Fig. 3.1(b). The measured coupling map (Fig. 3.2(f)) shows a very similar shape except for a slight vertical elongation likely owing to imperfect calibration of the piezo actuator gains.

In addition to the 2D coupling map in Fig. 3.2(f), we took two fine linear scans starting at the deepest null found and moving radially outward in the $\pm y$ directions in 12 nm steps (see Fig. 3.3). The deepest null measured, with SMF1 and SMF2 on the optical axis, was $\eta_{\text{star}} = 6 \times 10^{-5}$ (0.006%). The maximum coupling efficiency for the line scans, corresponding to the peak planet coupling, was $\eta = 8\%$ and 15% for the $\pm y$ directions, respectively, revealing an asymmetry in the coupling map. We compare our line scan measurements with the theoretical line profiles for an ideal system ($F\#$=5.0) and our setup ($F\#$=3.1). The laboratory-measured line profiles are in close agreement with our theoretical predication showing a minor departure at $\alpha \lesssim 0.02\ \lambda/D$ and $\alpha \gtrsim 0.3\ \lambda/D$. We expect that optimizing the focal ratio would improve the theoretical maximum coupling efficiency from 12% up to a maximum of 19% and the peak would shift from $\alpha = \lambda/D$ to $\alpha = 0.86\ \lambda/D$.

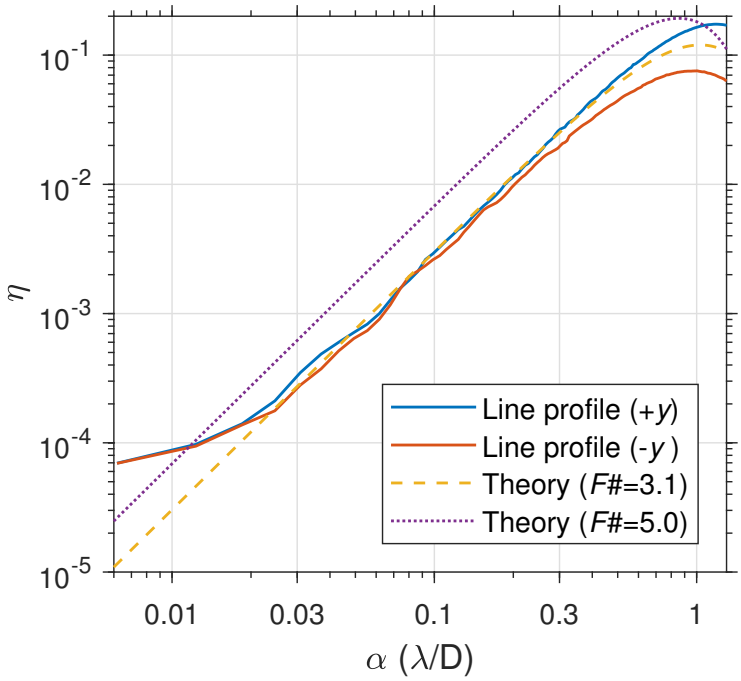


Figure 3.3: Linear scans of SMF2 in the $\pm y$ directions with a 12 nm step size. The best achieved null $\eta_{\text{star}} = \eta(0) = 6\times10^{-5}$, is likely limited by static aberrations. Our measurements match well with the theoretical line profiles for our $F\# = 3.1$ system but $F\# = 5.0$ is required to achieve the ideal performance.

### 3.6 Discussion

Though the experimental PSFs (Fig. 3.2(b,d)) are in close agreement with theory (Fig. 3.2(a,c)), the diffraction rings are slightly more pronounced than expected. This is likely due to spherical aberration unseen by our wavefront sensor, which we used in a diverging beam after L2's focus and therefore discarded all power terms.

Using our wavefront measurements, taken at the focus with the vortex mask offset such that the phase singularity was outside of the iris, we estimate the minimum possible $\eta_{\text{star}}$ by numerically computing Eq. 3.1. As in Ruane, Wang, et al. (2018), we determined the sensitivity of the null to low-order Zernike aberrations, $Z_n^m$. For each Zernike mode, we fit the response function $\eta_{\text{star}} = (b\omega)^2$, where $b$ is the sensitivity coefficient and $\omega$ is the RMS wavefront error in units of waves. By orthogonality, the sensitivity coefficient is zero for all Zernike modes $Z_n^m$ where $m \neq \pm1$. The precision of the piezo actuators mitigates the tip and tilt errors such that these are also negligible. Thus, our experimental nulls are likely limited by coma aberrations. Table 3.1 lists the measured wavefront error in the coma modes ($m = \pm1$) as well as their corresponding $b$ value and predicted contribution to $\eta_{\text{star}}$.

Table 3.1: Measured wavefront error, $\omega$, in the coma Zernike modes, $Z_n^{\pm 1}$, and expected stellar leakage, $\eta_{\text{star}} = (b\omega)^2$, for (0°,90°) aberrations, where $b$ is the aberration sensitivity coefficient. All other modes have $b = 0$.

| Modes | $\omega$ (waves RMS) | $b$ | $\eta_s$ |
|---|---|---|---|
| $Z_3^{\pm 1}$ | (-1.7,-2.8)$\times 10^{-3}$ | 2.15 | (1.3,3.6)$\times 10^{-5}$ |
| $Z_5^{\pm 1}$ | (0.1,-0.2)$\times 10^{-3}$ | 1.12 | (1.3,5.0)$\times 10^{-8}$ |
| $Z_7^{\pm 1}$ | (-0.7,0.0)$\times 10^{-3}$ | 0.67 | (2.2,0.0)$\times 10^{-7}$ |
| **Total** | | | $5.0 \times 10^{-5}$ |

Taking the linear combination of the error contributions predicts a minimum of $\eta_{\text{star}} = 5.0 \times 10^{-5}$, which is in good agreement with the minimum measured value, $\eta_{\text{star}} = 6.0 \times 10^{-5}$.

The line scans presented in Fig. 3.3 reveal an asymmetry in peak coupling efficiency around the donut. In that case, to achieve the smallest value of $\eta_{\text{star}}$, we scanned the position of the vortex mask in addition to SMF2. Using numerical simulations, we find that in the presence of coma aberrations, the optimal null occurs when the vortex mask is slightly off-center, causing the coupling map to become asymmetric. This implies that, when observing an exoplanet with a known orbit around its host star, it may be possible to deliberately misalign the vortex in the pupil to create an asymmetric coupling map which preferentially couples more light at the location of the planet. Maximizing the throughput for the planet is important as the integration time scales as the inverse square of the planet's coupling efficiency, $\eta^{-2}$, in the stellar photon noise limited regime (Ruane, Wang, et al., 2018).

The pupil shape has little influence on the VFN's performance (Ruane, Wang, et al., 2018); the results presented here are also valid for non-circular, obstructed, and segmented apertures. In fact, the pupil created by the iris used in these experiments was only quasi-circular, with 10 flat edges. Future experiments will use a pupil mask that mimics the boundaries of an actual telescope pupil.

We have demonstrated the VFN concept in monochromatic light using a simple, inexpensive optical system. However, exoplanet spectroscopy requires similar starlight suppression levels in polychromatic light ($\Delta\lambda/\lambda \approx 0.2$). We plan to build a polychromatic testbed to demonstrate this using off-axis parabolic mirrors instead of lenses, a carefully matched $F\#$, and broadband vortex masks optimized for the optical and infrared. Vortex masks that apply the same phase pattern as a function of wavelength

have been demonstrated using polarization dependent, or "vector", methods: liquid crystals (Mawet, Serabyn, et al., 2009), sub-wavelength gratings (Mawet, Riaud, et al., 2005), and photonic crystal structures (Murakami et al., 2013). Achromatic scalar masks are also possible (Swartzlander, 2006).

Furthermore, we plan to integrate a polychromatic VFN into an adaptive optics system with a deformable mirror, similar to previous fiber injection instruments tested by our team (Mawet, Ruane, et al., 2017), which will allow us to develop wavefront sensing and control techniques to maintain the null in the presence of realistic wavefront errors and flux levels. Ultimately, our goal is to integrate a VFN module into the Keck Planet Imager and Characterizer at the W.M. Keck Observatory (Mawet, Delorme, et al., 2017) to open up the possibility of characterizing the reflected light spectrum of giant exoplanets whose properties have so far only been inferred from stellar radial velocity measurements. This will pave the way to characterizing smaller, potentially habitable planets with future large-aperture telescopes.

## 3.7 Conclusions

We have demonstrated the VFN concept in a laboratory for the first time. Using a prototype system designed for monochromatic light, we demonstrated a stellar coupling fraction of $\eta_{\rm star} = 6.0 \times 10^{-5}$ and peak planet coupling efficiencies of $\eta$=8-15% at an angular separation of $\alpha \approx \lambda/D$. These results match the expected performance for our F#=3.1 setup and thereby validate the model described by Ruane, Wang, et al. (2018). As such, we predict that using the ideal $F\#$ for the fiber and minimizing wavefront errors will yield $\eta = 19\%$ at 0.86 $\lambda/D$ in all azimuthal directions. We have also identified a clear pathway to achieving similar performance in polychromatic light and to developing the wavefront sensing and control techniques needed for on-sky operation.

The VFN concept is a promising approach to reducing the stellar photon noise that otherwise inhibits the characterization of exoplanets whose angular separations are within the inner working angle of conventional coronagraphs. We expect that this technique will open the possibility to measure the reflected light spectrum of exoplanets inferred from stellar radial velocity measurements and thereby allow for the detailed characterization of their atmospheres for the first time. Several confirmed planets are at angular separations of $\alpha \lesssim \lambda/D$ in the infrared, which is currently too close to the star to characterize by other means, but lie within the collecting region of a VFN. We envisage that vortex fiber nulling will significantly

increase the number of exoplanets, from rocky worlds to gas giants, characterized by current and future ground- and space-based telescopes.

**Funding.** National Science Foundation (NSF) (AST-1602444);

**Acknowledgments.** Part of this work was supported by the Jet Propulsion Laboratory, California Institute of Technology, under contract with NASA.

## References

Anglada-Escudé, G. et al. (Aug. 2016). "A terrestrial planet candidate in a temperate orbit around Proxima Centauri". In: *Nature* 536.7617, pp. 437–440. DOI: 10.1038/nature19106. arXiv: 1609.03449 [astro-ph.EP].

Beijersbergen, M. W. et al. (1994). "Helical-wavefront laser beams produced with a spiral phaseplate". In: *Opt. Commun.* 112, pp. 321–327. DOI: 10.1016/0030-4018(94)90638-6.

Bonfils, X. et al. (2017). "A temperate exo-Earth around a quiet M dwarf at 3.4 parsecs". In: *Astron. Astrophys.* 613, A25. DOI: 10.1051/0004-6361/201731973.

Bracewell, R. N. (1978). "Detecting nonsolar planets by spinning infrared interferometer". In: *Nature* 274, p. 780. DOI: 10.1038/274780a0.

Haguenauer, P. and E. Serabyn (Apr. 2006). "Deep nulling of laser light with a single-mode-fiber beam combiner". In: *Appl. Opt.* 45.12, pp. 2749–2754. DOI: 10.1364/AO.45.002749.

Marrucci, L., C. Manzo, and D. Paparo (2006). "Optical Spin-to-Orbital Angular Momentum Conversion in Inhomogeneous Anisotropic Media". In: *Phys. Rev. Lett.* 96.16, 163905, p. 163905. DOI: 10.1103/PhysRevLett.96.163905.

Mawet, D., J.-R. Delorme, et al. (2017). "A fiber injection unit for the Keck Planet Imager and Characterizer". In: *Proc. SPIE* 10400, p. 1040029. DOI: 10.1117/12.2274891. URL: http://dx.doi.org/10.1117/12.2274891.

Mawet, D., G. Ruane, et al. (2017). "Observing Exoplanets with High-dispersion Coronagraphy. II. Demonstration of an Active Single-mode Fiber Injection Unit". In: *Astrophys. J.* 838.2, p. 92. DOI: 10.3847/1538-4357/aa647f.

Mawet, D., E. Serabyn, et al. (Feb. 2009). "Optical Vectorial Vortex Coronagraphs using Liquid Crystal Polymers: theory, manufacturing and laboratory demonstration". In: *Optics Express* 17.3, pp. 1902–1918. DOI: 10.1364/OE.17.001902. arXiv: 0912.0311 [astro-ph.IM].

Mawet, D., P. Riaud, et al. (2005). "Subwavelength surface-relief gratings for stellar coronagraphy". In: *Appl. Opt.* 44.34, pp. 7313–7321. DOI: 10.1364/AO.44.007313.

Murakami, N. et al. (2013). "Design and laboratory demonstration of an achromatic vector vortex coronagraph". In: *Opt. Express* 21, pp. 7400–7410. DOI: 10.1364/OE.21.007400.

Ruane, G., D. Mawet, et al. (Jan. 2018). "Vortex coronagraphs for the Habitable Exoplanet Imaging Mission concept: theoretical performance and telescope requirements". In: *Journal of Astronomical Telescopes, Instruments, and Systems* 4, 015004, p. 015004. DOI: 10.1117/1.JATIS.4.1.015004. arXiv: 1803.03909 [astro-ph.IM].

Ruane, G., J. Wang, et al. (Nov. 2018). "Efficient Spectroscopy of Exoplanets at Small Angular Separations with Vortex Fiber Nulling". In: *Astrophysical Journal* 867.2, 143, p. 143. DOI: 10.3847/1538-4357/aae262. arXiv: 1809.06483 [astro-ph.IM].

Shaklan, S. and F. Roddier (1988). "Coupling starlight into single-mode fiber optics". In: *Appl. Opt.* 27.11, pp. 2334–2338. DOI: 10.1364/AO.27.002334.

Swartzlander, G. A. (2001). "Peering into darkness with a vortex spatial filter". In: *Opt. Lett.* 26.8, pp. 497–499. DOI: 10.1364/OL.26.000497.

– (July 2006). "Achromatic optical vortex lens". In: *Optics Letters* 31.13, pp. 2042–2044. DOI: 10.1364/OL.31.002042.

Wang, J. et al. (Apr. 2017). "Observing Exoplanets with High Dispersion Coronagraphy. I. The Scientific Potential of Current and Next-generation Large Ground and Space Telescopes". In: *The Astronomical Journal* 153.4, 183, p. 183. DOI: 10.3847/1538-3881/aa6474. arXiv: 1703.00582 [astro-ph.EP].

*Chapter 4*

# LABORATORY DEMONSTRATIONS

The previous chapter experimentally validated the VFN concept in the laboratory for the first time, demonstrating nulls in the visible at a single wavelength and showing off-axis coupling that enables small-separation observations. This chapter builds on that work via subsequent laboratory demonstrations of VFN with improved performance. It consolidates work originally presented over 3 conference proceedings and a draft of a paper that was ultimately not submitted. Taken together, this work demonstrates the key elements needed for scientifically meaningful on-sky VFN observations. The monochromatic results in Sec. 4.1 demonstrate deep nulls and off-axis coupling in-line with theory to validate the concept in this simpler, single-wavelength regime. The broadband results in Sec. 4.2 extend the performance to polychromatic light, as needed for spectrally-dispersed detection and characterization. Finally, Sec. 4.3 presents an improved testbed designed and built as part of this thesis for continued fiber nulling experiments with wider capabilities.

The original proceedings from which this chapter is derived are listed below. When text in this chapter is pulled directly from one of these works, it is denoted as such.

Echeverri, D. et al. (Sept. 2019). "The vortex fiber nulling mode of the Keck Planet Imager and Characterizer (KPIC)". In: *Society of Photo-Optical Instrumentation Engineers (SPIE) Conference Series*. Vol. 11117. Society of Photo-Optical Instrumentation Engineers (SPIE) Conference Series, 111170V, p. 111170V. DOI: 10.1117/12.2528529. arXiv: 1909.03538 [astro-ph.IM].

Echeverri, D. et al. (Dec. 2020). "Detecting and characterizing close-in exoplanets with vortex fiber nulling". In: *Optical and Infrared Interferometry and Imaging VII*. Ed. by P. G. Tuthill, A. Mérand, and S. Sallum. Vol. 11446. Society of Photo-Optical Instrumentation Engineers (SPIE) Conference Series, 1144619, p. 1144619. DOI: 10.1117/12.2563142. arXiv: 2012.04239 [astro-ph.IM].

Echeverri, D. et al. (Sept. 2021). "Broadband vortex fiber nulling: high-dispersion exoplanet science at the diffraction limit". In: *Techniques and Instrumentation for Detection of Exoplanets X*. Ed. by S. B. Shaklan and G. J. Ruane. Vol. 11823. Society of Photo-Optical Instrumentation Engineers (SPIE) Conference Series, 118230A, 118230A. DOI: 10.1117/12.2597160. arXiv: 2210.15910 [astro-ph.EP].

---

### 4.1 Monochromatic Experiments

The text in this section is derived primarily from Echeverri, Ruane, Calvin, et al. (2020). We first demonstrated VFN in a laboratory environment in 2019 (Chapter 3 - Echeverri, Ruane, Jovanovic, Mawet, et al., 2019). At the time, we reported null depths of $6 \times 10^{-5}$ and a peak planet coupling between 8 and 15% with a charge 1 vortex mask in monochromatic light using a 635 nm laser. The measured null was consistent with the expected value of $5 \times 10^{-5}$ based on the wavefront errors in the system. The planet coupling peak was less than the theoretical maximum of 19% for a charge 1 vortex but this was due to a mismatched F# in the system; given the actual F#, we could only achieve a theoretical azimuthally-averaged peak of 12%. Thus, though the coupling efficiency was not optimal, the system and its performance were well understood and we validated much of the VFN theory.

Since then, the testbed for those experiments (Sec. 3.3) was improved to achieve better performance. Figure 4.1 shows a diagram and picture of the testbed as used for these updated results. The main change was that the pupil diameter was adjusted to around 2.1 mm, to set an F# closer to 5, based on the ideal value for the expected MFD of the SMF. A minor modification was also made to how the total light was measured with the normalization power meter (PM). Measurements of coupling efficiency, $\eta$, as defined by the overlap integral in Sec. 2.2 (Eq. 2.8), require knowledge of the total light incident on the fiber plane, $\int |E(\mathbf{r})|^2 \, dA$. We mounted the normalization PM (Thorlabs PM100D, S120C) that samples this value on a translation stage so that it could be automatically inserted into the beam after each coupling scan. This significantly improved our ability to optimize the system performance since we could regularly determine the null without having to remove the nulling fiber stage and insert the PM manually, which requires re-optimizing the fiber position for subsequent scans. However, due to space constraints and the limited automated range of the focus (Z) axis on the nulling fiber stage, the PM

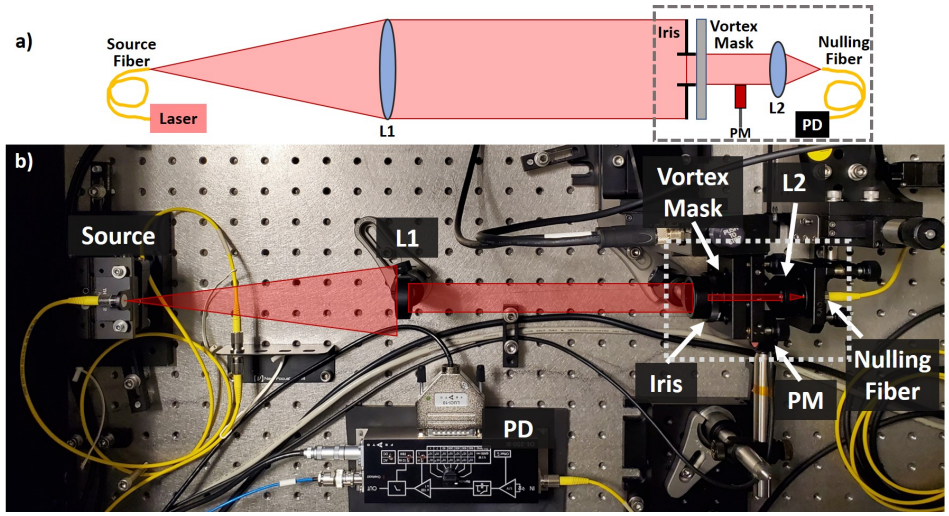


Figure 4.1: (a) Schematic of the transmissive VFN testbed at Caltech. The source fiber projects light onto the collimating lens, L1. An iris then sets the pupil diameter before passing the beam to the vortex mask. An aspheric focusing lens, L2, images the beam onto the nulling fiber which is connected to a photodiode, PD, for coupling measurements. A retractable power meter, PM, can be moved into the beam path to measure the power for normalization. (b) Picture of the Caltech transmissive VFN testbed.

had to be placed before the final lens L2. We therefore accounted for reflection and transmission losses from the lens using empirically-measured throughput values of the lens at the operating wavelength. In this way, the PM reading was corrected to represent the actual power reaching the nulling fiber plane.

These modifications resulted in a similar null depth but much higher planet coupling than what was achieved in Chapter 3. The new on-axis (i.e., star) coupling was measured at $6.6 \times 10^{-5}$, which matches the fact that the wavefront error did not change much from when the previous result was reported, so we were still limited by the coma aberrations in the system. The azimuthally-averaged peak planet coupling was measured at 16% and thus closer to the 19% theoretical maximum. The measured two-dimensional coupling efficiency map is shown in Fig. 4.2(a), along with the simulated ideal coupling map for charge 1 VFN. The azimuthally-averaged line profile is shown in the solid blue line of Fig. 4.2(b). The coupling still did not reach the full potential of an ideal VFN, shown as the dashed blue line in the same figure. We believe this may be due to the calibration between the normalization power meter and the final photodiode. If so, this could be fixed by changing the way the normalization is done so as to use a single detector for both. The reduced coupling could also be due to an uncertainty on the true SMF core

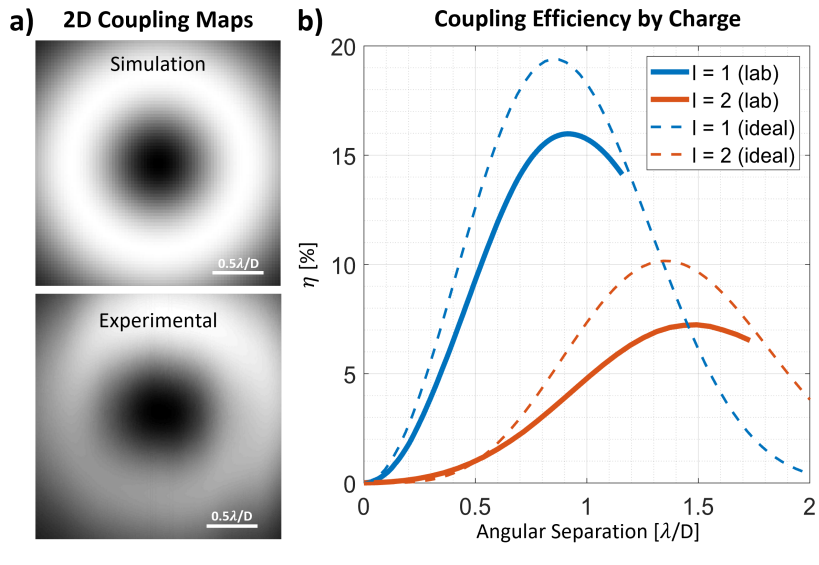


Figure 4.2: (a) 2D coupling maps with a charge 1 vortex mask in simulation (top) and experiment (bottom). (b) Monochromatic coupling efficiency line profiles for charge 1 (blue) and charge 2 (orange). The theoretical best (i.e., ideal) coupling, determined from simulation, is shown in the dotted lines while the experimental coupling is shown in the solid lines.

diameter. We set the pupil size for this experiment based on the manufacturer's specification of the SMF core but there is a large uncertainty on this value due to manufacturing variability (ref. internal communications with Thorlabs). In fact, for the polychromatic experiments in Sec. 4.2, we empirically determined that the ideal pupil diameter was 2.45 mm, rather than the 2.1 mm used here, so this likely had an effect on the performance here but was not confirmed when this text was originally presented in Echeverri, Ruane, Calvin, et al. (2020).

We also tested a charge 2 vortex mask in the laboratory to validate charge 2 VFN monochromatically. This is a broadband vector vortex mask designed for 418-868 nm wavelengths (Tabiryan et al., 2017). We initially tested the vortex using the same 635 nm laser as in the last experiments but found that the performance was not as good as expected. Once we switched to a 780 nm laser, the performance was much better. In this layout, the on-axis (i.e., star) coupling was measured at $4.7 \times 10^{-5}$ while the azimuthally-averaged peak planet coupling was 7.2%. The coupling profile and the corresponding theoretical coupling for charge 2 are shown in orange in Fig. 4.2(b). As with the charge 1 experiments, the coupling is close to, but not quite as high as, the theoretical maximum. We believe this may be due to the same reasons mentioned for charge 1.

## 4.2 Broadband Experiments

With the broadband vortex mask validated in monochromatic light, we proceeded to test VFN in polychromatic light using this new mask. An initial attempt at broadband experiments was made using the same test setup as the monochromatic tests but with a broadband light source. This resulted in a null of $4.5 \times 10^{-4}$ with an azimuthally-averaged peak planet coupling of 4.5% at 10% bandwidth ($\Delta\lambda/\lambda$) centered around 790 nm (Echeverri, Ruane, Jovanovic, Hayama, et al., 2019; Echeverri, Ruane, Calvin, et al., 2020). However, based on the amount of wavefront error in the system, we found that we should have achieved deeper nulls. We later determined that those results were limited by chromatic first-order leakage from the vector vortex mask. This section thus presents the updates made to the testbed to mitigate the polarization-dependent chromatic errors. It also presents the resulting performance in broadband light. This work was originally included in Echeverri, Ruane, Jovanovic, Delorme, et al. (2021) and then prepared for publication in a dedicated paper. That paper was ultimately not submitted due to new results, published in Echeverri, Xuan, et al. (2023) and reproduced in Chapter 6, which were in broadband, with higher spectral resolution, and using the on-sky instrument such that they supplanted the laboratory results. The following text is derived from that unpublished paper.

### Testbed Modifications for Broadband

Figure 4.3 shows the optical layout as used for the final polychromatic experiments. The key changes with respect to Sec. 4.1 are that a broadband light source and circular polarizers were added, the nulling fiber stage was controlled with different actuators, and the normalziation PM was moved to after lens L2. The new source was a supercontinuum white light source (NKT Photonics SuperK EXR-4) with a tunable filter (NKT Photonics SuperK VARIA) that could select bandwidths from 6 to 100 nm wide centered between 400 and 840 nm wavelengths. The actuators for the nulling fiber were changed to new piezoelectric linear stages (PI Q-545.240) that operate in closed-loop with an accuracy of 6 nm and total range of 26 mm. The closed-loop operation, a new feature over the previous actuators, removed uncertainty on the spatial scale of the scans due to hysterisis. The increased range on the nulling fiber stage allowed us to move the normalization PM downstream of lens L2. It thus sampled the power immediately before the nulling fiber such that a correction for the transmission of the lens was no longer needed, which reduced that possible source of error.

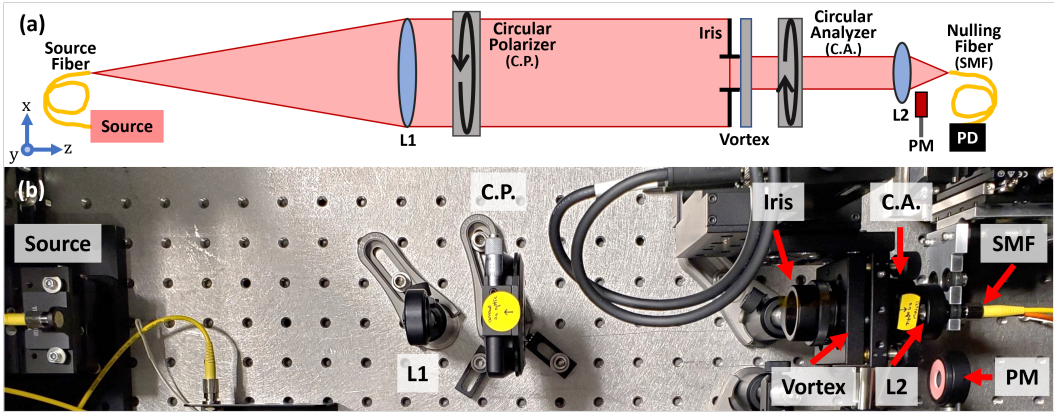


Figure 4.3: (a) Schematic of the VFN testbed at Caltech. Light from a single mode fiber source is collimated by lens L1 before passing through a circular polarizer (C.P.), iris, vortex mask, and circular analyzer (C.A.). Lens L2 focuses the light onto another single mode fiber (Nulling Fiber) that is connected to a photodiode (PD) which measures the power through the fiber. An optical power meter (PM) can be translated into the optical path between L2 and the nulling fiber to measure the power incident on the fiber. (b) Matching picture of the testbed as described by the schematic.

The biggest change was the addition of the circular polarizers to correct for chromatic leakage from the vector vortex mask. In the monochromatic experiments, there were enough degrees of freedom between moving the vortex and nulling fiber to find a position that achieved deep nulls at a single wavelength. However, there is no single location for all wavelengths in polychromatic light. A practical limitation in vector vortex masks is that there can be a wavelength-dependent retardance error which results in a fraction of the incoming light being transmitted without obtaining the azimuthal vortex phase (Ruane, Mawet, et al., 2019). This leaked light couples into the SMF in the original Airy pattern and results in stellar leakage due to errors in the vortex mask itself. Though we do not have measurements of the retardance error for the charge 2 vortex used in these experiments, we estimate that the chromatic leakage previously limited us to about the $10^{-4}$, based on the polychromatic null depths described above without the circular polarizers. Additionally, we suspect that the retardance error was worse at shorter wavelengths, pushing us to around 785 nm rather than 635 nm for deep nulling as presented in the monochromatic results with this charge 2 mask.

The Circular polarizers address the retardance errors by filtering out the light without the vortex ramp. For a given circular polarization state, right-handed or left-handed, the on-axis leakage from a vector vortex mask appears as light in the same polar-

ization state after the vortex while the light with the desired phase ramp switches to the orthogonal polarization state (Ruane, Mawet, et al., 2019). We leverage this by placing opposite-handed polarizers up and downstream of the vortex. The upstream polarizer, labeled C.P. in Fig. 4.3, prepares the light so that the vortex only recieves a single polarization, right-hand circular in this case. The vortex imparts its azimuthal phase ramp on most of the light and flips its polarization to left-hand circular. We then filter for left-hand circular light using another circular polarizer, referred to as the circular analyzer (C.A.), so that the leakage, which is right-handed in our system, is removed and we can achieve deeper nulls. As usual, the relative clocking angle between the two polarizers is important for achieving the best performance (Llop-Sayson et al., 2021). We tuned this clocking by fixing the C.A.'s orientation and rotating the C.P. to minimize the transmitted power with the vortex entirely removed from the system. This ensures that the polarizers are orthogonal to each other and maximally suppress the vortex leakage. We achieved an extinction ratio of 520:1 in 635 nm laser light with our commercialy available, monochromatic circular polarizers (Thorlabs CP1R633 and CP1L633). Given that the leakage term was estimated at $\sim 10^{-4}$, this extinction ratio mitigates the leakage to far below the null floor from wavefront error. The fact that the polarizers are monochromatic and hence designed for a specific wavelength means that they operate best at that wavelength, but they can still filter the chromatic leakage from the vortex to a lesser degree at nearby wavelengths. This ultimately limited the null depth at wider bandwidths as described below.

An additional modification to the testbed for these experiments was an empirical tuning of the pupil diameter to optimize the F# given the uncertainty in the MFD of the SMF. We optimized the pupil diameter to maximize the non-vortex, on-axis coupling by offsetting the vortex mask so that the beam passed through a region of the optic at least 2 pupil diameters away from the phase singularity. This meant the beam picked up a slight phase tilt but did not have the vortex phase and thus the PSF was a typical Airy Pattern. We tuned the iris size until we achieved a coupling efficiency of $\sim$ 76% including fiber losses. This is close to the theoretical maximum coupling of $\sim$ 80% for a circular, unobstructed beam coupling into a SMF (Shaklan et al., 1988). We measured the pupil diameter using two different methods: (1) a knife-edge test and (2) pupil imaging. Both methods measured a diameter of 2.45 mm which, combined with the 11 mm L2 lens, set a system F# of 4.5.

**Procedure**

The vortex position for these tests was optimized by scanning the mask laterally in the pupil plane. Moving the vortex shifts the power around the circular bright fringe and moves the null slightly so at each vortex location, we scanned the nulling fiber to measure the full coupling efficiency map. We also scanned the fiber in focus so that we simultaneously optimized all the main degrees of freedom in the system to get the best performance. This process was repeated until we minimized the relative integration time, $\tau \propto \eta_s/\eta_p^2$ (see Eq. 2.21 in Sec. 2.5), to provide the best combination of null depth and simultaneous planet throughput. To ensure that we found the optimal alignment for broadband performance, and thus were not chasing good performance at a single wavelength, these scans were done at a 50 nm bandwidth centered around 650 nm.

We measured the wavefront through the full system by reverse-injecting light from the nulling fiber. For this measurement, a Shack-Hartmann wavefront sensor (ImagineOptic HASO4-Broadband) was placed between the source stage and lens L1, facing L1 so that the cumulative wavefront error from all the optics was sampled. Due to the small pupil, there were only ~18 samples across the beam and hence we could only measure the low-order wavefront aberrations in the system. We determined that the total low-order wavefront error was about 9 nm RMS.

With this done, the system was aligned and ready to test at various bandwidths. We used a central wavelength of 650 nm since the polarizers mitigated the chromatic zeroth-order leakage and allowed us to switch back to shorter wavelengths. We varied the bandwidths from 6 nm (1%) to 100 nm (15%). A two-dimensional (transverse) nulling fiber scan was performed at each bandwidth to measure the system performance for all points in the field. For any given point, the coupling efficiency was computed as the power through the fiber, measured with the PD, divided by the power incident on the fiber, measured on the PM. The value from the PD was corrected to account for Fresnel reflections at the fiber faces (3.5%) and propagation losses through the 2 m fiber (0.4%). We converted the power measured on the PM to the same units as the PD by carefully calibrating the scaling factor between the two. This calibration was done at each bandwidth used in the experiments by setting the VARIA tunable filter to the desired bandwidth, measuring its output directly on the PD, and then immediately measuring it on the PM. The ratio between these two was found to be the same and repeatable across all bandwidths. Finally, we verified the VARIA bandwidths by measuring the output spectrum on

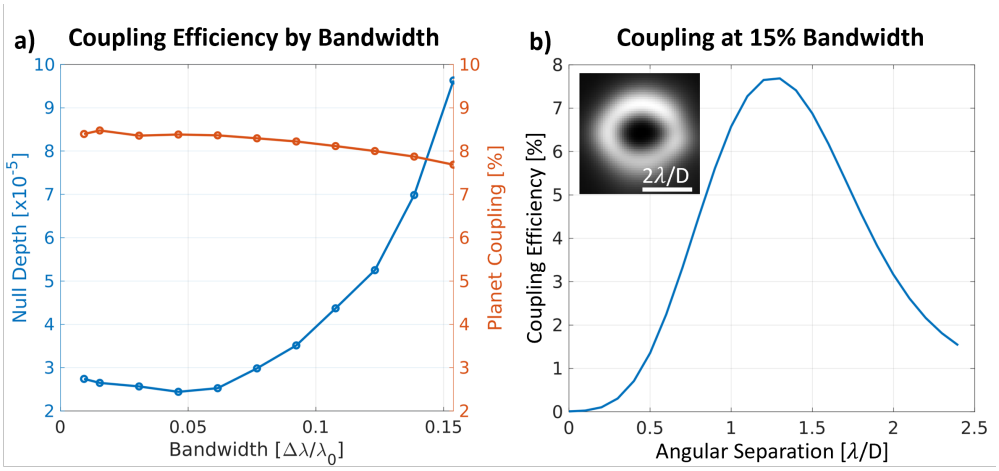


Figure 4.4: (a) VFN performance at all tested bandwidths. The blue curve shows the null depth and corresponds to the left y-axis while the orange curve is the peak planet coupling and corresponds to the right y-axis. These experiments were performed at various bandwidths centered around 650 nm light such that a 15% bandwidth corresponds to a bandpass from about 600 to 700 nm. (b) VFN coupling for the 15% bandwidth sample. The inset shows the full 2D coupling map obtained by scanning the nulling fiber while the adjacent line profile shows the radial average of the inset. The peak planet coupling from (a) corresponds to the maximum coupling in (b) for each bandwidth sample.

an optical spectrum analyzer (OSA - Thorlabs OSA202C).

**Broadband Results**

Figure 4.4(a) shows the measured VFN performance versus the sampled bandwidths. We achieved nulls, shown in blue, of $< 10^{-4}$ out to the widest bandwidth of 15%. For bandwidths less than 7% the null leveled out at about $2.5 \times 10^{-5}$ indicating that our setup is achromatic down to this level. At these small bandwidths the null is primarily limited by wavefront error in the optical setup. We confirmed this with a model of the system that predicts the performance using the known properties of our testbed. The model starts with an image of the pupil, applies the known low-order wavefront errors as measured with the wavefront sensor, adds the charge 2 vortex phase with the known offset in vortex-centering from the vortex scans, and then Fourier Transforms to determine the system PSF. This PSF is convolved with the fundamental mode of the SMF, assumed to be Gaussian for simplicity, to generate the predicted coupling efficiency map for our system. That model predicts a null of $1.4 \times 10^{-5}$, mostly driven by the wavefront error, which is within a factor of 2 of the aforementioned measured null floor in our system.

The experimental null starts to degrade beyond 7% bandwidth, most likely because the polarizers were designed for monochromatic 633 nm light. This means that the chromatic leakage from the vortex is poorly filtered towards the edges of the band and starts to dominate the null performance at larger bandwidths. The fact that the crossover from the wavefront-limited to leakage-limited regime occurs at 7% is an element of our specific testbed; with the polarizers, we can push the chromatic leakage below the wavefront error leakage but only for small bandwidths where the polarizers achieve good extinction ratios. We could increase the bandwidth over which we achieve wavefront-limited nulls of about $2.5\times10^{-5}$ by replacing our current polarizers with polychromatic ones. Alternatively, with a vector vortex mask with lower retardance error over the desired bands, the chromatic leakage from the vortex would be smaller and the polarizers could be removed from the system entirely. However, we felt these modifications were unnecessary for this simple demonstration given that we manage to demonstrate reasonably deep, well understood, VFN nulls over a 15% bandwidth without them. These chromatic leakage effects are not a limitation of VFN itself but of the manufacturing capabilities of vector vortex masks and of the quarter-wave plates in the circular polarizers. Other HCI techniques deal with these issues as well and there is a general interest in improving vector vortex masks. There is also promise in scalar vortex masks which are not polarization-dependent (Ruane, Mawet, et al., 2019), have been shown to reach contrasts similar to the current VFN null in dual polarization (Desai, Llop-Sayson, et al., 2021), and can be implemented with VFN (Ruane, Echeverri, et al., 2019).

As for the off-axis coupling, Fig. 4.4(b) shows the full coupling map (inset) as well as the radially-averaged line profile for the 15% bandwidth sample using our charge 2 vortex. The coupling map has the expected bright fringe. We achieve an azimuthally-averaged peak coupling efficiency of just under 8% for the 15% bandwidth sample. Figure 4.4(a) shows that the peak coupling at the other bandwidths is just above 8%, such that the planet coupling is mostly achromatic. The very slight gradual decrease in coupling with bandwidths could be due to the chromatic defocus of lens L2 or because the PSF changes size with wavelength slightly faster than the fibermode. However, the loss in coupling when going out to 15% bandwidth, commensurate with on-sky observing bands, is <0.5% here. Assuming a Gaussian fiber mode, the peak planet coupling for a charge 2 vortex should be 10%. Our laboratory experiments are within 2% of that value.

Table 4.1: Summary of best VFN laboratory demonstrations

| Condition | Bandwidth | Wavelength | Charge | Null | Peak |
|---|---|---|---|---|---|
| Mono. | – | 635 nm | 1 | $6.6 \times 10^{-5}$ | 16% at 0.9 $\lambda/D$ |
| | – | 780 nm | 2 | $4.7 \times 10^{-5}$ | 7.2% at 1.45 $\lambda/D$ |
| Poly. | 7.7% | 650 nm | 2 | $2.5 \times 10^{-5}$ | 8.2% at 1.3 $\lambda/D$ |
| | 15.4% | 650 nm | 2 | $9.7 \times 10^{-5}$ | 7.8% at 1.3 $\lambda/D$ |

Monochromatic reference: Echeverri, Ruane, Calvin, et al. (2020)
Polychromatic reference: Echeverri, Ruane, Jovanovic, Delorme, et al. (2021)

To summarize, we achieved wavefront-limited nulls of about $2.5 \times 10^{-5}$ for bandwidths below 7%. Our vector vortex mask was polychromatic but our circular polarizers were monochromatic such that the null was leakage-limited at wider bandwidths. Nevertheless, we reached nulls of $< 10^{-4}$ out to 15% bandwidth with our simple testbed made primarily of off-the-shelf elements. There is a clear path for better broadband null depths by using polychromatic circular polarizers or a vortex with lower retardance errors at wider bandwidths. The peak planet coupling remained steady at about 8% and is close to the predicted maximum of 10%. Table 4.1 summarizes the key monochromatic and polychromatic results presented in this and the previous section.

### 4.3 The Polychromatic Reflective Testbed (PoRT)

The transmissive testbed used in the prior experiments has worked well but is limited by the chromatic effects introduced by the lenses, as well as a few other design issues. This drove us to design a new testbed, building on the successes of the last but with reflective elements where possible to enable truly polychromatic performance. This section presents the new testbed, describes how it was designed, and highlights key results from the first experiments using it. Most of this section is derived from Echeverri, Ruane, Calvin, et al. (2020). Note that the testbed was originally designed with two versions, a simplified version very similar to the original transmissive bench and an expanded version that adds a DM. I have omitted the simplified version from this section since we built the full version from the get-go due to requirements set by the planned experiments.

Figure 4.5(a) shows a CAD model of the testbed, which we have called the Polychromatic Reflective Testbed, or "PoRT." A single fiber illuminates an off-axis parabolic mirror (OAP), OAP1, with a 280.3 mm focal length to collimate the light. The focal

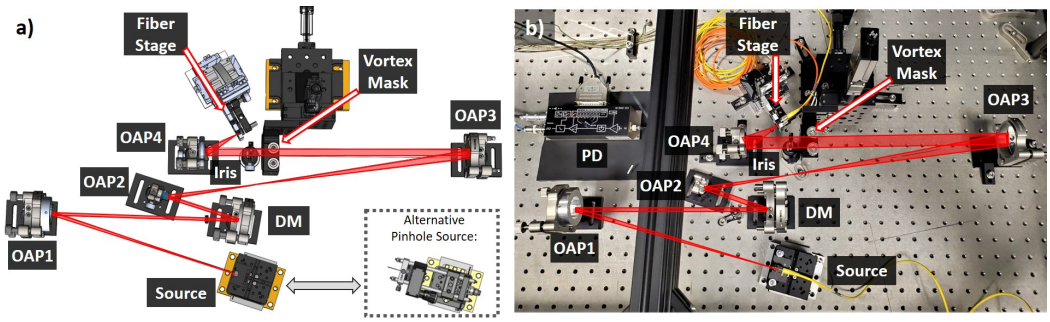


Figure 4.5: (a) CAD model of the PoRT testbed at Caltech. The light from the source is collimated by OAP1 and projected onto the DM for wavefront control capabilities. The pupil is then relayed to the vortex mask through a magnifying set of OAPs (OAP2 and OAP3). An iris defines the pupil and sets the desired diameter to yield the correct F# with OAP4, which focuses the light onto the nulling fiber. Two source mechanisms are available, one with an SMF holder and another with a pinhole to ensure the source remains unresolved for deep nulling experiments. (b) Photo of the testbed during a mechanical fit test. The vertical black beam near OAP2 is part of the enclosure that isolates PoRT and is not actually in the beampath.

length was selected to ensure that the OAP is sufficiently close to the fiber to capture an adequate amount of the light while still being far enough to keep the fiber tip unresolved. For certain charge 1 vortex experiments where the angular size of the source may limit the achievable null, we have also designed an alternate source that supports a pinhole. This source utilizes a cage system that can support additional optics upstream of the pinhole. As such, if a vector vortex mask mandates the use of a circular polarizer, it can be added here to mitigate the wavefront error it may introduce. The pinhole source is shown in the inset of Fig. 4.5(a).

The light from OAP1 is projected onto a $12 \times 12$ actuator, 3.5 $\mu$m stroke deformable mirror (DM - Boston Micromachines Corporation Multi-DM) so that the wavefront within the system can be controlled. This is a major improvement over the previous testbed in which several experiments were limited by the wavefront aberrations present in the optics and the alignment. With a DM, the wavefront can be carefully tuned to minimize the coma and astigmatism aberrations that charge 1 and charge 2, respectively, are sensitive to (Ruane, Echeverri, et al., 2019). The DM also has a custom, removable optical window with an anti-reflection coating from 550 to 2400 nm and a wedge to ensure any back-reflected ghosts are led out of the optical path. The DM cannot operate above approximately 30% relative humidity, so a dry-air system was designed which ensures the humidity in the testbed is kept below this level.

An optical relay, composed of OAP2 and OAP3, magnifies the beam and sends it towards the vortex. The focal lengths of the OAPs are 114 mm and 334.9 mm, respectively, for a magnification factor of 2.94. The vortex sits on a translation stage with computer-controlled actuators (Zaber X-NA08A50-E09), so that its position can be scanned as was done in the experiments on the previous testbed. Immediately after the vortex, an iris defines the pupil. Since this testbed was designed to operate across many different wavelengths from the visible to near-infrared (600 to 2400 nm), the pupil diameter needs to be changed depending on the SMF in use for a given experiment. The original design used a manual iris, as shown in Fig. 4.3, but it has since been changed to a motorized iris with a diameter range from 1 to 14 mm. This enables us to easily scan the system F# to make sure it is optimally tuned for the nulling fiber's MFD, as was done manually for the broadband experiments in the previous section. The nominal diameter for $\lambda$ = 650 nm is ~11.2 mm.

After the iris, a final OAP with a focal length of 54.4 mm, OAP4, focuses the light onto the tip of the nulling fiber. The nulling fiber stage has been upgraded from the previous design to hold up to four optical fibers. This allows us to readily switch between fibers for different experiments and also lets us have a multi-mode fiber (MMF) for normalization measurements. The MMF has a core diameter of 105 $\mu$m so that it collects the majority of the incident light. A bifurcated fiber is then used to combine the nulling SMF and the MMF inside a single fiber cladding that can be fed into a photodiode. This two-fiber design will enable us to perform the coupling and normalization measurements on the same detector, thereby simplifying the analysis and removing any uncertainties regarding the calibration between multiple detectors. A power meter has also been added on a translating stage immediately before the nulling fiber stage so that it can be inserted into the beam as was done in the broadband experiments. This way the normalization can be done using the old technique as well, in case the MMF causes issues. The nulling stage itself is the same one utilized in the broadband experiments with high-precision piezoelectric linear stages (PI Q-545.240) that can operate in closed-loop to mitigate hysteresis in the piezos and uncertainties about the scan step size.

**First Results**

The PoRT testbed was aligned and started operating in 2022. A key benefit of PoRT is its versatility. At its core, the testbed provides: a fiber injection unit with full control over the fiber position, a pupil plane with a translation stage, and a deformable mirror for managing the wavefront within the system. Furthermore,

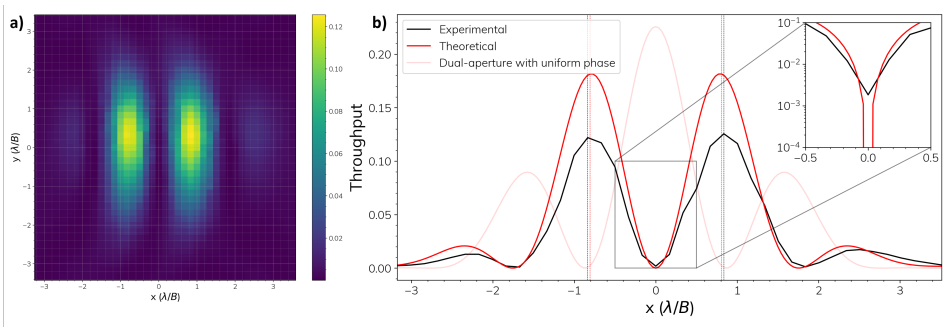


Figure 4.6: (a) Two dimensional coupling map from the DAFN experiments on the PoRT testbed. The map shows the expected two-lobed structure with a null at the center where the star would be aligned. (b) Linescans through the horizontal center of coupling map. The solid red line shows the theoretical ideal performance while the solid black line shows measured performance. The vertical dotted lines denote the location of the peak off-axis coupling efficiency, indicating where the light from an off-axis companion would be maximally transmitted through to the detector. The light dotted red curve in the background shows the theoretical coupling from constructive interference assuming no phase shift between the two apertures. The inset on the right shows the performance near the on-axis null point.

the use of reflective powered optics allows the bench to easily switch from visible to near-infrared wavelengths. PoRT thus serves as a general-purpose fiber nulling testbed.

In this spirit, the first experiments performed on the testbed were for validating the dual-aperture fiber nulling (DAFN) concept (Wang et al., 2020). DAFN combines two telescope apertures with a pi phase shift between the two. In this way, it is very similar to the concept behind the Palomar Fiber Nuller (PFN - Serabyn et al., 2010). The preliminary application for DAFN is on the Large Binocular Telescope Interferometer (LBTI). The concept was initially tested at The Ohio State University but was then further developed using PoRT by Anusha Pai Asnodkar. Given PoRT's design, the only modification requried for DAFN was to add a pupil mask with two sub-apertures replicating the LBTI apertures. The pi phase shift was then applied using the DM. Figure 4.6 presents the results from those experiments. Panel (a) in the figure presents the coupling efficiency map, with the emblematic two-lobed structure and central nulled region. Panel (b) presents a horizontal crosscut through the measured coupling map along with the theoretical expected performance. Using PoRT, Anusha demonstrated an on-axis null depth of $2 \times 10^{-3}$ and a peak coupling efficiency of 12% at the expected $0.8\,\lambda/B$ separation, where $B$ is the baseline between the two interferometric apertures. The off-axis coupling has the right form though

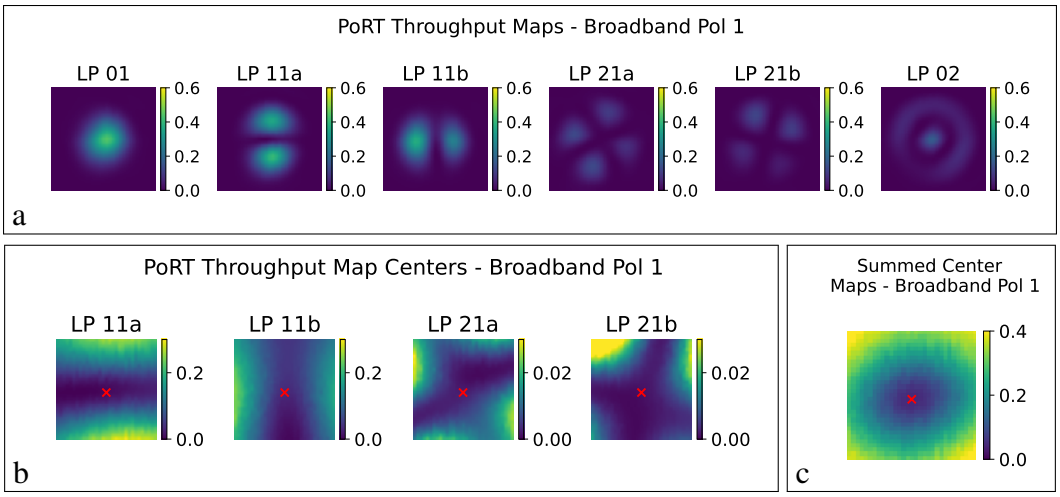


Figure 4.7: Laboratory PLN results measured on PoRT, using an SLD light source from 1450 nm to 1625 nm injected with a polarization-maintaining fiber. (a) Throughput maps of all ports across the PLN field of view. b) Throughput maps of the nulled ports with fine spatial sampling of the center (note that the LP 21 maps are on a different color scale from the LP 11 maps). The red crosses indicate the axial center of the lantern, identified using the map in part (c). c) The summed throughput of the four maps in part (b). The location of minimum summed throughput is taken to be the lantern center, where $\eta_s$ is measured. - Original figure from Xin et al. (in prep).

the peak is 6% lower than the theoretical maximum. These results demonstrated that PoRT was operational, adaptable, and capable of nulling.

Another set of experiments on PoRT aimed at demonstrating the photonic lantern nulling (PLN) concept in the laboratory for the first time. This work, performed by Yinzi Xin, and the related results have been submitted in a paper which is currently under review for JATIS. PLN has a strong heritage in the VFN concept though it leverages the mode-selective capabilities of certain photonic lanterns (Xin et al., 2022). This provides increased off-axis coupling and enables PLN to constrain the companion position. The main modifications required for these experiments on PoRT were to replace the nulling SMF with a photonic lantern, and to swap the source to a Super-Luminescent Diode (SLD) with a polarization-maintaining fiber so that the effects of polarization on PLN could be assessed. Given the design of PoRT, both of these modifications were very simple to implement. Figure 4.7 presents some of the key broadband results. Panel (a) shows the off-axis coupling maps through each of the ports in the lantern; these maps are in strong agreement with the expected morphology from the lantern in use. Panel (b) shows just the

nulled region where the star would be aligned on the nulled ports, while panel (c) shows the combined coupling for those four nulled ports. In the linearly-polarized (LP) 11a and LP 11b ports, Yinzi demonstrated on-axis nulls of $\sim 8 \times 10^{-3}$ and $\sim 3 \times 10^{-2}$, respectively. The peak off-axis coupling on each of these ports was 40.4% and 37.4%, respectively. For more information on the PLN concept, and these results, refer to (Xin et al., 2022, and Xin et al., in prep.). The use of PoRT for these experiments enabled rapid development and validation of the PLN concept in both monochromatic and broadband light.

Future experiments planned for PoRT include further development of the PLN concept as well as a return to VFN tests. The VFN tests will center around validating new vortex designs, including scalar vortex masks (Ruane, Mawet, et al., 2019; Desai, Ruane, et al., 2023) which have shown great promise for VFN (see Sec. 8.1 in this thesis and Ruane, Echeverri, et al., 2019). The testbed can also be used for developing and testing wavefront control algorithms tailored to VFN, leveraging the sensitivities to only specific Zernike polynomials.

## References

Desai, N., J. Llop-Sayson, et al. (Sept. 2021). "High contrast demonstrations of novel scalar vortex coronagraph designs at the high contrast spectroscopy testbed". In: *Techniques and Instrumentation for Detection of Exoplanets X*. Ed. by S. B. Shaklan and G. J. Ruane. Vol. 11823. Society of Photo-Optical Instrumentation Engineers (SPIE) Conference Series, 118230Q, 118230Q. DOI: 10.1117/12.2603953. arXiv: 2205.10870 [astro-ph.IM].

Desai, N., G. Ruane, et al. (Apr. 2023). "Laboratory demonstration of the wrapped staircase scalar vortex coronagraph". In: *Journal of Astronomical Telescopes, Instruments, and Systems* 9, 025001, p. 025001. DOI: 10.1117/1.JATIS.9.2.025001. arXiv: 2305.05076 [astro-ph.IM].

Echeverri, D., G. Ruane, B. Calvin, et al. (Dec. 2020). "Detecting and characterizing close-in exoplanets with vortex fiber nulling". In: *Optical and Infrared Interferometry and Imaging VII*. Ed. by P. G. Tuthill, A. Mérand, and S. Sallum. Vol. 11446. Society of Photo-Optical Instrumentation Engineers (SPIE) Conference Series, 1144619, p. 1144619. DOI: 10.1117/12.2563142. arXiv: 2012.04239 [astro-ph.IM].

Echeverri, D., G. Ruane, N. Jovanovic, J.-R. Delorme, et al. (Sept. 2021). "Broadband vortex fiber nulling: high-dispersion exoplanet science at the diffraction limit". In: *Techniques and Instrumentation for Detection of Exoplanets X*. Ed. by S. B. Shaklan and G. J. Ruane. Vol. 11823. Society of Photo-Optical Instrumentation Engineers (SPIE) Conference Series, 118230A, 118230A. DOI: 10.1117/12.2597160. arXiv: 2210.15910 [astro-ph.EP].

Echeverri, D., G. Ruane, N. Jovanovic, T. Hayama, et al. (Sept. 2019). "The vortex fiber nulling mode of the Keck Planet Imager and Characterizer (KPIC)". In: *Society of Photo-Optical Instrumentation Engineers (SPIE) Conference Series*. Vol. 11117. Society of Photo-Optical Instrumentation Engineers (SPIE) Conference Series, 111170V, p. 111170V. DOI: 10.1117/12.2528529. arXiv: 1909.03538 [astro-ph.IM].

Echeverri, D., G. Ruane, N. Jovanovic, D. Mawet, et al. (May 2019). "Vortex fiber nulling for exoplanet observations I. Experimental demonstration in monochromatic light". In: *Optics Letters* 44.9, p. 2204. DOI: 10.1364/OL.44.002204. arXiv: 1811.02083 [astro-ph.IM].

Echeverri, D., J. W. Xuan, et al. (July 2023). "Vortex fiber nulling for exoplanet observations: implementation and first light". In: *Journal of Astronomical Telescopes, Instruments, and Systems* 9, 035002, p. 035002. DOI: 10.1117/1.JATIS.9.3.035002. arXiv: 2309.06514 [astro-ph.IM]. URL: https://doi.org/10.1117/1.JATIS.9.3.035002.

Llop-Sayson, J. et al. (Sept. 2021). "New method to achieve the proper polarization state for a vector vortex coronagraph". In: *Techniques and Instrumentation for Detection of Exoplanets X*. Ed. by S. B. Shaklan and G. J. Ruane. Vol. 11823. Society of Photo-Optical Instrumentation Engineers (SPIE) Conference Series, 118230P, 118230P. DOI: 10.1117/12.2594871. arXiv: 2108.07371 [astro-ph.IM].

Ruane, G., D. Echeverri, et al. (Sept. 2019). "Vortex fiber nulling for exoplanet observations: conceptual design, theoretical performance, and initial scientific yield predictions". In: *Society of Photo-Optical Instrumentation Engineers (SPIE) Conference Series*. Vol. 11117. Society of Photo-Optical Instrumentation Engineers (SPIE) Conference Series, 1111716, p. 1111716. DOI: 10.1117/12.2528555. arXiv: 1908.09780 [astro-ph.IM].

Ruane, G., D. Mawet, et al. (Sept. 2019). "Scalar vortex coronagraph mask design and predicted performance". In: *Society of Photo-Optical Instrumentation Engineers (SPIE) Conference Series*. Vol. 11117. Society of Photo-Optical Instrumentation Engineers (SPIE) Conference Series, 111171F, 111171F. DOI: 10.1117/12.2528625. arXiv: 1908.09786 [astro-ph.IM].

Serabyn, E. et al. (July 2010). "The potential of rotating-baseline nulling interferometers operating within large single-telescope apertures". In: *Optical and Infrared Interferometry II*. Ed. by W. C. Danchi, F. Delplancke, and J. K. Rajagopal. Vol. 7734. Proc. SPIE, 77341E, 77341E. DOI: 10.1117/12.857753.

Shaklan, S. and F. Roddier (1988). "Coupling starlight into single-mode fiber optics". In: *Appl. Opt.* 27.11, pp. 2334–2338. DOI: 10.1364/AO.27.002334.

Tabiryan, N., H. Xianyu, and E. Serabyn (2017). "High efficiency broadband liquid crystal polymer vector vortex waveplates". In: *IEEE Aerospace Conference*, pp. 1–7. DOI: 10.1109/AERO.2017.7943757.

Wang, J. and C. Jurgenson (Nov. 2020). “Exoplanet Sciences with Nulling Interferometers and a Single-mode Fiber-fed Spectrograph”. In: *The Astronomical Journal* 160.5, 210, p. 210. DOI: 10.3847/1538-3881/abb5a3. arXiv: 2007.15529 [astro-ph.IM].

Xin, Y. et al. (Oct. 2022). “Efficient Detection and Characterization of Exoplanets within the Diffraction Limit: Nulling with a Mode-selective Photonic Lantern”. In: *The Astrophysical Journal* 938.2, 140, p. 140. DOI: 10.3847/1538-4357/ac9284. arXiv: 2209.07644 [astro-ph.IM].

*Chapter 5*

# THE KPIC VFN MODE

The laboratory results presented in the previous chapter laid the foundation for an on-sky demonstration of VFN. Concurrent with the VFN efforts, our team was developing an AO-coupled, SMF-fed instrument called the Keck Planet Imager and Characterizer (KPIC). This provided a unique opportunity to test VFN with KPIC. Thus, this chapter introduces the first on-sky VFN demonstrator, included as a dedicated mode in the KPIC instrument. The first part of the chapter pulls from Echeverri, Ruane, Jovanovic, Hayama, et al. (2019) to briefly summarize KPIC and introduce the VFN mode. This includes a technical simulation of the predicted on-sky null and off-axis coupling. That simulation is then supplemented with subsequent simulations used to predict the relationship between on-sky RMS wavefront residuals and the resulting null depth. The chapter closes out with a brief laboratory characterization of the KPIC VFN vortex mask, taken from Echeverri, Ruane, Calvin, et al. (2020), followed by a deeper characterization of the KPIC VFN mode as integrated in the instrument prior to deployment to the telescope. That second characterization was not previously included in any published work.

Taken as a whole, this chapter introduces the KPIC VFN mode and presents simulations and laboratory characterizations used to predict the instrument's capabilities. Note that a more-detailed explanation of the instrument design is included in the next chapter as part of a published paper.

---

*Excerpt From*

## The Vortex Fiber Nulling Mode of the Keck Planet Imager and Characterizer (KPIC)

Echeverri, D. et al. (Sept. 2019). "The vortex fiber nulling mode of the Keck Planet Imager and Characterizer (KPIC)". In: *Society of Photo-Optical Instrumentation Engineers (SPIE) Conference Series.* Vol. 11117. Society of Photo-Optical Instrumentation Engineers (SPIE) Conference Series, 111170V, p. 111170V. DOI: 10.1117/12.2528529. arXiv: 1909.03538 [astro-ph.IM].

## 5.1 Introduction

The Keck Planet Imager and Characterizer (KPIC - Mawet, Wizinowich, et al., 2016; Mawet, Delorme, et al., 2017; Jovanovic, Mawet, et al., 2019) is an instrument designed to link the Keck adaptive optics (AO) system (Wizinowich et al., 2000) to NIRSPEC, a high-resolution near-infrared spectrograph (Martin et al., 2018). KPIC accomplishes this by coupling light from a point-like source into a single-mode fiber (SMF) (Jovanovic, Schwab, et al., 2017), allowing for conventional stellar spectroscopy as well as direct spectroscopy of low mass companions, including giant exoplanets. In scenarios where the companion of interest is resolved with respect to the star (roughly speaking, when the angular separation is $> \lambda/D$, where $\lambda$ is the wavelength and $D$ is the telescope diameter), the starlight may be minimized at the position of the planet using a coronagraph and speckle nulling techniques (Pezzato et al., 2019; Mawet, Ruane, et al., 2017). However, in situations where the planet-star angular separation is $\sim \lambda/D$, fiber nulling interferometry (Bracewell, 1978; Haguenauer et al., 2006; Serabyn et al., 2019) may be a more effective method for reducing the amount of starlight entering the spectrograph. KPIC will have such an interferometric mode, based on the vortex fiber nulling (VFN) technique (Ruane, Wang, et al., 2018; Echeverri, Ruane, Jovanovic, Mawet, et al., 2019; Ruane, Echeverri, et al., 2019), to enable spectroscopy of close-in companions. Here we provide estimates of the on-sky performance of the KPIC VFN mode given the current AO performance.

## 5.2 The KPIC VFN Mode

Given the simplicity of implementing VFN and the recent progress on laboratory demonstrations, we are preparing to add a VFN mode to the KPIC instrument as part of an upcoming upgrade. This mode shares many modules with the other KPIC modes. As shown in Fig. 5.1(a), KPIC can directly accept the AO-corrected light from the telescope, or it can use its own near-infrared pyramid wavefront sensor (PyWFS - Bond et al., 2018) and high-order deformable mirror (DM - Boston Micromachines Corporation Kilo-DM) for active wavefront control. Regardless of the wavefront sensor, the corrected beam then passes through the vortex mask and atmospheric dispersion compensator (ADC) for VFN operations.[1] A tip-tilt mirror (TTM) aligns the stellar PSF with the science SMF that feeds NIRSPEC (see Fig. 5.1c) to null the starlight. Feedback for the TTM control loop is provided

[1] 2023 Updates: The PyWFS has not been used with VFN due to necessary software updates; this is covered in Secs. 5.5 and 6.7. Also, the ADC will be installed in early 2024; see Sec. 8.3.

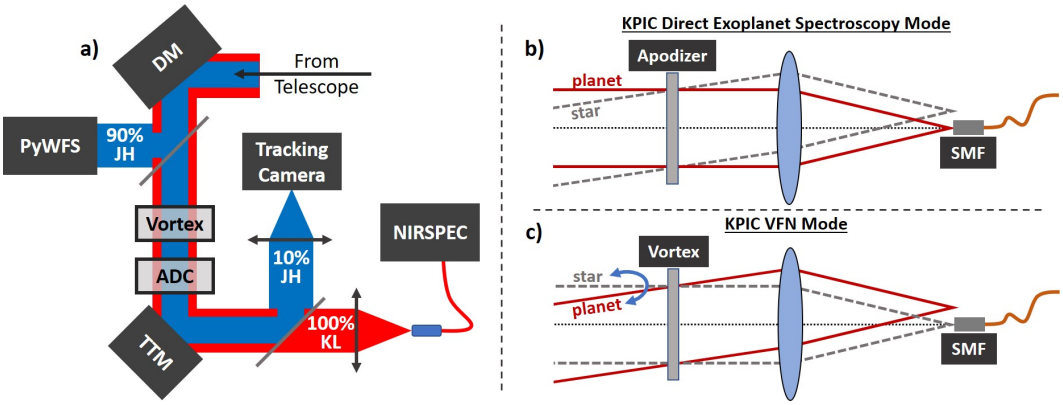


Figure 5.1: (a) Diagram of the KPIC VFN mode. Light arrives from the telescope after passing through the facility AO system. The near-infrared pyramid wavefront sensor (PyWFS) and high-order deformable mirror (DM) further correct the wavefront before allowing the beam to pass through the vortex mask and then the atmospheric dispersion compensator (ADC). The tip-tilt mirror (TTM) centers the star PSF on the fiber which feeds NIRSPEC, the high-resolution near-infrared spectrograph. A dichroic reflects $J$ and $H$ bands to a tracking camera, which provides simultaneous imaging for PSF tracking, calibration, and control algorithms. Light in the science channel ($K$ band) transmits through the dichroic and is routed to NIRSPEC via the SMF. $L$ band is unused in the initial VFN configuration. (b) Nominal KPIC observation mode for direct exoplanet spectroscopy with the apodizer in the pupil and the planet aligned to the fiber. (c) KPIC VFN mode with the vortex mask in the pupil and the star aligned to the fiber.

primarily by the tracking camera which images the PSF just before the final focusing optics, but further feedback can also be obtained at a slower cadence using the slit-viewing camera of NIRSPEC.

Thus, the VFN mode (Fig. 5.1(c)) is slightly different from the direct exoplanet spectroscopy mode of KPIC (Fig. 5.1(b)), which a) uses an optional apodizer instead of a vortex and b) aligns the planet with the fiber. The direct spectroscopy mode is better suited for characterization of known exoplanets at larger separations from their host-stars ($> \lambda/D$), while the VFN mode is better for blind or targeted search campaigns and characterization of close-in companions ($\sim \lambda/D$).

In order to enable the VFN mode, a charge 2 $K$ band vector vortex mask will be installed in the pupil stage alongside the apodizer, as shown in Fig. 5.2(a). Pezzato et al. (2019) describe this module and the custom-designed apodization mask it carries in detail. A charge 2 vortex mask was chosen for VFN based on the predicted and early on-sky performance of KPIC. Although a charge 1 vortex yields higher planet throughput at smaller angular separations, which can significantly decrease

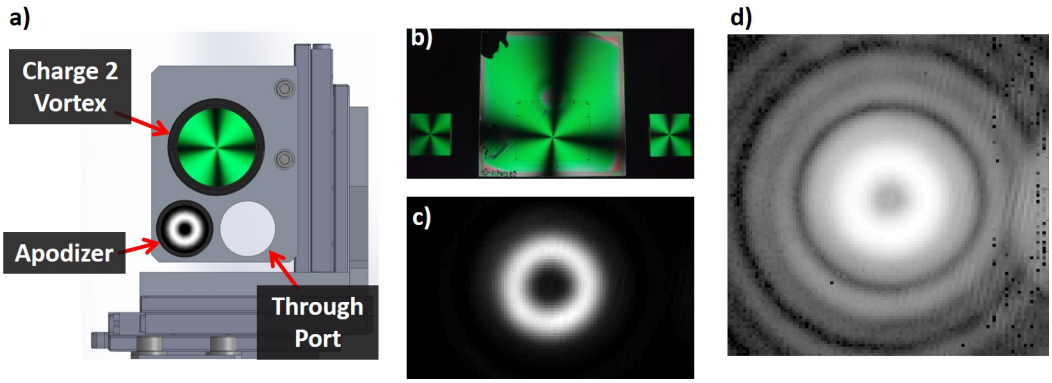


Figure 5.2: (a) Model of the pupil mask stage for KPIC. (b) Charge 2 $K$-band vector vortex masks being considered for deployment in KPIC as viewed in cross-polarization. (c) The PSF produced by the vortex masks in (b) when placed in a pupil plane, which takes on the expected donut shape. (d) Same as (c), but on a logarithmic scale.

the integration time needed to observe an exoplanet, this improved planet sensitivity comes at the cost of increased sensitivity to tip-tilt errors. For example, to achieve a null depth of $\eta_s = 10^{-4}$, a charge 1 VFN system requires less than 0.01 $\lambda/D$ RMS tip-tilt jitter whereas a charge 2 needs 0.1 $\lambda/D$ for a similar null depth (Ruane, Echeverri, et al., 2019). While a charge 2 vortex has reduced planet coupling, it relaxes tip-tilt requirements, which will be useful during the early stages of VFN development. As more on-sky measurements of the AO performance are made, we will reconsider whether a charge 1 or 2 vortex is optimal for the current performance.

We chose to start with $K$ band (2.2 $\mu m$) operation first for similar reasons; the wavefront errors scale with wavelength. Nevertheless, we have considered the possibility of including $H$ band (1.65 $\mu m$) or $J$ band (1.25 $\mu m$) operation in the future and have left a clear path to implementing this capability if the AO performance allows for it. Longer wavelengths are also possible, but the performance may be limited by thermal background.

Given these design considerations, we have started testing charge 2 $K$ band vortex masks in the lab (see Fig. 5.2(b)). We measured the transmission of these masks at 2 $\mu$m to be $> 99\%$. We also put these vortex masks in the pupil plane of a simple optical system to image their PSF. The resulting PSFs (Fig. 5.2(c-d)) show the expected donut pattern. We plan to further validate these masks with polychromatic coupling measurements on the upgraded VFN testbed, as well as in the KPIC instrument prior to deployment (see Sec. 5.7).

## 5.3 Predicted On-Sky VFN Performance

To predict the performance of the KPIC VFN mode, we have started simulating the system assuming wavefront errors based on PyWFS measurements made during KPIC on-sky engineering runs. The PyWFS provides the residual wavefront error sampled at 1 kHz. Although the PyWFS beam path has optics that are non-common with the VFN beam path, we assume that the measurements represent the wavefront just before the vortex mask. In practice, image sharpening routines will be run on the tracking camera during the daytime before any KPIC observation run to minimize the non-common path aberrations. The PyWFS also provides the residual tip-tilt error at 1 kHz which we feed into the simulator as well. For now, these simulations assume that the TTM is not being used for fast control so we apply the tip-tilt residuals from the PyWFS directly. Additionally, the simulator also includes the predicted residual atmospheric dispersion left over by a future ADC.

For this paper, we used PyWFS data obtained on June 17$^{\text{th}}$, 2019 during an on-sky engineering run. Figure 5.3 shows the residual wavefront errors measured by the PyWFS. Figure 5.3(a) is a sample of the wavefront residuals while Fig. 5.3(b) has the tip-tilt residuals in milliarcseconds (mas) for the full 60 seconds of data at 1 kHz. The average seeing that night was about 0.6 arcseconds. The average RMS wavefront residuals in the minute-long sample were 150 nm while the tip and tilt residuals were 2.6 and 2.5 mas RMS respectively. [2] The spatial wavefront sampling shown in Fig. 5.3(a) is sufficient for simulating the VFN performance since VFN is fairly insensitive to high-frequency aberrations (Ruane, Wang, et al., 2018).

In the simulator, we decompose the real wavefront data into Zernike coefficients and then reconstruct the wavefront as projected onto the real Keck pupil. Figure 5.4 shows the final frame, or time-step, of the simulator for a charge 2 (Fig. 5.4(a)) and charge 1, (Fig. 5.4(b)) VFN case. As such, the reconstructed wavefront at this final time step is shown in the upper left plots. We then add in the tip-tilt residuals from Fig. 5.3(b) at the given time sample as well as the predicted chromatic dispersion left over from the ADC to get the net pupil phase as a function of wavelength. We apply the vortex phase assuming an ideal, achromatic charge 1 or charge 2 vortex mask and calculate the resulting PSF at five sample wavelengths across the band. The upper middle plot of Figs. 5.4(a,b) shows the broadband PSF, which would be imaged on the tracking camera.

[2] See Sec. 5.4 which addresses the accuracy of the tip-tilt from the PyWFS for KPIC applications

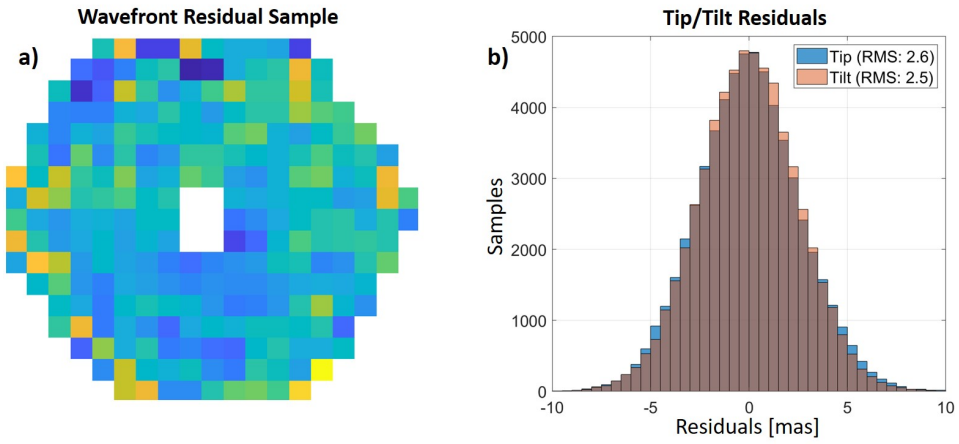


Figure 5.3: (a) Sample of the PyWFS wavefront residuals shown as projected onto the low-order facility DM. The average RMS wavefront residual over the 60 seconds of data was 150 nm. (b) tip-tilt residuals as reported by the PyWFS. The RMS tip and tilt residuals for the 1 minute sample are 2.6 and 2.5 mas respectively.

To get the coupling efficiencies across the band, we compute the overlap integral (Eq. 2.8) for every point in the field at each sample wavelength. The resulting two-dimensional (2D) coupling map is shown in the upper right plot of Figs. 5.4(a,b) for the central operating wavelength of 2.2 $\mu$m. We calculate the predicted planet coupling, $\eta_p$, as the average for all points between 0.8-1.0 $\lambda/D$ for the charge 1 case and 1.3-1.5 $\lambda/D$ for charge 2 to account for uncertainties in the planet location. The region used in this average is shown between the two red circles superimposed on the 2D coupling map and encompasses the separation at which the theoretical peak coupling occurs for each vortex charge. The resulting planet coupling, plotted against time, is shown in the lower left plot of Figs. 5.4(a,b). The time-averaged planet coupling is shown at the bottom left of this plot. Under these assumptions, we find that the predicted time-averaged planet coupling is 8% for a charge 2 vortex and just over 14% for charge 1.

In order to compute the star coupling, $\eta_s$, we must choose where to place the SMF in our simulations. Due to the tip-tilt residuals, the PSF moves around with respect to the SMF much faster than we can track and compensate-for with the current TTM control loop. This means that taking the null point in the coupling map at each frame would be an unfair representation of the actual on-sky performance since we would be assuming that we can align the PSF with the SMF core infinitely fast. We therefore take the average of all the coupling maps and find the optimal null location in this time-averaged map. We then place our simulated fiber at that location and

compute the coupling efficiency there at each time sample. This is representative of what we expect from a realistic TTM control loop which will tend to average out the tip-tilt residuals. The resulting star coupling is shown in the lower middle plot of Figs. 5.4(a,b). The time-averaged null depth is reported in the upper left corner of this plot. Given the wavefront residuals used in this simulation as well as the predicted ADC and tip-tilt residuals, we get an average null depth of 0.6% ($6\times10^{-3}$) for the charge 2 case and 1.3% ($1.3\times10^{-2}$) for charge 1. The final, lower right, plot in Figs. 5.4(a,b) shows the instantaneous coupling efficiency for the star and planet at each of the 5 sample wavelengths across our *K* band simulation. This assumes a flat source spectrum for both the star and planet.

Thus, Fig. 5.4(a) represents the predicted performance for the planned KPIC Charge 2 VFN mode while Fig. 5.4(b) shows a possible charge 1 case for comparison. As expected, the planet coupling at the peak planet location increases, to 14%, with the charge 1 vortex mask but the null depth also degrades to 1.3%. The tradeoff is whether the degradation in null depth is worth the access to closer companions.

The images shown in Fig. 5.4 are stills of the final frame in the simulation. The video versions of these figures, showing the instantaneous wavefront, PSF, and coupling, are available from CaltechDATA server at `https://doi.org/10.22002/c7w1j-je834` and `https://doi.org/10.22002/9nwep-9rz27`.

The results of these simulations indicate that the current PyWFS performance is sufficient for obtaining $< 10^{-2}$ nulls while coupling 8% of the planet light with a charge 2 vortex as planned. We can expect that this performance will improve further once the high-order DM is integrated into the KPIC system. However, these simulations are preliminary and there are other effects that may impact the VFN performance including realistic polarization aberrations, on-sky ADC residuals, and non-common path aberrations. We are also working towards simulating the characterization capabilities of the KPIC VFN mode by injecting simulated planet atmospheric spectra, accounting for the planet-star contrast ratios, applying the throughput losses in the rest of the system, and attempting to extract molecules from the resulting signal (Wang et al., 2017).[3]

[3]Update: These simulations were presented in Echeverri, Ruane, Jovanovic, Delorme, et al. (2021).

(a) Charge 2 VFN case as currently planned for KPIC

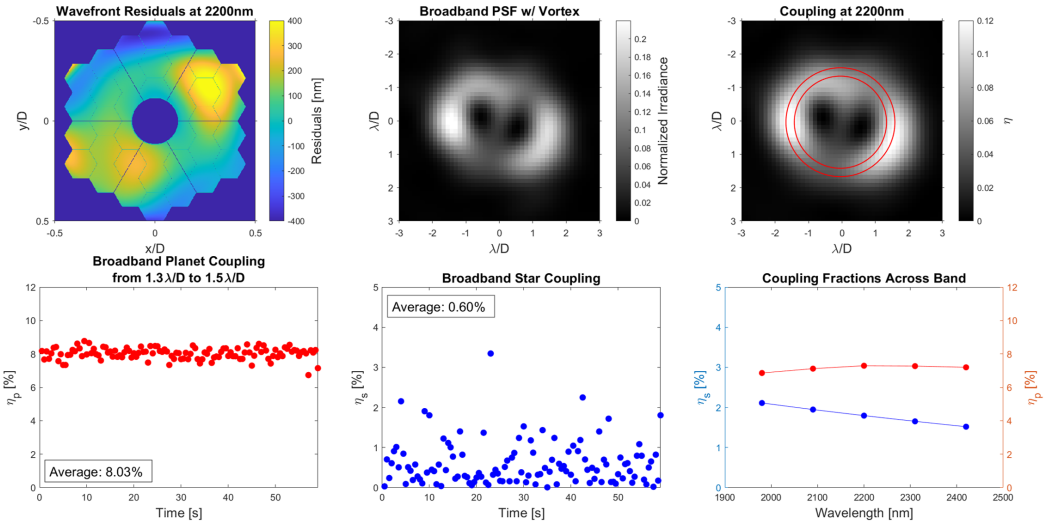


(b) Potential charge 1 KPIC VFN case

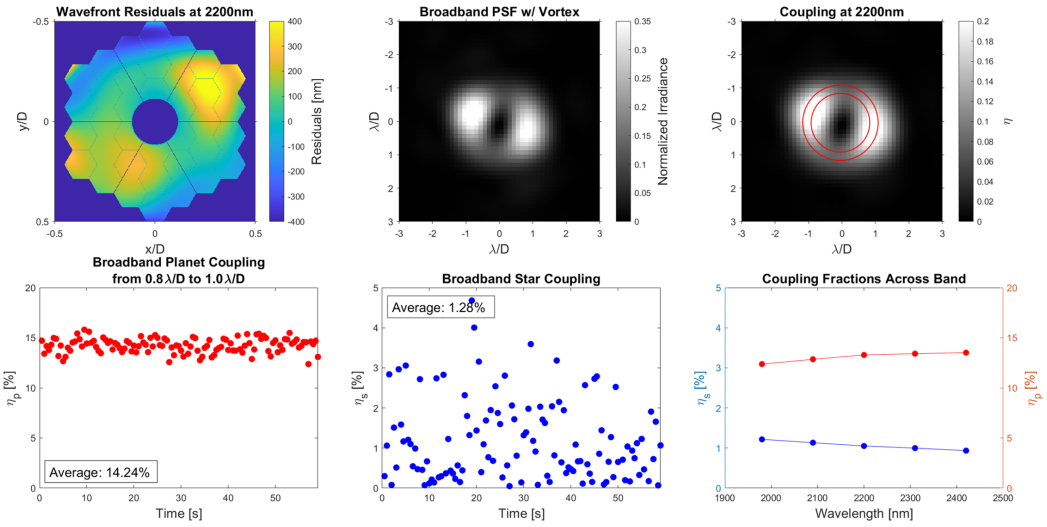


Figure 5.4: KPIC VFN performance simulations given the on-sky performance of the PyWFS as well as the predicted ADC residuals with an ideal vortex mask of (a) charge 2 and (b) charge 1. The upper left plot in each is the reconstructed PyWFS residuals. The upper middle plot is the system PSF while the upper right is the corresponding coupling efficiency for all points within a $6\times6\,\lambda/D$ field of view. The lower left plot shows the average coupling for a planet within the region bound by the two red circles in the coupling map. The lower middle plot is the star coupling. The lower right plot is the planet and star coupling at each of the 5 sample wavelengths across the *K* band. Note that these are stills of the last frame in the corresponding videos, so the top rows and and bottom right plots are for the last time sample only. The videos are available at `https://doi.org/10.22002/c7w1j-je834` and `https://doi.org/10.22002/9nwep-9rz27`

*Supplemental Work*

## 5.4 Comment on Tip-Tilt Magnitude

Figure 5.3 shows that the tip-tilt residuals reported by the PyWFS were around 2.5 mas RMS per axis. In a later paper (Sec. 6.4), the jitter residuals were reported at around 6-7 mas RMS as measured on the KPIC tracking camera (Echeverri, Xuan, et al., 2023). The discrepancy between the two values points to the PyWFS under-reporting the tip-tilt experienced by KPIC. This could be due to a differential jitter between the PyWFS plate and the KPIC plate, a source of jitter downstream of the pickoff, or simply that the PyWFS is not decomposing the jitter term fully from the other terms in its reconstructor. Regardless, for KPIC modeling and simulations, we trust the residuals measured on the tracking camera more than those measured by the PyWFS since the tracking camera sits at a focal plane immediately before the SMF in KPIC such that the jitter should be much closer to what the SMF experiences. Sections 6.4 and 8.4 provide more information on the tip-tilt measurements with the tracking camera and the control used to mitigate them.

## 5.5 Effect of On-Sky Wavefront Residuals

Section 5.3 presented predictions made in 2019 of the KPIC VFN performance based on simulations using the measured on-sky wavefront residuals from the PyWFS. Shortly after, I extended these simulations to predict the null depth given an RMS wavefront residual value. I started with the same on-sky June 17, 2019 data and decomposed the wavefronts in each time sample into Zernike polynomials projected onto the Keck aperture. The polynomials were then used to reconstruct the wavefront at higher resolution, the vortex phase was applied, and the corresponding PSF at each time step was computed. This process is identical to the process for the prior simulations, except that no tip-tilt errors or ADC residuals were applied. Without tip-tilt errors, the PSF is assumed to be centered at the same location in all samples so the overlap is computed only on-axis to determine the corresponding null. The RMS wavefront error on the reconstructed pupil was computed for each time sample and then averaged over the full set, as was the null, to determine the performance for a given magnitude of wavefront residuals. This process was repeated with a uniform multiplicative factor on all the Zernike polymials for the reconstruction, to scale the wavefront residuals assuming a fixed relative power density across the Zernikes.

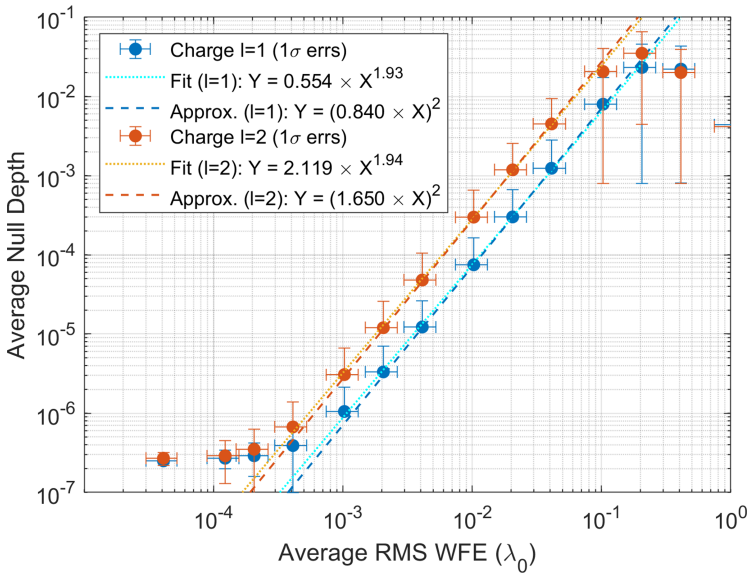


Figure 5.5: Approximate relationship between on-sky RMS wavefront residuals and the corresponding null depth for VFN with charge 1 (blue) and charge 2 (orange). Wavefront residuals measured on-sky from the PyWFS on June 17, 2019 are used. A power law fit is done for each charge and the best-fit equations are shown in the legend. A fit is also done forcing a second-order power law, given expected quadratic dependence.

Figure 5.5 shows the resulting relationship, with charge 1 in orange and charge 2 in blue. The errors bars represent the $1\sigma$ point in the RMS wavefront error (WFE) and the resulting null depth for each case. A power law with a free term for the exponent was fit to the data and the best-fit result is shown in the dotted lines while the equations are shown in the figure legend. Both best-fit equations yield a power close to 2, which matches expectation nicely given the quadratic dependence on WFE presented in Sec. 2.6. We thus also fit a second-order power law with the coefficient included into the exponent to match the form $\eta_s = (b\omega)^2$; the best-fit equations for this are also included in the legend. Overall, charge 1 and charge 2 perform similarly well, with only a factor of 2 difference in the coefficient (i.e., a factor of 4 difference in resulting null). This factor of 2 might imply a bias towards higher astigmatism in the PyWFS residuals. It could also reflect the fact that charge 1 VFN is only sensitive on coma while charge 2 is sensitive to astigmatism primarily but also coma with a fourth-order dependence (Ruane, Echeverri, et al., 2019), such that the small starlight leakage from the extra coma dependence may be worsening the achievable null. Regardless, the contribution to starlight leakage from wavefront error for both charge 1 and 2 result can reach down to $\lesssim 10^{-2}$ for 0.05 waves (~100 nm) RMS of

WFE. Note that Fig. 5.5 only provides the null depth contribution from wavefront error, whereas the nulls predicted in the simulations from Sec. 5.3 include tip-tilt and ADC residuals, leading to worse null depths for charge 1 in particular since it is more sensitive to pointing errors.

These results should be applied with careful consideration and reservation since they are only an approximation with many caveats. One caveat was already mentioned in Sec. 5.3: the wavefront residuals provided by the PyWFS have around 20 samples across the pupil such that they only provide insight into the low-order aberrations. This is intimately related to the fitting error introduced by the Zernike decomposition. Earlier, the WFE from the June 2019 night was reported to have 150 nm RMS. That value was the RMS on the raw, low-spatial-resolution wavefronts. Taking the reconstructed wavefronts, the same data set shows ~90 nm RMS of WFE. A major part of the difference between these two values is likely due to the effective low-pass-filtering introduced in the decomposition, which serves to smooth the spatial samples. As mentioned before, this should have a relatively small effect on the VFN null, and hence the accuracy of the results here, since the null is primarily guided by low-order aberrations. The larger challenge is in correctly converting from the true RMS value to the relevant RMS value as set by this analysis. A rough scaling factor of 90/150 (~0.6) can be used to convert between the two, based on this dataset.

Another, possibly significant, caveat is the implicit assumption on the power spectral density (PSD) of the wavefront aberrations. This analysis uses PyWFS data from a single night and the WFE is purposely scaled in a way that keeps the PSD constant. If the PSD changes significantly across nights or based on observing conditions, then the results could change, especially if the power in the coma and astigmatism terms changes significantly. There is a source of assurance towards this end though. We also have PyWFS telemetry from a separate night more than a year later (November 1, 2020), which I reduced in the same way though without rescaling the Zernike polynomials to generate the full curve. This data point gives a "true" RMS WFE (i.e., on the raw data) of 85 nm and a reconstructed RMS WFE of 65 nm, such that this night showed better on-sky PyWFS performance. The predicted null depth from the simulation is $2.9\times10^{-3}$; this is in very nice agreement with the best-fit curve from the 2019 data which predicts $2.4\times10^{-3}$ given the 0.3 waves RMS WFE. The assumption on the PSD may have larger implications when the KPIC PyWFS is not used. It is unclear how much the PSD may change, and hence how much the resulting null contribution may differ, when the Keck facility Shack-Hartmann wavefront sensor

(SHWFS) is used or if these best-fit values are assumed for wavefront sensors at other facilities.

The uncertainties on the accuracy of the analysis kept this RMS WFE to null approximation out of publications. Nevertheless, it provides a rough idea of the magnitude of the effect and is a decent reference for comparing the null contribution from on-sky WFE versus other terms. The quadratic dependence still holds, as it is an intrinsic property arising from the null's dependence on WFE (see Sec. 2.6). Thus, it can be used for approximating the relative improvement of the null given a known relative improvement on the wavefront error, as is done in Sec. 6.7. This analysis begets further work to estimate the null given on-sky wavefront residuals. Future work could use approximations of the PSD from general expectations of AO performance. It could also obtain wavefront residual measurements from the Keck SHWFS or from the PyWFS at higher spatial resolution, or from the AO system of another telescope to model different scenarios.

## 5.6 Preliminary KPIC Vortex Characterization

At the end of Sec. 5.2, we presented PSF images of the $K$ band vortex masks designated for use in the KPIC VFN mode along with a throughput >99% for the masks with 2 $\mu$m laser light. Those results have since been supplemented with additional characterization prior to deployment at the Telescope. This section presents a preliminary manual characterization using the testbed presented in Calvin et al. (2021) (see Sec. 3.1 therein). The text and figure for this section are derived directly from Sec. 5 of Echeverri, Ruane, Calvin, et al. (2020).

The optical vortex planned for KPIC VFN has been bonded to its mask holder and has been mounted in the KPIC "coronagraph" stage as shown in Fig. 5.6(a,b). There is currently a near-to-mid infrared testbed in the ET Lab that is used for testing other elements of the KPIC instrument prior to deployment. This bench is relatively simple but it provides a readily-accessible pupil plane where optics can be validated. We used this bench to do some preliminary measurements of the vortex performance.

The vortex PSF was already imaged on this bench and those results were shown Echeverri, Ruane, Jovanovic, Hayama, et al. (2019). For these new results, we added a Keck-like pupil mask to simulate the hexagonal shape, central obstruction, and spiders present on the Keck aperture. With this mask in place, we retook the images of the vortex PSF. The left plot in Fig. 5.6(c) shows the experimental PSF

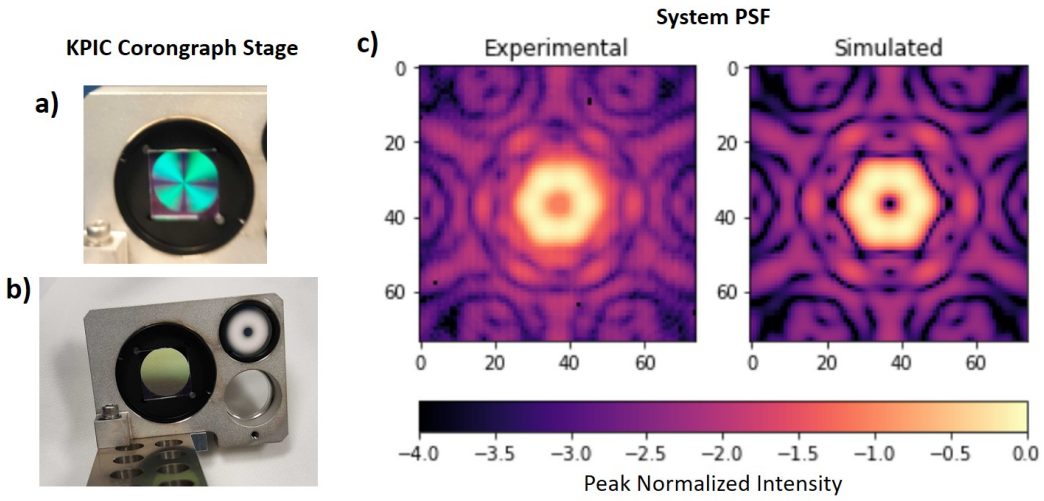


Figure 5.6: (a) K-band charge 2 vortex glued into its mask holder and seen through crossed polarizers to show the vortex pattern. (b) KPIC "coronagraph" stage with the apodizer and vortex masks. (c) Experimental vs. simulated PSF for the Keck aperture with the charge 2 vortex mask in the beam.

while the right plot shows the expected PSF based on simulations. There is a close visual agreement between the two, but we can quantify the similarity by computing the overlap integral between the two images. This computation reveals that the experimental PSF is a 98.6% match to the simulation.

We then measured the coupling efficiency at the null point as well as at the peak planet location. This system is not ideal for fiber coupling experiments since there is no way way to scan the fiber but there is a flat fold mirror that can be used to move the PSF over the fiber tip. Though the mirror is not at a true pupil plane, it is close enough for a quick and dirty measurement of the coupling. The null point, and hence star coupling, was measured to be just under 1% while the peak coupling was measured at just over 8%. The 8% is relatively close to the theoretical maximum of 11% for a charge 2 vortex on a Keck-like aperture. It is possible that the loss of 3% is due to a slight defocus introduced by the vortex mask that cannot be easily fixed with the lack of actuators on this bench. It could also be due to the fact that the 8% measurement was made by simply tilting the mirror linearly outward from the null in a single direction to scan the coupling line profile. Since the VFN coupling map on the Keck aperture is not axially symmetric, it is possible that this line scan passed through one of the regions with slightly lower coupling. The 1% null depth is much worse than we would expect from a VFN system with such low wavefront error but given the limitations of this bench and the fact that there is no way to scan the fiber

or vortex to optimize the alignment, it is likely that there is room for improvement on the polycrhomatic reflective testbed (PoRT - Sec. 4.3). We believe that once these tests are repeated on PoRT, which is designed for coupling measurements and optimization, we will achieve deeper null depths on the order of what we have demonstrated in visible wavelengths already.

## 5.7 KPIC VFN Laboratory Integration

The previous section presented a preliminary characterization of the KPIC VFN vortex masks. Those tests used a temporary testbed, and the coupling maps were measured by manually scanning the PSF over the bundle. We planned to perform subsequent tests using PoRT but, due to the COVID-19 pandemic and other delays, PoRT was not built in time. This section thus presents a more detailed characterization from 2022, this time using the actual KPIC instrument plate as built and tested in the laboratory prior to deployment to the telescope. These results have not previously been published.

KPIC was designed as a phased upgrade to the Keck facility AO system. Phase I was commissioned in 2018 and brought the core modules for coupling light into an SMF. Phase II brought several upgrades, including the VFN mode. To accomplish the swap from Phase I to II, each phase had its own version of the plate that holds the fiber injection unit (FIU). This allowed us to pull the full FIU for Phase I out of the Keck AO bench and easily swap it for the Phase II plate when the time came. For more details on the Phase II design and its deployment, refer to Echeverri, Jovanovic, et al. (2022) as well as Echeverri, Xuan, et al. (2023), which further details the KPIC VFN design within the the plate, and is reproduced in this thesis starting in Sec. 6.1. Since we have spares of most modules from the Phase I plate, this duplicate-plate design also allowed us to test the Phase II instrument in the laboratory with all elements installed before shipping it to the telescope.

Though we had spares for all elements in the FIU, we did not have a replica in the laboratory of the back end of the instrument. This meant we had to make a replacement fiber extraction unit (FEU) and had to find an alternative detector to NIRSPEC for our measurements. We did this by re-imaging the output of the SMF onto a near-infrared power meter (PM - Thorlabs PM100D, S148C) to create a temporary FEU. For coupling efficiency measurements, we also need to measure the power incident on the fiber tip to determine the normalization, as was done for the laboratory experiments in Chapter 4. Luckily, Phase II has the SMF and the lens

that couples light into the SMF on a translating stage, referred to as the multiport (see Echeverri, Jovanovic, et al., 2022, for details). This allowed us to move those elements out of the beam completely and measure the power immediately before the final coupling lens in the laboratory. To account for the transmission losses through the coupling lens, we used a spare replica, with the same anti-reflection coating and glass substrate, to image the incoming light onto the PM. Thus, the only remaining terms left to account for in our normalization were the Fresnel losses and transmission losses from the SMF itself. These were carefully measured with a separate setup and determined to be 95%. With that, we had everything we needed to perform properly-calibrated coupling efficiency scans with the Phase II plate in the laboratory. Note that with the instrument deployed at the telescope, this normalization measurement is no longer possible since the inclusion of this PM and the ability to insert it around the multiport was a temporary modification made only for the laboratory testing.

When operating off-sky (i.e., using internal light sources), the KPIC aperture is circular, while on-sky (i.e., pointing at a star) it is defined by the Keck primary and has Keck's characteristic hexagonal shape with a secondary obscurration and struts to support it. We replicated the Keck aperture using a pupil mask with the scale dimensions of the secondary and with oversized struts; the struts were oversized since at-scale they would be impractically narrow (10 $\mu$m wide). This mask can be placed adjacent to the vortex mask in the pupil stage, allowing us to test KPIC VFN with a circular aperture or the operational Keck aperture. We also obtained a charge 1 vector vortex mask designed for $K$ band. This mask was an engineering-grade sample to validate manufacturing capabilities, so it had high zero-order leakage that ultimately affected the achievable null and prevented us from deploying it to the instrument. Nevertheless, between the two aperture masks and two vortex masks, we were able to test four scenarios for the KPIC VFN mode: charge 1 and 2 with the Keck aperture as well as charge 1 and 2 with the circular aperture.

The procedure for the tests was as follows. An SMF was connected to a 2 $\mu$m laser (Thorlabs LFL2000) and the output of that fiber was placed in the input focal plane for KPIC to act as the source. The fiber alignment mirror (FAM) in KPIC, which sits in a pupil plane, was used to steer the beam over the SMF. We scanned the PSF in two-dimensional (2D) square grids spanning 2.5 $\lambda/D$. At each point in the scan, the power transmitted through the fiber was measured on the power meter (PM). At the end of each scan, the multiport was moved so that the power incident on the fiber

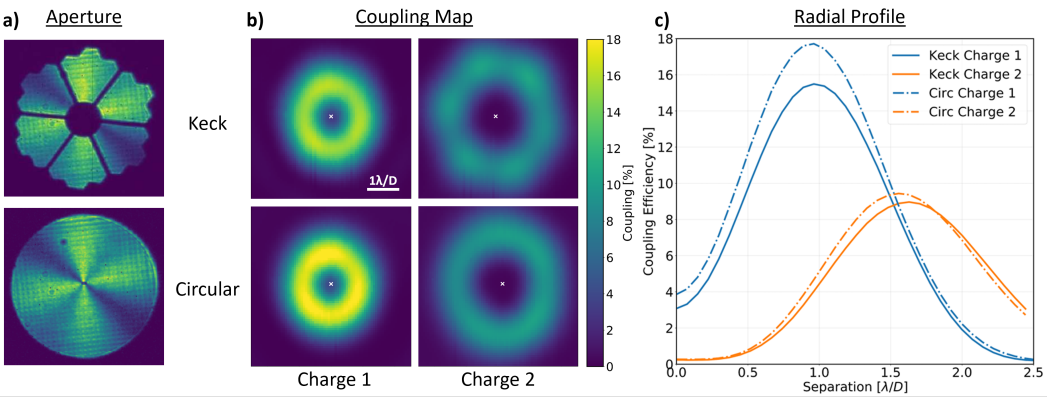


Figure 5.7: Laboratory validation of the KPIC VFN mode prior to deployment. All data taken with a 2 $\mu$m laser source. (a) Pupil images from the KPIC tracking camera with the charge 2 vortex mask. Top image has the replica Keck aperture mask and bottom has a 12 mm diameter circular iris. A single linear polarization from the Wollaston prism is shown, revealing the azimuthal variation as in Fig. 5.6. (b) Coupling maps of 2.5×2.5 $\lambda/D$ region, measured on a power meter at the output of the SMF and normalized by the power at the input of the SMF. Top row is for the Keck aperture while bottom row is for the circular aperture. Left column is charge 1, right column is charge 2. All maps shown on the same colorscale. (c) Radial profile of the coupling maps. Calculated as the azimuthal average centered on the white crosshair in each map.

could be sampled with the same PM, then the beam was blocked and a background measurement was taken. The background was subtracted from the transmitted and incident power measurements. The transmitted power was then divided by 0.95 to account for the fiber losses, and finally the incident power value was divided from the scan data to provide the coupling efficiency ($\eta$, Eq. 2.8). For each test, the desired aperture mask and vortex mask were mounted onto the pupil stage. The DM was used to empirically tune the wavefront by scanning through amplitudes of Zernike aberrations and repeating the 2D coupling maps to optimize for the best null and simultaneous peak off-axis coupling efficiency.

Figure 5.7(a) shows pupil images from the KPIC tracking camera with the Keck (top) and circular (bottom) aperture masks on the charge 2 vortex. The azimuthal variation in intensity is due to the fact that the KPIC pupil-viewing mode has a Wollaston prism that splits the light into linear polarization states. As explained by Mawet, Serabyn, et al. (2010), when the light from a charge 2 vector vortex mask is decomposed into linear states, the resulting intensity pattern has a characteristic X-shape. This can be seen in our pupil images here as well as in Fig. 5.2(b) and

Table 5.1: Null and peak coupling of the KPIC VFN mode in the laboratory.

| Aperture | Charge | Null | Peak |
|---|---|---|---|
| Keck | 1 | $3.1 \times 10^{-2}$ | 15.5% |
| | 2 | $2.4 \times 10^{-3}$ | 9.0% |
| Circular | 1 | $3.9 \times 10^{-2}$ | 17.7% |
| | 2 | $2.7 \times 10^{-3}$ | 9.4% |

Fig. 5.6(a).

The best 2D coupling maps are shown in Fig. 5.7(b). The top row shows the maps for the Keck aperture while the bottom row has the circular aperture results. The left column is for charge 1 and the right is for charge 2. The color axis for all the maps has been set to range from 0 to 18% so that the visual intensity between maps encodes the relative coupling efficiency. As expected, we see that the charge 1 results in a brighter and smaller pair of coupling maps than charge 2, indicating that charge 1 achieves higher coupling efficiency and accesses smaller separations. The charge 2 case with the Keck mask clearly shows a six-lobed pattern, characteristic of the six-sided Keck aperture.

We assessed the off-axis coupling efficiency by taking the azimuthal average of each map to generate a radial profile. The center point, around which the profile was computed is denoted by the white crosshair, and was determined as the point that yielded the highest peak off-axis coupling. For the charge 1 scans, this center point coincided with the deepest on-axis null point. For the charge 2 scans, the center point was slightly offset from the point with the deepest rejection, but the resulting difference in null depth between the "true" on-axis null and the center point for the radial scan was an order of magnitude smaller than the null values. The radial profiles are shown in Fig. 5.7(c), with the solid curves denoting the Keck aperture and the dot-dashed curves denoting the circular aperture. The blue curves denote charge 1 cases and the orange curves denote charge 2. The two charge 1 cases achieve a peak coupling 15.5% and 17.7% at just under 1 $\lambda/D$. Meanwhile, the charge 2 cases achieve 9.0% and 9.4% just beyond $1.5\lambda/D$, with the circular aperture peaking at a slightly smaller separation than the Keck aperture, as expected (Ruane, Echeverri, et al., 2019). The charge 2 measurements resulted in null depths $< 3 \times 10^{-3}$, while charge 1 yielded nulls between 3 and $4 \times 10^{-2}$. Table 5.1 lists the peak coupling values along with the null depth at the white crosshair for each case.

The measured performance for the charge 2 mask matches nicely with expectation given the properties of the mask. Assuming that the wavefront in the system was successfully optimized by the Zernike scans for these tests, and that the tip-tilt jitter was negligible in the laboratory environment, then the null values reported here are dominated by the zero-order leakage in the vortex. These masks were designed and characterized by Mawet, Serabyn, et al. (2010). They report that the expected attenuation, based on the standard deviation of the retardance, was $\sim 5 \times 10^{-3}$ in the 15% bandwidth of the $K_s$ filter centered at 2.15 $\mu$m. This means that for VFN, we can expect the null floor from that zero-order leakage term to be just over $3 \times 10^{-3}$ on the Keck aperture and just under $4 \times 10^{-3}$ for the circular aperture. This is based on the fact that the resulting Airy PSF of the leakage will couple into the SMF with ~65% efficiency on the Keck aperture and with ~80% on the circular aperture (see Eq. 2.28 in Sec. 2.6 for more details). Our measured null values are very close to these expected values.

The charge 1 vortex mask performed an order of magnitude worse than the charge 2 mask, which was also expected since the zero-order leakage on the engineering-grade charge 1 mask is significantly higher. The vendor measured the transmittance of the optic through circular polarizers to provide a direct measure of the leakage term. At 2 $\mu$m, the leakage is about $8 \times 10^{-2}$, which leads to an expected VFN null of 5 and $6.5 \times 10^{-2}$ for the two apertures. Our demonstrated nulls are slightly better though still close to these values.

The nominal KPIC VFN mode deployed to the telescope is the charge 2 vortex with a Keck aperture when on-sky. As such, the contribution from the zero-order leakage to the on-sky null for the instrument at 2 $\mu$m is $2.4 \times 10^{-3}$. This means that the on-sky null will likely be limited by other leakage terms such as the residual atmospheric wavefront aberrations. Since the charge 2 vortex mask has a central operating wavelength of 2.225 $\mu$m (Mawet, Serabyn, et al., 2010), the zero-order contribution will be slightly lower towards the center of the science band.

## References

Bond, C. Z. et al. (2018). "Adaptive optics with an infrared pyramid wavefront sensor". In: *Proc. SPIE* 10703. DOI: 10.1117/12.2314121. URL: https://doi.org/10.1117/12.2314121.

Bracewell, R. N. (1978). "Detecting nonsolar planets by spinning infrared interferometer". In: *Nature* 274, p. 780. DOI: 10.1038/274780a0.

Calvin, B. et al. (Feb. 2021). "Enhancing Direct Exoplanet Spectroscopy with Apodizing and Beam Shaping Optics". In: *Publications of the Astronomical Society of the Pacific* 133.1020, 024503, p. 024503. DOI: 10.1088/1538-3873/abdace. arXiv: 2102.11499 [astro-ph.IM].

Echeverri, D., N. Jovanovic, et al. (Aug. 2022). "Phase II of the Keck Planet Imager and characterizer: system-level laboratory characterization and preliminary on-sky commissioning". In: *Ground-based and Airborne Instrumentation for Astronomy IX*. Ed. by C. J. Evans, J. J. Bryant, and K. Motohara. Vol. 12184. Society of Photo-Optical Instrumentation Engineers (SPIE) Conference Series, 121841W, 121841W. DOI: 10.1117/12.2630518. arXiv: 2210.15915 [astro-ph.EP].

Echeverri, D., G. Ruane, B. Calvin, et al. (Dec. 2020). "Detecting and characterizing close-in exoplanets with vortex fiber nulling". In: *Optical and Infrared Interferometry and Imaging VII*. Ed. by P. G. Tuthill, A. Mérand, and S. Sallum. Vol. 11446. Society of Photo-Optical Instrumentation Engineers (SPIE) Conference Series, 1144619, p. 1144619. DOI: 10.1117/12.2563142. arXiv: 2012.04239 [astro-ph.IM].

Echeverri, D., G. Ruane, N. Jovanovic, J.-R. Delorme, et al. (Sept. 2021). "Broadband vortex fiber nulling: high-dispersion exoplanet science at the diffraction limit". In: *Techniques and Instrumentation for Detection of Exoplanets X*. Ed. by S. B. Shaklan and G. J. Ruane. Vol. 11823. Society of Photo-Optical Instrumentation Engineers (SPIE) Conference Series, 118230A, 118230A. DOI: 10.1117/12.2597160. arXiv: 2210.15910 [astro-ph.EP].

Echeverri, D., G. Ruane, N. Jovanovic, T. Hayama, et al. (Sept. 2019). "The vortex fiber nulling mode of the Keck Planet Imager and Characterizer (KPIC)". In: *Society of Photo-Optical Instrumentation Engineers (SPIE) Conference Series*. Vol. 11117. Society of Photo-Optical Instrumentation Engineers (SPIE) Conference Series, 111170V, p. 111170V. DOI: 10.1117/12.2528529. arXiv: 1909.03538 [astro-ph.IM].

Echeverri, D., G. Ruane, N. Jovanovic, D. Mawet, et al. (May 2019). "Vortex fiber nulling for exoplanet observations I. Experimental demonstration in monochromatic light". In: *Optics Letters* 44.9, p. 2204. DOI: 10.1364/OL.44.002204. arXiv: 1811.02083 [astro-ph.IM].

Echeverri, D., J. W. Xuan, et al. (July 2023). "Vortex fiber nulling for exoplanet observations: implementation and first light". In: *Journal of Astronomical Telescopes, Instruments, and Systems* 9, 035002, p. 035002. DOI: 10.1117/1.JATIS.9.3.035002. arXiv: 2309.06514 [astro-ph.IM]. URL: https://doi.org/10.1117/1.JATIS.9.3.035002.

Haguenauer, P. and E. Serabyn (Apr. 2006). "Deep nulling of laser light with a single-mode-fiber beam combiner". In: *Appl. Opt.* 45.12, pp. 2749–2754. DOI: 10.1364/AO.45.002749.

Jovanovic, N., C. Schwab, et al. (Aug. 2017). "Efficient injection from large telescopes into single-mode fibres: Enabling the era of ultra-precision astronomy". In: *Astronomy and Astrophysics* 604, A122, A122. DOI: 10.1051/0004-6361/201630351. arXiv: 1706.08821 [astro-ph.IM].

Jovanovic, N., D. Mawet, et al. (2019). "The Keck Planet Imager and Characterizer: demonstrating advanced exoplanet characterization techniques for future extremely large telescopes". In: *Proc. SPIE* 11117-31.

Martin, E. C. et al. (2018). "An overview of the NIRSPEC upgrade for the Keck II telescope". In: *Proc. SPIE* 10702, 107020A. DOI: 10.1117/12.2312266.

Mawet, D., J.-R. Delorme, et al. (2017). "A fiber injection unit for the Keck Planet Imager and Characterizer". In: *Proc. SPIE* 10400, p. 1040029. DOI: 10.1117/12.2274891. URL: http://dx.doi.org/10.1117/12.2274891.

Mawet, D., G. Ruane, et al. (2017). "Observing Exoplanets with High-dispersion Coronagraphy. II. Demonstration of an Active Single-mode Fiber Injection Unit". In: *Astrophys. J.* 838.2, p. 92. DOI: 10.3847/1538-4357/aa647f.

Mawet, D., E. Serabyn, et al. (Jan. 2010). "The Vector Vortex Coronagraph: Laboratory Results and First Light at Palomar Observatory". In: *The Astrophysical Journal* 709.1, pp. 53–57. DOI: 10.1088/0004-637X/709/1/53. arXiv: 0912.2287 [astro-ph.IM].

Mawet, D., P. Wizinowich, et al. (2016). "Keck Planet Imager and Characterizer: concept and phased implementation". In: *Proc. SPIE* 9909, p. 99090D. DOI: 10.1117/12.2233658.

Pezzato, J. et al. (Sept. 2019). "Status of the Keck Planet Imager and Characterizer phase II development". In: *Society of Photo-Optical Instrumentation Engineers (SPIE) Conference Series*. Vol. 11117. Society of Photo-Optical Instrumentation Engineers (SPIE) Conference Series, 111170U, 111170U. DOI: 10.1117/12.2529685. arXiv: 1909.06487 [astro-ph.IM].

Ruane, G., D. Echeverri, et al. (Sept. 2019). "Vortex fiber nulling for exoplanet observations: conceptual design, theoretical performance, and initial scientific yield predictions". In: *Society of Photo-Optical Instrumentation Engineers (SPIE) Conference Series*. Vol. 11117. Society of Photo-Optical Instrumentation Engineers (SPIE) Conference Series, 1111716, p. 1111716. DOI: 10.1117/12.2528555. arXiv: 1908.09780 [astro-ph.IM].

Ruane, G., J. Wang, et al. (Nov. 2018). "Efficient Spectroscopy of Exoplanets at Small Angular Separations with Vortex Fiber Nulling". In: *Astrophysical Journal* 867.2, 143, p. 143. DOI: 10.3847/1538-4357/aae262. arXiv: 1809.06483 [astro-ph.IM].

Serabyn, E. et al. (Oct. 2019). "Nulling at short wavelengths: theoretical performance constraints and a demonstration of faint companion detection inside the diffraction limit with a rotating-baseline interferometer". In: *Mon. Notices Royal Astron. Soc.*

489.1, pp. 1291–1303. DOI: 10.1093/mnras/stz2163. arXiv: 1908.05977 [astro-ph.IM].

Wang, J. et al. (Apr. 2017). "Observing Exoplanets with High Dispersion Coronagraphy. I. The Scientific Potential of Current and Next-generation Large Ground and Space Telescopes". In: *The Astronomical Journal* 153.4, 183, p. 183. DOI: 10.3847/1538-3881/aa6474. arXiv: 1703.00582 [astro-ph.EP].

Wizinowich, P. et al. (2000). "First Light Adaptive Optics Images from the Keck II Telescope: A New Era of High Angular Resolution Imagery". In: *Publications of the Astronomical Society of the Pacific* 112, pp. 315–319. DOI: 10.1086/316543.

*Chapter 6*

# KPIC VFN FIRST LIGHT

With the instrument built and characterized in the lab, the KPIC VFN mode was ready to deploy to the telescope. This was done in February 2022 and commissioning observations began shortly thereafter. This chapter covers the first light results from the KPIC VFN mode. The core of the chapter is a reproduction of Echeverri, Xuan, Jovanovic, Ruane, et al. (2023), where the KPIC VFN design was formally published in detail and the first technical results from the on-sky commissioning were presented. The paper included predictions of the detection sensitivity for the instrument, derived from measurements of the on- and off-axis throughput on-sky. I have further supplemented the results from that paper with additional simulations that compare the VFN mode against KPIC's nominal DS mode, to determine which mode is better for different observations.

---

## Vortex Fiber Nulling for Exoplanet Observations: Implementation and First Light

Echeverri, D. et al. (July 2023). "Vortex fiber nulling for exoplanet observations: implementation and first light". In: *Journal of Astronmical Telescopes, Instruments, and Systems* Vol. 9, 035002, p. 035002. DOI: 10.1117/1.JATIS.9.3.035002. arXiv: 2309.06514 [astro-ph.IM]. URL: https://doi.org/10.1117/1.JATIS.9.3.035002

### 6.1 Abstract

Vortex fiber nulling (VFN) is a single-aperture interferometric technique for detecting and characterizing exoplanets separated from their host star by less than a diffracted beam width. VFN uses a vortex mask and single mode fiber to selectively reject starlight while coupling off-axis planet light with a simple optical design that can be readily implemented on existing direct imaging instruments that can feed light to an optical fiber. With its axially symmetric coupling region peaking within the inner working angle of conventional coronagraphs, VFN is more efficient at

detecting new companions at small separations than conventional direct imaging, thereby increasing the yield of on-going exoplanet search campaigns. We deployed a VFN mode operating in K band (2.0−2.5 $\mu$m) on the Keck Planet Imager and Characterizer (KPIC) instrument at the Keck II Telescope. In this paper we present the instrument design of this first on-sky demonstration of VFN and the results from on-sky commissioning, including planet and star throughput measurements and predicted flux-ratio detection limits for close-in companions. The instrument performance is shown to be sufficient for detecting a companion $10^3$ times fainter than a $5^{\text{th}}$ magnitude host star in 1 hour at a separation of 50 mas ($1.1\lambda/D$). This makes the instrument capable of efficiently detecting substellar companions around young stars. We also discuss several routes for improvement that will reduce the required integration time for a detection by a factor >3.

## 6.2 Introduction

The National Academies' Astro2020 Decadal Review identified exoplanet science as a key frontier in the coming decade and specifically emphasized development in direct imaging (National Academies of Sciences, Engineering, and Medicine, 2021). Through high spectral resolution characterization of light from the exoplanet itself, direct imaging provides unique insight into exoplanet properties including atmospheric composition (Konopacky et al., 2013; Ruffio, Konopacky, et al., 2021; J. J. Wang, Ruffio, et al., 2021; J. Wang, Kolecki, et al., 2022; Xuan, J. Wang, et al., 2022; J. Wang, J. J. Wang, et al., 2023), spin (Snellen, Brandl, et al., 2014; Bryan et al., 2020; Xuan, Bryan, et al., 2020), planetary radial velocity (Ruffio, Horstman, et al., 2023; J. J. Wang, Ruffio, et al., 2021; Delorme et al., 2021), and cloud coverage (Crossfield et al., 2014). However, of the more than 5,400 confirmed exoplanets to date, less than 50 have been detected with direct imaging (Akeson et al., 2013). A major limitation to direct detection is that young, giant exoplanets amenable to direct imaging seem to be rarer than originally expected at wide separations ($\gtrsim$10 AU or correspondingly 0.1″ for stars within 100 parsec) (Bowler et al., 2018). This has led to a yield of only a few new planets in previous imaging surveys of hundreds of stars (Nielsen et al., 2019; Vigan et al., 2021). By combining Hipparcos (Perryman et al., 1997; van Leeuwen, 2007) and Gaia (Gaia Collaboration et al., 2018; Gaia Collaboration, 2021) astrometry to identify and target accelerating stars that show promise for harboring a substellar companion (Kervella et al., 2019; Brandt, 2021; De Rosa, Nielsen, Rameau, et al., 2019), the yield of recent direct imaging surveys has been improved (Currie et al., 2023; Kuzuhara et al., 2022; Franson et al., 2023;

De Rosa, Nielsen, Wahhaj, et al., 2023; Hinkley, Lacour, et al., 2023). Nevertheless, these campaigns use coronagraphs which are limited to separations $\gtrsim 3\lambda/D$ from the star ($\sim$13 AU at 100 parsec for $\lambda$=2.2 $\mu$m and $D$=10 m), where $\lambda$ is the wavelength and $D$ is the telescope diameter. Radial velocity (RV) surveys (Fulton et al., 2021; Rosenthal et al., 2021) suggest that the peak in the giant planet population is closer-in to the star than state-of-the-art AO imaging survey instruments can currently access (Macintosh et al., 2014; Beuzit et al., 2019), indicating that the yield can be further improved by unlocking access to these smaller separations.

Larger telescopes, such as the upcoming Extremely Large Telescopes (ELTs), will target smaller physical separations than their predecessors due to the scaling of $\lambda/D$ but they will still be limited in angular resolution by their coronagraphs. Additionally, observing in short wavelengths enables the detection of planets at smaller physical separations for the same scaling reason but accessing $\sim 1\lambda/D$ would allow those same planets to be further characterized, after detection, at longer wavelengths without disappearing behind the inner working angle of the coronagraph. Thus, new technologies are still needed to push to $\sim 1\lambda/D$ though few methods currently exist. Sparse aperture masking (SAM) has a long history working in this regime, and has even been deployed on the James Webb Space Telescope. Since SAM does not remove the starlight though, the demonstrated ground-based contrast is currently around 7 magnitudes ($1.6 \times 10^{-3}$) in L' band ($\sim 3.8\ \mu m$) at 80 mas ($1\lambda/D$ in L' on Keck) (Sallum et al., 2019; Hinkley, Carpenter, et al., 2011). Long-baseline multi-aperture interferometers such as the very successful VLTI-GRAVITY can also access this angular separation range (GRAVITY Collaboration et al., 2017); in 2023, the GRAVITY instrument demonstrated a detection of a companion at a contrast of $8.2 \times 10^{-5}$ with a separation of 86 mas (Hinkley, Lacour, et al., 2023). Dark hole digging with GRAVITY (Pourré et al., 2022) or long-baseline multi-aperture nullers such as the VLTI-Asgard/NOTT projects are also an option (Defrère, Hinz, et al., 2015; Defrère, Bigioli, et al., 2022). Nevertheless, GRAVITY, ASGARD/NOTT, and other such projects require complex and costly one-of-a-kind infrastructure and thus are not suitable for widespread implementation.

Vortex Fiber Nulling (VFN) is a single-aperture, interferometric technique that sidesteps many of these limitations and can provide access to planets between 0.5 and $2.0\lambda/D$, or less, in a full 360° region around a host star all at once. It builds on the heritage of previous fiber nulling techniques (Serabyn et al., 2019) which utilize the spatial and modal filtering properties of a single-mode fiber (SMF)

to simplify the optical design of classical nullers. When used in unison with conventional coronagraphs following up on Gaia-Hipparcos accelerators, VFN can improve the separation coverage and bridge the gap between direct imaging and RV and transit surveys (Echeverri, Ruane, Jovanovic, Delorme, et al., 2021; Ren et al., 2023). VFN also has direct application to the Habitable Worlds Observatory mission recommended by the Astro2020 Decadal Review. The stringent pointing and wavefront control requirements set by the mission's coronagraph instrument, which are on the order of tens of picometers (Gaudi et al., 2020; The LUVOIR Team, 2019), far exceed the requirements for VFN (Ruane, Echeverri, et al., 2019). This means that with very few modifications, a VFN mode on the telescope would open a new search area around targets and thereby increase the mission yield.

Initially proposed in 2018 (Ruane, J. Wang, et al., 2018) and demonstrated in the lab shortly thereafter (Echeverri, Ruane, Jovanovic, Mawet, et al., 2019; Echeverri, Ruane, Calvin, et al., 2020; Echeverri, Ruane, Jovanovic, Delorme, et al., 2021), VFN is now operating on-sky at the Keck II Telescope. This paper introduces the first VFN instrument and covers results from the on-sky commissioning phase. Section 6.3 briefly describes the VFN technique while Section 6.4 presents the optical design, requirements, and how the instrument operates. Section 6.5 reports the observations obtained from April 2022 to January 2023 to determine the on-sky measured star and planet throughput. Section 6.6 uses these throughput measurements to determine sensitivity and detection limits, showing that VFN is ready for science observations. Finally, Section 6.7 presents the next steps for improving the instrument performance.

## 6.3 The Vortex Fiber Nulling Concept

The VFN concept places an optical vortex mask upstream of an injection unit that couples light from a point-source into a single-mode fiber (Ruane, J. Wang, et al., 2018). The vortex imparts an azimuthal phase ramp of the form $\exp(il\theta)$, where $l$ is an integer known as the charge and $\theta$ is the azimuthal coordinate (Swartzlander, 2001; Swartzlander, 2009). Figure 6.1(a) shows the phase ramp for charge 1 and 2 vortex masks. In this paper, we assume the vortex is in a pupil plane as shown in Fig 6.1(b). However, it can also be placed in a focal plane with nearly identical performance. The pupil implementation has the benefit that the ideal F# for planet coupling with the vortex is the same as without the vortex. This design allows VFN to be added as a complementary mode to high-contrast imaging instruments with existing fiber injection units without changing the system F# (Ruane, Echeverri,

et al., 2019). The vortex phase propagates through the system to the SMF plane and is selectively filtered by the fiber. At the fiber plane, the fraction of light, $\eta(r)$, that couples into the fiber's axially symmetric fundamental mode, $\Psi(r)$, for an incident electric field, $E(r, \theta)$, is given by the overlap integral,

$$\eta(r) = \left| \int \Psi(r) E(r, \theta) dA \right|^2 , \tag{6.1}$$

where $r$ and $\theta$ are radial coordinates centered on the fiber and $E$ and $\Psi$ are normalized by their individual total power such that $\int |\Psi(r)|^2 \, dA = 1$ and $\int |E(r, \theta)|^2 \, dA = 1$. Thus $\eta$ provides the fraction of total light incident on the fiber plane that couples into the SMF. Due to the vortex phase, the electric field for a point source aligned to the fiber can be expressed in the form $E(r, \theta) = f(r) \exp(il\theta)$. The overlap integral is then separable and has an azimuthal term, $\int_0^{2\pi} \exp(il\theta) d\theta$, that computes to zero for non-zero integer values of $l$. This results in theoretically perfect rejection of on-axis light and this central region with zero coupling is thus referred to as the "null". For off-axis point sources, the vortex phase is not symmetric over the fiber mode, which results in a non-zero coupling efficiency at small angular separations from the optical axis. An exoplanet can thus be observed by aligning its host star onto the center of the SMF so that the star is rejected while the off-axis planet light couples in and is carried by the fiber to a detector.

The coupling efficiency for the exoplanet depends on its separation and the charge of the vortex, as shown in Fig. 6.1(c). Charge $l$=1, the solid blue line, has a peak of $\eta$~20% at 0.9 $\lambda/D$ and $l$=2, the dashed orange line, has $\eta$~10% at 1.4 $\lambda/D$. These values assume a circular unobstructed pupil but very similar performance, to within ±1%, is achieved on the apertures of most major telescopes (Ruane, Echeverri, et al., 2019). For reference without the vortex, the maximum coupling on a circular aperture is $\eta$~80% at 0 $\lambda/D$ (i.e., on-axis). A key benefit of VFN is that the coupling efficiency is axially symmetric and creates a ring, shown in the inset of Fig. 6.1(c), where light is transmitted through the fiber. This allows VFN to simultaneously search a complete annular region around a star all at once for new companions. Other SMF-based direct imaging instruments achieve higher throughput by observing without a vortex but they require a raster scan around the star or multiple fibers to cover the same area (Lovis et al., 2017).

VFN can theoretically achieve bandwidths of $\Delta\lambda/\lambda \gtrsim 50\%$ or more since the null is wavelength independent and the mode-field diameter (MFD) of SMFs, which sets the coupling efficiency, scales roughly with the diffraction in the focal plane. In

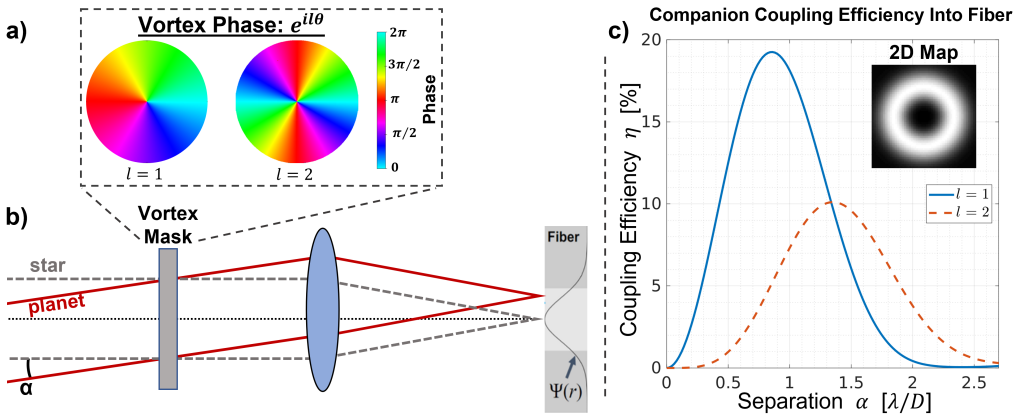


Figure 6.1: (a) Azimuthally varying phase pattern introduced by a charge $l = 1$ and charge $l = 2$ vortex mask. (b) Diagram of a VFN system with the vortex mask upstream of an SMF in the image plane. The star is aligned with the SMF such that the target planet lands at an off-axis angle, $\alpha$, with respect to the fundamental mode of the fiber, $\Psi(r)$. (c) Coupling efficiency, $\eta$, versus angular separation from the optical axis, $\alpha$, for a charge 1 (solid blue) and 2 (dashed orange) VFN system, assuming a circular aperture. The inset shows the coupling efficiency for all points in a field-of-view centered on the star/fiber, displaying the axial symmetry in the coupling profile.

practice, the bandwidth is limited by the chromaticity of the vortex mask and the transmission of the SMF; current technology can achieve bandwidths commensurate with astronomical bands of ~20%, dominated by leakage in vector vortex masks.

As with other nulling and coronagraphic techniques, VFN is sensitive to tip-tilt pointing errors and wavefront aberrations. However, the degree to which the null is affected depends on the vortex charge. The null for charge 1 follows a second-order power law for tip-tilt and coma aberrations while charge 2 is only second-order for astigmatism (Ruane, Echeverri, et al., 2019). All other aberrations either do not affect the null or have a fourth-order effect such that they are insignificant compared to tip, tilt, coma, and astigmatism (Ruane, Echeverri, et al., 2019). Aberrations also affect VFN's bright fringe, though the main effect for modest aberrations is to slightly distort the ring while leaving the average radial coupling peak relatively unaffected. Further implications of wavefront error (WFE) on observations and the achievable on-sky performance are covered in Secs. 6.6 and 6.7.

For more details on the underlying principles behind the VFN concept, we refer readers to the original VFN paper by Ruane, J. Wang, et al. (2018) and subsequent

works which flesh out the concept, design requirements, and related trades (Ruane, Echeverri, et al., 2019; Echeverri, Ruane, Jovanovic, Hayama, et al., 2019). VFN was demonstrated in the laboratory at visible wavelengths with monochromatic nulls (Echeverri, Ruane, Jovanovic, Mawet, et al., 2019; Echeverri, Ruane, Calvin, et al., 2020) of $\sim 5\times10^{-5}$ and polychromatic nulls of $<10^{-4}$ with a 15% bandwidth (Echeverri, Ruane, Jovanovic, Delorme, et al., 2021).

### 6.4 A VFN Mode for KPIC

Given the successful demonstration of VFN in the laboratory and the simplicity with which it can be implemented on existing SMF-fed instruments, we added a VFN demonstrator mode to the Keck Planet Imager and Characterizer (KPIC) instrument at the Keck II Telescope. KPIC is a bridge between the facility Adaptive Optics (AO) system (Wizinowich et al., 2000) and NIRSPEC (McLean, Becklin, et al., 1998; McLean, Graham, et al., 2000; Martin et al., 2018), the existing slit-based high-resolution infrared spectrograph at Keck Observatory. KPIC uses SMFs to spatially filter residual starlight and background while coupling planet light and providing a highly stable linespread function on the detector (Mawet, Delorme, et al., 2017). KPIC has been deployed in phases, with Phase I bringing the core elements of the fiber injection unit needed to couple light into the fiber. This phase was commissioned in 2018 (Delorme et al., 2021) and allowed KPIC to operate in "direct spectroscopy" (DS) mode, in which the fiber is aligned directly with the targeted exoplanet. With a resolving power of $R{=}\lambda/\Delta\lambda \sim 35,000$ in $K$ band (2.0-2.5 $\mu$m), the KPIC DS mode provided the first high-resolution spectra of HR 8799 c, d and e. This led to the first spin measurements for the planets along with constraints on the planet radial velocity and atmospheric properties (J. J. Wang, Ruffio, et al., 2021; J. Wang, J. J. Wang, et al., 2023). Robust measurements of atmospheric abundances have also been demonstrated with KPIC DS mode data (Xuan, J. Wang, et al., 2022; J. Wang, Kolecki, et al., 2022). Though the DS mode maximizes coupling efficiency, it requires precise knowledge of the companion position so it is only practical for characterization of known companions rather than for making new detections. Deployed in February 2022, Phase II of KPIC brought several upgrades including a vortex mask to enable VFN (Echeverri, Jovanovic, et al., 2022). The VFN mode's wider, annular coupling region allows KPIC to search for new exoplanets at small separations and expands the proven capabilities of the DS mode to previously unknown systems.

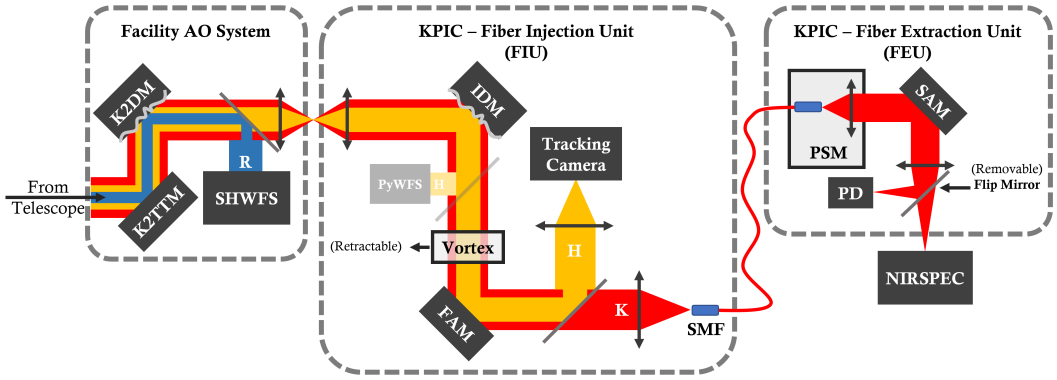


Figure 6.2: Schematic diagram of the KPIC VFN mode. The facility AO system feeds AO-corrected light to the fiber injection unit (FIU) which includes the vortex and SMF necessary for VFN. The FIU also includes a fiber alignment mirror (FAM) and tracking camera for aligning the stellar PSF with the SMF. The fiber extraction unit (FEU) reimages the output of the SMF and aligns it with the input of NIRSPEC. A flip miror in the FEU optionally picks off the light to go to a dedicated photodetector (PD) rather than NIRSPEC for fast readouts during calibrations. Note that various elements in the optical layout have been omitted for simplicity since they are not relevant to the VFN mode; Jovanovic, Calvin, et al. (2020) and Echeverri, Jovanovic, et al. (2022) provide the layout of the optical path in the Phase II DS mode.

### Optical Layout

For a detailed description of the Phase II instrument design, optical layout, performance, and other non-VFN KPIC modes, we refer readers to the general Phase II instrument paper in preparation by Jovanovic et al. In the meantime, we defer to two other publications which describe most of the Phase II design (Jovanovic, Calvin, et al., 2020; Echeverri, Jovanovic, et al., 2022). We also note that many of the individual elements of the instrument, particularly the tracking system and fiber bundle, remain largely unchanged from the original Phase I design reported by Delorme et al. (2021). This section covers only the aspects related to the KPIC VFN mode.

Figure 6.2 shows the optical layout of KPIC when observing in the new VFN mode. The Facility AO system, composed of a tip-tilt mirror (K2TTM), a 349-actuator deformable mirror (K2DM), and a Shack-Hartmann Wavefront Sensor (SHWFS) operating in the visible (400-950 nm), feeds AO-corrected light to the fiber injection unit (FIU) of KPIC. The first element in the FIU is a dedicated 1000-actuator deformable mirror (IDM) internal to KPIC which is currently used

to provide wavefront offsets and non-common-path aberration (NCPA) corrections for the various KPIC modes. An optional dichroic after the IDM can be inserted to send light to a near-infrared pyramid wavefront sensor (PyWFS) (Bond et al., 2020) though that sensor is not currently used for VFN observations; the capabilities unlocked by the PyWFS will be covered in Section 6.7. A relay (not shown) then sends the light to a translating pupil stage which holds the vortex mask for VFN. The system currently uses a narrowband charge 2 vector vortex mask characterized by Mawet, Serabyn, et al. (2010) to have a central wavelength of 2.225 $\mu$m such that KPIC VFN observations are currently focused on K band and are not limited on-sky by the vortex leakage within the ~500 nm width of the band. Another relay (not shown) sends the light to a dedicated fast tip-tilt mirror, called the fiber alignment mirror (FAM), used to steer the star's point spread function (PSF) to the desired position relative to the SMF and control residual jitter from the AO system. The FAM works in closed loop with a tracking camera that receives light short of 1.85 $\mu$m reflected to it by a pickoff dichroic. The tracking camera is a First Light Imaging C-RED2 detector (Gibson et al., 2020) that forms an image with minimal NCPA relative to the final fiber plane. Wavelengths longer than 1.85 $\mu$m are transmitted through the dichroic to a triplet lens which focuses the light onto a fiber bundle containing four SMFs whose cores are separated by ~125 $\mu$m (~800 mas in K-band). These SMFs are identical though the relative coupling efficiency into each varies slightly; for simplicity, we will generally refer to the bundle as "the SMF" indicating the science fiber within the bundle chosen for maximum coupling on a given day.

The fiber extraction unit (FEU) collimates the output of the SMF and projects the pupil onto the slit alignment mirror (SAM), which is conjugate to the cold stop inside NIRSPEC. The SMF and collimating lens sit on the pupil-steering mechanism (PSM) which can be translated to ensure the collimated beam is centered on the cold stop. The SAM steers the reimaged PSF from the SMF to align with the NIRSPEC slit. These two actions ensure maximum throughput to the detector, which provides the final spectra. A flip mirror can be optionally inserted into the beam just before the NIRSPEC input to send the light to a single-pixel InGaAs photodetector (PD: Thorlabs PDA10DT) which is used for fast readouts during calibrations. Note that various elements in the optical path have been omitted here for simplicity since they are not relevant to the VFN mode or to this work. However, the design presented in this section covers all elements relevant to the KPIC VFN mode.

**Tracking System**

The tracking system plays a key role since VFN places strict requirements on the positioning accuracy of the star over the center of the fiber to maintain the null. The requisite accuracy depends on the vortex charge: a charge 2 vortex, like the one currently installed, requires that the star be within $0.3\lambda/D$ ($\lesssim$ 13.5 mas) on average to maintain a null of $<10^{-3}$ but charge 1 requires better than $0.04\lambda/D$ ($\lesssim$ 1.8 mas) for the same null level (Ruane, Echeverri, et al., 2019). Besides the requirement on average PSF position, the requirement on acceptable root-mean-square (RMS) jitter (standard deviation of the PSF position) is $0.18\lambda/D$ ($\lesssim$ 8 mas) RMS for charge 2 and $0.03\lambda/D$ ($\lesssim$ 1.3 mas) RMS for charge 1 to maintain a null $<10^{-3}$ (Ruane, Echeverri, et al., 2019).

The facility AO system currently provides sufficiently low jitter residuals, ~6-7 mas RMS, for our charge 2 vortex. However, the average PSF position slowly drifts beyond the requirement when not corrected by the KPIC tracking system. The KPIC tracking camera is used to identify the PSF position and drive the dedicated FAM to compensate for residual pointing errors (Delorme et al., 2021). During daytime calibrations, a two-dimensional (2D) tip-tilt scan is performed with the FAM to scan the PSF over the SMF and identify the camera pixel coordinates that center the beam on the fiber. Once on-sky, these coordinates are used as the "goal" to which the PSF is driven. The system has proven to be extremely stable such that the coordinates only drift by a fraction of a pixel over days but we still do the 2D scan before each night to ensure optimal coupling. The PSF from a vortex has a ring-like intensity profile (Swartzlander, 2001; Kotlyar et al., 2007) such that standard centroiding algorithms like center-of-mass, quadratic fitting, and Gaussian fitting, do not generally work without modification. The tracking camera on KPIC operates in H band (1.48-1.70 $\mu$m) though, rather than the design wavelength for the vortex of 2.225 $\mu$m. Thus, the PSF seen by the camera is a combination of the VFN ring plus an Airy PSF arising from the chromatic leakage term in the vector vortex mask (Ruane, Mawet, et al., 2019). The zero-order leakage from our vortex mask is large enough in H band that the PSF has a clear Airy pattern core on the tracking camera. This allows us to identify the star using a 2D Gaussian fitting algorithm that provides sub-pixel accuracy since the Airy core is oversampled at 4.1 pixels per full-width at half-maximum. Operating in closed loop with the FAM, the KPIC tracking system accurately maintains the average PSF position to within $\sim$ 0.2 mas. However, the system currently focuses on slow drift only and the jitter residuals remain roughly the same as received from the AO system. Control over the jitter is

primarily limited by the tracking loop software and resonances in the system. There is on-going work to improve the control software to operate faster and specifically reduce the jitter residuals.

**Calibration and Observing Procedure**

Calibrations for the KPIC VFN mode are currently limited by the calibration light source. This source is a broadband, thermal lamp coupled into a SMF to inject light at the input of the facility AO bench and is too faint to measure the VFN null on the PD. Thus the system needs to first be fully aligned and calibrated in the DS mode so that NIRSPEC, which is orders of magnitude more sensitive than the PD and can detect the signal at the VFN null point, can be used to apply corrections for the VFN mode. The DS calibrations involve fiber finding, as described in Sec. 6.4, followed by an NCPA correction on the PD to quickly minimize wavefront aberrations at the fiber plane. The DS NCPA correction is performed by scanning each Zernike aberration with varying amplitudes using the IDM to determine where the maximum coupling occurs. The output of the fiber, still in the DS mode, is then aligned to NIRSPEC by scanning the PSM and the SAM to make sure the beam passes unimpeded through the NIRSPEC pupil and slit. With KPIC aligned to maximize the DS mode performance, the vortex is translated into the beam and a smaller set of Zernike aberrations and amplitudes are scanned to minimize the on-axis signal as measured by NIRSPEC. This minimizes the wavefront aberrations in the VFN mode and optimizes the null depth.

Two additional calibrations are performed on-sky before switching to the target of interest. First, a star with many spectral lines and a well-known radial velocity is observed to obtain a wavelength solution for the night. Then an A0 telluric standard star is observed to sample the telluric features in the desired patch of sky. With those calibrations complete, the target host star's spectrum is measured by aligning it with the center of the fiber and taking exposures with the vortex out, such that the star is well-coupled into the SMF. This measurement is used in post-processing to fit for the residual starlight on top of the companion signal and as a radiometric calibration of the throughput achieved on the given night. Finally, the vortex is moved into the beam to null the star and observe the companion. The background in KPIC spectra is primarily dominated by instrumental background within NIRSPEC due to a light leak in the spectrograph first reported by López et al. (2020). Thus, background spectra are generally taken off-sky at the beginning or end of the night with the same integration time as used on-sky during the night. To account for possible variations

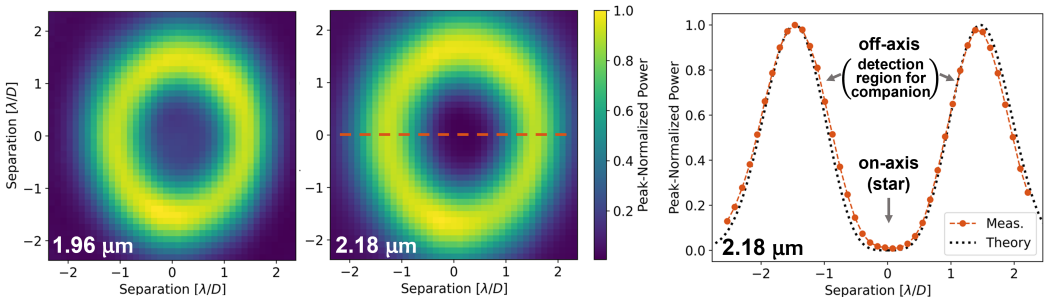


Figure 6.3: Coupling maps of the KPIC VFN mode as measured at the telescope using an internal calibration source. The 2D maps show the power coupled into the fiber as a function of the image position measured using NIRSPEC at 1.96 $\mu$m (left) and 2.18 $\mu$m (middle). The orange dot-dashed curve in the right plot is a horizontal crosscut through the middle of the 2.18 $\mu$m coupling map, as indicated by the dashed orange line in the 2D map. The black dotted line in the right plot is the theoretical expected performance. The center region, with low power, is where the star would be while the sides, with higher coupled power, are where the companion would be. All plots and curves are normalized to the peak value in their corresponding data.

in the background level over time, a "nodding" technique can instead be used where the star is bounced between two fibers so that each NIRSPEC frame has a fiber with the target spectrum and another with the background, enabling nod-subtraction. For VFN observations, this is often not needed since the residual coupled starlight due to wavefront aberrations yields a stellar photon noise that is at least an order of magnitude above the background photon noise for stars with a K band magnitude of 6 or brighter.

### System Validation

Once installed at the telescope, the KPIC VFN mode was tested using an internal light source to validate the system performance. An SMF was inserted at the focal plane input of the FIU, indicated by the converging point in the left panel of Fig. 6.2, to simulate a diffraction-limited focused beam received from the AO system. The FAM was then used to scan the PSF over the fiber to sample the coupling versus the image position, thereby generating a 2D map of the power coupled into the fiber from each point in the VFN field-of-view (FOV). Using NIRSPEC as the detector, this scan provided a spectrally-resolved coupling map. Figure 6.3 shows the average coupled power in the shortest and middle K band echelle orders on NIRSPEC (centered at 1.96 $\mu$m and 2.18 $\mu$m). The center region of the 1.96 $\mu$m coupling map has more power because it is further from the design wavelength of the narrowband

vortex in use and hence has higher leakage and a worse null. The bright region for both coupling maps is relatively constant regardless of azimuthal angle, and the orange dot-dashed crosscut in the rightmost plot shows the symmetry across two sides of the map. The high symmetry is an indicator that the WFE in the system as corrected for this test was very low, as WFE leads to a shift in power around the bright fringe. There is a slight vertical elongation in the maps which is due to an asymmetric response in the FAM axes from the way this scan was performed and is not a real effect from VFN; the on-sky coupling region is symmetric but has a gentle 6-lobed modulation due to the Keck primary mirror's hexagonal shape (Ruane, Echeverri, et al., 2019). The crosscut is in nice agreement with the black dotted line that is a two-sided, peak-normalized replica of the orange charge 2 curve from Fig. 6.1(c) showing the theoretically expected performance. This validates the fact that VFN has a near-circularly-symmetric bright fringe capable of simultaneously searching a full annular region around a star.

## 6.5 On-Sky Commissioning

The VFN mode was installed on KPIC alongside the other Phase II upgrades in February 2022. On-sky commissioning began shortly thereafter, with observations performed on UT 14 April 2022, 14 November 2022, and 6 January 2023. A total of 5 stars were observed for this dataset, all of them known to not have companions within the VFN FOV and to have a small enough angular diameter such that they could be considered point sources (<0.03 $\lambda/D$). To test for known multiplicity, the stars were cross-referenced against the Ninth Catalog of Spectroscopic Binaries (SB9 - Pourbaix et al., 2004) as well as the Washington Double Star Catalog (WDS - Mason et al., 2021). None of the targets were present in the SB9 and only one, 79 Cyg, was present in the WDS though its closest companion entry is at 1.6″ (>35 $\lambda/D$) and hence far out of the VFN FOV. In addition, both HD 213179 and 79 Cyg are present in the catalog of calibrator stars for interferometers (Swihart et al., 2017) such that they have been further pre-vetted for use in interferometric observations. The angular diameters were obtained from the Mid-infrared stellar Diameters and Fluxes (MDF) Catalog (Cruzalèbes et al., 2019).

### Measurables

The measurable performance metric for KPIC is the counts per spectral channel on NIRSPEC, from which the end-to-end (E2E) throughput of the instrument can be computed. This throughput, encompassing all losses in the optical path, is different

than the coupling efficiency, $\eta$, defined in Eq. 6.1. Coupling efficiency is the power coupled into the fiber normalized by the power incident on the fiber and hence only considers losses due to modal mismatch between the SMF fundamental mode and the system PSF. In the laboratory, we have been able to measure the coupling efficiency directly by measuring the flux incident on the fiber tip with a power meter and comparing to the power at the immediate output of the fiber (Echeverri, Ruane, Jovanovic, Mawet, et al., 2019; Echeverri, Ruane, Jovanovic, Delorme, et al., 2021). KPIC, however, does not currently have a way of sampling the power incident on the fiber or immediately after the fiber so the coupling efficiency cannot be directly determined; NIRSPEC flux and E2E throughput are the closest accessible measures. As shown in Sec. 6.6, the E2E throughput is sufficient for computing the expected SNR for a given observation.

The E2E throughput, $T$, is computed by comparing the counts on NIRSPEC to the expected flux for the given star. This is done with the throughput calculator in the KPIC Data Reduction Pipeline.[1] The star's effective temperature is first used to generate a blackbody curve which is scaled by the star's apparent $K$ band magnitude and the collecting area of the Keck primary mirror (76 $m^2$). The measured counts on NIRSPEC for a given frame are converted to flux assuming a detector gain of $g$=3.03 [$e^-$/ADU] (López et al., 2020) and accounting for the frame integration time. The ratio of the two fluxes is then computed at each spectral channel and the end result is a wavelength-dependent throughput measurement, $T(\lambda)$ which includes all losses in the optical path from the top of the atmosphere to the detector including atmospheric transmission, optical coatings, coupling efficiency, quantum efficiency, and more. The detected signal, in counts [ADU], for an object can then be computed as

$$F(\lambda) = \frac{T(\lambda)\Phi(\lambda)_{object} A \tau}{g}, \tag{6.2}$$

where $\Phi$ is the photometric flux for the object, $A$ is the collecting area, $\tau$ is the integration time, and $g$ is the detector gain. In this formulation, $T$ includes the quantum efficiency of the detector and so has units of [$e^-$/ph]. $\Phi$ is the photon flux in the desired spectral bandwidth, $\Delta\lambda$, of the spectral channel such that it has units of [ph/s/$m^2$]. We note that in this paper, we define a spectral channel as a single column of pixels perpendicular to the axis of dispersion. The re-imaged fiber results in a Gaussian-like PSF in this direction such that ~3 pixels in the column are combined into a channel. The line-spread function of the NIRSPEC slit is

[1] `https://github.com/kpicteam/kpic_pipeline`

Table 6.1: Observations for VFN Commissioning

| Date (UT) | Star | Seeing (DIMM) | Mag. (K band) | Spectral Type | Diam. (mas) | Elevation (°) | On-Axis Throughput (%) | |
|---|---|---|---|---|---|---|---|---|
| | | | | | | | VFN | DS |
| 14 Apr 2022 | HIP 62944 | 1" | 4.12 | K3III | 0.71 | 75 | 0.07 | 2.15 |
| 14 Nov 2022 | HD 213179 | 0.6" | 2.98 | K2II | 1.27 | 63 | 0.11 | 3.23 |
| | 79 Cyg | 0.6" | 5.66 | A0V | 0.24 | 71 | 0.06 | 1.72 |
| 6 Jan 2023 | HIP 14719 | N/A | 6.32 | A0V | 0.18 | 70 | 0.07 | 2.55 |
| | HIP 18717 | N/A | 6.07 | A0V | 0.21 | 83 | 0.06 | 2.32 |

Seeing from Maunakea Weather Center seeing monitors. Conditions were unavailable for 6 Jan 2023.
Magnitude, spectral type, and diameter from the MDF Catalog (Cruzalèbes et al., 2019).
Elevation is the average elevation of the target during the observations.
On-axis throughput is the average in echelle order 4 with the star aligned to the center of the SMF.

oversampled to ~3 pixels as well such that 3 spectral channels are combined to form a single spectral resolution element. Given the $R$~35,000 resolution of KPIC in K band, and the 3-pixel coverage, a spectral channel, as defined in this paper, thus subtends approximately $\Delta\lambda$=2.1×10$^{-5}$ $\mu$m in the spectrum.

Due to the dependence of the coupling efficiency on angular separation, as shown in Fig. 6.3, the throughput is also separation dependent such that it would more properly be expressed as $T(\lambda, \alpha)$, where $\alpha$ is the on-sky angular separation. However, for simplicity, we will refer to the $\alpha$=0 throughput as "on-axis," and other throughput measurements as "off-axis" with a specification for the separation. For SNR calculations, it is necessary to know $T$ for both the planet and the star. The star throughput in the VFN mode is measured by targeting a known-single star and observing it centered on the fiber through the vortex to provide the on-axis value. The planet throughput is measured by offsetting the star over the fiber so that it acts as an off-axis point source in the same way that the planet would at the offset separation.

**Observations**

For VFN commissioning, several throughput measurements were made on 5 stars over 3 separate nights. The target stars, their key properties, the nights on which they were observed, and the observing conditions are listed in Table 6.1.

The on-axis throughput was measured with multiple samples per star to account for

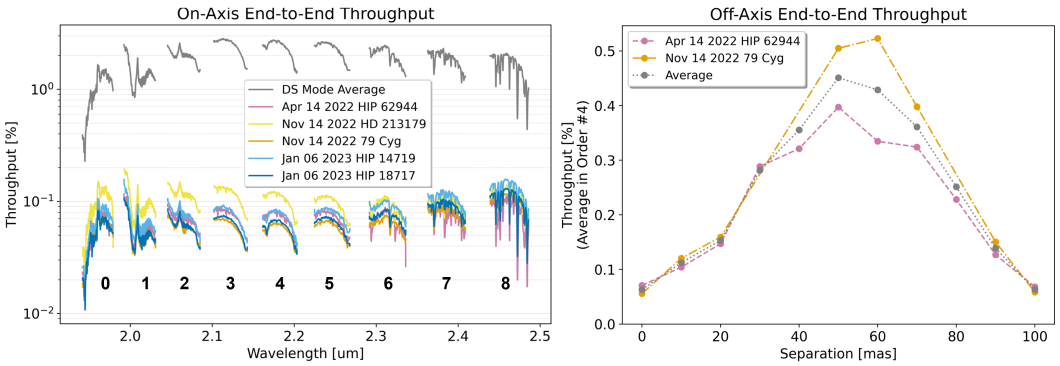


Figure 6.4: Left: End-to-end on-axis throughput. The grey line shows the average DS mode throughput for all of the nights. The other lines are the VFN mode throughput measurements, where each line is the median of multiple samples on the given target. The spectra have been downsampled to R=3,500 to smooth out spectral lines for a simpler view. The VFN mode measurements represent the throughput for the host star during a VFN observation. Right: Average end-to-end throughput in echelle order 4 (2.16-2.20 $\mu$m) for points at varying separations. This represents the companion throughput given the off-axis separation from the host star. The orange dot-dashed line is for the data on 79 Cyg, the pink dashed line is for the HIP 62944 data, and the gray dotted line is the average of the two. Note that the y-axis is re-scaled compared to the on-axis plot.

variability in seeing and turbulence within individual NIRSPEC frames. The left panel of Fig. 6.4 shows the on-axis throughput in the DS mode (no vortex; grey) and VFN mode (with vortex; all other colors). The DS mode line is the average of the DS mode throughput measurements for all the targets. The VFN mode lines are the median of the various samples for each target. Note that the spectra are downsampled from the true spectral resolution of 35,000 to 3,500 in this figure for visualization purposes. The $\sim$ 20 nm gaps along the wavelength axis are due to the format of the two-dimensional spectra generated by the cross-disperser on the NIRSPEC detector. The resulting windows of signal are the echelle orders and are numbered in KPIC from zero to eight from left to right (short to long wavelengths). Note that KPIC orders 0 to 8 correspond to NIRSPEC orders 39 to 31, respectively, following the conventional NIRSPEC numbering; we renumber them in KPIC for simplicity. The average on-axis throughput in echelle order 4, the middle order on NIRSPEC, is included as the rightmost columns in Table 6.1 for both modes on each star. The VFN mode on-axis measurements represent the throughput for the host star in a VFN observation since the star is aligned to the center of the fiber.

The off-axis throughput was measured by scanning the stellar PSF along a radial line away from the center of the fiber. This samples various separations so that a line profile of throughput versus separation can be generated. The throughput for a companion at a given separation can then be determined from these curves. Line scans were only performed on two of the targets due to time constraints. The right panel of Fig. 6.4 shows the average throughput in echelle order 4 for these two line scans. The orange dot-dashed curve from the November data on 79 Cyg is a single radial scan while the pink dashed curve from April on HIP 62944 is the average of two scans on opposite sides of the star. The gray dotted curve is the average of the 79 Cyg and and HIP 62944 data to provide a representative off-axis throughput for the KPIC VFN mode.

## 6.6 Analysis

Figure 6.4 shows that the VFN on-axis throughput achieved on-sky is consistent across multiple targets and over nine months. All the VFN measurements are over an order of magnitude lower than the DS mode (grey) throughput, showing that the VFN mode is successfully rejecting the on-axis starlight. The rightmost columns in Table 6.1 show that the VFN mode consistently reduces the on-axis throughput in echelle order 4 by a factor of $\sim 3\times10^{-2}$ relative to the DS mode, with the more recent January data showing the best relative reduction. The HD 213179 measurement seems to be a slight outlier with the highest VFN on-axis star throughput in Fig. 6.4, but it is still within a factor of 2 from the lowest throughput measurement, which was achieved on 79 Cyg that same night. The other four on-axis measurements are all within a factor of 1.3 from each other with the average for each star in echelle order 4 varying between 0.056% and 0.073%. Improvements in starlight rejection may be achieved through the work described in Section 6.7 but we see that the system can already be reliably calibrated and controlled to the same level over months and the performance is stable and predictable.

As described in the beginning of Sec. 6.5, KPIC does not have a way to measure the coupling efficiency, $\eta$, defined in Sec. 6.3. However, we can approximate the VFN coupling using the throughput ratio to the DS mode and making assumptions about the DS performance based on knowledge from KPIC Phase I. The on-axis ratio is

$$\frac{T_{VFN}}{T_{DS}} \approx \frac{\eta_{VFN}}{\eta_{DS,ap}\mathrm{SR}},$$

where $\eta_{VFN}$ is the VFN coupling efficiency, $\eta_{DS,ap}$ is the coupling efficiency term for the DS mode set by the aperture shape, and SR is the Strehl ratio in DS mode

which has a direct impact on coupling efficiency (Jovanovic, Schwab, et al., 2017). Other throughput terms (transmission of optics, quantum efficiency, etc.) cancel out since they are equal for both modes. For the Keck aperture, $\eta_{DS,ap}$ is at most 67%, assuming no static WFE in the telescope or instrument, and SR∼55% as set by the SHWFS for stars with the brightness in our dataset (Wizinowich, 2015). Note that by the Maréchal approximation (Ross, 2009), 55% corresponds to ∼250 nm RMS of wavefront error. Taking the HIP 18717 data, which shows the best VFN starlight rejection, we get $T_{VFN} = 0.06\%$ and $T_{DS} = 2.32\%$, which provides $\eta_{VFN}\approx 9.5 \times 10^{-3}$. In 2019, we predicted that the KPIC VFN mode would achieve $6 \times 10^{-3}$ by using KPIC Phase I wavefront measurements from the PyWFS (Echeverri, Ruane, Jovanovic, Hayama, et al., 2019) which, as described in Sec. 6.7, has smaller residuals than the SHWFS. In those predictions, the residual WFE was the key limiting term for the charge 2 vortex.

This estimate of the on-axis VFN coupling efficiency shows that the on-sky null roughly matches expectation though there is some discrepancy. The estimate makes several assumptions that need to be further evaluated before a precise on-axis coupling efficiency can be reported. For example, $\eta_{DS,ap}$ and SR may be lower than assumed, the power spectrum of the WF residuals may be different with the SHWFS and hence might include more low-order WFE that VFN is sensitive to, and there may be additional unaccounted-for losses such as a smaller aperture size in the VFN mode, among other inaccuracies in the estimate. We will rely on throughput for the remainder of the paper since it is measurable and well-determined in KPIC as described earlier.

The average off-axis throughput in echelle order 4 (gray curve in right plot of Fig. 6.4) shows a peak of 0.45% at 50 mas, with the true maximum likely occurring somewhere between the 50 and 60 mas samples given the shape of the curve. From Fig. 6.1(c), the peak is expected to occur at around $1.4\lambda/D$ which at 2.2 $\mu$m on the Keck Telescope would be ∼60 mas. Thus, the location of the maximum is in close agreement with the predicted performance, especially for the 79 Cyg line scan. The line scan data provides the throughput for an off-axis point source meaning that KPIC VFN would obtain 0.45% of the total light from a companion at 50 mas from its host star.

We can contextualize the VFN companion throughput by comparing to the KPIC DS mode. In the DS mode, the analogous throughput is provided by the on-axis value since the SMF is aligned to the companion. The rightmost column in Table 6.1

shows that on the two stars for which we took VFN line scans, the DS mode achieved an average on-axis throughput of 2.15% and 1.72%. The off-axis peak in the VFN mode was 0.40% and 0.52%, respectively, as shown in the right plot of Fig. 6.4. Thus, the end-to-end throughput for the companion in the VFN mode is 20 to 30% of that in the DS mode. This is a key result to highlight. The relative VFN throughput is higher than intuited from the ~10% peak in Fig. 6.1(c) because of the distinction made between coupling efficiency and throughput at the beginning of Sec. 6.5. Coupling efficiency, and hence Fig. 6.1, consider the coupled power relative to the total power incident on the fiber whereas here we are considering the relative throughput for VFN versus DS mode. The DS mode does not couple all the light incident on the SMF either; the maximum DS coupling on the Keck aperture is 67% (Ruane, Echeverri, et al., 2019). Thus, in the absence of WFE, VFN achieves 16.5% of the DS mode coupling. Additionally, the DS mode is more sensitive to WFE than the VFN mode. In the VFN mode, low-order aberrations simply shift power around the bright fringe but average over time to no net loss since the throughput can be instantaneously increased or decreased for a given off-axis position. In the DS mode, all aberrations strictly decrease the on-axis (companion) throughput. We refer readers to the lower-left panel of Fig. 7a in Echeverri, Ruane, Jovanovic, Hayama, et al. (2019) which shows that in the presence of realistic on-sky WFE, the VFN coupling only drops from 11% to 8% and remains relatively constant at that value as the WFE varies.

We note that the majority of the losses in the instrument, in both VFN and DS mode, are due to the number of optics in the optical path, not the use of single mode fibers. Delorme et al. (2021) demonstrate this with a detailed accounting of losses in the KPIC Phase I system.

We can further contextualize the VFN performance more generally by comparing to an unresolved (i.e., seeing-limited) observation without a fiber. In this unresolved case, there is no starlight suppression so both the companion and star have the same instrument throughput. In the VFN case, the companion throughput is approximately 6.9 times higher than the star throughput, given the system performance presented above. This increases the effective contrast relative to the star by the same amount, allowing the VFN mode to target fainter companions. The next section further explores the VFN performance and predicted SNR limits.

**SNR Formulas**

The performance of an observation can be predicted by using the end-to-end throughput values to determine the expected signal on the detector and from there, computing the SNR for the companion. The SNR per spectral channel, including typical noise sources, is

$$\mathrm{SNR} = \frac{S_p}{\sqrt{S_s + S_p + S_b + \mathrm{RN}}},$$

where $S_p$ and $S_s$ are the planet and star signal per Eq. 6.2 but without the gain term to maintain units of [$e^-$/s], $S_b$ is the thermal background signal, and RN is the read noise squared per frame on the detector. As mentioned in Sec. 6.4, the background signal in KPIC data is primarily dominated by instrumental background inside NIRSPEC and can be expressed as $S_b = B_c n_{pix} \tau$, where $n_{pix}$=3 is the number of pixels combined for a spectral channel and $B_c$ is the number of background electrons received per second. In Phase II of KPIC, $B_c$ is wavelength dependent but is generally ~1 [$e^-$/pix/s]. The read noise accumulates on a per-frame basis and can be expressed as $\mathrm{RN} = R_c^2 n_{pix} n_{frame}$ where $R_c$ was measured at ~10 [$e^-$/pix/frame] by López et al. (2020)

Given the linear range of 25,000 ADU per pixel for NIRSPEC (López et al., 2020), the residual VFN starlight throughput, and the electron rate of the background, the exposure time of individual frames can be set to make read noise irrelevant for KPIC VFN observations. For faint targets, long exposures can be acquired such that the background signal will outpace the read noise and the observation will be primarily background-limited. For bright targets, short exposures will be needed to avoid saturating on the starlight signal but the star will thus outpace the read noise such that the observation becomes stellar-photon-noise-limited.

The read noise will therefore be omitted from further SNR calculations in this work without loss of generality given that the frame exposure time for an observation is set to ensure that other terms dominate. The SNR equation now simplifies to

$$\mathrm{SNR} = \frac{T_p \epsilon \Phi_s A \sqrt{\tau}}{\sqrt{\Phi_s A (T_s + \epsilon T_p) + B_c n_{pix}}}, \tag{6.3}$$

where the full expressions for the stellar, planet, and background signals have been filled in. $T_s$ and $T_p$ are the star (on-axis) and planet (off-axis) throughput respectively, $\Phi_s$ is the flux of the star, and $\epsilon$ is the photometric flux ratio between the planet and the star, $\Phi_p/\Phi_s$. Solving for $\tau$ in Eq. 6.3, the total integration time required to

achieve a goal SNR per spectral channel can then be expressed as

$$\tau = \left(\frac{\mathrm{SNR}}{T_p \epsilon \Phi_s A}\right)^2 \left(\Phi_s A(T_s + \epsilon T_p) + B_c n_{pix}\right). \tag{6.4}$$

For bright stars, a further simplification can be made by omitting the background noise and assuming observations are stellar-photon-noise-limited. The background noise will remain one tenth of the stellar photon noise, and hence regarded as negligible, for

$$\frac{S_s}{S_b} = 10 = \frac{T_s \Phi_s A}{B_c n_{pix}}.$$

This leads to a stellar K band magnitude of 6 below which the contribution of the background photon noise to the SNR can be ignored in favor of the dominating stellar photon noise. At a magnitude of 8, the background noise becomes equivalent to the stellar noise and beyond that, it starts to dominate. Equation 6.4 thus simplifies to

$$\tau = \frac{T_s}{T_p^2} \frac{\mathrm{SNR}^2}{\epsilon^2 \Phi_s A}, \tag{6.5}$$

in the stellar-photon-noise-limited regime.

**Predicted Performance and Detection Limits**

Using Eq. 6.4 and the throughput values presented above, we can predict the KPIC VFN capabilities from the on-sky commissioning performance. Given that the typical VFN on-axis throughput in echelle order 4 is between 0.056% and 0.073%, a value of $T_s$=0.065% will be assumed for this section. The average line scan performance (gray dotted curve in the right plot of Fig. 6.4) will be used for $T_p(\alpha)$ with a peak value of 0.45% at $\alpha$=50 mas and interpolating on the curve for other separations as needed. To define a goal SNR value, we consider the abundance of science data acquired with KPIC throughout Phase I and Phase II, and find that the instrument can detect a companion at a cross-correlation function (CCF) SNR of 3-5 when the SNR per spectral channel is around 1. This boost between CCF SNR and SNR per channel is primarily guided by the number of lines in the spectra (Snellen, de Kok, et al., 2015; J. Wang, Mawet, et al., 2017) and is currently limited by the ability to account for systematics such as spectral fringing. Thus, for this work, we will only consider a companion "detected" when a goal SNR per spectral channel of 3 has been met to ensure an unambiguous detection.

With these values, Fig. 6.5 shows the integration time required to reach an SNR per channel of 3 on a companion at a varying flux ratio ($\epsilon$) and separation ($\alpha$) from a

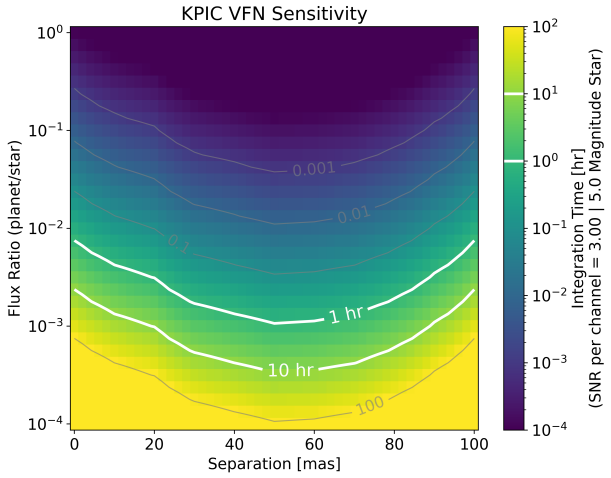


Figure 6.5: Integration time required to reach an SNR per spectral channel of 3.0 on a companion at a given flux ratio and separation around a star with a K band magnitude of 5. This assumes the current KPIC VFN charge 2 performance demonstrated on-sky in this paper. The white lines show the 1 hour and 10 hour contours while light grey lines show other powers of 10. This includes planet and star photon noise along with background noise, but neglects read noise which is negligible. For a 5$^{\text{th}}$ magnitude star as shown here, stellar photon noise dominates.

Table 6.2: Values for SNR calculation in Fig. 6.5

| Observing Parameters | |
|---|---|
| Star Throughput ($T_s$) | 0.065% |
| Peak Companion Throughput ($T_p$) | 0.45% |
| Star K Band Magnitude | 5.0 |
| Central Wavelength ($\lambda$) | 2.18 $\mu$m |
| Channel Width ($\Delta\lambda$) | $2.1 \times 10^{-5}$ $\mu$m |
| Photon Rate for a 5$^{\text{th}}$ mag. Star ($\Phi_s$) | 1,000 ph/s/m$^2$ |
| Goal SNR per Channel | 3.0 |
| **Instrument Constants** | |
| Collecting Area ($A$) | 76 m$^2$ |
| Background Electron Rate ($B_c$) | 1 e$^-$/pix/s |
| Pixels Per Channel ($n_{pix}$) | 3 |

host star with a K band magnitude of 5. The white contour lines show the 1 and 10 hour detection limits. Table 6.2 summarizes the values used for these calculations. The results show that, given the current instrument performance, the KPIC VFN mode should be able to detect companions within 1 hour down to a flux ratio of $10^{-3}$ around stars brighter than fifth magnitude.

On fainter stars, KPIC VFN will start to become background-noise limited due to the NIRSPEC instrument background (see Sec. 6.4) but can still detect companions several hundred times fainter than their host star. For example, the current performance enables the instrument to detect a system like GQ Lup AB (Neuhäuser et al., 2005) in under 1 hour if the brown dwarf companion ($K$=13) was located at 50 mas from its host star ($K$=7.1).

Note that this result uses the VFN performance in echelle order 4 (~2.15-2.20 $\mu$m), which is at the center of the K band window covered by KPIC. However, the CO bandhead, which contains the bulk of the spectral lines used for detection on KPIC, starts at ~2.29 $\mu$m and extends longwards such that it subtends echelle orders 6 to 8. Thus, these are the key orders in which higher SNR is most valuable, even if they are not where the current monochromatic charge 2 vortex mask used by the KPIC VFN mode achieves the deepest starlight rejection. The left plot in Fig. 6.4 shows that the starlight rejection in echelle order 8 is approximately two times worse than order 4. This leads to a correction factor of ~2 in the required integration time if only order 8 were considered. Realistically, a detection combines multiple orders such that the integration time will likely be somewhere between the order 4 and order 8 values.

A key point to make is that Fig. 6.5 is valid for a companion at a given separation regardless of the on-sky position angle since the VFN coupling is axially symmetric. This makes VFN a prime technique for new detection campaigns. Other techniques may achieve a higher SNR in less time for a known companion when they can be aligned directly to maximize throughput on the target. However, those techniques cannot simultaneously cover the full region that VFN covers, so the integration time required to search the same area as VFN with equivalent SNR is significantly higher.

## 6.7 Next Steps

The current KPIC VFN performance is promising and consistent over months, and demonstrates that the instrument mode is ready for on-sky operation in surveys searching for new companions. There is, nevertheless, still room for further improvement through on-going work on both the hardware and software. These efforts

primarily target either improving the starlight rejection (smaller $T_s$) or increasing the planet throughput (larger $T_p$).

**Improving Starlight Rejection**

With a charge 2 vortex mask, like the one currently installed in the instrument, the largest source of coupled starlight is due to wavefront aberrations. This is because charge 2 is significantly less sensitive to tip-tilt jitter, differential atmospheric refraction (DAR), and the finite angular size of the star (Ruane, Echeverri, et al., 2019). The current tip-tilt residuals of ~6-7 mas RMS put jitter at the next largest source of starlight but likely an order of magnitude or more below the starlight from WFE, making improved wavefront control the best way to reduce the coupled starlight.

One route for accomplishing this is to switch from using the SHWFS to the PyWFS. The latter has an improved sensitivity to low order wavefront aberrations, which are what VFN is most sensitive to given its small working angle. The PyWFS has demonstrated an improvement, over the SHWFS, of a factor of 2 in raw contrast at small separations ($\sim 2\lambda/D$) with the NIRC2 charge 2 vortex coronagraph (Bond et al., 2020), which would correspond to a reduction of $\sqrt{2}$ in WFE. Furthermore, predictive control is being implemented with the PyWFS and preliminary results show a reduction by a factor of ~1.2 in the median RMS wavefront residuals on-sky compared to the default integrator control (van Kooten et al., 2021). As shown in Fig. 6.2, the PyWFS is already installed in the system and, in fact, it was the primary wavefront sensor for KPIC during Phase I. It is still being recommissioned for Phase II operations but requires only software modifications to support the new elements of the system. Once available for KPIC observations, it should provide a reduction by a factor of >1.5 in RMS WFE which in turn would yield a reduction of 2.25 in coupled starlight since the VFN starlight rejection is quadratically dependent on WFE (Ruane, Echeverri, et al., 2019). For targets with bright host stars where the observation is currently stellar photon-noise limited, this leads to a corresponding factor of 2.25 reduction in integration time compared to the performance from Section 6.6. An additional reduction in WFE can also be expected from the increased temporal bandwidth provided by a new real time computer being installed in the summer of 2023 to upgrade the facility AO system. The improvement from this upgrade is harder to predict.

**Improving Planet Throughput**

An alternative to reducing the coupled starlight is to improve the planet throughput. As shown by Eq. 6.4 and 6.5, the integration time is inversely proportional to the square of the planet throughput such that this is a more efficient and direct route for improvement. The current planet throughput is already close to the best that can be achieved with a charge 2 mask but, as explained in Section 6.3, a charge 1 mask has close to double the throughput. Charge 1 also has the added benefit of peaking in throughput at 0.9 rather than $1.4\lambda/D$, allowing KPIC VFN to target companions at even smaller separations. As such, a charge 1 vortex mask will be added to the KPIC pupil stage as part of a service mission scheduled for the Winter of 2023. This promises to increase the planet throughput to $T_p$=0.8%, a factor of 1.8 higher than its current value, and therefore reduce the required integration time to achieve the same SNR by a factor of 3.25. It is important to note that the charge 1 mask is no more sensitive to WFE than the charge 2 mask since they both have a similar quadratic dependence on specific, complementary aberrations (Ruane, Echeverri, et al., 2019). However, charge 1 is more sensitive to tip-tilt jitter and DAR, which would then become the limiting terms in the achievable starlight rejection, setting a new $T_s$~0.2% limit.

To have the starlight contribution from jitter with a charge 1 mask be below the contribution from the current wavefront residuals, jitter would need to be reduced by about a factor of 3 to below 2 mas RMS. Switching to the PyWFS should help with the jitter residuals since the pyramid is able to sense and correct tip and tilt better than the SHWFS. Additionally, the tracking system described in Section 6.4 is currently being overhauled to reduce software overheads and operate faster, thereby allowing it to target higher frequencies, including several resonances that add a significant amount of power to the jitter residuals. Recent off-sky testing has shown an increase in control frequency by more than a factor of two and the control algorithm is now being adjusted from a simple integrator to specifically notch the known resonances. Between these two modifications, we expect to reduce the tip-tilt jitter so that starlight leakage from it is below that from the current wavefront residuals.

In addition to the jitter, the DAR will be a limiting factor with the charge 1 mask. An atmospheric dispersion compensator (ADC) has been designed specifically to meet the VFN requirements following the same methodology of J. J. Wang, Wallace, et al. (2020) and will be installed in the system alongside the charge 1 vortex mask. This

will correct the DAR to below 1 mas at the edges of the band so that the starlight leakage from DAR will be two orders of magnitude or more below that from residual on-sky WFE.

### 6.8 Conclusion

This paper presented the first on-sky demonstration of VFN, a new interferometric nulling technique aimed at both detecting and characterizing companions at or within one diffraction beam width from their host star. This first VFN prototype worked as expected and was shown to enable the detection of companions $10^3$ times fainter than the central host in 1 hour at a separation of 50 mas. The new mode, available as part of the KPIC instrument, will be used to search for and characterize companions indirectly detected by Gaia and RV surveys. We have clearly identified areas for improvements such as better wavefront and jitter control for enhanced starlight suppression. We will also be replacing the existing charge 2 vortex mask with an optimized charge 1 vortex, close to doubling the effective off-axis throughput, and thereby reducing the required integration time by a factor of 3.25. With its simple design and implementation in fiber-fed direct imaging instruments, the demonstration of VFN on sky with KPIC is a key milestone towards future instruments such as Keck-HISPEC and TMT-MODHIS (Mawet, Fitzgerald, et al., 2022), both of which have baselined VFN as a core mode. Fiber nulling is currently being considered for a possible implementation on the Habitable Worlds Observatory mission, enabling the detection and characterization of exoplanets at inner working angles substantially smaller than standard coronagraphs typically allow.

**Disclosures.** The authors have no relevant financial interests and no potential conflicts of interest to disclose in this work.

**Acknowledgments.** D. Echeverri is supported by a NASA Future Investigators in NASA Earth and Space Science and Technology (FINESST) fellowship under award #80NSSC19K1423. D. Echeverri also acknowledges support from the Keck Visiting Scholars Program (KVSP) to install the Phase II upgrades required for KPIC VFN.

Funding for KPIC has been provided by the California Institute of Technology, the Jet Propulsion Laboratory, the Heising-Simons Foundation (grants #2015-129, #2017-318 and #2019-1312), the Simons Foundation (through the Caltech Center for Comparative Planetary Evolution), and the NSF under grant AST-1611623.

The authors wish to recognize and acknowledge the very significant cultural role and reverence that the summit of Maunakea has always had within the indigenous Hawaiian community. We are most fortunate to have the opportunity to conduct observations from this mountain.

**Code, Data, and Materials Availability.** The code for reducing the spectra and calculating E2E throughput is freely available on GitHub in the *kpic_pipeline* repository at https://github.com/kpicteam/kpic_pipeline. This work used the *4514a56* commit from 5 Sep 2022. All KPIC data will be available via the Keck Observatory Archive (KOA) at https://www2.keck.hawaii.edu/koa/public/koa.php.

---

## *Supplemental Work*

### 6.9 KPIC VFN Versus DS Mode

Section 6.6 presented the KPIC VFN mode's ability to detect companions given the demonstrated on-sky throughput values. We noted that this sensitivity curve is valid for a companion at any position angle since the VFN coupling efficiency is axially symmetric around the star. In contrast, the DS mode achieves higher companion throughput but requires the fiber to be well-aligned on the companion, otherwise the throughput rapidly falls off. This means that the VFN mode achieves a higher SNR for a larger area around the star, making it better for search campaigns looking for new companions. The resulting implications drive the decision point for which mode to observe with in KPIC, VFN or DS, given the current system performance and the target under consideration. This section digs into that trade more directly. A brief version of this work was included in Echeverri, Xuan, Jovanovic, Delorme, et al. (2023), though the results have since been updated slightly for this thesis.

In the photon-noise-limited regime (i.e., ignoring background noise and read noise), Eq. 6.3 simplifies to

$$\mathrm{SNR} = \frac{T_p}{\sqrt{T_s + \epsilon T_p}} \epsilon \sqrt{\Phi_s A \tau}, \tag{6.6}$$

providing the SNR per spectral channel for the observation. From this, we can directly compare a VFN mode observation versus a DS mode observation for a given target by taking the ratio of the SNRs,

$$\mathrm{SNR}_{\mathrm{ratio}} = \frac{T_{pV}}{T_{pD}} \sqrt{\frac{T_{sD} + \epsilon T_{pD}}{T_{sV} + \epsilon T_{pV}}}. \tag{6.7}$$

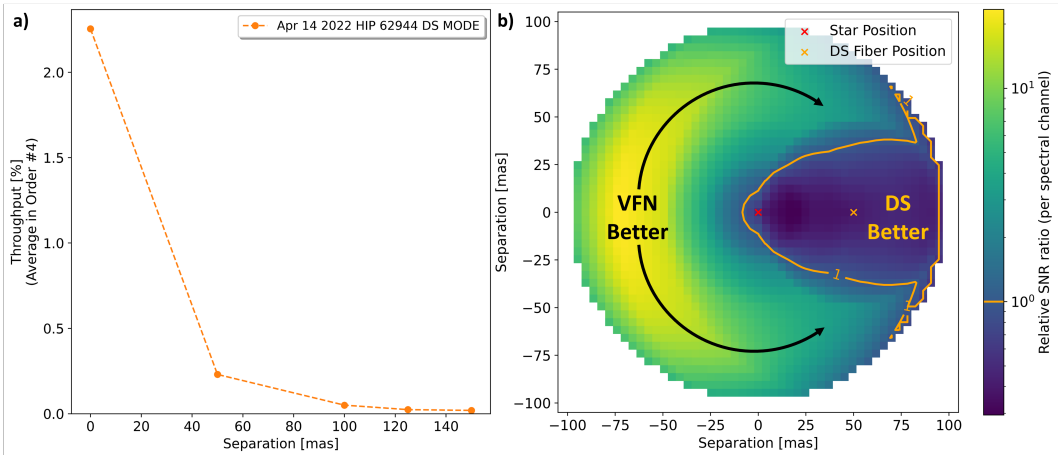


Figure 6.6: (a) Average end-to-end throughput in echelle order 4 (2.16−2.20 $\mu$m) for points at varying separations using the KPIC DS mode. The on-axis (0 mas) point represents the companion throughput in DS mode while the other points represent the star throughput given the companion-host separation. (b) Ratio of SNR per spectral channel for a VFN mode observation relative to an analogous DS mode observation. The fiber in the VFN mode observation is aligned to the central red "x" while in the DS mode, the fiber is aligned to the orange "x" at 50 mas to the right. The orange contour denotes the region where the SNR ratio is $< 1$ such that the DS mode outperforms the VFN mode. Outside of the contour, the VFN mode outperforms. This assumes a photon-noise-limited observation and a companion to star flux ratio of $10^{-2}$.

The subscript $_{pV}$ and $_{sV}$ denote the VFN mode planet and star throughput while the $_{pD}$ and $_{sD}$ denote the DS mode values. When the $\mathrm{SNR_{ratio}}$ is greater than one, the VFN mode would result in a higher SNR and hence is preferable. Meanwhile, values less than one mean the DS mode is preferable.

From the average curve in the right plot of Fig. 6.4, we have the VFN mode throughput for companions anywhere in the field ($T_{pV}$). We also have the throughput for the star ($T_{sV}$) as 0.065% based on the average VFN mode on-axis throughput in echelle order 4 throughout the commissioning data. For the DS mode throughput values, we need the on-axis and off-axis throughput to determine the companion and star values, respectively. An on-sky line scan with the DS mode was taken on April 14, 2022 on HIP 62944. The resulting average throughput in echelle order 4 as a function of separation is shown in Fig. 6.6(a). The peak on-axis throughput is 2.23% but it drops by a factor of 10 at 50 mas and continues to decrease beyond there.

By sampling different points in the curve based on the fiber position relative to the star and the companion, we determine the necessary throughput values for Eq. 6.7. For example, consider an observation of a companion with a well-known orbital position at 50 mas from its host star. The VFN throughput values are $T_{pV} = 0.45\%$ and $T_{sV} = 0.065\%$, from Table 6.2 while the DS values are $T_{pD} = 2.23\%$ and $T_{sV} = 0.23\%$. With a companion at a flux ratio of $\epsilon = 10^{-2}$, the resulting $\mathrm{SNR}_{\mathrm{ratio}}$ is just under 0.4 such that observing with the VFN mode in this scenario currently results in a worse detection than observing with the DS mode. This assumes that the SMF in DS mode was accurately aligned to the companion position to achieve maximum throughput; that is only possible if the companion orbit is well known.

Consider now the case of a companion with a poorly constrained orbit or, similarly, a search for new companions around a star. Since the VFN mode aligns to the star, there is no need to offset onto a specific companion position such that VFN enables KPIC to search a much wider region around the star at once than the DS mode. Meanwhile, the DS mode would need to be aligned to an off-axis point for the search; let this point be the same 50 mas offset from the star for consistency. The companion throughput now depends on how far it is from the center of the SMF. If the companion is located in a small region around the DS mode fiber location, the DS mode will achieve higher SNR than the VFN mode, but outside of that region, the VFN mode will do better. Figure 6.6(b) shows the $\mathrm{SNR}_{\mathrm{ratio}}$ for all points around the star within the VFN field of view ($\sim 2\lambda/D$ or $\sim$100 mas in K band). The SMF for the VFN mode is aligned to the central red "x" while for the DS mode, the fiber is aligned to the orange "x" 50 mas to the right. A planet-star flux ratio of $\epsilon = 10^{-2}$ is assumed and the host star is assumed to be brighter than a K band magnitude of 6 so that background noise is negligible and Eq. 6.7 is valid. The orange contour denotes the region where the ratio crosses one. As such, we find that if the companion lies within the orange contour, the DS mode achieves a higher SNR. Meanwhile, if the companion lies outside of the contour, the VFN mode does better. This means that the DS mode outperforms when the companion position is known and the fiber can be aligned to better than $\sim$35 mas; otherwise the VFN mode outperforms. In a broader sense, this means that the VFN mode is better for new detections where a wide search region is preferable while the DS mode is better for characterizing known companions.

Note that Fig. 6.6(b) makes several assumptions about the DS mode off-axis coupling. For example, the DS line scan used for these calculations had a relatively

large step size of 50 mas, so the throughput for intermediate values was linearly interpolated and could be different given the true form of the off-axis coupling. Additionally, this off-axis throughput curve was obtained from a single line scan on a single night, so the performance could change depending on the observing conditions or even on the position angle of the scan if the wavefront residuals led to an asymmetric PSF. The figure should be reassessed and further validated with additional DS mode and VFN mode line scans. Finally, the figure also assumes the current KPIC VFN mode performance such that as we improve the performance through the modifications explained in Sec. 6.7, the orange contour region will shrink. In fact, given enough improvement, the VFN mode will outperform the DS mode for all points within its $\sim 2.5\lambda/D$ FOV, in which case VFN would be preferable even for characterizing known companions. This would likely be the case for a VFN mode behind an Extreme AO system.

## References

Akeson, R. L. et al. (Aug. 2013). "The NASA Exoplanet Archive: Data and Tools for Exoplanet Research". In: *Publ. Astron. Soc. Pac.* 125.930, p. 989. DOI: 10.1086/672273. arXiv: 1307.2944 [astro-ph.IM].

Beuzit, J.-L. et al. (Nov. 2019). "SPHERE: the exoplanet imager for the Very Large Telescope". In: *Astronomy and Astrophysics* 631, A155, A155. DOI: 10.1051/0004-6361/201935251. arXiv: 1902.04080 [astro-ph.IM].

Bond, C. Z. et al. (2020). "Adaptive optics with an infrared pyramid wavefront sensor at Keck". In: *Journal of Astronomical Telescopes, Instruments, and Systems* 6.3, pp. 1–21. DOI: 10.1117/1.JATIS.6.3.039003. URL: https://doi.org/10.1117/1.JATIS.6.3.039003.

Bowler, B. P. and E. L. Nielsen (2018). "Occurrence Rates from Direct Imaging Surveys". In: *Handbook of Exoplanets*. Ed. by H. J. Deeg and J. A. Belmonte, 155, p. 155. DOI: 10.1007/978-3-319-55333-7_155.

Brandt, T. D. (June 2021). "The Hipparcos-Gaia Catalog of Accelerations: Gaia EDR3 Edition". In: *The Astrophysical Journal Supplement Series* 254.2, 42, p. 42. DOI: 10.3847/1538-4365/abf93c. arXiv: 2105.11662 [astro-ph.GA].

Bryan, M. L. et al. (Dec. 2020). "As the Worlds Turn: Constraining Spin Evolution in the Planetary-mass Regime". In: *The Astrophysical Journal* 905, p. 37. ISSN: 0004-637X. DOI: 10.3847/1538-4357/abc0ef.

Crossfield, I. J. M. et al. (Jan. 2014). "A global cloud map of the nearest known brown dwarf". In: *Nature* 505.7485, pp. 654–656. DOI: 10.1038/nature12955. arXiv: 1401.8145 [astro-ph.EP].

Cruzalèbes, P. et al. (Dec. 2019). "A catalogue of stellar diameters and fluxes for mid-infrared interferometry". In: *Mon. Notices Royal Astron. Soc.* 490.3, pp. 3158–3176. DOI: 10.1093/mnras/stz2803. arXiv: 1910.00542 [astro-ph.SR].

Currie, T. et al. (Apr. 2023). "Direct imaging and astrometric detection of a gas giant planet orbiting an accelerating star". In: *Science* 380.6641, pp. 198–203. DOI: 10.1126/science.abo6192. arXiv: 2212.00034 [astro-ph.EP].

De Rosa, R. J., E. L. Nielsen, J. Rameau, et al. (Dec. 2019). "Detection of a Low-mass Stellar Companion to the Accelerating A2IV Star HR 1645". In: *The Astronomical Journal* 158.6, 226, p. 226. DOI: 10.3847/1538-3881/ab4ef7. arXiv: 1910.10172 [astro-ph.SR].

De Rosa, R. J., E. L. Nielsen, Z. Wahhaj, et al. (Apr. 2023). "Direct imaging discovery of a super-Jovian around the young Sun-like star AF Leporis". In: *Astronomy and Astrophysics* 672, A94, A94. DOI: 10.1051/0004-6361/202345877. arXiv: 2302.06332 [astro-ph.EP].

Defrère, D., P. M. Hinz, et al. (Jan. 2015). "FIRST-LIGHT LBT NULLING INTERFEROMETRIC OBSERVATIONS: WARM EXOZODIACAL DUST RESOLVED WITHIN A FEW AU OF $\eta$ Crv". In: *The Astrophysical Journal* 799.1, p. 42. DOI: 10.1088/0004-637X/799/1/42. URL: https://dx.doi.org/10.1088/0004-637X/799/1/42.

Defrère, D., A. Bigioli, et al. (2022). "L-band nulling interferometry at the VLTI with Asgard/Hi-5: status and plans". In: *Optical and Infrared Interferometry and Imaging VIII*. Ed. by A. Mérand, S. Sallum, and J. Sanchez-Bermudez. Vol. 12183. International Society for Optics and Photonics. SPIE, 121830H. DOI: 10.1117/12.2627953. URL: https://doi.org/10.1117/12.2627953.

Delorme, J.-R. et al. (July 2021). "Keck Planet Imager and Characterizer: a dedicated single-mode fiber injection unit for high-resolution exoplanet spectroscopy". In: *Journal of Astronomical Telescopes, Instruments, and Systems* 7, 035006, p. 035006. DOI: 10.1117/1.JATIS.7.3.035006. arXiv: 2107.12556 [astro-ph.IM].

Echeverri, D., N. Jovanovic, et al. (Aug. 2022). "Phase II of the Keck Planet Imager and characterizer: system-level laboratory characterization and preliminary on-sky commissioning". In: *Ground-based and Airborne Instrumentation for Astronomy IX*. Ed. by C. J. Evans, J. J. Bryant, and K. Motohara. Vol. 12184. Society of Photo-Optical Instrumentation Engineers (SPIE) Conference Series, 121841W, 121841W. DOI: 10.1117/12.2630518. arXiv: 2210.15915 [astro-ph.EP].

Echeverri, D., G. Ruane, B. Calvin, et al. (Dec. 2020). "Detecting and characterizing close-in exoplanets with vortex fiber nulling". In: *Optical and Infrared Interferometry and Imaging VII*. Ed. by P. G. Tuthill, A. Mérand, and S. Sallum. Vol. 11446. Society of Photo-Optical Instrumentation Engineers (SPIE) Conference Series, 1144619, p. 1144619. DOI: 10.1117/12.2563142. arXiv: 2012.04239 [astro-ph.IM].

Echeverri, D., G. Ruane, N. Jovanovic, J.-R. Delorme, et al. (Sept. 2021). "Broadband vortex fiber nulling: high-dispersion exoplanet science at the diffraction limit". In: *Techniques and Instrumentation for Detection of Exoplanets X*. Ed. by S. B. Shaklan and G. J. Ruane. Vol. 11823. Society of Photo-Optical Instrumentation Engineers (SPIE) Conference Series, 118230A, 118230A. DOI: 10.1117/12.2597160. arXiv: 2210.15910 [astro-ph.EP].

Echeverri, D., G. Ruane, N. Jovanovic, T. Hayama, et al. (Sept. 2019). "The vortex fiber nulling mode of the Keck Planet Imager and Characterizer (KPIC)". In: *Society of Photo-Optical Instrumentation Engineers (SPIE) Conference Series*. Vol. 11117. Society of Photo-Optical Instrumentation Engineers (SPIE) Conference Series, 111170V, p. 111170V. DOI: 10.1117/12.2528529. arXiv: 1909.03538 [astro-ph.IM].

Echeverri, D., G. Ruane, N. Jovanovic, D. Mawet, et al. (May 2019). "Vortex fiber nulling for exoplanet observations I. Experimental demonstration in monochromatic light". In: *Optics Letters* 44.9, p. 2204. DOI: 10.1364/OL.44.002204. arXiv: 1811.02083 [astro-ph.IM].

Echeverri, D., J. W. Xuan, N. Jovanovic, J.-R. Delorme, et al. (2023). "First light of the vortex fiber nulling mode on the Keck planet imager and characterizer". In: *Techniques and Instrumentation for Detection of Exoplanets XI*. Ed. by G. J. Ruane. Vol. 12680. International Society for Optics and Photonics. SPIE, p. 126800M. DOI: 10.1117/12.2677656. URL: https://doi.org/10.1117/12.2677656.

Echeverri, D., J. W. Xuan, N. Jovanovic, G. Ruane, et al. (July 2023). "Vortex fiber nulling for exoplanet observations: implementation and first light". In: *Journal of Astronomical Telescopes, Instruments, and Systems* 9, 035002, p. 035002. DOI: 10.1117/1.JATIS.9.3.035002. arXiv: 2309.06514 [astro-ph.IM]. URL: https://doi.org/10.1117/1.JATIS.9.3.035002.

Franson, K. et al. (Feb. 2023). "Astrometric Accelerations as Dynamical Beacons: Discovery and Characterization of HIP 21152 B, the First T-dwarf Companion in the Hyades". In: *The Astronomical Journal* 165, p. 39. ISSN: 0004-6256. DOI: 10.3847/1538-3881/aca408. (Visited on 03/14/2023).

Fulton, B. J. et al. (July 2021). "California Legacy Survey. II. Occurrence of Giant Planets beyond the Ice Line". In: *The Astrophysical Journal Supplement Series* 255.1, 14, p. 14. DOI: 10.3847/1538-4365/abfcc1. arXiv: 2105.11584 [astro-ph.EP].

Gaia Collaboration (May 2021). "Gaia Early Data Release 3. Summary of the contents and survey properties". In: *Astronomy and Astrophysics* 649, A1, A1. DOI: 10.1051/0004-6361/202039657. arXiv: 2012.01533 [astro-ph.GA].

Gaia Collaboration et al. (Aug. 2018). "Gaia Data Release 2. Summary of the Contents and Survey Properties". In: *Astronomy and Astrophysics* 616, A1. ISSN: 0004-6361. DOI: 10.1051/0004-6361/201833051.

Gaudi, B. S. et al. (Jan. 2020). "The Habitable Exoplanet Observatory (HabEx) Mission Concept Study Final Report". In: *arXiv e-prints*, arXiv:2001.06683, arXiv:2001.06683. DOI: 10.48550/arXiv.2001.06683. arXiv: 2001.06683 [astro-ph.IM].

Gibson, R. K. et al. (Jan. 2020). "Characterization of the C-RED 2: a high-frame rate near-infrared camera". In: *Journal of Astronomical Telescopes, Instruments, and Systems* 6, 011002, p. 011002. DOI: 10.1117/1.JATIS.6.1.011002. arXiv: 1911.04567 [astro-ph.IM].

GRAVITY Collaboration et al. (June 2017). "First light for GRAVITY: Phase referencing optical interferometry for the Very Large Telescope Interferometer". In: *Astronomy and Astrophysics* 602, A94, A94. DOI: 10.1051/0004-6361/201730838. arXiv: 1705.02345 [astro-ph.IM].

Hinkley, S., S. Lacour, et al. (Mar. 2023). "Direct discovery of the inner exoplanet in the HD 206893 system. Evidence for deuterium burning in a planetary-mass companion". In: *Astronomy & Astrophysics* 671, L5, p. L5. DOI: 10.1051/0004-6361/202244727. arXiv: 2208.04867 [astro-ph.EP].

Hinkley, S., J. M. Carpenter, et al. (Apr. 2011). "Observational Constraints on Companions Inside of 10 AU in the HR 8799 Planetary System". In: *The Astrophysical Journal Letters* 730.2, L21, p. L21. DOI: 10.1088/2041-8205/730/2/L21. arXiv: 1102.3914 [astro-ph.EP].

Jovanovic, N., B. Calvin, et al. (Dec. 2020). "Enhanced high-dispersion coronagraphy with KPIC phase II: design, assembly and status of sub-modules". In: *Society of Photo-Optical Instrumentation Engineers (SPIE) Conference Series*. Vol. 11447. Society of Photo-Optical Instrumentation Engineers (SPIE) Conference Series, 114474U, 114474U. DOI: 10.1117/12.2563107. arXiv: 2012.06638 [astro-ph.IM].

Jovanovic, N., C. Schwab, et al. (Aug. 2017). "Efficient injection from large telescopes into single-mode fibres: Enabling the era of ultra-precision astronomy". In: *Astronomy and Astrophysics* 604, A122, A122. DOI: 10.1051/0004-6361/201630351. arXiv: 1706.08821 [astro-ph.IM].

Kervella, P. et al. (Mar. 2019). "Stellar and substellar companions of nearby stars from Gaia DR2. Binarity from proper motion anomaly". In: *Astronomy and Astrophysics* 623, A72, A72. DOI: 10.1051/0004-6361/201834371. arXiv: 1811.08902 [astro-ph.SR].

Konopacky, Q. M. et al. (Mar. 2013). "Detection of Carbon Monoxide and Water Absorption Lines in an Exoplanet Atmosphere". In: *Science* 339.6126, pp. 1398–1401. DOI: 10.1126/science.1232003. arXiv: 1303.3280 [astro-ph.EP].

Kotlyar, V. V. et al. (2007). "Diffraction of a finite-radius plane wave and a Gaussian beam by a helical axicon and a spiral phase plate". In: *J. Opt. Soc. Am. A* 24.7, pp. 1955–1964. DOI: 10.1364/JOSAA.24.001955.

Kuzuhara, M. et al. (Aug. 2022). "Direct-imaging Discovery and Dynamical Mass of a Substellar Companion Orbiting an Accelerating Hyades Sun-like Star with SCExAO/CHARIS". In: *The Astrophysical Journal Letters* 934.2, L18, p. L18. DOI: 10.3847/2041-8213/ac772f. arXiv: 2205.02729 [astro-ph.SR].

López, R. A. et al. (Dec. 2020). "Characterization and performance of the upgraded NIRSPEC on the W. M. Keck Telescope". In: *Society of Photo-Optical Instrumentation Engineers (SPIE) Conference Series*. Vol. 11447. Society of Photo-Optical Instrumentation Engineers (SPIE) Conference Series, 114476B, 114476B. DOI: 10.1117/12.2563075.

Lovis, C. et al. (Mar. 2017). "Atmospheric characterization of Proxima b by coupling the SPHERE high-contrast imager to the ESPRESSO spectrograph". In: *Astronomy and Astrophysics* 599, A16, A16. DOI: 10.1051/0004-6361/201629682. arXiv: 1609.03082 [astro-ph.EP].

Macintosh, B. et al. (Sept. 2014). "First light of the Gemini Planet Imager". In: *Proceedings of the National Academy of Science* 111.35, pp. 12661–12666. DOI: 10.1073/pnas.1304215111. arXiv: 1403.7520 [astro-ph.EP].

Martin, E. C. et al. (2018). "An overview of the NIRSPEC upgrade for the Keck II telescope". In: *Proc. SPIE* 10702, 107020A. DOI: 10.1117/12.2312266.

Mason, B. D. et al. (June 2021). "VizieR Online Data Catalog: The Washington Visual Double Star Catalog (Mason+ 2001-2020)". In: *VizieR Online Data Catalog*, B/wds, B/wds.

Mawet, D., J.-R. Delorme, et al. (2017). "A fiber injection unit for the Keck Planet Imager and Characterizer". In: *Proc. SPIE* 10400, p. 1040029. DOI: 10.1117/12.2274891. URL: http://dx.doi.org/10.1117/12.2274891.

Mawet, D., E. Serabyn, et al. (Jan. 2010). "The Vector Vortex Coronagraph: Laboratory Results and First Light at Palomar Observatory". In: *The Astrophysical Journal* 709.1, pp. 53–57. DOI: 10.1088/0004-637X/709/1/53. arXiv: 0912.2287 [astro-ph.IM].

Mawet, D., M. P. Fitzgerald, et al. (Aug. 2022). "Fiber-fed high-resolution infrared spectroscopy at the diffraction limit with Keck-HISPEC and TMT-MODHIS: status update". In: *Ground-based and Airborne Instrumentation for Astronomy IX*. Ed. by C. J. Evans, J. J. Bryant, and K. Motohara. Vol. 12184. Society of Photo-Optical Instrumentation Engineers (SPIE) Conference Series, 121841R, 121841R. DOI: 10.1117/12.2630142.

McLean, I. S., E. E. Becklin, et al. (Aug. 1998). "Design and development of NIRSPEC: a near-infrared echelle spectrograph for the Keck II telescope". In: *Infrared Astronomical Instrumentation*. Ed. by A. M. Fowler. Vol. 3354. Society of Photo-Optical Instrumentation Engineers (SPIE) Conference Series, pp. 566–578. DOI: 10.1117/12.317283.

McLean, I. S., J. R. Graham, et al. (Aug. 2000). "Performance and results with the NIRSPEC echelle spectrograph on the Keck II telescope". In: *Optical and IR Telescope Instrumentation and Detectors*. Ed. by M. Iye and A. F. Moorwood. Vol. 4008. Society of Photo-Optical Instrumentation Engineers (SPIE) Conference Series, pp. 1048–1055. DOI: 10.1117/12.395422.

National Academies of Sciences, Engineering, and Medicine (2021). *Pathways to Discovery in Astronomy and Astrophysics for the 2020s*. The National Academies Press. ISBN: 978-0-309-46586-1. DOI: 10.17226/26141.

Neuhäuser, R. et al. (May 2005). "Evidence for a co-moving sub-stellar companion of GQ Lup". In: *Astronomy and Astrophysics* 435.1, pp. L13–L16. DOI: 10.1051/0004-6361:200500104. arXiv: astro-ph/0503691 [astro-ph].

Nielsen, E. L. et al. (July 2019). "The Gemini Planet Imager Exoplanet Survey: Giant Planet and Brown Dwarf Demographics from 10 to 100 au". In: *The Astronomical Journal* 158.1, 13, p. 13. DOI: 10.3847/1538-3881/ab16e9. arXiv: 1904.05358 [astro-ph.EP].

Perryman, M. A. C. et al. (July 1997). "The HIPPARCOS Catalogue". In: *Astronomy and Astrophysics* 323, pp. L49–L52. DOI: https://ui.adsabs.harvard.edu/abs/1997A&A...323L..49P.

Pourbaix, D. et al. (Sept. 2004). "SB$^9$: The ninth catalogue of spectroscopic binary orbits". In: *Astronomy and Astrophysics* 424, pp. 727–732. DOI: 10.1051/0004-6361:20041213. arXiv: astro-ph/0406573 [astro-ph].

Pourré, N. et al. (Aug. 2022). "Digging a dark hole in GRAVITY: towards Jupiter-like observations at the astronomical unit scale". In: *Optical and Infrared Interferometry and Imaging VIII*. Ed. by A. Mérand, S. Sallum, and J. Sanchez-Bermudez. Vol. 12183. Society of Photo-Optical Instrumentation Engineers (SPIE) Conference Series, 121830V, p. 121830V. DOI: 10.1117/12.2629823.

Ren, B. B. et al. (Feb. 2023). "Planet search with the Keck/NIRC2 vortex coronagraph in the $M_s$ band for Vega". In: *Astronomy and Astrophysics* 670, A162, A162. DOI: 10.1051/0004-6361/202244485. arXiv: 2301.07714 [astro-ph.EP].

Rosenthal, L. J. et al. (July 2021). "The California Legacy Survey. I. A Catalog of 178 Planets from Precision Radial Velocity Monitoring of 719 Nearby Stars over Three Decades". In: *The Astrophysical Journal Supplement Series* 255.1, 8, p. 8. DOI: 10.3847/1538-4365/abe23c. arXiv: 2105.11583 [astro-ph.EP].

Ross, T. S. (Apr. 2009). "Limitations and applicability of the Maréchal approximation". In: *Appl. Opt.* 48.10, pp. 1812–1818. DOI: 10.1364/AO.48.001812. URL: https://opg.optica.org/ao/abstract.cfm?URI=ao-48-10-1812.

Ruane, G., D. Echeverri, et al. (Sept. 2019). "Vortex fiber nulling for exoplanet observations: conceptual design, theoretical performance, and initial scientific yield predictions". In: *Society of Photo-Optical Instrumentation Engineers (SPIE) Conference Series*. Vol. 11117. Society of Photo-Optical Instrumentation Engineers

(SPIE) Conference Series, 1111716, p. 1111716. DOI: 10.1117/12.2528555. arXiv: 1908.09780 [astro-ph.IM].

Ruane, G., D. Mawet, et al. (Sept. 2019). "Scalar vortex coronagraph mask design and predicted performance". In: *Society of Photo-Optical Instrumentation Engineers (SPIE) Conference Series*. Vol. 11117. Society of Photo-Optical Instrumentation Engineers (SPIE) Conference Series, 111171F, 111171F. DOI: 10.1117/12.2528625. arXiv: 1908.09786 [astro-ph.IM].

Ruane, G., J. Wang, et al. (Nov. 2018). "Efficient Spectroscopy of Exoplanets at Small Angular Separations with Vortex Fiber Nulling". In: *Astrophysical Journal* 867.2, 143, p. 143. DOI: 10.3847/1538-4357/aae262. arXiv: 1809.06483 [astro-ph.IM].

Ruffio, J.-B., K. Horstman, et al. (Mar. 2023). "Detecting Exomoons from Radial Velocity Measurements of Self-luminous Planets: Application to Observations of HR 7672 B and Future Prospects". In: *The Astronomical Journal* 165.3, 113, p. 113. DOI: 10.3847/1538-3881/acb34a. arXiv: 2301.04206 [astro-ph.EP].

Ruffio, J.-B., Q. M. Konopacky, et al. (Dec. 2021). "Deep Exploration of the Planets HR 8799 b, c, and d with Moderate-resolution Spectroscopy". In: *AJ* 162, p. 290. ISSN: 0004-6256. DOI: 10.3847/1538-3881/ac273a.

Sallum, S. and A. Skemer (Jan. 2019). "Comparing nonredundant masking and filled-aperture kernel phase for exoplanet detection and characterization". In: *Journal of Astronomical Telescopes, Instruments, and Systems* 5, 018001, p. 018001. DOI: 10.1117/1.JATIS.5.1.018001. arXiv: 1901.01266 [astro-ph.IM].

Serabyn, E. et al. (Oct. 2019). "Nulling at short wavelengths: theoretical performance constraints and a demonstration of faint companion detection inside the diffraction limit with a rotating-baseline interferometer". In: *Mon. Notices Royal Astron. Soc.* 489.1, pp. 1291–1303. DOI: 10.1093/mnras/stz2163. arXiv: 1908.05977 [astro-ph.IM].

Snellen, I. A. G., B. R. Brandl, et al. (May 2014). "Fast spin of the young extrasolar planet $\beta$ Pictoris b". In: *Nature* 509.7498, pp. 63–65. DOI: 10.1038/nature13253.

Snellen, I. A. G., R. J. de Kok, et al. (Apr. 2015). "Combining high-dispersion spectroscopy with high contrast imaging: Probing rocky planets around our nearest neighbors". In: *Astronomy & Astrophysics* 576, A59, A59. DOI: 10.1051/0004-6361/201425018. arXiv: 1503.01136 [astro-ph.EP].

Swartzlander, G. A. (2001). "Peering into darkness with a vortex spatial filter". In: *Opt. Lett.* 26.8, pp. 497–499. DOI: 10.1364/OL.26.000497.

– (Sept. 2009). "The optical vortex coronagraph". In: *Journal of Optics A: Pure and Applied Optics* 11.9, 094022, p. 094022. DOI: 10.1088/1464-4258/11/9/094022.

Swihart, S. J. et al. (Jan. 2017). "A Catalog of Calibrator Stars for Next-generation Optical Interferometers". In: *The Astronomical Journal* 153.1, 16, p. 16. DOI: 10.3847/1538-3881/153/1/16. arXiv: 1610.04600 [astro-ph.SR].

The LUVOIR Team (Dec. 2019). "The LUVOIR Mission Concept Study Final Report". In: *arXiv e-prints*, arXiv:1912.06219, arXiv:1912.06219. DOI: 10.48550/arXiv.1912.06219. arXiv: 1912.06219 [astro-ph.IM].

van Kooten, M. A. et al. (Sept. 2021). "Status of predictive wavefront control on Keck II adaptive optics bench: on-sky coronagraphic results". In: *Techniques and Instrumentation for Detection of Exoplanets X*. Ed. by S. B. Shaklan and G. J. Ruane. Vol. 11823. Society of Photo-Optical Instrumentation Engineers (SPIE) Conference Series, 118231F, 118231F. DOI: 10.1117/12.2594863. arXiv: 2108.08932 [astro-ph.IM].

van Leeuwen, F. (Nov. 2007). "Validation of the New Hipparcos Reduction". In: *Astronomy and Astrophysics* 474, pp. 653–664. ISSN: 0004-6361. DOI: 10.1051/0004-6361:20078357.

Vigan, A. et al. (July 2021). "The SPHERE infrared survey for exoplanets (SHINE). III. The demographics of young giant exoplanets below 300 au with SPHERE". In: *Astronomy and Astrophysics* 651, A72, A72. DOI: 10.1051/0004-6361/202038107. arXiv: 2007.06573 [astro-ph.EP].

Wang, J. J., J.-B. Ruffio, et al. (Oct. 2021). "Detection and Bulk Properties of the HR 8799 Planets with High-resolution Spectroscopy". In: *The Astronomical Journal* 162.4, 148, p. 148. DOI: 10.3847/1538-3881/ac1349. arXiv: 2107.06949 [astro-ph.EP].

Wang, J. J., J. K. Wallace, et al. (Dec. 2020). "An atmospheric dispersion corrector design with milliarcsecond-level precision from 1 to 4 microns for high dispersion coronagraphy". In: *Society of Photo-Optical Instrumentation Engineers (SPIE) Conference Series*. Society of Photo-Optical Instrumentation Engineers (SPIE) Conference Series 11447, 1144754, p. 1144754. DOI: 10.1117/12.2562654. arXiv: 2012.06007 [astro-ph.IM].

Wang, J., J. R. Kolecki, et al. (Apr. 2022). "Retrieving the C and O Abundances of HR 7672 AB: A Solar-type Primary Star with a Benchmark Brown Dwarf". In: *The Astronomical Journal* 163.4, 189, p. 189. DOI: 10.3847/1538-3881/ac56e2. arXiv: 2202.02477 [astro-ph.EP].

Wang, J., D. Mawet, et al. (Apr. 2017). "Observing Exoplanets with High Dispersion Coronagraphy. I. The Scientific Potential of Current and Next-generation Large Ground and Space Telescopes". In: *The Astronomical Journal* 153.4, 183, p. 183. DOI: 10.3847/1538-3881/aa6474. arXiv: 1703.00582 [astro-ph.EP].

Wang, J., J. J. Wang, et al. (Jan. 2023). "Retrieving C and O Abundance of HR 8799 c by Combining High- and Low-resolution Data". In: *The Astronomical Journal* 165.1, 4, p. 4. DOI: 10.3847/1538-3881/ac9f19. arXiv: 2209.15484 [astro-ph.EP].

Wizinowich, P. et al. (2000). “First Light Adaptive Optics Images from the Keck II Telescope: A New Era of High Angular Resolution Imagery”. In: *Publications of the Astronomical Society of the Pacific* 112, pp. 315–319. DOI: 10.1086/316543.

Wizinowich, P. (Oct. 2015). “Adaptive optics in astronomy”. In: *Contemporary Physics* 56.4, pp. 432–450. DOI: 10.1080/00107514.2015.1041765.

Xuan, J. W., M. L. Bryan, et al. (Mar. 2020). “A Rotation Rate for the Planetary-Mass Companion DH Tau b”. In: *The Astronomical Journal* 159, p. 97. ISSN: 0004-6256. DOI: 10.3847/1538-3881/ab67c4.

Xuan, J. W., J. Wang, et al. (Oct. 2022). “A Clear View of a Cloudy Brown Dwarf Companion from High-resolution Spectroscopy”. In: *The Astrophysical Journal* 937 (2), p. 54. ISSN: 0004-637X. DOI: 10.3847/1538-4357/ac8673.

*Chapter 7*

# KPIC VFN DETECTIONS

The previous chapter presented the as-built and deployed characterization of the first on-sky VFN demonstrator, yielding SNR and sensitivity predictions based on the measured first-light performance. Thus, so far in this thesis, we have taken the VFN technique from a theoretical concept to a working observing mode at a major telescope. This chapter now presents the first science results from the instrument. Using the KPIC VFN demonstrator, we detected 3 faint M-dwarf companions with flux ratios between 70 and 430 and at separations of 35-55 mas ($0.7-1.2\,\lambda/D$ at 2.3 $\mu$m). Though these results deal with low-mass stellar companions ($\sim$0.15$-$0.32 $M_\odot$), and so do not reach down to planetary mass, they provide a first-glimpse at the scientific potential of VFN. Of note, the results here represent the first direct detection of all three of these companions, as they were previously only known from RV and/or astrometric observations. These results also represent the first demonstration of high-spectral-resolution nulling on-sky, paving the way for future nulling techniques and instruments.

---

## Vortex Fiber Nulling for Exoplanet Observations: First Direct Detection of M Dwarf Companions around HIP 21543, HIP 50319, and HIP 94666

Echeverri, D. et al. (Apr. 2024). "Vortex Fiber Nulling for Exoplanet Observations: First Direct Detection of M Dwarf Companions around HIP 21543, HIP 94666, and HIP 50319". In: *The Astrophysical Journal Letters* 965.2, L15, p. L15. DOI: 10.3847/2041-8213/ad3619. arXiv: 2403.17295 [astro-ph.EP].

**Abstract**

Vortex fiber nulling (VFN) is a technique for detecting and characterizing faint companions at small separations from their host star. A near-infrared ($\sim$2.3 $\mu$m) VFN demonstrator mode was deployed on the Keck Planet Imager and Characterizer (KPIC) instrument at the Keck Observatory and presented earlier. In this paper,

we present the first VFN companion detections. Three targets, HIP 21543 Ab, HIP 94666 Ab, and HIP 50319 B, were detected with host-companion flux ratios between 70 and 430 at and within one diffraction beamwidth. We complement the spectra from KPIC VFN with flux ratio and position measurements from the CHARA Array to validate the VFN results and provide a more complete characterization of the targets. This paper reports the first direct detection of these three M dwarf companions, yielding their first spectra and flux ratios. Our observations provide measurements of bulk properties such as effective temperatures, radial velocities, and vsin $i$, and verify the accuracy of the published orbits. These detections corroborate earlier predictions of the KPIC VFN performance, demonstrating that the instrument mode is ready for science observations.

## 7.1 Introduction

Decades of radial velocity (RV) surveys have revealed that giant planets are most likely to orbit between 1-10 AU from their host stars (Fulton et al., 2021; Rosenthal et al., 2021). This puts the bulk of the giant planet population inside the inner working angle of conventional coronagraphs (Macintosh et al., 2014; Beuzit et al., 2019), meaning that interferometry provides the best opportunity for detecting these planets in the near-infrared. Vortex fiber nulling (VFN) is a single-aperture interferometric technique for detecting and characterizing faint companions at small separations (Ruane, J. Wang, et al., 2018; Echeverri, Ruane, Jovanovic, Mawet, et al., 2019; Ruane, Echeverri, et al., 2019; Echeverri, Ruane, Jovanovic, Delorme, et al., 2021). VFN's simple optical design makes it easy to implement on existing and upcoming high-contrast imaging instruments with a fiber injection unit, thereby providing access to companions at $\lesssim 1\ \lambda/D$ ($\lesssim$5 AU at 100 parsec for wavelength $\lambda$=2.3 $\mu$m and telescope diameter $D$=10 m). An on-sky VFN demonstrator is now operational (Echeverri, Xuan, et al., 2023) in the Keck Planet Imager and Characterizer (KPIC - Mawet, 2021; Delorme et al., 2021; Echeverri, Jovanovic, et al., 2022; Jovanovic et al. in prep.) instrument at the Keck II Telescope. Ignoring systematics such as fringing, the KPIC VFN mode's on-sky performance is sufficient for detecting companions in 1 hour in K band (2.0-2.4 $\mu$m) at separations of 30-80 mas and 1000 times fainter than their host (Echeverri, Xuan, et al., 2023). We now present the first detections using this new mode.

The nominal KPIC observing mode, referred to as direct spectroscopy (DS) since it aligns a single-mode fiber directly to the desired target, does not use a coronagraph and provides $R\sim$35,000 spectra that have been used extensively to spectroscopically

characterize exoplanets and brown dwarf companions (J. J. Wang et al., 2021; J. Wang, Kolecki, et al., 2022; J. Wang, J. J. Wang, et al., 2023; Ruffio et al., 2023; Delorme et al., 2021; Xuan et al., 2022; Finnerty, Schofield, Sappey, et al., 2023). The KPIC VFN mode provides similar spectra at smaller separations without requiring prior knowledge of the exact position of the companion, thereby allowing it to detect new companions. However, its single axially-symmetric detection region cannot constrain the companion position nor flux ratio, as the two parameters are degenerate. We therefore complement the KPIC VFN observations in this paper with CHARA observations using the MIRC-X/MYSTIC beam combiners (Anugu et al., 2020; Setterholm et al., 2023), which have a demonstrated history of success at these angular separations (e.g., Roettenbacher, Monnier, Fekel, et al., 2015; Roettenbacher, Monnier, Henry, et al., 2015; Thomas et al., 2021; De Furio et al., 2022; Lanthermann et al., 2023)

The three companions covered here were previously known only from RV and/or astrometric observations. Our results therefore present their first direct detections, and provide the first spectra and flux ratios for the companions.

### 7.2 Targets

We targeted three nearby G stars with known companions at small separations. Table 7.1 lists the targets and basic parameters of the primary star while the remainder of this section provides previously-known details on each target.

**HIP 21543** (HD 29310, vB 102) is a triple system in the Hyades cluster with an inner single-lined spectroscopic binary (SB1) on a $734 \pm 0.3$ day orbit and an outer visual companion on a 128 year orbit (Griffin, 2012; Tokovinin, 2018; Griffin et al., 1988; Mason, McAlister, et al., 1993). The inner SB1 is the target of this paper. Tokovinin, 2021 combines RV observations with the astrometric wobble of the outer companion (referred to as B) to provide a refined orbit for both the inner (referred to as Aa,Ab) and outer components. The mass ratio for Aa,Ab from their orbits is 0.29 such that given the estimated mass for Aa of 1.13 $M_{\odot}$, Ab is about 0.32 $M_{\odot}$. Bender et al., 2008 reported weak lines from Ab, which would make this a double-lined spectroscopic binary with a direct detection, but Tokovinin, 2021 found that the measured RVs for the Ab lines are inconsistent with the astrometric wobble measurements. We note that the Tokovinin, 2021 orbits show Ab and B counter-orbiting around the central Aa star, implying an unusual orbital architecture for the system.

An orbit for the inner Aa,Ab component is also reported in the Gaia DR3 non-single star (NSS) solutions (Gaia Collaboration et al., 2022; Holl et al., 2023). The listed orbital period is 739 ± 7 days, consistent with the Tokovinin, 2021 value. From isochrone fitting, Gaia estimates the mass of Aa at 1.01 ± 0.06 $M_\odot$ which allows them to predict the mass of Ab at 0.21 ± 0.03 $M_\odot$ (see Gaia DR3 `binary_masses` table, Gaia Collaboration et al. 2022). With the Gaia-derived masses, we roughly estimate the ΔK mag between Aa and Ab. For Aa, we use the 2MASS K magnitude assuming it is dominated by the brighter primary star and neglecting its variability as a BY Draconis variable since the V band variability amplitude is only 0.03 mag (Lockwood et al., 1984), and likely even less in K band. Thus we estimate an absolute magnitude $M_K = 2.77$ given the Gaia parallax of 22.69 mas for the distance. For Ab, we use the latest version of the main-sequence dwarf table (MSDT) by Pecaut et al. (2013) to estimate $M_K \approx 7.6$ assuming 0.21 $M_\odot$. This gives ΔK ∼ 4.83 for a flux ratio of ∼85 between the stars. A similar procedure but using the Tokovinin masses yields ΔK ∼ 4.06 (flux ratio ∼40).

**HIP 94666** (HD 180683) is also a triple system. There is an inner SB1 (Aa,Ab) with an orbital period of 1210 days provided by Tokovinin, 2018. The outer visual companion, B, is on a ∼3000 year orbit at 3.6" (Riddle et al., 2015; Roberts et al., 2017). Though a full orbital solution is not provided in these prior works, the Gaia DR3 NSS table has a solution with a period of 1211 ± 29 days that is consistent with the published period for Aa,Ab. Gaia did not spectroscopically detect this system, so the `binary_masses` table only provides a mass for Aa, $1.11^{+0.06}_{-0.10}$ $M_\odot$. However, given the primary mass, we can solve for the mass ratio, $q$, between Ab/Aa using the Thiele-Innes orbital elements from Gaia DR3 NSS. We obtain $q \approx 0.22$ which yields ∼0.24 $M_\odot$ for Ab. We estimate the flux ratio as done for HIP 21543; the 2MASS K magnitude yields an absolute $M_K = 2.23$ for Aa given the 15.52 mas Gaia parallax and the MSDT yields $M_K \approx 7.3$ for Ab. We thus predict ΔK ∼ 5.07 (flux ratio ∼105).

**HIP 50319** (HD 89010, 35 Leo) is a SB1 binary (A,B) with an orbital period of ∼537 days (Tokovinin, 2014). The Gaia NSS table again provides a full orbital solution, with a period of 524 ± 6 days. The `binary_masses` table does not provide a mass for either star so we use the Tokovinin, 2014 mass of ∼1.34 $M_\odot$ for A and the Gaia orbit to determine a mass ratio $q \approx 0.11$, and hence a mass for B of ∼0.15 $M_\odot$. As done for the other two targets, the 2MASS K magnitude gives an absolute $M_K = 1.88$ for A given the 32.09 mas Gaia parallax. From the MSDT, $M_K \approx 8.4$ for B, so we estimate ΔK ∼ 6.52 (flux ratio ∼405).

Table 7.1: Targets and Observations

| Target (HIP) | Mag. (K band) | Spec. Type | Dist. (pc) | Pred. Flux Ratio (K) | Date Observed (UT) | Instrument | Obs. Band | Spectral Resol. | Int. Time (min) | Pred. Sep. (mas ; AU [; $\lambda/D$][a] ) | Pred. RV (km/s) | Bary. RV (km/s) |
|---|---|---|---|---|---|---|---|---|---|---|---|---|
| 21543 | 5.992 | G0 | 44.1 | 40-85 | 2022 Oct 12 | VFN | K | 35,000 | 36[b] | 48.7 ; 2.1 ; 1.0 | -7.9 | 22.8 |
| | | | | | 2021 Oct 22 | MIRC-X<br>MYSTIC | H<br>K | 50<br>50 | 10 | 20.5 ; 0.9 | | |
| | | | | | 2022 Sep 22 | MIRC-X<br>MYSTIC | H<br>K | 50<br>100 | 28 | 47.3 ; 2.1 | | |
| 94666 | 6.280 | G0 | 64.4 | 105 | 2023 May 09 | VFN | K | 35,000 | 48 | 37.3 ; 2.4 ; 0.8 | 13.5 | 14.1 |
| | | | | | 2023 May 15 | MIRC-X<br>MYSTIC | H<br>K | 50<br>100 | 9 | 38.1 ; 2.5 | | |
| 50319 | 4.345 | G0 | 31.2 | 405 | 2023 May 06 | VFN | K | 35,000 | 123 | 48.7 ; 1.5 ; 1.0 | -9.2 | -28.3 |
| | | | | | 2023 May 23 | MIRC-X<br>MYSTIC | H<br>K | 50<br>50 | 46 | 41.9 ; 1.3 | | |
| | | | | | 2023 May 24 | MIRC-X<br>MYSTIC | H<br>K | 50<br>50 | 37 | 41.5 ; 1.3 | | |

[a] $\lambda/D$ only provided for VFN observations, assuming $\lambda = 2.3$ $\mu$m and $D = 10$ m.

[b] Observations were made on two fibers, with 36 min per fiber. Only one fiber was used for the analysis.

NOTE- K magnitude from the 2MASS All-Sky Catalog. Spectral type from the Henry Draper Catalog and Extension. Distance derived from parallax in the Gaia DR3 NSS table. Predicted flux ratio is explained in Sec. 7.2. Integration times do not include calibrators, only the on-source time integrating for the companion. Predicted separation and RV at the time of observation use the Gaia NSS orbital solution, except for HIP 21543 for which the Tokovinin, 2021 orbit was used. Pred. RV is the relative value between the primary and companion. Earth barycentric RV is computed as the average over the dataset. RV values only provided for the VFN data since CHARA cannot measure them.

## 7.3 Observations and Data Analysis

Observations of the three targets were made with both KPIC VFN and CHARA MIRC-X/MYSTIC. VFN provides high-resolution spectra while CHARA gives the position and flux ratio. This lets us verify the VFN performance in terms of calibrated flux ratio and also ensures that the published orbital parameters are well-enough constrained that the target was indeed within the current VFN field of view (~30-80 mas) at the time of observation. Table 7.1 lists observing parameters including dates, spectral band, spectral resolution, and integration time. It also lists the predicted flux ratio, separation, and relative RV at the time of observation based on the published orbits summarized above. The listed barycentric RV, computed with the `Astropy` python package, was used to translate our measured RVs from the instrument frame to the Earth-Sun barycenter, such that RVs are reported with respect to this point.

The VFN observations are done following a similar procedure to that presented in previous KPIC papers (e.g., J. J. Wang et al., 2021). This involves: (1) observing a M giant to derive a wavelength solution, (2) observing a A0 standard star to sample the telluric transmission, (3) observing the primary star, and then (4) observing the companion. However, in contrast with the direct spectroscopy (DS) observations where we offset the fiber to the companion in step four, VFN stays on-axis but inserts a vortex mask so that the primary star is nulled and the companion is preferentially coupled. The analysis procedure is nevertheless identical to that used for KPIC DS observations. That is, we jointly fit the VFN mode spectra with contributions from the primary and the companion, along with a physical model of the fringing introduced by Fabry-Perot cavities from transmissive optics in the instrument (Finnerty, Schofield, Delorme, et al., 2022, Xuan et al., submitted). To model the primary star signal, we use the empirical spectra from on-axis DS observations taken in step three above. This assumes the companion signal is negligible compared to the primary star signal since the companion is significantly fainter and less-efficiently coupled. For the companion model, we interpolate over a grid of BT-Settl (CIFIST) spectra (Allard et al., 2012), varying effective temperature ($T_{\rm eff}$) and surface gravity ($\log g$) while assuming solar metallicity. Additionally, we fit the RV shift and projected rotational rate ($v \sin i$) of the companion. For more details on the forward model framework, see J. J. Wang et al., 2021 and Xuan et al., 2022. We only use KPIC echelle order 6 (~2.29 to 2.34 $\mu$m - NIRSPEC order 33) in this paper since it covers the CO bandhead where we expect many strong absorption lines from the M dwarf companions. Furthermore, this echelle order is

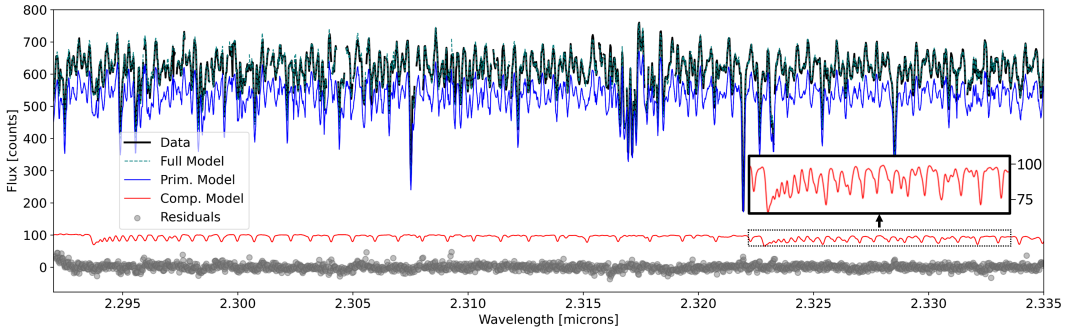


Figure 7.1: Spectrum at R∼35,000 from VFN observations of HIP 21543. Only KPIC echelle order 6, the one used for the forward model fits, is shown. The raw spectrum has been median-filtered to remove the continuum and is in solid black while best-fit full model is in dashed cyan; the two often overlap such that combined, they may appear green. Various components of the best-fit model are also shown: primary star spectrum (blue), companion spectrum (red), and residuals (grey dots). The companion spectrum is about five times fainter than that of the primary after partial nulling of the latter by VFN.

close to the central wavelength of 2.225 $\mu$m where the vortex provides the deepest nulls (Echeverri, Xuan, et al., 2023). Figure 7.1 shows the observed spectrum for HIP 21543 along with the best-fit model and its various components, as an example of the elements that go into the forward model and how it compares to the data. For a consistency check, we also do a dedicated fit to the DS mode (i.e., no nulling) spectra using BT-Settl models to obtain properties for the primary, including its RV which is used to derive a relative RV between the primary and companion. This relative RV is compared to the expected value from the published orbits.

The Michigan InfraRed Combiner – eXeter (MIRC-X – Anugu et al., 2020) and the Michigan Young STar Imager (MYSTIC - Setterholm et al., 2023) on the Georgia State University Center for High Angular Resolution Astronomy (CHARA) Array (ten Brummelaar et al., 2005) were used to search for binary companions to all three targets. HIP 94666 and HIP 50319 were observed in 2023 specifically for a brief VFN follow-up program, with the HIP 50319 observations occurring on two nights. HIP 21543 had been observed twice in the past for other programs, so we used these archival data. See Table 7.1 for additional observing information. We reduce the interferometric data with the public `mircx_pipeline` (Anugu et al., 2020). After transfer function calibration using stars with known sizes estimated by Search Cal (Chelli et al., 2016), we look for a binary companion using a simple grid search, fitting only to the closure phases, and fixing the diameter of the primary

estimated from photometry (0.26 mas for HIP 21543 and 0.53 mas for HIP 50319; irrelevant for HIP 94666 due to non-detection with CHARA). Simultaneous MIRC-X and MYSTIC data were taken on each night. However, each instrument had different spectral resolutions and thus different interferometric fields-of-view and contrast sensitivities. Coupled with varying seeing conditions and different total observing times, there are some nights for which we are unable to recover reliable companion detections with both instruments. We report our results in Table 7.3, where we have applied the final wavelength correction terms found in Torres et al. (2022). With such a limited "pilot program" dataset, our error estimate procedure is crude and uncertain; position errors are estimated using a simple analysis of the chi-squared surface immediately surrounding the best-fit companion position (see Fig. 7.2), while upper limits on contrasts are derived from the contrast ratios from the best-fitting noise peaks.

## 7.4 Results and Discussion

The VFN observations yielded confident detections on two of the companions while the third, HIP 50319 B, gave a tentative detection. The CHARA observations yielded two confident detections and one non-detection, HIP 94666 Ab. We make a first pass here at characterization to showcase the science capabilities of VFN, especially when combined with input from CHARA. Tables 7.2 and 7.3 summarize the best-fit values derived from the VFN and CHARA observations, respectively. The CHARA results provide the first flux ratio and direct position measurements for the companions. The VFN fits fail to properly constrain $\log g$ for the companions, which is partly due to the relatively low SNR and small wavelength coverage ($\sim$2.29$-$2.34 $\mu$m). In addition, constraining fundamental properties of M dwarfs, such as $T_{\rm eff}$ and $\log g$, is a challenging task and still remains somewhat model-dependent (e.g., Rajpurohit et al., 2018). We nevertheless provide the first constraints on RV, $v \sin i$, and $T_{\rm eff}$ for these companions. Given the high amplitude of residual primary flux in VFN spectra, the fringing signal is stronger than in previous KPIC DS papers. Thus, fringing is the dominant error in these VFN results, though its effect will be mitigated in future observations (see Sec. 7.5).

Table 7.2: Fitted Parameters from VFN

| Target (HIP) | MJD | Prim. RV (km/s) | Comp. RV (km/s) | Rel. RV (km/s) | $T_{\rm eff}$ ($K$) | $v \sin i$ (km/s) |
|---|---|---|---|---|---|---|
| 21543 | 59864.52 | $37.0^{+0.5}_{-0.6}$ | $45.3^{+0.4}_{-0.5}$ | $-8.3^{+0.6}_{-0.8}$ | $3480^{+90}_{-70}$ | $9.7^{+2.1}_{-0.9}$ |
| 94666 | 60073.62 | $-10.2^{+0.2}_{-0.2}$ | $-24.6^{+0.6}_{-0.5}$ | $14.4^{+0.6}_{-0.5}$ | $4090^{+320}_{-230}$ | $< 7.2$[a] |
| 50319 | 60070.29 | $-35.4^{+0.1}_{-0.1}$ | $-17.2^{+0.9}_{-0.8}$ | $-18.2^{+0.9}_{-0.8}$ | $3300^{+130}_{-140}$ | $< 10.1$[a] |

[a] Upper limit set at $2\sigma$.

NOTE- MJD is the average value during the observation. Primary and companion RV values are with respect to the Earth-Sun barycenter using the barycentric RV correction from Table 7.1. $T_{\rm eff}$ and $v \sin i$ in this table are for the companion.

Table 7.3: Fitted Parameters from CHARA

| Target (HIP) | MJD | Instrument | Flux Ratio | Obs. Band | Sep. (mas) | PA (E of N) | Error Ellipse | | |
|---|---|---|---|---|---|---|---|---|---|
| | | | | | | | Major Ax. (mas) | Minor Ax. (mas) | PA of Major Ax. (°) |
| 21543 | 59509.323 | MIRC-X | 73 | H | 18.95 | 31.83 | 0.15 | 0.10 | 313 |
| | | MYSTIC | 59 | K | 18.88 | 32.28 | 0.10 | 0.07 | 326 |
| | 59844.485 | MIRC-X | 75 | H | 50.24 | 170.35 | 0.12 | 0.08 | 344 |
| | | MYSTIC | 81 | K | 50.43 | 170.37 | 0.70 | 0.50 | 66 |
| 94666 | 60079.470 | MIRC-X | > 70 | H | ... | ... | ... | ... | ... |
| | | MYSTIC | > 40 | K | ... | ... | ... | ... | ... |
| 50319 | 60087.201 | MIRC-X | > 180 | H | ... | ... | ... | ... | ... |
| | | MYSTIC | 407 | K | 56.83 | 71.64 | 0.26 | 0.11 | 69 |
| | 60088.201 | MIRC-X | > 200 | H | ... | ... | ... | ... | ... |
| | | MYSTIC | 451 | K | 57.00 | 71.81 | 0.69 | 0.31 | 65 |

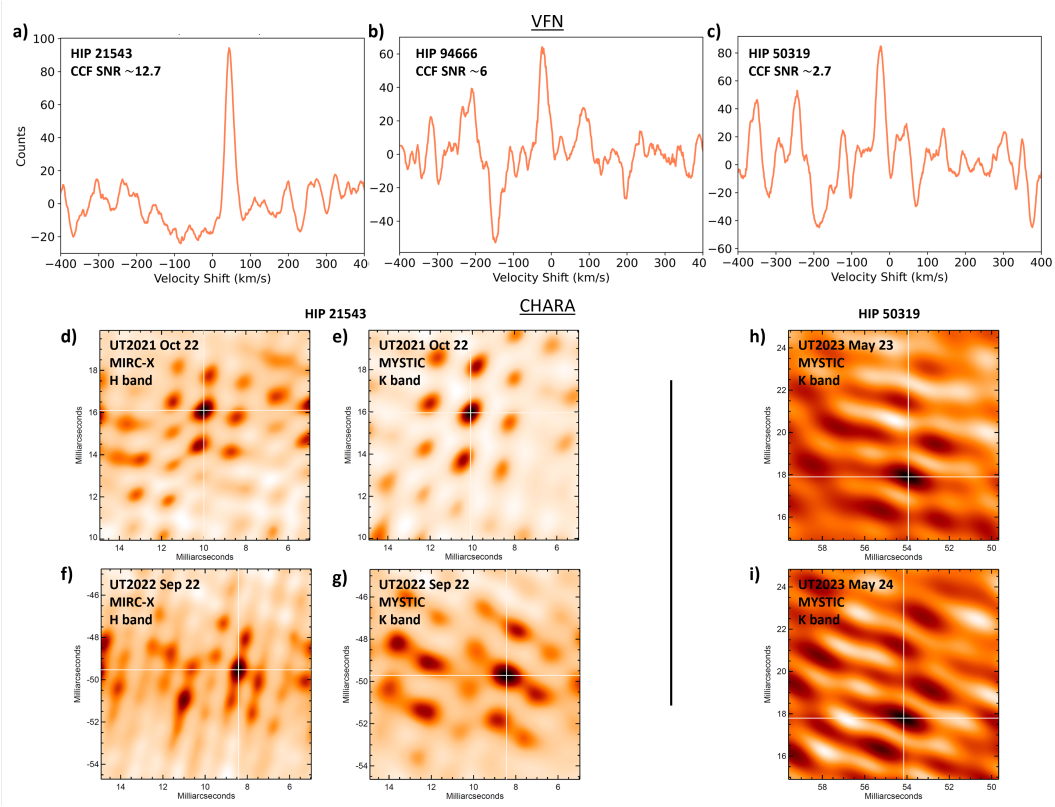


Figure 7.2: Top row: CCF between the best-fit model and the measured spectra for (a) HIP 21543, (b) HIP 94666, and (c) HIP 50319. The CCF SNR is included in the top left of the plots. The periodic oscillations in the CCF for HIP 50319 are due to residual fringing that was not fully removed in the fits, limiting us to a tentative detection on this target. Lower two rows: CHARA detection maps for HIP 21543 and HIP 50319. HIP 94666 is omitted as it was not detected by CHARA. The axes mark distance in milliarcseconds from the primary, with North up and East left. The white crosshairs denote the detected companion. Four maps are shown for HIP 21543, two for MIRC-X (d,f) and two for MYSTIC (e,g), across both nights. HIP 50319 has two maps (h,i), both from MYSTIC, one for each night. The upper left text in the CHARA maps denotes the observing night, beam combiner, and band for each plot.

**HIP 21543** shows a strong detection with both instruments. The cross-correlation function (CCF) between the best-fit model and the VFN data is shown in Fig. 7.2(a). The CCF signal-to-noise ratio (SNR), computed as the peak compared to the standard deviation of the wings out to ±1000 km/s, is 12.7. Our relative RV of $-8.3^{+0.6}_{-0.8}$ km/s between the primary and the companion on UT 2022 October 12 agrees with the expected value of -7.9 km/s from the Tokovinin orbit and is close to -6.9 km/s from the Gaia orbit. The best-fit $T_{\rm eff}$ just over 3450 $K$ for Ab is slightly higher than, though still consistent with, the expected $3200-3300$ $K$ from MSDT given the mass estimates. CHARA detected Ab with both MIRC-X and MYSTIC on both nights, as shown in Fig. 7.2(d-g). The resulting separations of 18.9 mas and 50.3 mas for the two epochs are consistent with the expected values from both the Tokovinin orbit (20.5 and 47.3 mas) and the Gaia orbit (22.0 and 52.8 mas). The CHARA data also yield a K band flux ratio from MYSTIC of 70 ± 11 between Ab and Aa, which is between the expected flux ratios of 42 and 85, again from the Tokovinin and Gaia masses, respectively.

**HIP 94666** has a confident detection in the KPIC VFN data with a CCF SNR of 6 as shown in Fig. 7.2(b). Our relative RV of $14.4^{+0.6}_{-0.5}$ km/s on 2023 May 9 is close to the predicted value of 13.5 km/s from the Gaia orbital solution. The best-fit $T_{\rm eff}$ of 4100 $K$ is 800 $K$ higher than expected from the predicted masses though this could be because constraining $T_{\rm eff}$ for M dwarfs is particularly challenging as mentioned earlier. The CHARA observation yielded unreliable values in the short amount of integration time provided, such that we cannot provide position values and can only set lower limits on the flux ratio for the companion. We plan to re-observe this target with CHARA in 2024.

**HIP 50319** yielded a tentative VFN detection, with a CCF SNR of 2.7. The CCF, shown in Fig. 7.2(c), has prominent structure in the wings, reflecting the fact that the detection is primarily limited by residual fringing. However, the best-fit model provides several pieces of evidence supporting the validity of this detection. First, the best-fit RV of $-35.4 \pm 0.1$ km/s for the primary on 2023 May 6 is in-line with the published velocity of ~ -34 km/s (Deka-Szymankiewicz et al., 2018; Nordström et al., 2004). Our fit to the primary further gives a $T_{\rm eff}$ of 5480 ± 10 $K$ and $v \sin i$ of 3.9 ± 0.2 km/s, which are close to the published values of 5686 ± 7 $K$ (Deka-Szymankiewicz et al., 2018) and 5.5 km/s (Luck, 2017). Meanwhile, the fits to the companion spectrum show a RV of $-17.2^{+0.9}_{-0.8}$ km/s with a $T_{\rm eff} \approx 3300$ $K$. This $T_{\rm eff}$ is close to the expected value of around 3000 $K$ from the MSDT given the estimated

mass. The fact that the retrieved properties for the primary are in-line with prior measurements, and that the companion RV and $T_{\rm eff}$ are so different, provide strong evidence that our analysis is indeed detecting spectral lines from two distinct objects.

The relative RV of $-18.2^{+0.9}_{-0.8}$ km/s is two times larger than expected from the Gaia orbital solution for the time of observation. However, the CHARA MYSTIC observations, shown in Fig. 7.2(h,i), yielded solid detections that put the companion at a separation of around 57 mas for the two consecutive nights, rather than the Gaia-predicted separation of 42 mas. Thus, it is likely that the Gaia orbit has errors that should be corrected and which could explain the difference between our measured and expected position and RV values. Similar discrepancies between measured RVs and the NSS orbital solutions have been found in other studies (Tokovinin, 2023). The CHARA MYSTIC detections also provide a K band flux ratio of 429 ± 22, which agrees with the predicted value of 405 presented in Sec. 7.2. The MIRC-X data were unable to constrain the separation and only provided lower limits for the H band flux ratio.

The CHARA MYSTIC detection confirms that the companion was within the VFN field of view at the time of observation. It also shows that the published orbital solution has errors that could explain the larger-than-expected relative RV from VFN. This, combined with the measured $T_{\rm eff}$ of the primary and companion, suggests a promising KPIC VFN detection of HIP 50319 B.

## 7.5 Conclusion

In this paper we presented the first direct detection of three close-in low-mass stellar companions previously only known through indirect methods. For the most-challenging target, our VFN detection is tentative due to strong fringing which could not be fully fitted and removed. An upgrade to KPIC in February 2024 will replace the optics that introduce fringing, significantly reducing the effect of this error in future observations. We will also add a new vortex mask, doubling the off-axis throughput and pushing the peak coupling from 1.4 $\lambda/D$ to 0.9 $\lambda/D$. Nevertheless, the current performance is sufficient for detection and characterization, as we are able to retrieve effective temperatures, rotational velocities, and RV values for our companions that are generally consistent with expectations. These VFN detections were made at separations between 35 and 55 mas, corresponding to 0.7-1.2 $\lambda/D$ and about 2 AU. That is well within the typical inner working angle of conventional coronagraphs at these wavelengths, highlighting the power of cross-aperture nulling.

Previous single-telescope interferometric techniques have generally shown on-sky contrast limits of ∼1500 at $\lesssim$2.5 $\lambda/D$ (Gauchet et al., 2016; Sallum et al., 2019), leading to demonstrated companion detections at flux ratios of a few-hundred within 2 $\lambda/D$ (Hinkley et al., 2015; Lloyd et al., 2006; Biller et al., 2012). A prior cross-aperture fiber nuller detected $\eta$ Peg B with a flux ratio of 100 and measured the stellar diameter of the primary at a ratio of ∼2000 (Serabyn, Mennesson, Martin, et al., 2019). Our previous VFN paper predicted contrast limits of ∼1000 at ∼1 $\lambda/D$ (Echeverri, Xuan, et al., 2023), and this paper now adds companion detections with flux ratios around 100 and a tentative detection at ∼430. These VFN results also represent the first companion detection at these contrast levels with high ($R$>10, 000) spectral-resolution nulling on-sky, showcasing the power of combining nulling interferometry with high-resolution spectroscopy and complementing the capabilities of previous instruments. In addition, these results are obtained at or within the conventional diffraction limit.

To highlight the complementary nature of VFN, this paper combined KPIC VFN results with long-baseline interferometry observations from CHARA, allowing us to validate that we are close to our contrast predictions. Moreover, the CHARA-provided positions substantiate the published orbits, especially when combined with relative RV values from KPIC VFN, revealing some of the synergies between the two techniques. We find that the published orbits for the first two targets, HIP 21543 Ab and HIP 94666 Ab, are consistent with our results while the orbit for the third, HIP 50319 B, likely needs to be updated. These results open the door to detecting faint companions around young stars at separations within the inner working angle of typical coronagraphic imagers. Surveys with CHARA and VFN, as presented here, can target young stars with Gaia-Hipparcos astrometric accelerations indicative of substellar companions, to complement imaging surveys (e.g., Currie et al., 2021; Kuzuhara et al., 2022; De Rosa et al., 2023). This would provide a more efficient, complete, and high-resolution view of faint, close-in companions.

**Acknowledgments.**
D.E was supported by a NASA Future Investigators in NASA Earth and Space Science and Technology (FINESST) fellowship under award #80NSSC19K1423. D.E also acknowledges support from the Keck Visiting Scholars Program (KVSP) to install the KPIC Phase II upgrades required for KPIC VFN. J.X is supported by another FINESST award under #80NSSC23K1434 and also acknowledges support from the KVSP to commission KPIC Phase II.

Funding for KPIC has been provided by the California Institute of Technology, the Jet Propulsion Laboratory, the Heising-Simons Foundation (grants #2015-129, #2017-318, #2019-1312, and #2023-4598), the Simons Foundation (through the Caltech Center for Comparative Planetary Evolution), and the NSF under grant AST-1611623.

This work is based upon observations obtained with the Georgia State University Center for High Angular Resolution Astronomy Array at Mount Wilson Observatory. The CHARA Array is supported by the National Science Foundation under Grant No. AST-1636624 and AST-2034336. Institutional support has been provided from the GSU College of Arts and Sciences and the GSU Office of the Vice President for Research and Economic Development. S.K. and S.C. acknowledge funding for MIRC-X received from the European Research Council (ERC) under the European Union's Horizon 2020 research and innovation programme (Starting Grant No. 639889 and Consolidated Grant No. 101003096). J.D.M acknowledges funding for the development of MIRC-X (NASA-XRP NNX16AD43G, NSF-AST 1909165) and MYSTIC (NSF-ATI 1506540, NSF-AST 1909165).

The data presented herein were obtained at Keck Observatory, which is a private 501(c)3 non-profit organization operated as a scientific partnership among the California Institute of Technology, the University of California, and the National Aeronautics and Space Administration. The Observatory was made possible by the generous financial support of the W. M. Keck Foundation.

Part of this work was carried out at the Jet Propulsion Laboratory, California Institute of Technology, under contract with NASA (80NM00018D0004).

This work has made use of data from the European Space Agency (ESA) mission *Gaia* (`https://www.cosmos.esa.int/gaia`), processed by the *Gaia* Data Processing and Analysis Consortium (DPAC, `https://www.cosmos.esa.int/web/gaia/dpac/consortium`). Funding for the DPAC has been provided by national institutions, in particular the institutions participating in the *Gaia* Multilateral Agreement.

The authors wish to recognize and acknowledge the very significant cultural role and reverence that the summit of Maunakea has always had within the indigenous Hawaiian community. We are most fortunate to have the opportunity to conduct observations from this mountain.

**Facilities.** Keck:II (KPIC), CHARA (MIRC-X/MYSTIC)

**Software.**
KPIC DRP: (`https://github.com/kpicteam/kpic_pipeline`),
mircx_pipeline: (`https://gitlab.chara.gsu.edu/lebouquj/mircx_pipeline`),
Search Cal: (`https://www.jmmc.fr/english/tools/proposal-preparation/search-cal/`),
Astropy: (`https://www.astropy.org/index.html` - Astropy Collaboration, Price-Whelan, Lim, et al., 2022; Astropy Collaboration, Price-Whelan, Sipőcz, et al., 2018; Astropy Collaboration, Robitaille, et al., 2013)

---

## *Supplemental Work*

### 7.6 Extended Results

The results presented in this paper from the VFN spectra (Table 7.2) were obtained through a fit of the data using a forward model of the observations, as briefly described in Sec. 7.3. For further details on the methodology, refer to the upcoming paper by Xuan et al. titled "Atmospheric retrievals of the benchmark late-M companion HIP 55507 B." In this section I provide additional insight into the VFN results, including the posterior distributions from the fits and a brief look at the effect of fringing.

The analysis of the companion in the VFN data spans 10 parameters. The first four are properties of the companion: effective temperature ($T_{\rm eff}$), surface gravity ($\log g$), radial velocity (RV), and rotational velocity ($v \sin i$). The next two, companion flux and primary flux ($F_C$ and $F_P$), set the strength of the signal contributed from the two binary elements. The following three parameters tackle the fringing using a model assuming the wavelength-dependent transmission function for a Fabry-Perot Cavity (Perot et al., 1899), parameterized in our fits by the amplitude of the fringing (amp), the optical path difference (OPD), and the temperature of the glass cavity ($T_g$). The tenth fit parameter is an error multiple to account for possible underestimation in the data uncertainties. Wide priors are initially selected for the various parameters based on the predicted properties of the companion and observation. Then they are iteratively constrained to determine the final values.

The fit uses nested sampling with the `dynesty` python package (Speagle, 2020) to determine posterior distributions for the 10 parameters. The resulting distributions,

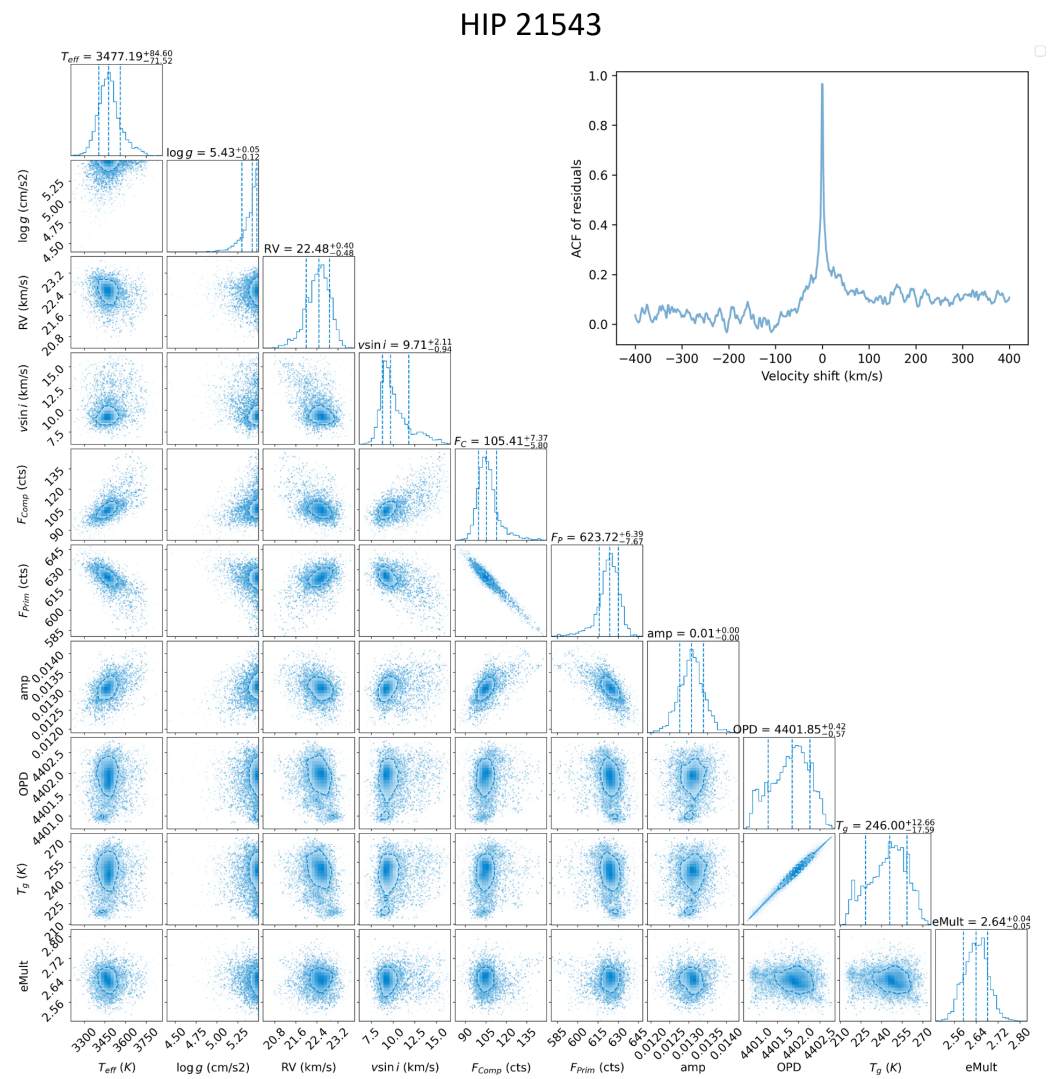


Figure 7.3: (Lower left) posterior distributions of the fit to the VFN data for HIP 21543. Note that the RV value is for the companion and is in the instrument frame, before barycentric correction using the value in Table 7.1. (Top right) auto-correlation function of the residuals, peak-normalized.

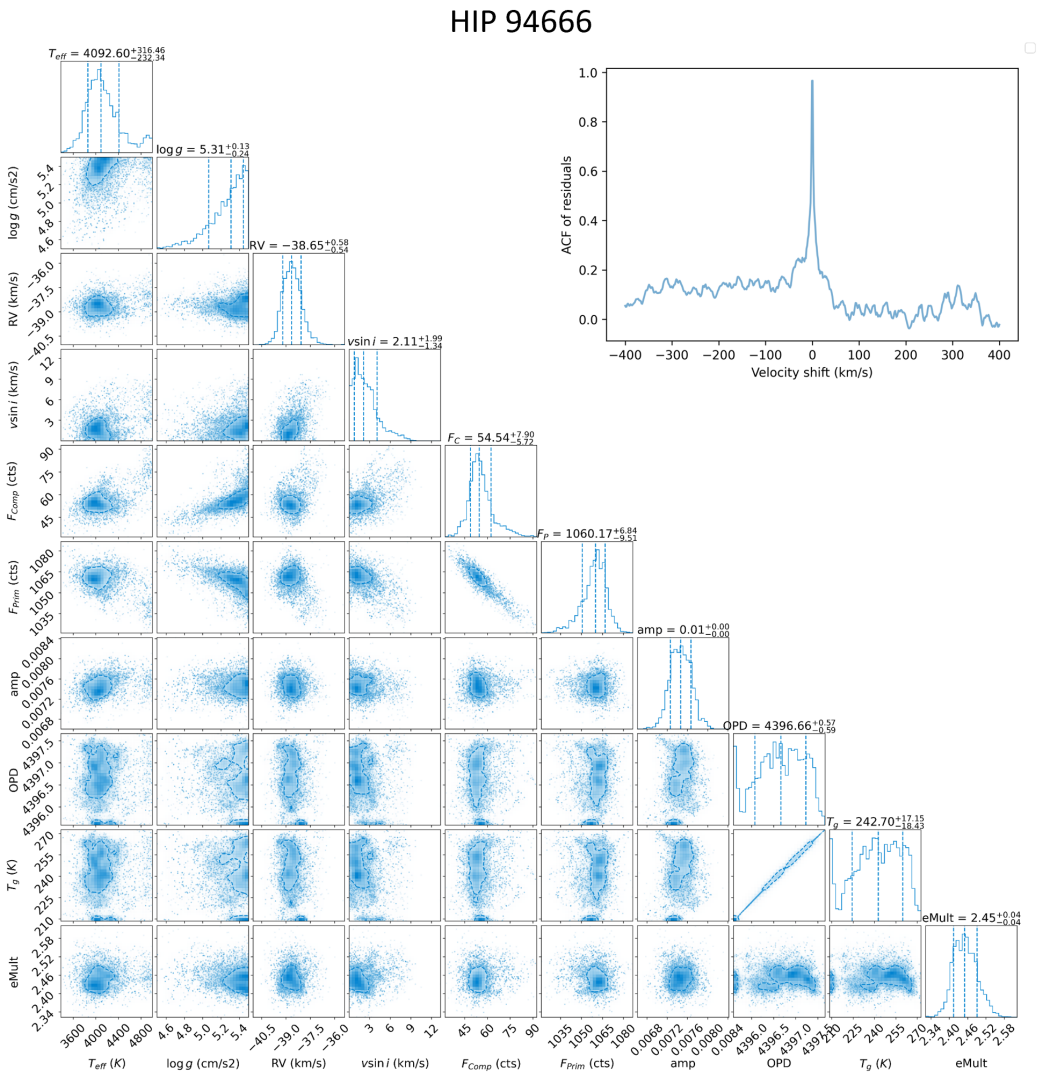


Figure 7.4: Same as Fig. 7.3 but for HIP 94666.

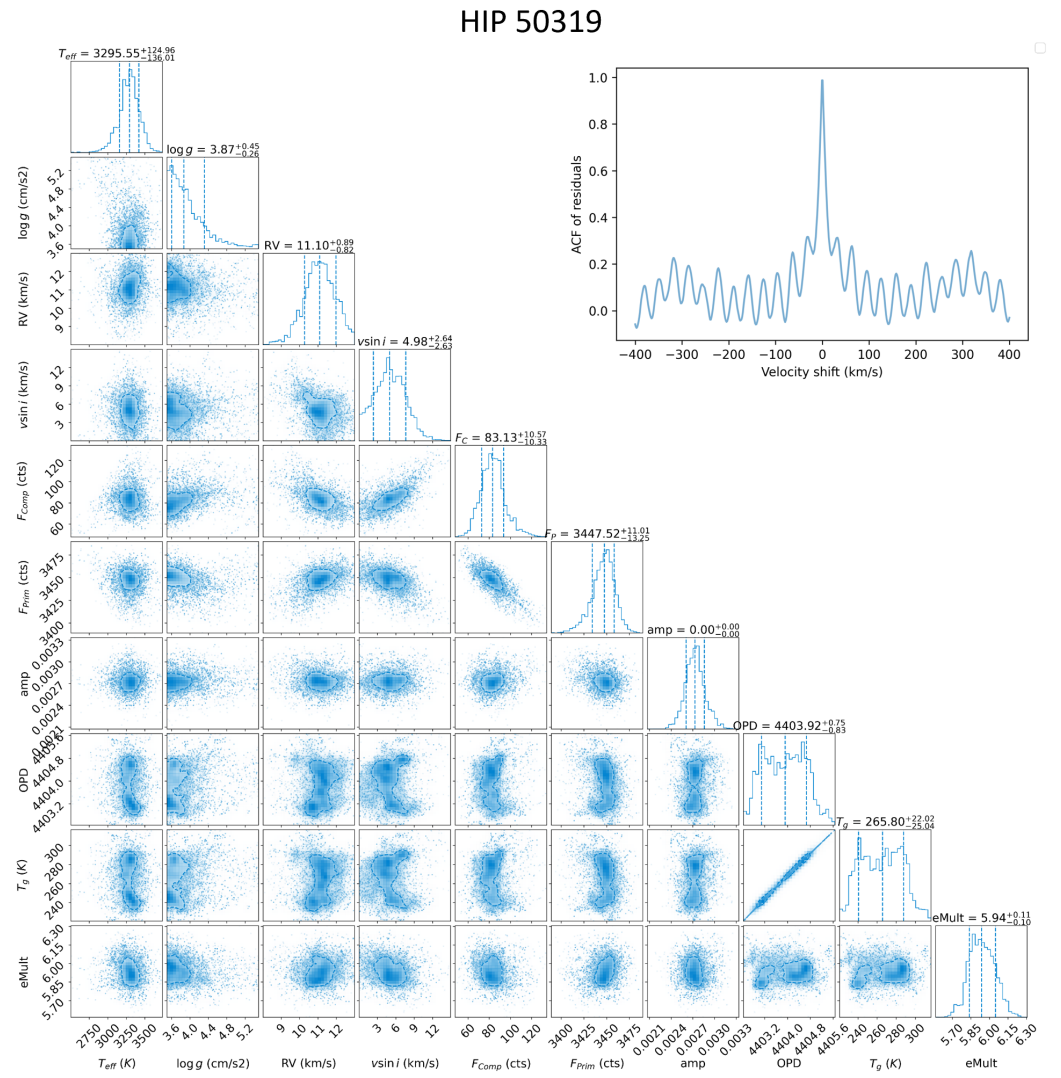


Figure 7.5: Same as Fig. 7.3 but for HIP 50319. The strong periodic structure in the wings of the ACF indicates the fringing remains a large part of the residuals for this object.

plotted using the `corner` package (Foreman-Mackey, 2016), for the three targets are shown in Figs. 7.3-7.5. Note that the RVs in the plots are in the instrument frame, before the barycentric correction is applied. In our results, the RV and $T_{\rm eff}$ are generally well-constrained though the measured $T_{\rm eff}$ for HIP 94666 was higher than predicted based on the expected masses. The $\log g$ hits the upper or lower bounds of the priors for all three targets, and we could not extend the range since the grid of BT-Settl models used for the companion did not extend further. This prevented us from constraining $\log g$ for any of the companions. However, as mentioned in the paper, fitting $T_{\rm eff}$ and $\log g$ for M-dwarfs remains a challenging task so it is not surprising that our fits struggled with the $\log g$ and produced an unexpectedly high $T_{\rm eff}$ for one target. Our fits were able to constrain the $v \sin i$ for HIP 21543 but only provided an upper limit for the the other two companions, as seen in the corner plots where the distributions extend into the lower limit. The best-fit fringing amplitude for HIP 21543 and HIP 94666 was around 1%, which is in line with the expected amplitude seen in other KPIC observations with similar SNR. Meanwhile, the fit to HIP 50319 yielded an unusually low amplitude of $\lesssim$0.3%. This ultimately resulted in a best-fit model for the observation that did not fully remove the actual fringing present in the data.

The main limitation for all KPIC observations thus far has been the fringing in the system. However, since KPIC VFN observes companions at very small separations from their primary star, the signal from the primary is generally much higher in VFN than in DS mode, even with the nulling effect provided by VFN. This means that the fringing, which is a percentage of the incident light, is stronger than most other noise sources in VFN observations, aside from the stellar photon noise. As such, fringing residuals were particularly limiting in these results. A good metric for the strength of the remaining fringing after fitting is the auto-correlation function (ACF) of the data minus the model, also known as the residuals. The ACF of the residuals for the best-fit model from each target is shown in the upper right of Figs. 7.3-7.5. HIP 50319 shows strong, periodic oscillation in the wings of the ACF, which is emblematic of significant fringing present in the residuals. Meanwhile, HIP 21543 and HIP 94666 have much flatter wings matching the fact that the fringing was better-handled for these. We ran several different fits, including using and combining different echelle orders for the spectra as well as trying different ranges of priors, but none of these mitigated the fringing residuals on HIP 50319. We additionally tried fitting the fringing on a sample-by-sample basis for the 41 NIRSPEC frames obtained on that target during the observation but this did not change the results or the residual

fringing by much.

For the time being, KPIC VFN observations of faint companions will likely remain fringing-limited but the service mission planned for early 2024 should help with this. The bulk of the fringing in our data is introduced by three optics: two dichroics in the fiber injection unit and the NIRSPEC entrance window (Finnerty, Schofield, Delorme, et al., 2022). The window is not a large concern since the angle of incidence for the light at that part of the beam path remains constant throughout the night, such that the fringing is constant and can generally be subtracted-out in the analysis. The incidence on the dichroics does change throughout the observations though so these fringes are time-variable, making them more challenging to fit and remove. The service mission will replace these dichroics with new ones that are wedges so that the internal reflection in the optics places the co-propagating "ghost" far from the core of the SMF. This should prevent the light with the Fabry-Perot effect from coupling into the fiber and therefore remove the bulk of the time-variable fringes in the data.

## 7.7 Note About Target Selection

Target selection for commissioning the KPIC VFN mode was challenging since the instrument is currently working in a regime without much precedent. Targets were considered based on the following constraints:

- The target should have a known companion with a prior detection to provide the following information on the system.
- The companion orbit should be well-enough constrained to ensure that it would fall within the VFN field of view at the time of observation. The field of view for commissioning was limited to 30-80 mas so as to provide at least 50% of the peak companion throughput.
- Both the primary and companion should be of spectral type G or later so that they have measureable spectral lines that can be used to distinguish the host signal from that of the companion. This proved to be a salient requirement as we tried to observe $\eta$ Peg B on 2022 November 14 without success despite all other requirements being met. $\eta$ Peg A is a G2-type star but the companion is likely an A5-type (Serabyn, Mennesson, and Martin, 2020), such that it has no lines for our spectral analysis to attach to.

- The relative RV at the time of observation should ideally be large enough that the spectral lines from each element, the host and the companion, can be disentangled in velocity space. This proved particularly helpful for the detection of HIP 50319 B, where the difference in radial velocity for the host and companion models provided confidence that lines from two different object were being detected.

- A bright host was also favorable since the required integration time to meet a goal SNR is inversely proportional to the host flux, as shown by Eq. 6.5. Having a bright host also helped with the AO and tracking performance such that it provided improved starlight rejection. Furthermore targets with an H band magnitude $\gtrsim 7^{\text{th}}$ magnitude are too faint for the current pointing control code to track on.

- Finally, the flux ratio had to be such that the companion would be detectable with KPIC VFN. We followed an incremental approach where we observed progressively more-challenging targets, starting with a flux ratio of 50 and ultimately progressing to 400. To determine the flux ratio, we either needed known photometry from the system or masses from which the flux could be derived as shown in Sec. 7.2.

- Once the target passed the prior requirements, the SNR for the observation was predicted following a procedure similar to what was explained in Sec. 6.6, primarily leaning on the SNR equation (Eq. 6.3). We used the orbital solution to set the flux ratio (from the mass ratio) and companion throughput (from the separation). A threshold SNR of 3 per spectral channel was used to select targets that would be "detectable."

To find targets meeting these requirements, we initially started with the Washington Double Star catalog (WDS - Mason, Wycoff, et al., 2021); `www.stelledoppie.it` was particularly useful for navigating the catalog and filtering systems, though we also used the VizieR interface as well. Nevertheless the WDS had very few options with the desired flux ratios and separations. This could be due to the fact that most entries in the catalog are visual binaries, and imaging techniques cannot generally push into the regime tackled by interferometers and nullers. We had more success with the Ninth Catalog of Spectral Binaries (SB9 - Pourbaix et al., 2004), since the sheer number of entries, and the separations spanned, were more favorable for our constraints. The Gaia NSS also proved to be a great resource since the DR3

sensitivity is already sufficient for detecting companions at mass ratios that lead to the desired flux ratios. The NSS also provides a full orbital solution that can be used to validate the position and RV requirements prior to observaiton. In fact, all three targets in the paper at the beginning of this chapter are present in the NSS and the orbital solutions were crucial to determining observability. However, the NSS orbits must be taken with careful consideration, since they can have errors as shown by our HIP 50319 B detection and noted by other studies (Tokovinin, 2023).

Two of our detected targets, HIP 21543 and HIP 94666, are triple systems with an outer visual companion and an inner, less-massive spectroscopic and astrometric companion. This is interesting since there is a breadth of work analyzing hierarchical stellar systems to determine occurrence rates, formation mechanisms, early evolution, and much more. The series of publications by Tokovinin and collaborators (Tokovinin, 2014; Tokovinin, 2018; Tokovinin, 2021; Tokovinin, 2023, among others) are a particularly useful resource as they collate information from imaging, astrometric, and RV surveys to provide orbital solutions and other detailed information on many of these systems. The Tokovinin (2021) orbits, for example, played a crucial role in our observations of HIP 21543. This also hints at a possible science application for VFN: the characterization of the inner companions on multiple systems. VFN observations provide high-resolution spectra of companions that would otherwise not be obtainable. Such spectra can then be used to tackle some of the formation and evolution questions at the heart of these multiplicity studies.

Note: some of the observing requirements listed at the start of this section were important for the commissioning tasks but will not be as crucial for future observations. For example, future KPIC VFN observations need not target systems with known companions since we will begin doing guided searches for new companions around accelerating stars. The presence of spectral lines in the host spectrum, and hence the host spectral type, is helpful but is also not critical for future observations as long as the companion has a different spectrum with lines that lead to properties that would distinguish it from the primary.

## References

Allard, F., D. Homeier, and B. Freytag (June 2012). "Models of very-low-mass stars, brown dwarfs and exoplanets". In: *Philosophical Transactions of the Royal Society of London Series A* 370.1968, pp. 2765–2777. DOI: 10.1098/rsta.2011.0269. arXiv: 1112.3591 [astro-ph.SR].

Anugu, N. et al. (Oct. 2020). "MIRC-X: A Highly Sensitive Six-telescope Interferometric Imager at the CHARA Array". In: *The Astronomical Journal* 160.4, 158, p. 158. DOI: 10.3847/1538-3881/aba957. arXiv: 2007.12320 [astro-ph.IM].

Astropy Collaboration, A. M. Price-Whelan, B. M. Sipőcz, et al. (Sept. 2018). "The Astropy Project: Building an Open-science Project and Status of the v2.0 Core Package". In: *The Astronomical Journal* 156.3, 123, p. 123. DOI: 10.3847/1538-3881/aabc4f. arXiv: 1801.02634 [astro-ph.IM].

Astropy Collaboration, A. M. Price-Whelan, P. L. Lim, et al. (Aug. 2022). "The Astropy Project: Sustaining and Growing a Community-oriented Open-source Project and the Latest Major Release (v5.0) of the Core Package". In: *The Astrophysical Journal* 935.2, 167, p. 167. DOI: 10.3847/1538-4357/ac7c74. arXiv: 2206.14220 [astro-ph.IM].

Astropy Collaboration, T. P. Robitaille, et al. (Oct. 2013). "Astropy: A community Python package for astronomy". In: *Astronomy and Astrophysics* 558, A33, A33. DOI: 10.1051/0004-6361/201322068. arXiv: 1307.6212 [astro-ph.IM].

Bender, C. F. and M. Simon (Dec. 2008). "The Detection of Low-Mass Companions in Hyades Cluster Spectroscopic Binary Stars". In: *The Astrophysical Journal* 689.1, pp. 416–429. DOI: 10.1086/592728. arXiv: 0808.3393 [astro-ph].

Beuzit, J.-L. et al. (Nov. 2019). "SPHERE: the exoplanet imager for the Very Large Telescope". In: *Astronomy and Astrophysics* 631, A155, A155. DOI: 10.1051/0004-6361/201935251. arXiv: 1902.04080 [astro-ph.IM].

Biller, B. et al. (July 2012). "A Likely Close-in Low-mass Stellar Companion to the Transitional Disk Star HD 142527". In: *The Astrophysical Journal Letters* 753.2, L38, p. L38. DOI: 10.1088/2041-8205/753/2/L38. arXiv: 1206.2654 [astro-ph.SR].

Chelli, A. et al. (May 2016). "Pseudomagnitudes and differential surface brightness: Application to the apparent diameter of stars". In: *Astronomy and Astrophysics* 589, A112, A112. DOI: 10.1051/0004-6361/201527484. arXiv: 1604.07700 [astro-ph.SR].

Currie, T. et al. (Sept. 2021). "A new type of exoplanet direct imaging search: a SCExAO/CHARIS survey of accelerating stars". In: *Techniques and Instrumentation for Detection of Exoplanets X*. Ed. by S. B. Shaklan and G. J. Ruane. Vol. 11823. Society of Photo-Optical Instrumentation Engineers (SPIE) Conference Series, 1182304, p. 1182304. DOI: 10.1117/12.2595001. arXiv: 2109.09745 [astro-ph.EP].

De Furio, M. et al. (Dec. 2022). "The Small Separation A-star Companion Population: First Results with CHARA/MIRC-X". In: *The Astrophysical Journal* 941.2, 118, p. 118. DOI: 10.3847/1538-4357/aca1ad. arXiv: 2211.01465 [astro-ph.SR].

De Rosa, R. J. et al. (Apr. 2023). "Direct imaging discovery of a super-Jovian around the young Sun-like star AF Leporis". In: *Astronomy and Astrophysics* 672, A94, A94. DOI: 10.1051/0004-6361/202345877. arXiv: 2302.06332 [astro-ph.EP].

Deka-Szymankiewicz, B. et al. (July 2018). "The Penn State - Toruń Centre for Astronomy Planet Search stars. IV. Dwarfs and the complete sample". In: *Astronomy and Astrophysics* 615, A31, A31. DOI: 10.1051/0004-6361/201731696. arXiv: 1801.02899 [astro-ph.SR].

Delorme, J.-R. et al. (July 2021). "Keck Planet Imager and Characterizer: a dedicated single-mode fiber injection unit for high-resolution exoplanet spectroscopy". In: *Journal of Astronomical Telescopes, Instruments, and Systems* 7, 035006, p. 035006. DOI: 10.1117/1.JATIS.7.3.035006. arXiv: 2107.12556 [astro-ph.IM].

Echeverri, D., N. Jovanovic, et al. (Aug. 2022). "Phase II of the Keck Planet Imager and characterizer: system-level laboratory characterization and preliminary on-sky commissioning". In: *Ground-based and Airborne Instrumentation for Astronomy IX*. Ed. by C. J. Evans, J. J. Bryant, and K. Motohara. Vol. 12184. Society of Photo-Optical Instrumentation Engineers (SPIE) Conference Series, 121841W, 121841W. DOI: 10.1117/12.2630518. arXiv: 2210.15915 [astro-ph.EP].

Echeverri, D., G. Ruane, N. Jovanovic, J.-R. Delorme, et al. (Sept. 2021). "Broadband vortex fiber nulling: high-dispersion exoplanet science at the diffraction limit". In: *Techniques and Instrumentation for Detection of Exoplanets X*. Ed. by S. B. Shaklan and G. J. Ruane. Vol. 11823. Society of Photo-Optical Instrumentation Engineers (SPIE) Conference Series, 118230A, 118230A. DOI: 10.1117/12.2597160. arXiv: 2210.15910 [astro-ph.EP].

Echeverri, D., G. Ruane, N. Jovanovic, D. Mawet, et al. (May 2019). "Vortex fiber nulling for exoplanet observations I. Experimental demonstration in monochromatic light". In: *Optics Letters* 44.9, p. 2204. DOI: 10.1364/OL.44.002204. arXiv: 1811.02083 [astro-ph.IM].

Echeverri, D., J. W. Xuan, et al. (July 2023). "Vortex fiber nulling for exoplanet observations: implementation and first light". In: *Journal of Astronomical Telescopes, Instruments, and Systems* 9, 035002, p. 035002. DOI: 10.1117/1.JATIS.9.3.035002. arXiv: 2309.06514 [astro-ph.IM]. URL: https://doi.org/10.1117/1.JATIS.9.3.035002.

Finnerty, L., T. Schofield, J.-R. Delorme, et al. (Aug. 2022). "On-sky performance and lessons learned from the phase I KPIC fiber injection unit". In: *Ground-based and Airborne Instrumentation for Astronomy IX*. Ed. by C. J. Evans, J. J. Bryant, and K. Motohara. Vol. 12184. Society of Photo-Optical Instrumentation Engineers (SPIE) Conference Series, 121844Y, 121844Y. DOI: 10.1117/12.2630276.

Finnerty, L., T. Schofield, B. Sappey, et al. (July 2023). "Keck Planet Imager and Characterizer Emission Spectroscopy of WASP-33b". In: *The Astronomical Journal* 166.1, 31, p. 31. DOI: 10.3847/1538-3881/acda91. arXiv: 2305.19389 [astro-ph.EP].

Foreman-Mackey, D. (June 2016). "corner.py: Scatterplot matrices in Python". In: *The Journal of Open Source Software* 1.2, p. 24. DOI: 10.21105/joss.00024. URL: https://doi.org/10.21105/joss.00024.

Fulton, B. J. et al. (July 2021). "California Legacy Survey. II. Occurrence of Giant Planets beyond the Ice Line". In: *The Astrophysical Journal Supplement Series* 255.1, 14, p. 14. DOI: 10.3847/1538-4365/abfcc1. arXiv: 2105.11584 [astro-ph.EP].

Gaia Collaboration et al. (June 2022). *Gaia Data Release 3: Stellar Multiplicity, a Teaser for the Hidden Treasure*. DOI: 10.48550/arXiv.2206.05595.

Gauchet, L. et al. (Oct. 2016). "Sparse aperture masking at the VLT. II. Detection limits for the eight debris disks stars $\beta$ Pic, AU Mic, 49 Cet, $\eta$ Tel, Fomalhaut, g Lup, HD 181327 and HR 8799". In: *Astronomy and Astrophysics* 595, A31, A31. DOI: 10.1051/0004-6361/201526404. arXiv: 1606.08498 [astro-ph.EP].

Griffin, R. F. (Mar. 2012). "Photoelectric Radial Velocities, Paper XVIII Spectroscopic Orbits for Another 52 Binaries in the Hyades Field". In: *Journal of Astrophysics and Astronomy* 33.1, pp. 29–200. DOI: 10.1007/s12036-012-9137-5.

Griffin, R. F. et al. (July 1988). "A Radial-Velocity Survey of the Hyades". In: *The Astronomical Journal* 96, p. 172. DOI: 10.1086/114800.

Hinkley, S. et al. (June 2015). "Discovery of Seven Companions to Intermediate-mass Stars with Extreme Mass Ratios in the Scorpius-Centaurus Association". In: *The Astrophysical Journal Letters* 806.1, L9, p. L9. DOI: 10.1088/2041-8205/806/1/L9. arXiv: 1505.03858 [astro-ph.EP].

Holl, B. et al. (June 2023). "Gaia Data Release 3. Astrometric orbit determination with Markov chain Monte Carlo and genetic algorithms: Systems with stellar, sub-stellar, and planetary mass companions". In: *Astronomy and Astrophysics* 674, A10, A10. DOI: 10.1051/0004-6361/202244161. arXiv: 2206.05439 [astro-ph.EP].

Kuzuhara, M. et al. (Aug. 2022). "Direct-imaging Discovery and Dynamical Mass of a Substellar Companion Orbiting an Accelerating Hyades Sun-like Star with SCExAO/CHARIS". In: *The Astrophysical Journal Letters* 934.2, L18, p. L18. DOI: 10.3847/2041-8213/ac772f. arXiv: 2205.02729 [astro-ph.SR].

Lanthermann, C. et al. (Apr. 2023). "Multiplicity of northern bright O-type stars with optical long baseline interferometry. Results of the pilot survey". In: *Astronomy and Astrophysics* 672, A6, A6. DOI: 10.1051/0004-6361/202245364. arXiv: 2302.03168 [astro-ph.SR].

Lloyd, J. P. et al. (Oct. 2006). "Direct Detection of the Brown Dwarf GJ 802B with Adaptive Optics Masking Interferometry". In: *The Asrophysical Journal* 650.2, pp. L131–L134. DOI: 10.1086/508771. arXiv: astro-ph/0607516 [astro-ph].

Lockwood, G. W. et al. (Sept. 1984). "The Photometric Variability of Solar-Type Stars. IV. Detection of Rotational Modulation among Hyades Stars." In: *Publications of the Astronomical Society of the Pacific* 96, pp. 714–722. ISSN: 0004-6280. DOI: 10.1086/131410. (Visited on 03/15/2023).

Luck, R. E. (Jan. 2017). "Abundances in the Local Region II: F, G, and K Dwarfs and Subgiants". In: *The Astronomical Journal* 153.1, 21, p. 21. DOI: 10.3847/1538-3881/153/1/21. arXiv: 1611.02897 [astro-ph.SR].

Macintosh, B. et al. (Sept. 2014). "First light of the Gemini Planet Imager". In: *Proceedings of the National Academy of Science* 111.35, pp. 12661–12666. DOI: 10.1073/pnas.1304215111. arXiv: 1403.7520 [astro-ph.EP].

Mason, B. D., G. L. Wycoff, et al. (June 2021). "VizieR Online Data Catalog: The Washington Visual Double Star Catalog (Mason+ 2001-2020)". In: *VizieR Online Data Catalog*, B/wds, B/wds.

Mason, B. D., H. A. McAlister, et al. (Jan. 1993). "ICCD Speckle Observation of Binary Stars. VII. A Duplicity Survey the Hyades Cluster". In: *The Astronomical Journal* 105, p. 220. DOI: 10.1086/116421.

Mawet, D. (Jan. 2021). "Enabling high-res exoplanet spectroscopy at Keck". In: *Nature Astronomy* 5, pp. 723–723. DOI: 10.1038/s41550-021-01429-6.

Nordström, B. et al. (May 2004). "The Geneva-Copenhagen survey of the Solar neighbourhood. Ages, metallicities, and kinematic properties of ~14 000 F and G dwarfs". In: *Astronomy and Astrophysics* 418, pp. 989–1019. DOI: 10.1051/0004-6361:20035959. arXiv: astro-ph/0405198 [astro-ph].

Pecaut, M. J. and E. E. Mamajek (Sept. 2013). "Intrinsic Colors, Temperatures, and Bolometric Corrections of Pre-main-sequence Stars". In: *The Astrophysical Journal Supplement Series* 208, p. 9. ISSN: 0067-0049. DOI: 10.1088/0067-0049/208/1/9.

Perot, A. and C. Fabry (Feb. 1899). "On the Application of Interference Phenomena to the Solution of Various Problems of Spectroscopy and Metrology". In: *The Astrophysical Journal* 9, p. 87. DOI: 10.1086/140557.

Pourbaix, D. et al. (Sept. 2004). "SB$^9$: The ninth catalogue of spectroscopic binary orbits". In: *Astronomy and Astrophysics* 424, pp. 727–732. DOI: 10.1051/0004-6361:20041213. arXiv: astro-ph/0406573 [astro-ph].

Rajpurohit, A. S. et al. (Feb. 2018). "Photospheric properties and fundamental parameters of M dwarfs". In: *Astronomy and Astrophysics* 610. ISSN: 14320746. DOI: 10.1051/0004-6361/201731507.

Riddle, R. L. et al. (Jan. 2015). "A Survey of the High Order Multiplicity of Nearby Solar-type Binary Stars with Robo-AO". In: *The Astrophysical Journal* 799.1, 4, p. 4. DOI: 10.1088/0004-637X/799/1/4. arXiv: 1411.0682 [astro-ph.SR].

Roberts Lewis C., J. et al. (Mar. 2017). "Continued Kinematic and Photometric Investigations of Hierarchical Solar-type Multiple Star Systems". In: *The Astronomical Journal* 153.3, 100, p. 100. DOI: 10.3847/1538-3881/153/3/100. arXiv: 1701.05865 [astro-ph.SR].

Roettenbacher, R. M., J. D. Monnier, F. C. Fekel, et al. (Aug. 2015). "Detecting the Companions and Ellipsoidal Variations of RS CVn Primaries. II. o Draconis, a Candidate for Recent Low-mass Companion Ingestion". In: *The Astrophysical Journal* 809.2, 159, p. 159. DOI: 10.1088/0004-637X/809/2/159. arXiv: 1507.03601 [astro-ph.SR].

Roettenbacher, R. M., J. D. Monnier, G. W. Henry, et al. (July 2015). "Detecting the Companions and Ellipsoidal Variations of RS CVn Primaries. I. $\sigma$ Geminorum". In: *The Astrophysical Journal* 807.1, 23, p. 23. DOI: 10.1088/0004-637X/807/1/23. arXiv: 1504.06628 [astro-ph.SR].

Rosenthal, L. J. et al. (July 2021). "The California Legacy Survey. I. A Catalog of 178 Planets from Precision Radial Velocity Monitoring of 719 Nearby Stars over Three Decades". In: *The Astrophysical Journal Supplement Series* 255.1, 8, p. 8. DOI: 10.3847/1538-4365/abe23c. arXiv: 2105.11583 [astro-ph.EP].

Ruane, G., D. Echeverri, et al. (Sept. 2019). "Vortex fiber nulling for exoplanet observations: conceptual design, theoretical performance, and initial scientific yield predictions". In: *Society of Photo-Optical Instrumentation Engineers (SPIE) Conference Series*. Vol. 11117. Society of Photo-Optical Instrumentation Engineers (SPIE) Conference Series, 1111716, p. 1111716. DOI: 10.1117/12.2528555. arXiv: 1908.09780 [astro-ph.IM].

Ruane, G., J. Wang, et al. (Nov. 2018). "Efficient Spectroscopy of Exoplanets at Small Angular Separations with Vortex Fiber Nulling". In: *Astrophysical Journal* 867.2, 143, p. 143. DOI: 10.3847/1538-4357/aae262. arXiv: 1809.06483 [astro-ph.IM].

Ruffio, J.-B. et al. (Mar. 2023). "Detecting Exomoons from Radial Velocity Measurements of Self-luminous Planets: Application to Observations of HR 7672 B and Future Prospects". In: *The Astronomical Journal* 165.3, 113, p. 113. DOI: 10.3847/1538-3881/acb34a. arXiv: 2301.04206 [astro-ph.EP].

Sallum, S. and A. Skemer (Jan. 2019). "Comparing nonredundant masking and filled-aperture kernel phase for exoplanet detection and characterization". In: *Journal of Astronomical Telescopes, Instruments, and Systems* 5, 018001, p. 018001. DOI: 10.1117/1.JATIS.5.1.018001. arXiv: 1901.01266 [astro-ph.IM].

Serabyn, E., B. Mennesson, S. Martin, et al. (Oct. 2019). "Nulling at short wavelengths: theoretical performance constraints and a demonstration of faint companion detection inside the diffraction limit with a rotating-baseline interferometer".

In: *Mon. Notices Royal Astron. Soc.* 489.1, pp. 1291–1303. DOI: 10.1093/mnras/stz2163. arXiv: 1908.05977 [astro-ph.IM].

Serabyn, E., B. Mennesson, and S. Martin (Dec. 2020). "Observing inside the coronagraphic regime with nulling interferometry". In: *Society of Photo-Optical Instrumentation Engineers (SPIE) Conference Series*. Vol. 11446. Society of Photo-Optical Instrumentation Engineers (SPIE) Conference Series, 114461K, 114461K. DOI: 10.1117/12.2562947.

Setterholm, B. R. et al. (Apr. 2023). "MYSTIC: a high angular resolution K-band imager at CHARA". In: *Journal of Astronomical Telescopes, Instruments, and Systems* 9, 025006, p. 025006. DOI: 10.1117/1.JATIS.9.2.025006.

Speagle, J. S. (Apr. 2020). "DYNESTY: a dynamic nested sampling package for estimating Bayesian posteriors and evidences". In: *Monthly Notices of the Royal Astronomical Society* 493.3, pp. 3132–3158. DOI: 10.1093/mnras/staa278. arXiv: 1904.02180 [astro-ph.IM].

ten Brummelaar, T. A. et al. (July 2005). "First Results from the CHARA Array. II. A Description of the Instrument". In: *The Astrophysical Journal* 628.1, pp. 453–465. DOI: 10.1086/430729. arXiv: astro-ph/0504082 [astro-ph].

Thomas, J. D. et al. (July 2021). "The orbit and stellar masses of the archetype colliding-wind binary WR 140". In: *Monthly Notices of the Royal Astronomical Society* 504.4, pp. 5221–5230. DOI: 10.1093/mnras/stab1181. arXiv: 2101.10563 [astro-ph.SR].

Tokovinin, A. (Mar. 2021). "Inner and Outer Orbits in 13 Resolved Hierarchical Stellar Systems". In: *The Astronomical Journal* 161.3, 144, p. 144. DOI: 10.3847/1538-3881/abda42. arXiv: 2101.02976 [astro-ph.SR].

Tokovinin, A. (Apr. 2014). "From Binaries to Multiples. II. Hierarchical Multiplicity of F and G Dwarfs". In: *The Astronomical Journal* 147.4, 87, p. 87. DOI: 10.1088/0004-6256/147/4/87. arXiv: 1401.6827 [astro-ph.SR].

– (Mar. 2018). "The Updated Multiple Star Catalog". In: *The Astrophysical Journal Supplement Series* 235.1, 6, p. 6. DOI: 10.3847/1538-4365/aaa1a5. arXiv: 1712.04750 [astro-ph.SR].

– (June 2023). "Spectroscopic Orbits of Subsystems in Multiple Stars. X (Summary)". In: *The Astronomical Journal* 165.6, 220, p. 220. DOI: 10.3847/1538-3881/acca19. arXiv: 2304.02706 [astro-ph.SR].

Torres, G. et al. (Dec. 2022). "The Orbits and Dynamical Masses of the Castor System". In: *The Astrophysical Journal* 941.1, 8, p. 8. DOI: 10.3847/1538-4357/ac9d8d. arXiv: 2210.16322 [astro-ph.SR].

Wang, J. J. et al. (Oct. 2021). "Detection and Bulk Properties of the HR 8799 Planets with High-resolution Spectroscopy". In: *The Astronomical Journal* 162.4, 148, p. 148. DOI: 10.3847/1538-3881/ac1349. arXiv: 2107.06949 [astro-ph.EP].

Wang, J., J. R. Kolecki, et al. (Apr. 2022). "Retrieving the C and O Abundances of HR 7672 AB: A Solar-type Primary Star with a Benchmark Brown Dwarf". In: *The Astronomical Journal* 163.4, 189, p. 189. DOI: 10.3847/1538-3881/ac56e2. arXiv: 2202.02477 [astro-ph.EP].

Wang, J., J. J. Wang, et al. (Jan. 2023). "Retrieving C and O Abundance of HR 8799 c by Combining High- and Low-resolution Data". In: *The Astronomical Journal* 165.1, 4, p. 4. DOI: 10.3847/1538-3881/ac9f19. arXiv: 2209.15484 [astro-ph.EP].

Xuan, J. W. et al. (Oct. 2022). "A Clear View of a Cloudy Brown Dwarf Companion from High-resolution Spectroscopy". In: *The Astrophysical Journal* 937 (2), p. 54. ISSN: 0004-637X. DOI: 10.3847/1538-4357/ac8673.

*Chapter 8*

# KPIC VFN UPGRADES

In the preceding chapter, we established the operational capability of the KPIC VFN mode by detecting and characterizing companions with high spectral resolution at unprecedented separations and flux ratios. Despite these achievements, the current performance of the system is limited by strong fringing from dichroics in the fiber injection unit. An upgrade is scheduled for February 2024 which should resolve the majority of the fringing issues by replacing the two problematic optics. During this service mission, we will also upgrade the system with a new charge 1 vortex mask to improve the off-axis throughput and access companions at smaller separations. This upgrade will bolster the sensitivity of the KPIC VFN mode, allowing it to detect fainter companions and thereby increase the yield in future surveys. However, the transition to charge 1 introduces various challenges that need to be addressed.

This chapter presents the steps that have been taken, or are currently underway, towards bringing a charge 1 vortex option to the KPIC VFN mode. We begin by briefly exploring a scalar vortex before covering the considerations that were made when designing and procuring the new vector vortex mask that will be deployed to the telescope. Then we go over the upgrades to related subsystems that will tackle the more-stringent requirements set by charge 1 operations. This includes a section on the atmospheric dispersion corrector and another section covering extensive work performed on the KPIC tracking system to reduce the tip-tilt jitter. The jitter work, performed in collaboration with the NASA Jet Propulsion Laboratory, spans all facets of the tracking system, so we cover system identification, software overhauls, and novel pointing control algorithms that have already reduced the on-sky jitter residuals by 25%.

---

## 8.1 Scalar VFN

Section 6.7 briefly covered the desire to move to a charge 1 vortex mask in KPIC. As a reminder, the instrument currently uses a charge 2 mask since it reduces the pointing sensitivity, allowing KPIC VFN to achieve deeper nulls in the presence

of tip-tilt jitter. However, under ideal conditions, both vortex charges can achieve perfect nulling (i.e., complete starlight rejection), yet charge 2 only reaches a peak off-axis coupling of about 10% at 1.4 $\lambda/D$ while charge 1 reaches about 20% at 0.9 $\lambda/D$ (see Sec. 2.5). On the Keck aperture, the increase in off-axis throughput is closer to 1.8×, leading to a reduction of 3.25× in required integration time. The reduction in integration time is already motivating but the smaller inner-working angle is also a major benefit, as it lets VFN drill down to smaller separations to better fill the gap between transit and direct imaging techniques.

For the upgrade to a charge 1 vortex mask in KPIC, we considered two options: vector and scalar. Vector vortex technology is the prevailing design for current vortex coronagraphs since it was discovered early-on that broadband performance can be achieved by stacking multiple liquid polymer layers (Mawet et al., 2009). However, vectorial methods of generating the necessary spiral phase suffer from zero-order leakage and polarization-dependence that can limit the achievable null depth, as described in Sec. 2.6. One method for mitigating this is with diffraction gratings that diffract the zero-order leakage out of the beam (Doelman et al., 2020). Alternatively, scalar vortex techniques completely sidestep these issues by relying on longitudinal phase delay rather than polarization-dependent geometric phase (Swartzlander, 2006; Ruane, Mawet, et al., 2019). Both options, vector and scalar, were considered for the KPIC VFN charge 1 upgrade and though we ultimately settled on the vector mask, the scalar option had many promising properties worth covering here.

There are many flavors of scalar vortex masks that can be used for VFN. Conceptually, the simplest is a continuous spiral phase plate that directly imparts the typical $\exp(il\theta)$ vortex phase through accumulated optical path delay in a transmissive substrate (Swartzlander, 2006). An alternative design, known as the "staircase," discretizes the ramp into multiple flat steps which makes it easier to manufacture while still approximating the true vortex phase (Lee et al., 2006; Desai et al., 2023). Reflective versions that are not affected by the change in refractive index across wavelengths are also possible through a spiral mirror (Campbell et al., 2012). The phase from all these masks can be approximately represented with a wavelength-dependent charge, $l(\lambda) = l_0\lambda_0/\lambda$, where $l_0$ is the design charge at the central wavelength, $\lambda_0$ (Ruane, Mawet, et al., 2019). Such a phase results in an on-axis null at the central wavelength that is theoretically zero in the absence of manufacturing and wavefront errors. However, Ruane, Echeverri, et al. (2019) showed that other wavelengths in

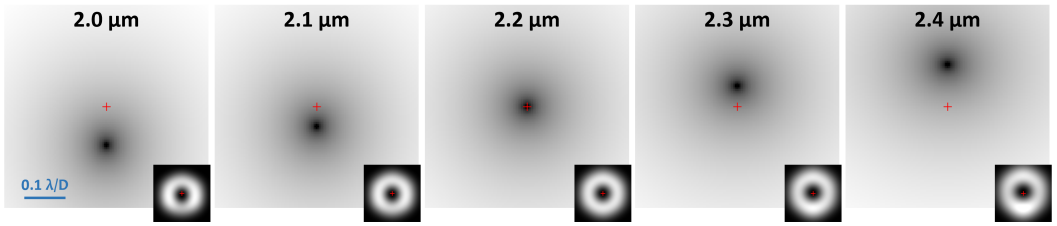


Figure 8.1: Two dimensional coupling maps for scalar VFN with a continuous charge 1 spiral phase plate. White maps have a logarithmic colorscale and span the central 0.25×0.25 $\lambda/D$ field of view to show the null. The lower right, black maps are a zoomed out version spanning 1.8×1.8 $\lambda/D$ with a linear colorscale to show the full bright fringe. The red 'X' in each map denotes the central, on-axis point; notice that the null shifts down/up with wavelength, indicating a chromatic dispersion introduced by the scalar vortex mask.

the pass band experience chromatic dispersion that manifests in the focal plane as a wavelength-dependent shift in the null position. This shift is visible in Fig. 8.1 where the central regions of the 2D coupling maps at five representative wavelengths across K band are shown. A deep null is still achieved at each wavelength but is displaced relative to the central wavelength.

Fig. 8.2(a) plots the displacement of the null along each axis as a function of wavelength. The shift only occurs along a single axis, in this case the vertical Y direction, and is roughly linear with wavelength. A linear fit to the motion reveals a slope of $p = 1.073$, such that across the 18% fractional width of K band, a total dispersion of ~0.2 $\lambda/D$ is introduced. Since the fiber can only be aligned with the null at a single wavelength (the on-axis point at the central wavelength), it effectively experiences a tilt at the other wavelengths which results in a chromatic null degradation as seen in Fig. 8.2(b). At the edges of the band, the null is reduced to $6 \times 10^{-3}$.

Ruane, Echeverri, et al. (2019) suggested using an optical wedge to mitigate this effect since the dispersion introduced by a wedge is also approximately linear over such bands. Though Eq. 11 for computing the wedge angle in that work was incorrect, the concept still holds, so we will derive here the correct equation. An optical wedge with a wedgle angle, $\alpha$, deviates an incident beam by

$$\delta \approx \alpha(n-1), \tag{8.1}$$

where the small angle approximation has been used and $n$ is the refractive index of the wedge substrate. This effect is shown schematically for the shortest (blue)

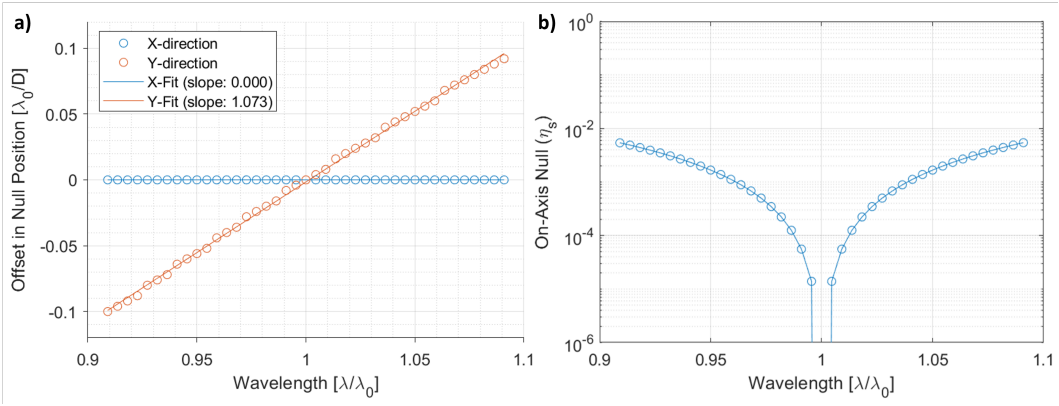


Figure 8.2: (a) Shift in null position as a function of wavelength assuming a scalar vortex mask with charge $l(\lambda) = l_0\lambda_0/\lambda$ . Best-fit lines to the data are also included, with the resulting slope shown in the plot legend. (b) Resulting null depth as a function of wavelength.

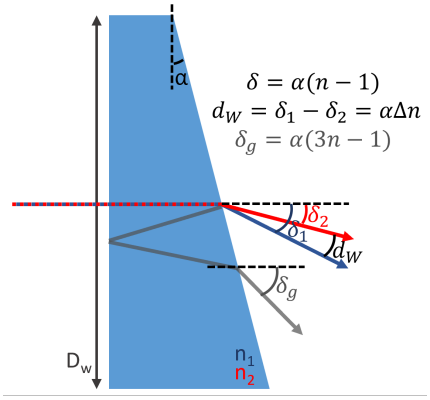


Figure 8.3: Diagram of the key parameters for an optical wedge to correct the dispersion introduced by a scalar mask for VFN. The output red and blue arrows represent the chromatically dispersed through-beam. $\delta_1$ and $\delta_2$ are the exit angle of the through-beam at the two edge wavelengths relative to the incident beam. The grey lines and arrow trace the path of the primary ghost generated from internal reflections in the substrate. $\delta_g$ is the exit angle of the primary ghost relative to the incident beam.

and longest (red) wavelengths in the pass band in the diagram from Fig. 8.3. This means that the relative angle between the two wavelengths, or the dispersion $d_W$, introduced by the wedge is $d_W = \alpha\Delta n$, where $\Delta n$ is the difference in refractive index for the two wavelengths. Now, the magnitude of the dispersion introduced by the vortex, $d_V$, at the plane of the wedge, can be computed from the slope of the null shift, $p$, and the fractional bandwidth, $B$ (=$\Delta\lambda/\lambda_0$), as $d_V = Bp\lambda_0/D_W$, where $D_W$ is the diameter of the beam at the wedge and $\lambda_0/D_W$ has been used to convert to radians. We want the wedge to cancel out the dispersion from the vortex so we set $d_W = d_V$. This yields

$$\alpha = \frac{p\Delta\lambda}{D_W\Delta n}, \tag{8.2}$$

as the angle for the optical wedge needed to correct the dispersion from the vortex and hence recombine the nulls at all wavelengths. For the KPIC VFN mode, which operates in K band (2.0 to 2.4 $\mu$m) and has a pupil diameter of $D_W = 12.5$ mm at the relevant plane, we can consider a wedge made of fused silica such that $\Delta n = 6.5\text{e}{-3}$ at 275 $K$ (Leviton et al., 2006). The wedge would thus need to have an angle of 5.3e−3 radians, or ∼18.2′.

Note that though this wedge would produce the desired dispersion between the wavelengths in the pass band, it would also introduce a net tilt in the optical path. The tilt at the central wavelength can be computed from Eq. 8.1 to be ∼7.9′ at the plane of the wedge, or ∼0.″54 projected on-sky (using a compression factor or magnification of 875 from the Keck primary to the KPIC pupil). This is well within the 4.″6 (projected on-sky) field of view of the KPIC tracking camera and within the 34′ (in the instrument) closed-loop range of the fiber alignment mirror. We can therefore use the camera to identify the net tilt and use the mirror to correct for it while still having sufficient control range for regular tip-tilt control operations. In this way, the wedge compensates for the dispersion from the scalar vortex mask and provides a broadband null of $< 10^{-5}$ across the full K band.

For simplicity, the wedge could be placed directly on the vortex mask so that the dispersion correction is applied within the mask itself without having to add additional mounts or elements to hold a separate optic. A beneficial side effect of this design is that it would also offset the internally-reflected “ghost,” shown in grey in Fig. 8.3, relative to main through-beam from the vortex. A “ghost” is a co-propagating beam of reduced intensity resulting from a back-reflection inside an optic. At the final focal-plane, ghosts lead to PSFs with similarly-reduced intensity but that can still couple into the fiber and result in chromatic fringing

on the spectrograph. With a wedge on the vortex mask, the ghost would exit the optic at $\delta_g = \alpha(3n - 1)$ relative to the incident beam so it would be offset from the through-beam by

$$\begin{aligned} \delta_g &= \alpha(3n - 1), \\ \gamma_{\text{ghost}} &= \delta_g - \delta_{\lambda_0} = 2\alpha n, \end{aligned} \tag{8.3}$$

at the wedge plane. For the central wavelength, $\lambda_0 = 2.2$ $\mu$m, our $\sim$18.2′ fused silica wedge would offset the ghost by 52′ at the wedge plane and hence by 3.″6 on-sky, putting it 80 $\lambda/D$ off-axis from the main beam. This is far beyond the VFN coupling region and would completely mitigate any fringing from the vortex mask. Another benefit of this scalar vortex solution is that it would be relatively easy and inexpensive to manufacture using standard lithography methods; a quote from ZEISS, the vendor that produced the staircase mask in Desai et al. (2023), was 2.5× cheaper for 8 scalar masks than a single equivalent vector vortex mask like the one described in the following section.

Despite the many benefits, we ultimately decided not to move forward with the scalar vortex due to the risk to the instrument from using an untested technology. Some of our concerns included: quality of manufacturing, uncertainty about the actual dispersion, and uncertainty about the PSF seen by the tracking camera. This final concern is particularly salient since the ability to centroid and track the PSF for tip-tilt control is of critical importance for charge 1 VFN, as described in Sec. 8.4. One possible solution for the tracking PSF problem would be to add an equivalent, but conjugate in phase, charge 1 scalar vortex mask immediately before the tracking camera to counteract the effect of the initial vortex and generate an Airy-like PSF. This solution, though also untested, could result in a significantly stronger tracking signal than relying on the out-of-band zero-order leakage of a vector vortex mask, as is currently done. The uncertainty of scalar VFN kept us from deploying such a mask to an operational instrument but the promise of simulations so far prompts laboratory demonstrations, including on PoRT (see Sec. 4.3), to mature the technology.

## 8.2 Vector Vortex Mask Specifications

Once we settled on using a vector mask for the charge 1 upgrade, we set requirements for the optic. Since VFN operates differently than conventional coronagraphs, and we place our vortex in a pupil plane in KPIC, we can reconsider the usual specifications for such masks and design one that is optimized for KPIC VFN from the start. This section covers the considerations made when designing and

procuring the vector vortex mask for the upgrade. Note that the table at the end of this section summarize the predicted on-sky null depth for the charge 1 KPIC VFN mode assuming the specifications are met.

The first specification to set was the total goal starlight leakage from the mask alone, as that constrains many of the subsequent design decisions. We settled on a leakage of $\leq 10^{-3}$ so that the contribution to the final instrument null from the vortex is below the contribution from the next largest sources of leakage: atmospheric wavefront residuals (WFR) and tip-tilt jitter. From Sec. 5.5, we predict that WFR will contribute around $10^{-3}$ with charge 1 based on the measurements from June 17, 2019 (~90 nm RMS on the reconstructed data). The current jitter residuals would contribute about $2 \times 10^{-2}$ but we plan to reduce the jitter by a factor of 3, to 2 mas RMS or less (see Sec. 8.4 below). Even with our ambitious goal of 2 mas RMS, the null floor from jitter would be $3 \times 10^{-3}$, thereby keeping the goal contribution of $\leq 10^{-3}$ from the vortex low enough to not dominate the on-sky null.

**Zero-order leakage**

We set the zero-order leakage specification such that less than 0.1% of the light ($< 10^{-3}$) exits the mask without acquiring the vortex phase ramp. Such leakage manifests in the final focal plane as an Airy PSF which, assuming no wavefront error, couples into the fiber with at-most 67% efficiency on the Keck aperture (see Sec. 2.6). Thus, the resulting null depth from starlight leakage in the zero-order term will be $< 7 \times 10^{-4}$. From Ruane, Mawet, et al. (2019), the fraction of light in the zero order term is proportional to $\epsilon^2/4$, where $\epsilon$ is the retardance error. This leads to a maximum retardance error specification of $6.3 \times 10^{-2}$ radians, or $< 3.6°$ at all wavelengths in the science band.

**Central defect and Clear aperture**

A significant difference from conventional vortex coronagraph requirements is that the size of the central defect, known as the "region of disorientation" where the the vector mask does not provide the appropriate vortex phase, is no longer a concern. With the vortex in a pupil plane with the Keck aperture, the obscuration from the secondary mirror blocks about 25% of the telecope diameter. Thus, given the 12.5 mm diameter of the beam at the vortex plane, the central defect could be up to 3 mm without affecting the on-sky performance. When off-sky, there is no secondary obscuration so the central defect does become a concern, though it still far less of an issue than in conventional vortex coronagraphs that place the vortex in

the focal plane. If we set the defect diameter for the KPIC VFN vortex to less than 200 $\mu$m, then 0.02% of the light will pass through it without acquiring the desired vortex phase, and hence the resulting null contribution from this term would be $< 2 \times 10^{-4}$. 200 $\mu$m is readily achievable (typical coronagraphs require $< 15\mu$m) so this drastically reduces the requirement while still keeping the central defect negligible in off-sky operations.

The trade-off with operating in the pupil is that the mask needs to provide the correct retardance over the optic's full clear aperture. In a typical coronagraph where the vortex sits in a focus, the vast majority ($> 80\%$) of the energy in the starlight is concentrated in the Airy core and more than 95% within the first four Airy rings. This makes the central region of the mask the highest priority. For pupil plane VFN, the energy is equally distributed over the mask in the pupil such that the retardance spec needs to be met over a wider region of the optic.

**Spot Defects**

In the same way, defects at any individual point in the pupil are less important since they represent a small fraction of the total light. This manifests as a less restrictive tolerance on spot defects and imperfections, which in a typical coronagraph would scatter light within the Lyot Stop and thereby increase the stellar leakage. Since vector vortex masks are made from many liquid crystal polymer (LCP) layers stacked together, spot defects can be introduced at multiple points in the process. Therefore, loosening the typical requirements here should make a large difference in the cost and ease of manufacturing since it increases the yield of usable LCP layers. We simulated the effect of spot defects in a putative charge 1 vortex mask to determine the requirements needed for the KPIC VFN mode.

The simulations introduced two types of spot defects: amplitude and phase. For simplicity, amplitude defects were modeled as opaque square spots in the pupil where the light is completely blocked. Meanwhile, phase defects were modeled as square regions where the retardance is zero, leading to a spot without the desired vortex phase. Both types of defect were randomly placed throughout the simulated pupil, varying the size of the defects from 13 $\mu$m to 4 mm (at the vortex plane) and the number of defects from 0 to 10,000. Two dimensional coupling efficiency maps were then computed, from which the null and azimuthally-averaged peak off axis coupling were determined. Each size and number combination for the defects was simulated 5 times and the results were averaged together to provide a representative

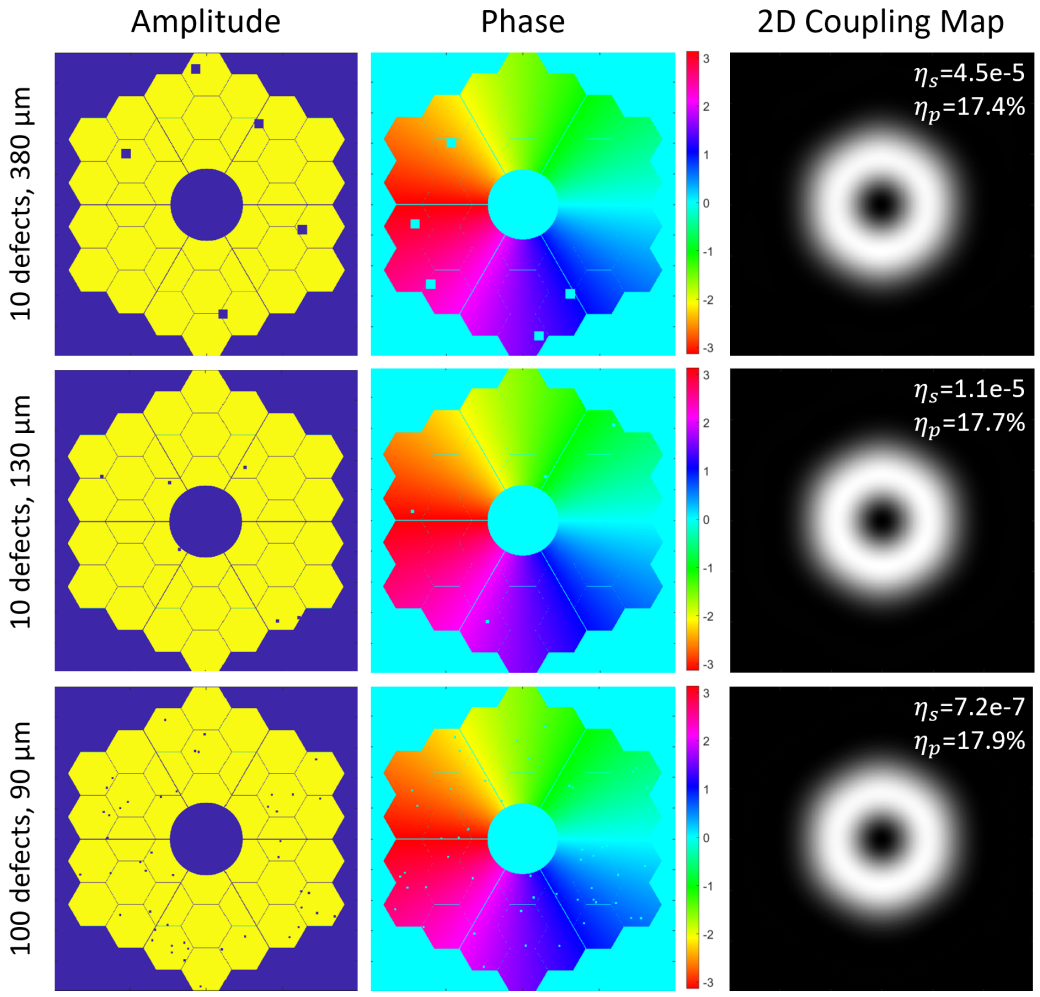


Figure 8.4: Three sample cases from the simulations on the effect of spot defects in the pupil plane vortex mask for VFN. The top row shows a case with 10 total (5 amplitude and 5 phase) defects of 380 $\mu$m in size at the vortex plane. The middle row shows 10 (6 amplitude, 4 phase) of 130 $\mu$m and the bottom row shows 100 (47 amplitude, 53 phase) of 90 $\mu$m. The resulting null and peak coupling efficiency for each sample case is included in the top-right corner of the 2D coupling maps. Note that the morphology of the maps, and hence the average peak coupling, is not noticeably affected by the defects.

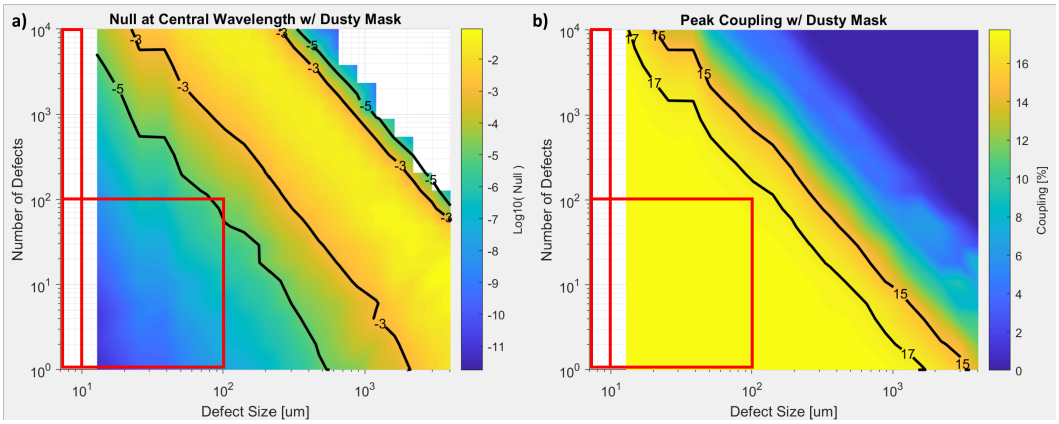


Figure 8.5: Sensitivity for charge 1 VFN to spot defects in a vortex mask in KPIC. (a) shows the effect of the defects on the null depth, with a logarithmic color-scale and black contours overlaid for $10^{-5}$ and $10^{-3}$. (b) shows the effect on the azimuthally-averaged peak coupling efficiency, with a linear scale and contours for 17% and 15%. The red boxes denote the resulting requirements set for the KPIC VFN mask to meet a goal of >17.8% peak coupling and $<10^{-5}$ null.

performance for the given case, independent of the random position of the defects. Figure 8.4 shows 3 sample cases for 10 defects of 130 and 380 $\mu$m in size and 100 defects of 90 $\mu$m. The resulting null for all three of these cases was $< 5 \times 10^{-5}$ and the off-axis coupling efficiency was only marginally affected, as shown in the top right text of the coupling maps. It is worth noting that even a 90 $\mu$m defect in a vortex mask for conventional coronagraphs would be unacceptable, so VFN is very robust to these types of manufacturing errors.

The results revealed that we can significantly reduce the spot defect requirements for the KPIC VFN vortex while still ensuring that such defects will not limit the on-sky null. Figure 8.5 shows the simulated sensitivity as a function of defect size and quantity over the aperture. The left panel (a) shows the effect on the null, with black lines denoting the contours in logarithmic scale for nulls of $10^{-5}$ and $10^{-3}$. The right panel (b) shows the effect on the azimuthally-averaged peak coupling, with black lines denoting the countours for 17% and 15%. As a reference, note that the ideal peak coupling would at-most reach 18% for charge 1 VFN on the Keck aperture. Thus, the peak coupling is primarily insensitive to spot defects up to a significant number and size combination. Once the first contour is crossed, the coupling drops off much more rapidly. Meanwhile, the null is more sensitive to spot defects, as expected, but can still tolerate a significantly higher number and size of defects than

conventional coronagraphs.

From these plots, we set the requirements for maximum number and size of spot defects on the mask. Rather than providing a function or contour curve for the vendor, we simplified the requirements into two branches: $<100$ defects of 100 $\mu$m and $<10^4$ defects of 10 $\mu$m. Regions meeting these requirements are shown in the plots as the two red boxes. This leads to a peak coupling efficiency $>17.8\%$ and null $<10^{-5}$ for the vast majority of scenarios. These requirements are far less stringent than what is usually set for conventional vortex coronagraphs such that the vendor should readily meet them and they have agreed to provide microscope images of different regions in the mask to validate the requirement.

**Fringing**

Since the vortex mask is located in a pupil plane, the thickness of the optic does not matter like it would in a conventional vortex coronagraph. However, being in collimated space makes the vortex mask susceptible to introducing internal ghosts that would lead to fringing. The mask is made of two pieces of glass sandwiching the LCP layers that generate the vortex phase. Each glass-air or glass-LCP interface spawns a Fresnel reflection that can lead to ghosts. The fringing effects from these ghosts can be mitigated in two ways. The first is to reduce the magnitude of the reflection through the use of anti-reflection (AR) coatings. The second is to wedge the glass as discussed for the scalar mask in Sec. 8.1. In talking with the vendor for our vector mask, we concluded that we should only AR coat the glass-air interfaces and wedge a single glass substrate. This will reduce the effect of fringing from the optic without adding unnecessary complications to the manufacturing process.

Figure 8.6 shows a diagram of the vector vortex mask with the glass substrates in blue, the LCP layers in green, and some of the key ghosts as colored arrows. Not all ghosts are represented here. However, any omitted ghosts will either exit the optic at the same angle and with the same intensity as one of the three ghosts shown in the diagram, or will experience more reflections which will decrease their intensity or increase the output angle relative to the main through-beam. For example, there is an omitted ghost similar to "Ghost 2" which will reflect off the left glass-LCP interface rather than the right one as shown in the diagram; this ghost will nevertheless exit with an angle very similar to, and at the same intensity as, Ghost 2. The same goes for other reflections within the optic. As such, the three included ghosts are representative of any problematic reflections in the mask.

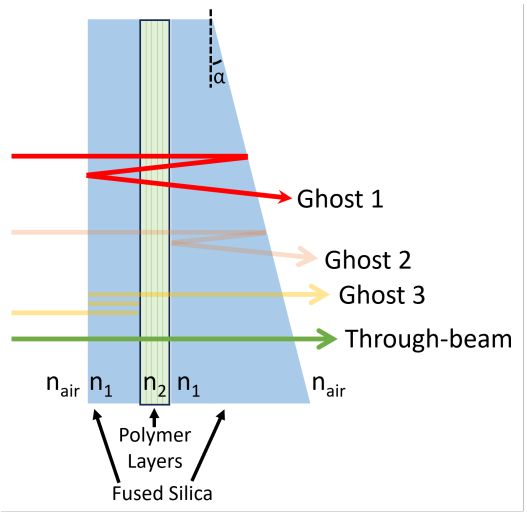


Figure 8.6: Schematic diagram of "ghosts" arising from internal reflections within a typical vector vortex mask. The LCP layers are sandwiched between two glass substrates. Fresnel reflections at the glass-air and glass-polymer interfaces generate ghosts that propagate through the optic and can leave the final surface at a similar angle to the main through-beam. Wedging the second glass substrate casts some ghosts to different angles that will mitigate the resulting fringing effect. Not all ghosts are shown here but rather a representative set denoting the key ghosts and their angles; other ghost reflections will occur but will either exit parallel to a ghost denoted here or will experience more reflections that decrease the intensity or increase the output angle relative to the main through-beam.

Given the constraints of only AR coating glass-air interfaces and wedging a single substrate, we can determine the impact of fringing and the necessary wedge angle. The LCP layers in our mask are index-matched to the fused silica substrate, such that the magnitude of the Fresnel reflections at the glass-LCP interfaces is $R_{\mathrm{LCP}}$~0.25%. We set the requirement for the AR coating at the glass-air interfaces such that $R_{\mathrm{air}}$<0.5%. Since the amplitude of the fringing goes as $2\sqrt{R_1 R_2}$, ghosts arising from the glass-LCP layers will be dominated by the Fresnel reflection at the glass-air interface. Additionally, the ghost arising from the two glass-air reflections (Ghost 1) will be the dominant ghost in terms of fringing amplitude.

Wedging one of the fused silica substrates casts some of the ghosts, including the dominant Ghost 1 in the diagram, away from the main through-beam so that they cannot couple into the fiber, thereby mitigating possible fringing from these reflections. Following Eq. 8.3, we set the wedge angle at $\alpha = 60.''6$ so that Ghosts 1 and 2 exit at 175″ from the main through-beam in the plane of the vortex mask. This

corresponds to 200 mas on-sky, or 4.4 $\lambda/D$, such that the ghost will couple into the fiber with ~0.1% efficiency. Combined with the AR coating that also reduces the ghost intensity relative to the main beam, this wedge will mitigate the fringing amplitude for Ghosts 1 and 2. Note that Ghost 3, which originates from reflections before the wedged surface, will exit the optic at the same angle as the main through-beam. The wedge therefore cannot address ghosts that arise before the final glass-air interface but these are less important than Ghost 1 since they are two times fainter given that the glass-LCP interfaces produce fainter reflections.

As explained in the scalar vortex design section (Sec. 8.1), the wedge will introduce a net tilt and dispersion across the science band. The net tilt from a 60.″6 wedge, determined by Eq. 8.1 at the central wavelength, will be 26.″4 at the vortex and hence only 30 mas on-sky. This can be readily corrected by the fiber alignment mirror, as long as the differential tilt between the measured tracking PSF ($\lambda$≈1.6 $\mu$m) and the science PSF on the fiber ($\lambda$≈2.2 $\mu$m) is accounted-for. The dispersion introduced across the science band is given by $d_W = \alpha\Delta n$ such that with $\Delta n$ = 3.4e−3 between the central and longest wavelengths, we get $d_W$=206 mas at the vortex. This corresponds to <0.25 mas projected on-sky, which provides a stellar leakage of $\sim 2 \times 10^{-5}$, well within our goal null for the vortex of $<10^{-3}$.

The specifications for reducing fringing from our vector vortex mask are thus an AR coating at the glass-air interfaces with <0.5% reflection in the science band, and a wedge angle of 60.″6 on the second glass substrate, assuming fused silica as the material. This leads to a fringing amplitude <0.7% for the co-propagating Ghost 3, which could not be tackled by the wedge, and less for other ghosts. The wedge will also result in a net tilt that will offset the PSF by 30 mas and will introduce stellar leakage at the edges of the band but the resulting null will still be $\ll 10^{-3}$ at all wavelengths, such that the resulting tilt and dispersion are not an issue.

**Wavelength coverage**

Ideally, the vortex would provide the desired null over the full K band. However, another place where we can decrease the challenge and cost of manufacturing is by providing a narrower spectral window for science, since it is more difficult to produce a mask with the desired retardance over a wider band.

The effective temperature of typical KPIC VFN targets is between 1200 and 4000 $K$, such that in K band, CO and $H_2O$ provide the majority of the spectral lines. The shorter KPIC echelle orders (0-2 on KPIC, 39-37, respectively, on NIRSPEC) are

dominated by $H_20$ whereas the longer orders (6-8 KPIC, 33-31 NIRSPEC) have more CO lines. However, the shorter orders also have strong telluric features that can limit the detection capabilities. With high-SNR observations, like the VFN detection of HIP 21543 in October 2022, both regions of K band can be used to detect the companion, with the detection in the longer wavelengths being slightly stronger than in the shorter wavelengths. However, combining the echelle orders for a detection across both regions does not significantly enhance the resulting SNR. Furthermore, for observations with lower SNR, only the longer orders lead to a detection and the shorter wavelengths do not improve the SNR at all. Thus, when considering only detection capabilities, the CO bandhead is the most useful and hence echelle orders 6-8 are the highest priority since this is where CO dominates and telluric features are scarce. For detailed characterization, where we will want to do things like compare molecular abundances, a wider spectral region may be of interest. The trade is therefore between detection and characterization capabilities at the expense of a higher-risk and costlier vortex mask.

Given these findings on the KPIC VFN detections so far, we considered two bandpasses for the charge 1 mask: 2.00−2.49 $\mu$m, spanning all of K band, and 2.22−2.49 $\mu$m, which would span echelle orders 5 through 8 on KPIC. We ultimately settled on the riskier wider-bandwidth option since the change in cost was about 20% but covering all of K band may allow us to do deeper characterizations in the future.

On a related yet paradoxical note, it is better for the vector vortex mask to exhibit large retardance errors, and hence high zero-order leakage, in H band. This is because the tracking camera operates in H band so higher zero-order leakage results in a more concentrated, Airy-like PSF that can be readily centroided. However, given the vendor's current capabilities, the H band performance cannot be controlled without risking the K band performance. We thus prioritized increased nulling in the science band and will need to adapt our PSF centroiding algorithms to identify the ring-like vortex PSF if the final mask is, ironically, too broadband. Similarly, the AR coating specification provided in the previous section should also minimize reflection in H band to maximize the available signal on the tracking camera. Our AR requirements therefore specify a reflection $< 0.5\%$ in the science band and $< 8\%$ in the tracking band, and the science band is chosen to span 2.0 to 2.49 $\mu$m for the best detection and characterization capabilities.

Table 8.1: Contributions from vortex mask to KPIC charge 1 null

| Null Term | Null Contribution | Comment/Assumptions |
|---|---|---|
| Zero-Order | $< 7 \times 10^{-4}$ | Retardance error <3.6° and ideal (67%) coupling on non-vortex PSF. |
| Central Defect | (on-sky) 0<br>(off-sky) $< 2 \times 10^{-4}$ | blocked by secondary mirror.<br>defect diameter <200 $\mu$m. |
| Spot Defects | $< 2 \times 10^{-5}$ | $\leq 10^{-5}$ from each red region in Fig. 8.5 |
| Wedge Disp. | ($\lambda_0$) 0<br>($\lambda_{\max}$) $2 \times 10^{-5}$ | Tracking centers PSF on $\lambda_0$ |
| Vortex Total | (on-sky) $< 7.4 \times 10^{-4}$<br>(off-sky) $< 9.4 \times 10^{-4}$ | At $\lambda_{\max}$; better at $\lambda_0$ |

NOTE- This follows the specifications listed in the rest of the section. Contribution from spot defects assumes maximum acceptable number and size of defects in the two requirement regions; it will likely be smaller. Wedge dispersion assumes 60.″6 angle on the second fused silica substrate. $\lambda_0$ is the central wavelength, $\lambda_{\max}$ is the edge.

**Final Vector Vortex Specifications**

Ultimately, the vector vortex was still expensive and challenging to procure since producing a polychromatic K band mask requires many more layers, and thicker layers, than our vendor, BeamCo, has done in the past. With the requirements listed above, the final null depth contribution from the mask will be $<7.4 \times 10^{-4}$ on-sky and $<9.4 \times 10^{-4}$ off-sky. Table 8.1 shows the contributions from the various vortex design elements. As expected, the largest contribution is the zero-order leakage term since minimizing the retardance error is the most challenging task. We nevertheless meet our goal of $<10^{-3}$ stellar leakage from the vortex mask.

The mask is currently being manufactured and will be delivered in the winter of 2023. Once it arrives, it will be characterized and validated in PoRT (see Sec. 4.3) prior to deployment in February 2024. If the as-delivered mask does not meet the desired null floor and off-axis coupling, we will fall back to the charge 1 vector vortex mask that BeamCo provided as a test sample, and which was characterized in Sec. 5.7. That mask produced a laboratory null of $3.1 \times 10^{-2}$ and an average peak off-axis coupling of 15.5% in 2.0 $\mu$m laser light on a Keck-like aperture (see Table 5.1). This is close to the goal of $<10^{-3}$ for the new mask but was measured at a single wavelength so it is unclear what the full K-band performance is.

## 8.3 Atmospheric Dispersion Corrector

The change to a charge 1 vortex means that KPIC VFN will be significantly more sensitive to differential atmospheric refraction (DAR) than it currently is with the charge 2 vortex. DAR is introduced by the Earth's atmosphere as light passes through a column of air that acts like a prism with a different refractive index at each wavelength. The resulting dispersion chromatically smears the PSF over the fiber such that it cannot be aligned to null at all wavelengths. The tracking script therefore strives to align the stellar PSF to null at the central wavelength, and the misalignments from DAR elsewhere lead to increasing stellar leakage and hence reduced companion SNR at other wavelengths. Since the dispersion grows towards the edges of the band relative to the central wavelength, the net effect is that DAR reduces the usable science bandwidth by washing out the outer wavelengths with starlight.

To mitigate the effect of DAR, the KPIC upgrade supplying the charge 1 vortex will also include an atmospheric dispersion compensator (ADC) that acts as a tunable prism capable of introducing an equal and opposite amount of dispersion. This section briefly covers the impact of uncorrected DAR as well as the predicted performance with the ADC. We talk about J band alongside K band here to provide an idea of the impact from DAR in possible future J band operation, since a J band science mode will soon be added to KPIC. However, there is currently no plan for J band VFN science or a J band vortex mask in KPIC and the emphasis with VFN remains on K band for the foreseeable future.

Wang et al. (2020) presented an initial design for the KPIC ADC which used two counter-rotating prisms, each composed of three optical wedges with different glass materials. This ADC design was ultimately not used due to poor transmission from the AR coatings but a new one has been designed following a similar process though using two wedges per prism instead, thereby improving the total throughput. In the original work, Wang et al. (2020) showed that the median observing conditions for Maunakea (276.15 $K$, 61400 Pa, 20% relative humidity) lead to a peak-to-valley (P-V) dispersion of 29.8 mas across K band and 81.1 mas across J band at a zenith angle of 60°. The bandwidth in K is slightly different in that paper than the specification set for the charge 1 mask: the paper uses 1980 to 2380 nm whereas the new mask will span 2000 to 2490 nm. However, given that the dispersion is shown to be roughly linear within an individual band, we can estimate that the P-V dispersion in the desired new region is about 36.5 mas. For the estimates in this thesis, we

Table 8.2: VFN performance without an ADC

| Band (nm) | Zenith (°) | Disp. at[a] Edges (mas) | Vortex Charge | Avg. Null at Edges | Fraction of[b] Band (%) | Bandwidth (nm) |
|---|---|---|---|---|---|---|
| | 30 | 11.17 | 1 | 9e-2 | 30 | 58 |
| J | | | 2 | 5e-3 | 100 | 190 |
| (1150-1340) | 60 | 33.50 | 1 | 1e-1 | 10 | 19 |
| | | | 2 | 1e-1 | 46 | 87 |
| | 30 | 6.08 | 1 | 1e-2 | 55 | 270 |
| K | | | 2 | 6e-5 | 100 | 490 |
| (2000-2490) | 60 | 18.25 | 1 | 8e-2 | 18 | 90 |
| | | | 2 | 4e-3 | 100 | 490 |

[a] Dispersion is reported at the edge wavelengths relative to the central wavelength in the band.
[b] Fraction of the original bandwidth for which the stellar leakage from DAR is less than leakage from wavefront or tip-tilt jitter residuals (see Table 8.3).
NOTE- Dispersion assumes median conditions for Maunakea (276.15 $K$, 61400 Pa, 20% relative humidity). Reported null is only the contribution from DAR.

only consider the median observing conditions as the original ADC design was able to comfortably meet the residual dispersion requirements in J and K band for the 95th percentile conditions (Wang et al., 2020); we expect that the new ADC design has similar robustness. We do, nevertheless, consider the change in dispersion as a function of zenith angle since it can be readily determined from the reported fiducial values by scaling according to

$$\delta_{\text{new}} = \frac{\tan(z_{\text{new}})}{\tan(z_{\text{fid}})} \times \delta_{\text{fid}}, \tag{8.4}$$

where $z$ is the zenith angle and $\delta$ is the P-V dispersion. The first three columns in Table 8.2 list the DAR without ADC correction over the actual KPIC bandwidth, assuming median observing conditions.

The spectrally-resolved null depth can be computed from these P-V dispersion values. Assuming linear dispersion within a band, the offset at each wavelength relative to the central wavelength is determined, and then the resulting star coupling is computed. Figure 8.7 shows the coupling efficiency as a function of separation in log scale to highlight the effect at small separations. From this analysis, the fifth column in Table 8.2 provides the null contribution from uncorrected DAR at

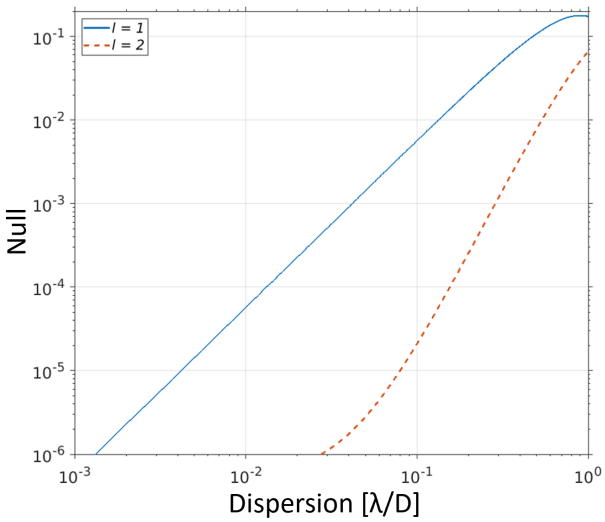


Figure 8.7: Null contribution, at each wavelength, for a given amount of dispersion. This is the same as the VFN coupling efficiency for an off-axis source, plotted here in log-scale to provide insight into the behavior at small separations.

the edges of J and K band, assuming the star is aligned to the fiber at the central wavelength.

We can contextualize these null values by comparing to the null contribution from wavefront and tip-tilt jitter residuals, listed in Table 8.3. Note that the tip-tilt jitter contribution assumes residuals of 2 mas RMS after the upgrade presented in Sec. 8.4, while the wavefront contribution uses the current AO residuals from Sec. 5.5. The combined null from these terms for charge 2 in K band is $4.4 \times 10^{-3}$. This is on-par with the contribution from DAR at the edges of the band at 60° zenith but a full order of magnitude larger than the DAR contribution at 30° zenith. Thus, the DAR is negligible for most observations with charge 2. This is not the case with charge 1 since the wavefront and tip-tilt null contribution will be $3 \times 10^{-3}$ after the tracking upgrades but the DAR is at $1 \times 10^{-2}$ even for 30° zenith. Another way to consider this is that the DAR will become the limiting term across 55% of K band with charge 1 at 30° and 18% at 60°. The two rightmost columns in Table 8.2 list the "effective bandwidth" set by DAR, defined as the fraction of K band where DAR is not the limiting term.

Figure 8.8 shows much of the same information as the previous tables but in a visual format. Each figure represents the stellar leakage at a specific observing band (J or K) and zenith angle (30° or 60°). The solid lines are the leakage due

Table 8.3: ADC requirements from jitter and wavefront residuals

| Band | Charge | Tip-Tilt Jitter | Wavefront Res. | Sum | Requirements (mas) TT+WFR | Requirements (mas) $10^{-3}$ |
|---|---|---|---|---|---|---|
| J | 1 | 6.1e-3 | 3.7e-3 | 9.8e-3 | 6.95 | 2.17 |
| | 2 | 3.7e-5 | 1.4e-2 | 1.4e-2 | 29.98 | 13.90 |
| K | 1 | 1.9e-3 | 1.1e-3 | 3.0e-3 | 6.80 | 3.78 |
| | 2 | 3.5e-6 | 4.4e-3 | 4.4e-3 | 37.78 | 24.18 |

NOTE- Null values are for the central wavelength. Contribution from tip-tilt jitter assumes 2 mas RMS residuals after improvements from Sec. 8.4. Wavefront contribution assumes the current 90 nm RMS residuals on the reconstructed pupil, as explained in Sec. 5.5. Requirements are set to beat the null from tip-tilt and wavefront residuals (TT+WFR) and $10^{-3}$ and are reported in P-V across the band assuming linear dispersion.

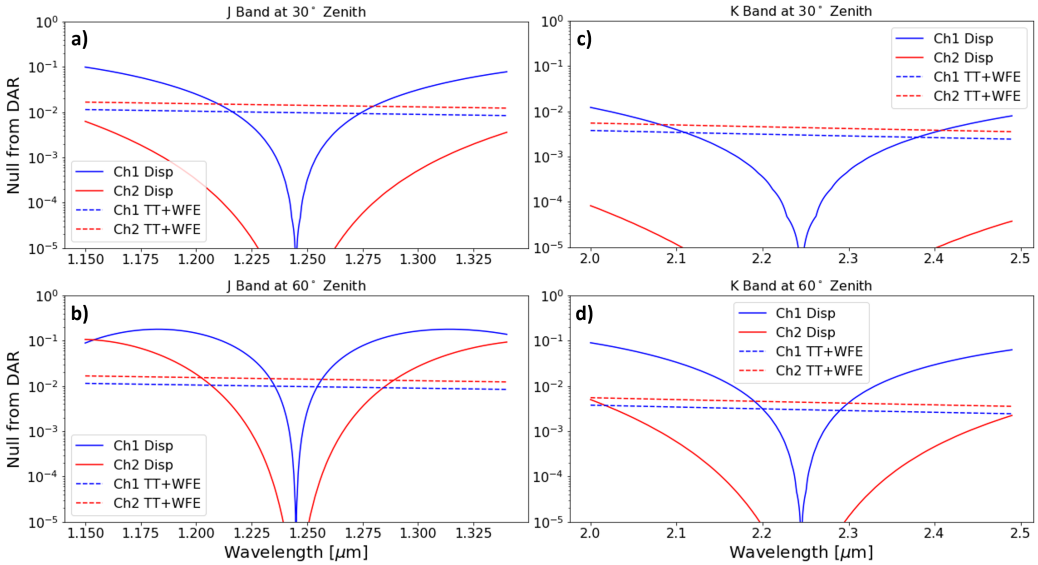


Figure 8.8: Null contribution across (left column) J band and (right column) K band for zenith angles of (top) 30° and (bottom) 60°. Blue lines are for charge 1 while red are for charge 2. Solid lines are the contribution from uncorrected DAR whereas the dashed lines are the combined contribution from tip-tilt and wavefront residuals, assuming 2 mas RMS jitter.

to uncorrected DAR (i.e., no ADC) as a function of wavelength while the dashed lines are the leakage due to other dominant terms, namely the sum of wavefront and tip-tilt residuals. Blue curves correspond to charge 1 and red to charge 2. The goal is to have the DAR null term be less than the null floor provided by the other terms. Anywhere that the solid lines are below the dashed lines is good since it means we are limited by wavefront and tip-tilt control capabilities as opposed to DAR. From Fig. 8.8(c and d), it is clear that for the planned charge 1 K band vortex upgrade, the DAR will limit the performance for a large part of the band.

Note that so far, this analysis has only considered the effect of DAR on the achievable null. Dispersion from DAR also reduces the VFN companion coupling since it moves the companion off the narrow coupling region. Figure 8.9 shows how the coupling efficiency changes due to DAR across the band assuming the fiber has been aligned with the star at the central wavelength and that the dispersion occurs along the radial axis between the star and the companion (the worst-case scenario). The companion is assumed to be at a separation corresponding to the peak off-axis coupling efficiency at the central wavelength; this is approximately 42 mas for charge 1 and 67 mas for charge 2 in K band. The green dashed lines are the coupling efficiency that would be achieved without any DAR, the solid blue line is for an observation at 30° zenith, and solid orange for 60° zenith. In K band at 30° with charge 1 there is a 2.5% degradation at the shortest wavelengths. However, the companion coupling at 60° degrades by more by 10% at the shortest wavelength. In J band, the effect of DAR is severe enough to set the coupling at 0% for much of the band with both charge 1 and 2 at 60°.

This raises the need for an ADC to ensure the DAR does not limit the star null or the companion coupling when moving to charge 1 on KPIC. Given that the null is more sensitive to DAR than the companion coupling, we can set the requirements for the ADC so that no part of the band has higher stellar leakage from residual DAR than tip-tilt jitter or wavefront residuals. We can also consider a more conservative case where the ADC requirements are set to keep its null contribution under $10^{-3}$ so that it is on-par with the contribution from the vortex mask itself and leaves room for further improvements in tracking and wavefront control. The two rightmost columns in Table 8.3 list the requirements by band and charge for these two scenarios. Considering only the imminent charge 1 K band upgrade, the requirements for ADC residuals are <6.80 mas P-V to beat the planned tip-tilt and wavefront residuals or <3.78 mas P-V to beat $10^{-3}$. Note that these requirements are listed as P-V dispersion

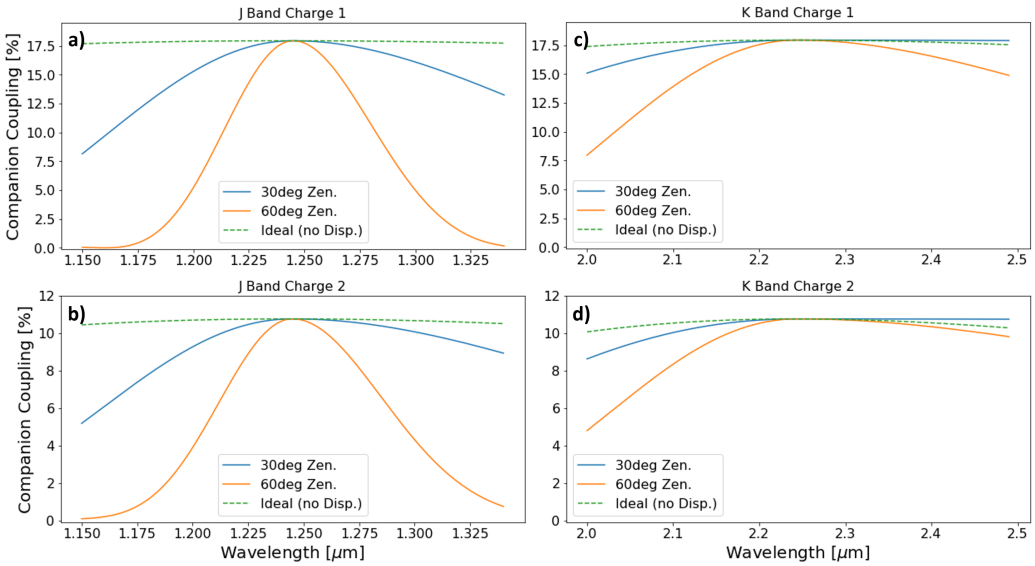


Figure 8.9: Companion coupling in the presence of uncorrected DAR for (left column) J band and (right column) K band with (top) charge 1 and (bottom) charge 2. Solid blue lines are for 30° zenith and solid orange are 60°, while dashed green are for the ideal case without dispersion.

across the band assuming linear dispersion and that the tracking system centers the PSF on the fiber at the central wavelength. The requirements can be rewritten more generally by halving the value and stating that no individual wavelength will be dispersed by more than this half-value relative to the wavelength centered on the fiber. We will nevertheless stick with the P-V formulation for simplicity.

The final ADC design that will be deployed with the charge 1 vortex uses glass substrates made of Ohara S-BAL42 and Ohara S-FTM16. The S-BAL42 element is wedged at 15.59° and the S-FTM16 element is at 15.54°. When clocked correctly, the residual P-V dispersion from this design at 30° zenith angle is 0.25 mas in J band and 2.18 mas in K band (over the original wavelengths spanning 1980 to 2390 nm). Though the dispersion may grow slightly when considering the expanded K band covering, it will readily meet both the TT+WFR requirement as well as the more-stringent $10^{-3}$ requirement at this zenith angle. At the time of this writing, the ADC was recently received and laboratory characterization and validation has begun; the results will be reported in a paper after deployment and on-sky demonstration.

## 8.4 Pointing Control

The designs in the previous two sections provide the optical elements necessary to run VFN with a charge 1 vortex. If the ADC and vortex meet the design specifications, neither will exceed a null contribution of $10^{-3}$. This means that the charge 1 VFN performance will likely be limited by atmospheric residuals from the AO system in the form of wavefront error and tip-tilt jitter. Of these two, the jitter will dominate since the current pointing residuals set a null floor of around $2\times10^{-2}$ whereas wavefront error provides a null around $10^{-3}$. Meanwhile, with the charge 2 mask, we have an estimated null floor of $\eta \approx 9.5\times10^{-3}$ (see Sec. 6.6) and a previously-predicted null of $6\times10^{-3}$ (see Sec. 5.3 and Fig. 5.4). This means that the null for the new charge 1 VFN mode will likely be around 2 to 3 times worse than the current charge 2 null. This reduction in null depth will effectively cancel any gains in integration time provided by the change to a charge 1 mask; the new off-axis throughput will increase by 1.8× (see Sec. 6.7), thereby reducing the relative integration time by a factor of 3.25, but the worsened null will increase the relative integration time by a factor of 2 to 3. We therefore need to improve the tip-tilt jitter residuals to actually see an improvement in instrument performance and hence make the charge 1 vortex mask upgrade worthwhile. Given the quadratic sensitivity of charge 1 on pointing residuals, an improvement in tip-tilt jitter by a factor of 2 would lead to a 4× deeper nuller and hence a similar 4× reduction in total integration time, while simultaneously providing access to closer-in planets with the reduced IWA of charge 1 VFN. The upgrades to the KPIC tracking system have already started and have shown a reduction by 25% in jitter residuals. This section presents the work done so far and the next steps to meet the requirements for charge 1 operation.

### Requirements and Original Tracking Performance

KPIC relies on a two-tiered control system to maintain the pointing on the fiber. The facility AO system tackles the bulk of the wavefront errors, including tip and tilt, to provide a clean, high-Strehl PSF and jitter residuals with an RMS amplitude of 6 to 7 mas. The KPIC tracking camera then identifies the star's PSF and uses the fiber alignment mirror (FAM) to point it to the desired SMF in the fiber bundle (see Sec. 6.4). For DS and charge 2 VFN operations, the current jitter residuals from the AO system do not limit the instrument performance, so the KPIC tracking system was originally designed to steer the PSF to the desired SMF in the fiber bundle and then perform low-frequency drift control that keeps the star's average position at the right location relative to the fiber. As a drift-control system, the original tracking

control implementation worked very well; it held the average position of the star's PSF at the desired location to within 0.15 mas whereas the facility AO system alone would allow the PSF to drift by up to 2 mas over 5 seconds.

Though the original KPIC tracking system was able to tackle low-order drift, it could not mitigate the high-frequency jitter residuals, which remained roughly the same as received from the facility AO regardless of whether or not the KPIC tracking system was performing its additional correction. Section 2.6 presented the VFN sensitivity to pointing errors like tip-tilt jitter. The null contribution from jitter follows a power law that scales as $\eta_{\text{jit}} \propto \sigma_{\text{jit}}^{2l}$. This makes charge $l = 1$ VFN much more sensitive to jitter than charge $l = 2$. As such, the charge 2 null contribution from jitter was $\eta < 10^{-3}$, making it a non-issue. For charge 1, the current jitter residuals would limit the null to $2{\times}10^{-2}$ (see. Fig. 2.8(b)). To set a null contribution from jitter of $\sim 8 \times 10^{-3}$, such that the null with charge 1 matches the current null value from charge 2, we would need to reduce the jitter by a factor of 1.6, so that it has an RMS amplitude of ~4 mas. This would provide a net factor of 3.25 reduction in integration time required to reach the same SNR as with charge 2 VFN, since the throughput is close-to-double with charge 1 while the null would remain the same.

To assess the limitations in the original tracking script, we measured the jitter residuals on-sky with the KPIC tracking loop on and off. This was done by saving the live images from the KPIC tracking camera and then centroiding them after-the-fact to determine the PSF position at each frame. Since the tracking camera is at a focal plane immediately adjacent to the fiber focal plane, it provides the most accurate measurements of the jitter seen by the fiber. This gives the "open-loop" input disturbances to the control system alongside the "closed-loop" performance for comparison. Note that open-loop here refers only to the KPIC tracking system; on-sky KPIC operations are always performed with the facility AO system in closed-loop to provide wavefront correction and a preliminary reduction in the input jitter. Figures 8.10(a-b) present the power spectral density (PSD) of the jitter with the KPIC loops open (blue) and closed (red) for the X- and Y-axes. The PSD breaks the total jitter into individual temporal frequencies to show which ones are contributing the most power. For consistency, this data was taken at 200 Hz since this was the absolute maximum setting for reliable closed-loop operation at the time. This revealed that both axes have spikes at ~20 Hz and ~30 Hz which introduce a significant fraction of the jitter. The y-axis also has a very large spike at ~60 Hz which contributes even more power than the other two for this axis. These "tones" consistently appeared in

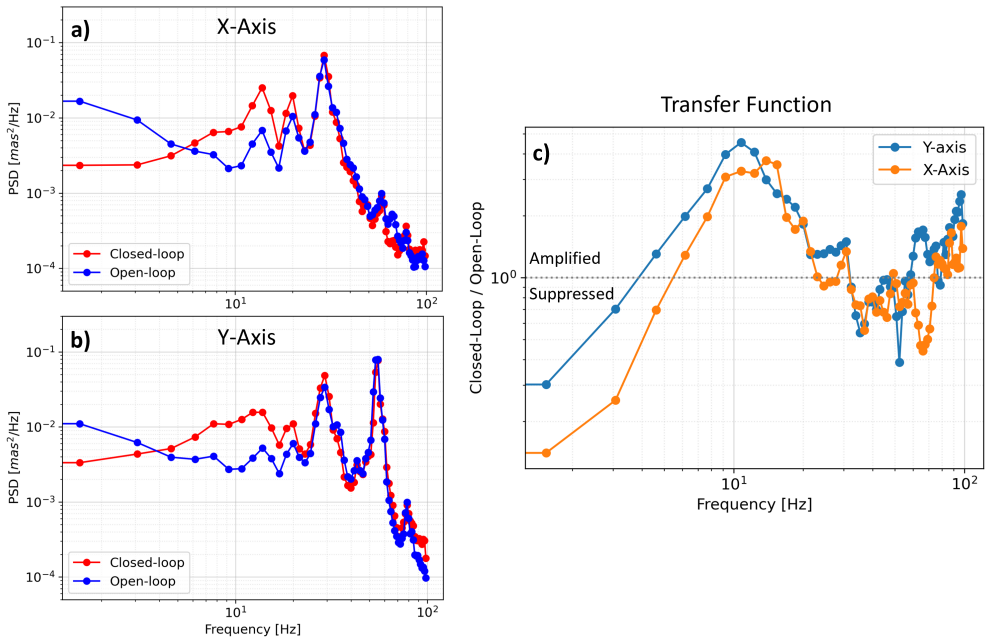


Figure 8.10: Performance of the original KPIC tracking system designed for drift control rather than jitter reduction. The left two plots show the PSD with open and closed loop operation, in blue and red, respectively. The upper (a) plot is for the X-axis and the lower (b) is for the Y-axis. Both axes have strong tones at at ~20 and 30 Hz, and the Y-axis has a more-prominent tone at 60 Hz. The right plot (c) shows the ratio of closed loop to open loop, which provides the system transfer function. This confirms that the system was able to mitigate low-frequencies (i.e., drift) but amplified the middle and high frequencies (jitter).

the PSD measurements across different nights with different observing conditions, indicating that they were likely something intrinsic to the system rather than from the atmosphere.

Taking the ratio of the closed-loop to open-loop performance provides the transfer function of the KPIC tracking control system. This shows how the system impacts the pointing accuracy at different frequencies. The transfer function is displayed for both axes in Fig. 8.10(c). The horizontal dotted line at a ratio of 1 separates the upper region, where the original control system was amplifying disturbances, from the lower region where it was successfully suppressing them. The low frequencies ($< 5$ Hz) were well-rejected, with the pointing errors getting down to $1/5^{\text{th}}$ of their input value at the lowest sampled frequency of 1 Hz. This reflects that the control system was successfully addressing the low-frequency "drift." However, the middle and high frequencies were strongly amplified by up to 5×, such that

rather than reducing the pointing jitter, the tracking loop was increasing it. Such a transfer curve is emblematic of a control system with a poorly-tuned gain relative to the available control bandwidth and latency. In this original design, the gain was tuned strictly considering the drift residual since reducing jitter was not part of the original requirements. This led to the large gain value that strongly suppressed low frequencies but unintentionally amplified high frequencies. The net effect was a control loop with good average positioning accuracy but poor jitter performance, such that the total RMS pointing residuals remained at around 6 to 7 mas.

**Redesigning the KPIC Tracking Control**

With this in mind, we set out to improve the KPIC tracking system to tackle jitter as well as drift. We took a bottom-up approach which started with characterizing the system, modifying the software to meet the new demands, then designing a new control algorithm, and finally testing this on-sky. This ultimately required a major overhaul with multiple layers of upgrades.

***Centroiding:*** Effective control requires accurate sensing for the feedback. In our tracking system, that involves accurately identifying and centroiding the PSF in the camera image to determine its position relative to the SMF. There are many different ways to compute a 2D centroid so we explored several options for the upgrade. The three key metrics for evaluation were: (1) that the centroiding algorithm should be accurate but (2) also fast and (3) operate with a fixed runtime. The speed requirement is a critical element so that the control loop can process images quickly and not be computation-limited. However, the fixed runtime is also important given the tonal nature of the input disturbances. The spikes are at very specific frequencies such that if we make sure that the control loop runs at a fixed frequency, then we can specifically target and mitigate the tones. The first algorithm considered was naturally the original KPIC algorithm. This used an iterative Gaussian fitting algorithm with 6 free parameters: amplitude, X-center, Y-center, standard deviation (STD) in X, and STD in Y. That proved to be exceedingly slow and computationally expensive. We therefore considered other fitting methods, including the 1D and 2D Gaussian functions, as well the quadratic fitting function, from the popular python Astropy Photutils package. We also wrote a new, stripped-down, custom Gaussian fitting function that removed many of the software overheads and fit a symmetric distribution to reduce the number of free parameters in the fit. In addition to the fitting methods, we tried two simple center-of-mass algorithms: the default from the Photutils package and one that we wrote ourselves – again stripping any overheads.

All of the methods were tested using a simulator of the KPIC tracking camera. This simulator generated images with realistic photon and read noise properties as well as varying amounts of wavefront error and tip-tilt jitter. With the known tip-tilt offsets for each simulated frame, the images were then fed to the various centroiding algorithms to test their accuracy and the robustness to noise and wavefront error. The new custom Gaussian fitting function not only produced the most accurate results but it also ran $10-100\times$ faster than the original KPIC function. However, all of the fitting methods, including the custom Gaussian, were iterative such that the computation time between frames varied significantly depending on the quality and shape of the PSF. These therefore failed to meet our third requirement of a fixed runtime. The custom center-of-mass algorithm proved to be the second-most accurate, delivering centroids with errors less than $1/10^{\text{th}}$ of a pixel even in the presence of significant wavefront error. Given the 7.24 mas/pixel platescale of the tracking camera, this $1/10^{\text{th}}$ corresponds to sub-milliarcsecond accuracy. The center-of-mass algorithm was also the fastest and had a theoretically-deterministic runtime since it only requires iteration and summation over a fixed number of pixels. We therefore settled on a custom center-of-mass algorithm for the centroiding.

***Control Software Overhaul:*** With an accurate, fast, and stable centroiding algorithm figured out, we proceeded to overhaul the rest of the control software to operate quickly and stably. We started by determining the loop speed limits set by the hardware. The tracking camera can run at several kHz, and the existing camera control software was an outlier since it was already written in C++ to quickly read and dump images into shared memory for other processes (i.e., the python tracking script) to access at will. As such, this element of the control system could already pull images at >1 kHz without missing frames. The hardware limitation was therefore at the FAM. We measured the step response of the FAM to determine the latency in communications and the mechanical rise time. Figure 8.11 shows the step response under three test conditions. The leftmost plot was taken with the KPIC default architecture where FAM commands were written in python to a shared memory which another python script read and sent to the mirror. This led to software overheads from the additional mirror control script, such that there was a 2.7 ms delay from when the command was written to when the mirror started moving. The middle plot shows an alternative software implementation where the additional python script is removed and commands are sent directly to the mirror from the tracking control code. This reduced the start delay by 0.6 ms, reflecting the overheads added by the extra software layer. Finally, the rightmost plot, Fig. 8.11(c),

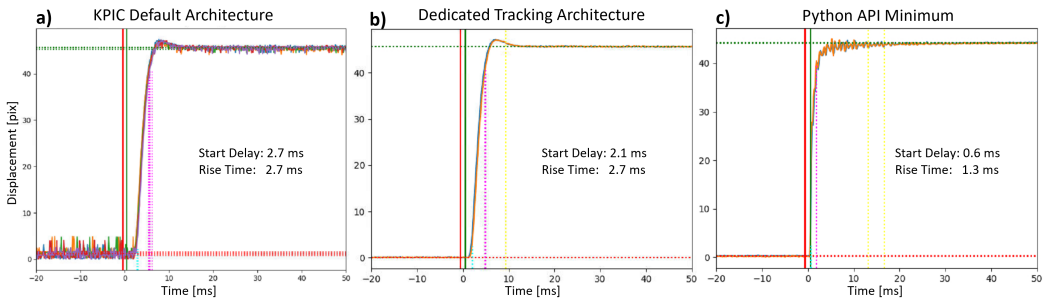


Figure 8.11: Baseline step responses for the KPIC FAM (a) through the full KPIC software architecture, (b) bypassing software overheads, and (c) turning off the mirror's firmware control loop. The interval between the vertical red and green lines denotes time when the move command was written in software. The vertical blue line shows when the PSF starts to move as seen by the tracking camera, and the purple lines denote the 90% rise time point. The rightmost option is the fastest but requires operating without the strain gauge sensors, which can lead to hysteresis and other issues from the piezo actuators. The middle option is the closest to the latest implementation, though this plot may still have overheads from python whereas the new control code is written in C++ and should have a slightly shorter start delay.

shows the step response when the mirror is operated without an additional firmware control loop provided by the vendor inside the mirror controller itself. This loop uses the strain gauge sensors in the mirror to ensure the mirror goes to the desired position, but adds additional firmware overheads of about 1.5 ms and slows the mirror rise time by 0.8 ms. In fact, the measured 0.6 ms delay in this dataset is within the uncertainty in the start-time measurement denoted by the red and green vertical lines. As such, plot (c) reflects the minimum possible step response of the mirror. However, operating in this mode would lead to undesired hysteresis, possible resonances, and other effects such that the vendor strongly discourages bypassing their embedded control loop. We therefore did not consider this option and settled on the middle option, where commands are sent directly to the mirror from the tracking control code. This provided a minimum latency of around 2 ms from when the control code tries to move the mirror to when the mirror actually starts moving.

We also did an accounting of the time needed for other elements within the original control architecture. To give an idea of this accounting, Fig. 8.12 shows a timing diagram made before the software overhaul began. The diagram assumes that the tracking camera (CRED2) is running at 200 FPS for a total of 5 ms available to complete all steps required in a single iteration of the control loop. The solid boxes

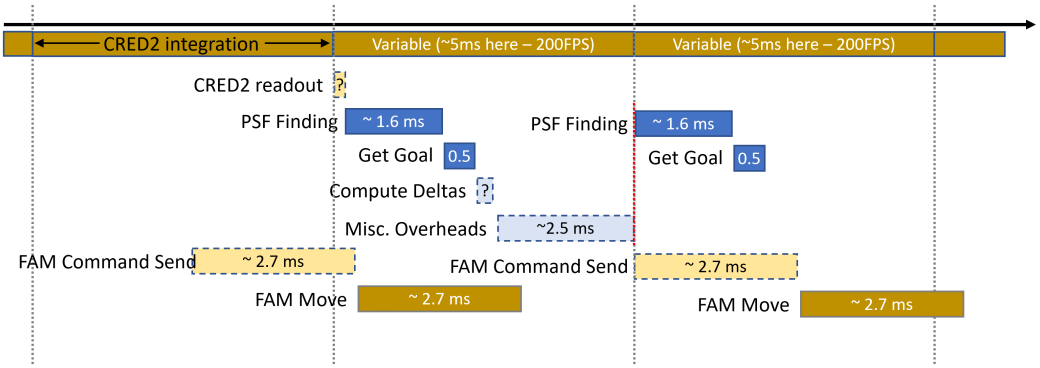


Figure 8.12: Preliminary timing diagram for the original KPIC tracking control script. This diagram shows the approximate time required for various steps in the the control loop. The tan and gold boxes are steps related to the hardware elements in the system, whereas the blue boxes are software elements. The camera can run at several kilohertz but is shown at 200 FPS to reflect the fact that the original software limited the control loop to around 150 to 200 Hz. Profiling tests revealed that the original control loop spent around 2.5 to 3 ms on miscellaneous overheads from unnecessary computations.

are values that were measured at the time, such as the FAM start delay and rise time, whereas the dashed boxes represent values that were inferred from timing tests of the software. This revealed that the majority of our our computation and software time, shown in blue, was spent in miscellaneous overheads from the original code. Thus, even though the camera could run faster than the assumed 200 FPS in the diagram, the original software would limit us to around 150 to 200 Hz.

We started stripping the control software of unnecessary elements to increase the operating frequency. This involved extensive profiling to identify bottlenecks and places where the code could be refactored to run faster. However, with the code running at around 250 Hz, timing instabilities started to appear and the internal variability of the python implementation became clear. As mentioned earlier, the timing stability is crucial to tackling the predominantly-tonal nature of the input disturbances for our system. Python and other interpreted languages can run extremely quickly, but the timing stability can vary significantly depending on the implementation and build. For our original KPIC software, it seems that the libraries in use and the multi-layered interactions between various control elements were leading to large instabilities that limited the performance at around 250 Hz. This is not surprising as the tracking script was originally written to only tackle drift, where

timing was not an issue. We therefore decided that the simplest route to meeting the new speed and stability requirements was to rewrite the tracking control software from scratch, carefully profiling and testing during the process. However, given the opportunity to rewrite the software, we also chose to switch to a compiled language which would not only be able to run faster, but would also be more stable. This would also put the KPIC tracking control system closer to a real-time implementation.

We considered writing the code in C but due to the available vendor-supplied libraries for the tracking camera and FAM, we settled on C++. The new code was written such that the main control loop only included the bare minimum steps needed for identifying the PSF and commanding the mirror. Other computations were moved to separate lower-cadence scripts that post shared memories with pre-computed values for the tracking script to pull as needed. For example, the software DAR correction now runs as a separate python script that reads the temperature and pressure sensors from the telescope to compute the offset needed to center the correct wavelength on the fiber in the presence of atmospheric refraction. The temperature, pressure, and zenith angle do not change quickly so the DAR does not need to be recomputed on every iteration as was done in the original script. Based on the FAM step response tests, we also removed the middle software layer in the FAM control so that the tracking script now communicates directly with the mirror. Several other similar modifications were made in the translation from python to C++.

This allowed us to run the control script and camera at 300 Hz, thereby increasing the maximum operating frequency by a factor of two. The new speed limitation for the script comes from a bug in the vendor-supplied library for the FAM, and we are working with the vendor to resolve it. Preliminary tests show that once the bug is fixed, the control loop should be able to run at 400 Hz. The timing stability with the new script is also significantly better than with the previous python implementation. However, there are still small instabilities that we believe are due to interruptions at the operating system level from the numerous other scripts that need to run on the computer at the same time to execute an observation. We are looking into processor shielding and other real-time mechanisms which would allow us to isolate specific CPUs for the tracking script and thereby set an extremely stable loop time.

***System Identification:*** With the new control script running faster and more stably than the original, we performed a detailed system identification procedure to measure the system's new latency and response. This was done by injecting a carefully designed signal composed of sinusoids with specific frequencies and phasing. The

so-called Schroeder-phased input signal has several useful properties for testing the plant in a control system (Schroeder, 1970; Rivera et al., 1993). For example, in the time-domain, the signal has a low crest factor such that it does not have any large peaks in amplitude that could over-exert the system. It also leads to robust measurements of system properties that are independent of noise and external disturbances.

For our KPIC tracking system tests, the new control software was modified to inject the Schroeder signal at the FAM command step. Thus, the new control script ran fully, with all its computations and latencies, to pull the images, identify the PSF, compute the centroid, and compute the desired mirror command. However, a flag was set in the software for tests so that rather than sending the computed control command at the next step, the test point from the Schroeder signal was sent to the mirror and the computed centroid was saved to memory. Then on the next loop iteration, everything was repeated but with the next test point from the signal. Thus, the signal was injected with the same mirror used for control and was sensed with the same camera used for sensing, in exactly the same software setup that the system would normally operate. By comparing the desired injected signal to the actual measured signal, we were able to determine properties of the system like the latency, clocking angle between the axes, gains in the amplitude, and much more. These tests were run with the KPIC internal light source so that no external vibrations or disturbances were added by the upstream optical train of the Keck AO system. After the software upgrades, the Schroeder tests showed that we could readily run the tracking system at 300 Hz, as the injected and measured signals closely matched each other. When we tried to run at 400 Hz, the measured signal was grossly distorted, which is what helped us identify the aforementioned bug in the vendor-supplied library.

The Schroeder-phased tests gave us a deep understanding of our control system and its ability to control and sense jitter. However, to design a dedicated controller, we had to assess the jitter residuals from the AO system as these would be the input disturbances to the KPIC tracking system. We repeated the on-sky open-loop PSD measurement shown in Figs. 8.10(a-b), but this time sampling the jitter up to 1 kHz. The higher-frequency sampling was achieved by free-running the camera at 2 kHz such that the images were pulled straight from the framegrabber and dumped into memory without passing through the control script. This allowed us to bypass computations and control elements in the control script which limit us to 300 FPS

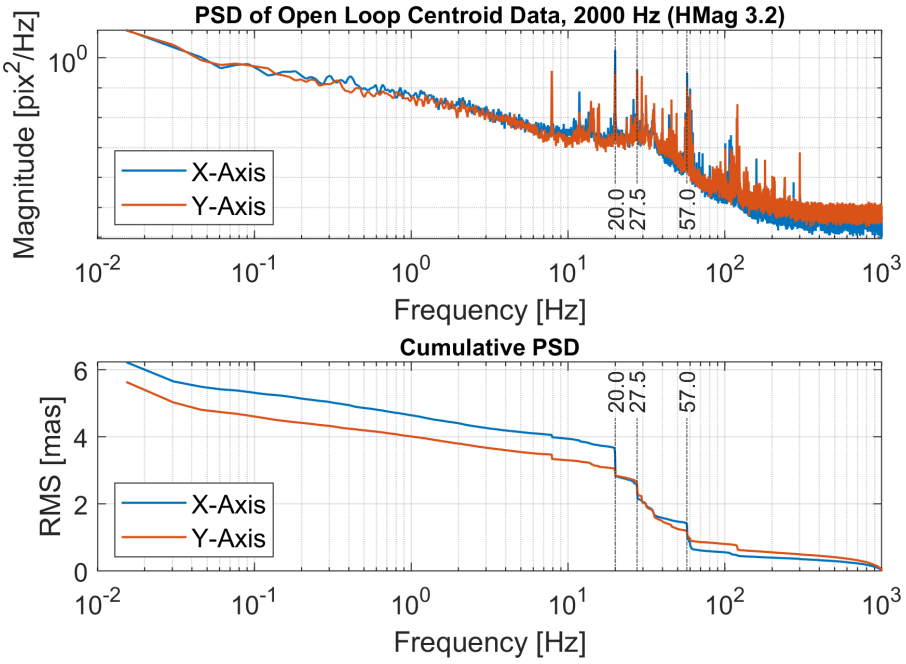


Figure 8.13: PSD of tip-tilt jitter residuals received from the Keck AO system with the KPIC tracking loop off. The top plot is analogous to the left plots in Fig. 8.10 but with significantly extended frequency coverage. The bottom plot is the cumulative PSD over the sampled frequencies. The sharp drops in the cumulative plot correspond to frequencies that contribute a significant amount of power. Three frequencies are marked with labeled vertical lines. These denote the three tones that consistently appear in the KPIC input jitter. For example, the first tone, at ~20 Hz contributes around 1 mas RMS to the total jitter in the tracking X-axis.

on the CRED2. We also sampled significantly lower frequencies down to $< 0.02$ Hz in the same dataset by obtaining a much longer time span of open-loop images. This dataset, shown in Fig. 8.13, thus provides the open-loop PSD over five orders of magnitude in frequency space.

Despite being taken several months after the dataset in Fig. 8.10, the new PSD also shows strong tonal features at ~20, ~30, and ~60 Hz. This validates that those tones are intrinsic to the optical train rather than the atmosphere. Additionally, since the tones do not appear in the PSD measurements made with the KPIC internal light source, they likely correspond to vibrations in the telescope structure or in the Keck AO beampath, but not something within the KPIC instrument itself. The cumulative PSD shown in the lower plot in of Fig. 8.13 reveals that the 20 and 60 Hz tones alone contribute about 2 mas RMS to the jitter in one axis. In this particular dataset, the jitter in the other axis seems to be dominated by the 30 Hz tone. The low frequencies

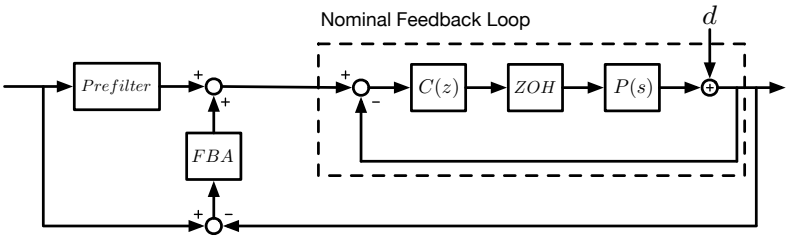


Figure 8.14: Control block diagram for the new KPIC tracking control system. User inputs for the goal pixel position of the star's PSF are first passed through a prefilter to smooth any large step changes and avoid inserting instabilities. The nominal feedback loop, denoted by the square box with dashed lines, is composed of the default control law $C(z)$, a firmware-implemented zero-order hold (ZOH) in the FAM controller, and the FAM itself $P(s)$, which are driven by feedback from the tracking camera. The feedback assist (FBA) compensator is an additional augmentation that can be enabled to add gain for attenuating specific disturbance frequencies.

($< 10$ Hz) are also contributing about 2 mas RMS to the total jitter. Furthermore, the left edge of the plot shows that on this night, which had better-than-usual observing conditions, the jitter residuals from the AO system were around 6 mas RMS, which is roughly consistent with previous open-loop measurements.

**Controller Design**

A dedicated controller was designed based on the results of the Schroeder-phased tests and the known input jitter residuals. The controller design was led by Joel Shields, a collaborator at JPL, who specializes in control systems such that this section only provides a top-level overview of the controller.

Figure 8.14 shows a schematic block diagram of the final tracking controller. The first element is a prefilter which is used to smooth-in step changes in the goal pixel location for the star's PSF. The KPIC tracking system sometimes needs to move the PSF from one SMF to another within the fiber bundle. This introduces extremely large steps (two orders of magnitude larger than the jitter residuals) which can make the control system unstable. However, profiling these step commands into the controller over several iterations mitigates their disturbances. The next element in the controller is the nominal control law. Given that the low frequencies in the input residuals contribute a significant amount of power, we targeted a baseline bandwidth around 10 Hz. However, this was limited by stability requirements and the operating

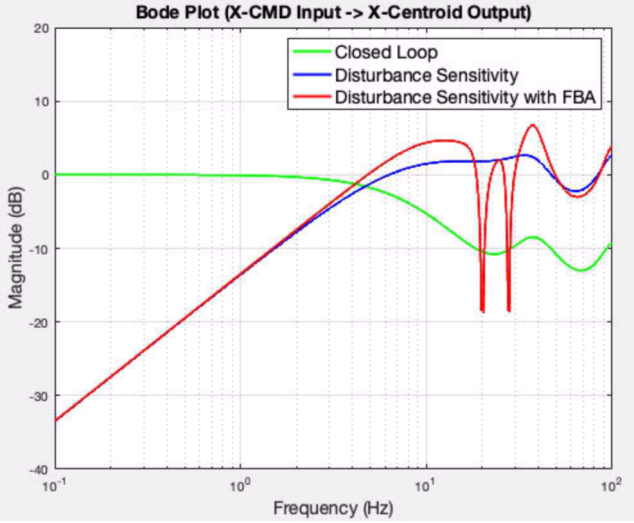


Figure 8.15: Transfer function for the KPIC feedback assist feature. The blue curve shows the disturbance sensitivity for the nominal feedback loop with a 7 Hz bandwidth. The red curve shows the sensitivity when FBA is enabled. The two narrow regions with deep disturbance rejection are centered on two of the tones from Fig. 8.13 so as to suppress the jitter at those frequencies.

frequency of 300 Hz, so we tested controllers with three different bandwidths: 3, 7, and 11 Hz. Though all three were stable in simulation, on-sky tests revealed that the 11 Hz was only marginally stable in practice. The 3 and 7 Hz controllers were nevertheless able to mitigate the low-frequency drift and were robust to impulses injected on the FAM as well as to changing PSF quality from wavefront residuals.

The prefilter and baseline control law described above make up the "nominal feedback loop" which deals with the low-frequency drift. However, even with the upper bandwidth of 7 Hz, this nominal design cannot tackle any of the tonal elements that contribute a large part of the jitter power. An augmentation called feedback assist (FBA) was thus added around the nominal loop. The FBA compensator acts as an additional feedback loop that can be enabled to address the tonal elements of the jitter. It works by increasing the gain at the specific frequencies of the tones, thereby suppressing them. These regions with additional gain are referred to as "ringers" and must be kept relatively narrow to ensure that overall the control loop remains stable. However, if the ringers are too narrow, then small shifts in the frequency of the tones can cause the ringers to miss them. Figure 8.15 shows the transfer functions for the overall control loop with and without FBA. The blue no-FBA curve has a smooth ramp up to the 7 Hz roll-over point where it mostly flattens out for

higher frequencies. Meanwhile, the red with-FBA curve shows two distinct regions of high gain around 20 and 30 Hz. These are ringers designed to suppress the first two jitter tones shown in Fig. 8.13. As shown in the figure, each ringer provides around 20 dB of rejection at the desired frequency but also amplifies disturbances in the surrounding frequencies. The ringers must therefore be carefully designed and tuned to ensure that they do not drive the controller unstable. As done with the bandwidth tuning, we designed and tested multiple controllers with an increasing number of ringers. Though all designs were stable in simulation, only the one-ringer design was stable in the off-sky tests. The stability for this design was further improved by switching to the less-aggressive bandwidth. Thus, our latest controller operates at 300 Hz with a bandwidth of 3 Hz and optional feedback assist that can be turned on to add a single ringer with 20 dB of gain at 20 Hz.

**Preliminary On-Sky Results**

We tested the new controller on-sky in late July 2023. A bright (H band magnitude 2.0) star was chosen to ensure a good signal to noise ratio on the tracking camera and a relatively clean PSF from the facility AO system. Figures 8.16 and 8.17 show sample PSD measurements from the three main test conditions: open-loop, closed-loop with only the nominal feedback, and closed-loop with the additional feedback assist enabled. The open-loop performance shows the usual 20 and 60 Hz tones with similar jitter contributions as previous measurements, while the 30 Hz tone was less pronounced on this night than in previous nights. The printed values on the left edge of the cumulative PSD plot show that the total open-loop RMS pointing residuals were around 6.5 and 5.1 mas for this night. The closed-loop, nominal feedback PSD has the drift clearly suppressed by between two and three orders of magnitude at the lowest sampled frequencies and seems to roll-over at 3 Hz as expected. Furthermore, no tones were mitigated in this nominal feedback sample, also as expected. The cumulative plot shows a completely flat spectrum for low frequencies, leading to residuals of 6.2 and 4.2 mas RMS. Finally, the rightmost plot with the FBA enabled shows the best performance. The low-frequencies are similarly suppressed with a roll-over at around 3 Hz. However, this time the 20 Hz tone is completely rejected. The top plot shows a deep notch from around 13 to 22 Hz, reaching more than 20 dB of rejection at the critical 20 Hz frequency. The bottom cumulative spectrum is flat at the low frequencies and then again in the notch region; the bulk of the power comes from the 30 to 60 Hz region where the controller could not tackle the disturbances. The final pointing residuals from

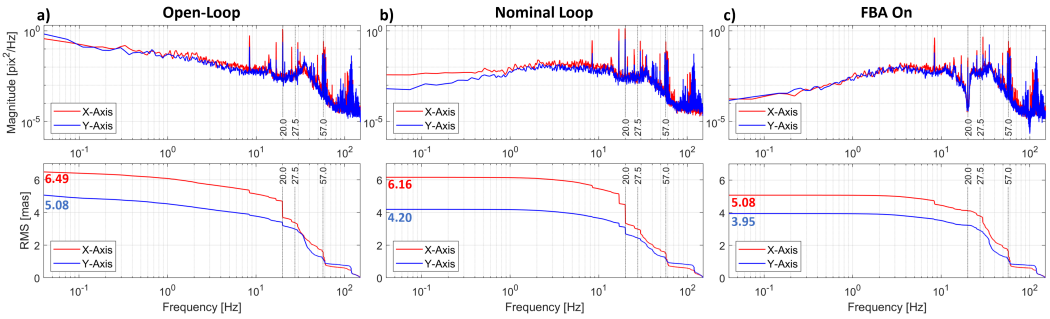


Figure 8.16: On-sky PSD for the new KPIC tracking control system in (a) open-loop, (b) closed-loop with only the nominal feedback, and (c) closed-loop with feedback assist enabled. Printed values on the left edge of the lower plots show the total cumulative RMS. This figure shows the same data as Fig. 8.17, but with test conditions separated to make it easier to discern the individual performance.

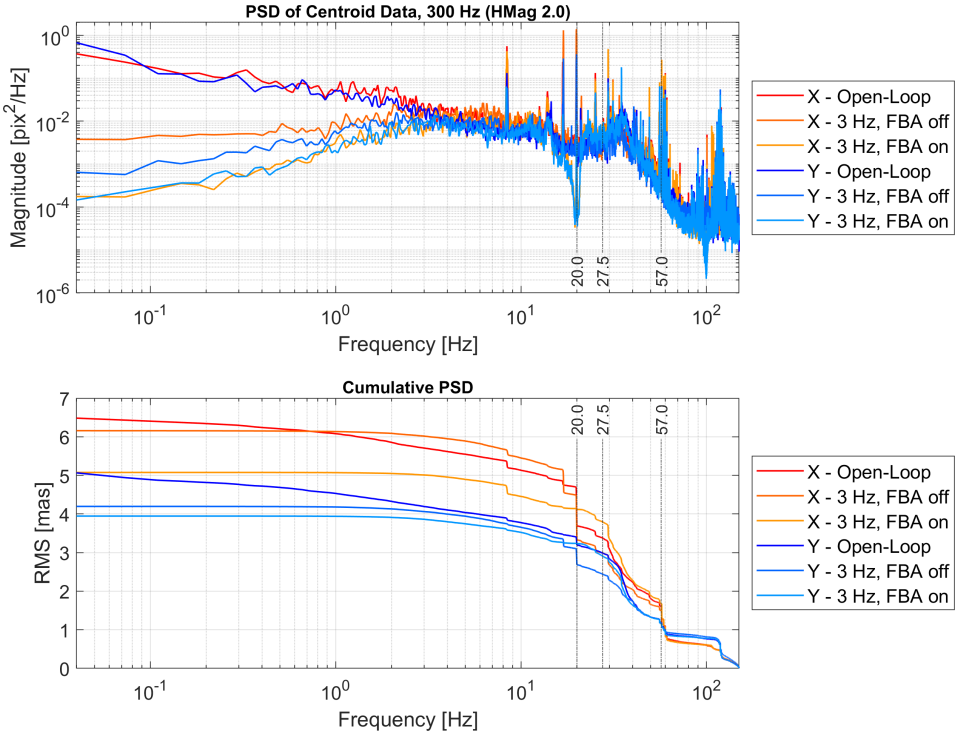


Figure 8.17: Same as Fig. 8.16 but with all curves overlaid for direct comparison.

this test case are 5.1 and 4.0 mas RMS. This corresponds to a ~25% reduction in pointing residuals compared to the open-loop sample and verifies that the ringers can successfully notch the tones while still allowing the nominal feedback element to address the drift.

We repeated these tests a few days later and showed very similar performance. However, the data on the later night was corrupted by a new, intermittent tone at

40 Hz which would appear in short (< 0.5 second) bursts. Such a tone had never appeared in prior data but was present in several samples on this night. Since the 40 Hz bursts appeared in some of the open-loop tests, we know that they were not introduced by our KPIC control loop. Therefore, we believe something in the AO system was likely acting up on the second night of tests, or something was causing the telescope structure to shake periodically. We were unable to perform any additional on-sky tests on other nights since the KPIC instrument was taken off-sky for the 2023 B semester (August 2023 to February 2024) shortly thereafter. We plan to continue our tests once the instrument returns on-sky after the service mission.

**Tracking Summary**

The new tracking control system is still being developed and requires additional work to meet the requirements for the charge 1 vortex upgrade. However, the modifications presented in this section lay the foundations for this work. The new control software already allows us to run the tracking system at 300 Hz and there is a clear path forward to reaching 400 Hz once the bug in the vendor-supplied library is fixed. Additional modifications to the operating system for the computer will also improve the timing stability of the control script. These upgrades will allow us to run with a higher bandwidth and additional ringers. The higher bandwidth will suppress more of the low-frequency drift from the atmosphere while the added ringers will tackle the tones that come from the telescope structure or the AO bench. This should allow us to reach our tracking goals for charge 1 given that the bulk of the power in the pointing residuals comes from these terms. In the meantime, the demonstrated on-sky improvement of 25% in RMS residuals is extremely encouraging. These first results serve to verify that the new controller design is sound and capable of addressing both drift and tonal jitter components. Once complete, this tracking work will be the subject of a journal paper.

**References**

Campbell, G. et al. (Mar. 2012). "Generation of high-order optical vortices using directly machined spiral phase mirrors". In: *Applied Optics* 51.7, p. 873. DOI: 10.1364/AO.51.000873. arXiv: 1107.1009 [physics.optics].

Desai, N. et al. (Apr. 2023). "Laboratory demonstration of the wrapped staircase scalar vortex coronagraph". In: *Journal of Astronomical Telescopes, Instruments, and Systems* 9, 025001, p. 025001. DOI: 10.1117/1.JATIS.9.2.025001. arXiv: 2305.05076 [astro-ph.IM].

Doelman, D. S. et al. (Apr. 2020). "Minimizing the Polarization Leakage of Geometric-phase Coronagraphs with Multiple Grating Pattern Combinations". In: *Publications of the Astronomical Society of the Pacific* 132.1010, 045002, p. 045002. DOI: 10.1088/1538-3873/ab755f. arXiv: 2002.05622 [astro-ph.IM].

Lee, J. H. et al. (Aug. 2006). "Experimental Verification of an Optical Vortex Coronagraph". In: *Physical Review Letters* 97.5, 053901, p. 053901. DOI: 10.1103/PhysRevLett.97.053901.

Leviton, D. B. and B. J. Frey (June 2006). "Temperature-dependent absolute refractive index measurements of synthetic fused silica". In: *Society of Photo-Optical Instrumentation Engineers (SPIE) Conference Series*. Ed. by E. Atad-Ettedgui, J. Antebi, and D. Lemke. Vol. 6273. Society of Photo-Optical Instrumentation Engineers (SPIE) Conference Series, 62732K, 62732K. DOI: 10.1117/12.672853.

Mawet, D. et al. (Feb. 2009). "Optical Vectorial Vortex Coronagraphs using Liquid Crystal Polymers: theory, manufacturing and laboratory demonstration". In: *Optics Express* 17.3, pp. 1902–1918. DOI: 10.1364/OE.17.001902. arXiv: 0912.0311 [astro-ph.IM].

Rivera, D. E., X. Chen, and D. S. Bayard (1993). "Experimental Design for Robust Process Control Using Schroeder-Phased Input Signals". In: *1993 American Control Conference*, pp. 895–899. DOI: 10.23919/ACC.1993.4792992.

Ruane, G., D. Echeverri, et al. (Sept. 2019). "Vortex fiber nulling for exoplanet observations: conceptual design, theoretical performance, and initial scientific yield predictions". In: *Society of Photo-Optical Instrumentation Engineers (SPIE) Conference Series*. Vol. 11117. Society of Photo-Optical Instrumentation Engineers (SPIE) Conference Series, 1111716, p. 1111716. DOI: 10.1117/12.2528555. arXiv: 1908.09780 [astro-ph.IM].

Ruane, G., D. Mawet, et al. (Sept. 2019). "Scalar vortex coronagraph mask design and predicted performance". In: *Society of Photo-Optical Instrumentation Engineers (SPIE) Conference Series*. Vol. 11117. Society of Photo-Optical Instrumentation Engineers (SPIE) Conference Series, 111171F, 111171F. DOI: 10.1117/12.2528625. arXiv: 1908.09786 [astro-ph.IM].

Schroeder, M. (1970). "Synthesis of low-peak-factor signals and binary sequences with low autocorrelation (Corresp.)" In: *IEEE Transactions on Information Theory* 16.1, pp. 85–89. DOI: 10.1109/TIT.1970.1054411.

Swartzlander, G. A. (July 2006). "Achromatic optical vortex lens". In: *Optics Letters* 31.13, pp. 2042–2044. DOI: 10.1364/OL.31.002042.

Wang, J. J. et al. (Dec. 2020). "An atmospheric dispersion corrector design with milliarcsecond-level precision from 1 to 4 microns for high dispersion coronagraphy". In: *Society of Photo-Optical Instrumentation Engineers (SPIE) Conference Series*. Society of Photo-Optical Instrumentation Engineers (SPIE) Conference Series 11447, 1144754, p. 1144754. DOI: 10.1117/12.2562654. arXiv: 2012.06007 [astro-ph.IM].

*Chapter 9*

# SUMMARY AND PERSPECTIVES

This thesis brought the vortex fiber nulling technique from a proposed concept in 2018 to a working instrument mode with demonstrated faint-companion detections in 2023. The chapters, summarized below, cover the various steps in this process. They include identifying the scientific motivation for VFN, validating the concept in the laboratory, designing the instrument mode, testing it on sky, and finally using it to directly detect and characterize three faint companions for the first time. With the completion of this thesis, VFN stands as a new cross-aperture nulling technique capable of detecting and spectroscopically characterizing faint companions at small angular separations from their host star. VFN modes on upcoming direct imaging instruments, some of which are presented at the end of this chapter, will extend the instruments' capabilities to separations that they otherwise could not access.

## 9.1 Summary

The first chapter presented the context, background, and scientific motivation for VFN. Given that 99% of all confirmed exoplanets so far have been detected indirectly, the chapter started with an overview of these indirect detection methods and what we have learned from them. It highlighted the finding that giant planets are most common between 1 to 10 AU from their host star, yet the prevailing techniques for spectroscopically characterizing them cannot access these critical separations. The chapter then introduced interferometry and nulling as a way to access and hence characterize exoplanets at these intermediate separations. Finally, it presented cross-aperture techniques which only rely on a single telescope. These techniques can therefore access well-within the inner working angle of conventional coronagraphs but are more readily implemented with less infrastructure than long-baseline interferometry. Chapter 2 followed-on by presenting the VFN concept itself. This started with the principles of fiber coupling, explained how the nulling effect is achieved with a single mode fiber, and then listed the primary error terms that can limit the VFN null. The chapter closed by covering some considerations for implementation, highlighting that VFN is adaptable to different design architectures and can therefore be readily implemented on existing and future instruments.

Chapters 3 and 4 covered the laboratory experiments validating VFN. Chapter 3 was a reproduction of my first journal paper, primarily serving as a proof of concept. In that paper, I demonstrated nulls of $6\times10^{-5}$ and an average peak off-axis coupling of 12% in monochromatic visible light using commercially available off-the-shelf optics. The paper also showed that the limitations in the system were well-understood, as my measurements of the wavefront error led to a null estimate that matched nicely with the measured null value. Chapter 4 built on these results by demonstrating deeper monochromatic nulls, extending the experiments to polychromatic light, and demonstrating VFN with charge 2. The key results are summarized in Table 4.1, which shows the best VFN laboratory performance. As with the previous chapter, I performed all of the VFN laboratory experiments presented in this chapter using a simple testbed which I aligned and for which I wrote all of the control and analysis software. Chapter 4 closes out by presenting a new nulling testbed (PoRT) which I designed and procured. PoRT's versatile design, along with my software, enabled other nulling projects to quickly demonstrate their first experiments. In the broader context of this thesis, Chapters 3 and 4 served to experimentally validate the VFN concept and demonstrated that it was ready for on-sky tests.

Chapters 5 and 6 therefore presented the first on-sky VFN demonstrator, included as an observing mode in the KPIC instrument. Chapter 5 pulled text from several conference papers where I presented the instrument design. In these papers, I also executed simulations to determine the expected performance for the new VFN mode. These simulations, based on on-sky measurements of wavefront and tip-tilt residuals, predicted that the planned charge 2 mode could achieve a null of $6\times10^{-3}$ and average peak off-axis coupling of 8%. The chapter closed out with my laboratory characterization of the as-built KPIC VFN mode prior to deployment. Table 5.1 summarizes the results from this characterization and validated that the VFN mode was ready for deployment. Chapter 6 then dove into the details of the new mode with a reproduction of my VFN first-light paper. In it I covered the full instrument design and observing strategy, along with an in-situ but off-sky characterization of the KPIC VFN performance as installed at the telescope. I then presented the technical results from on-sky commissioning and used these to derive detection sensitivity limits for the instrument mode. These limits predicted that KPIC VFN could detect a companion at a separation of $\sim1\ \lambda/D$ and at a flux ratio of $10^{-3}$.

Chapter 7 put the KPIC VFN mode to the test, presenting the first science results from VFN. This chapter was a reproduction of my latest journal paper, where we

used KPIC VFN to detect three faint companions at flux ratios between 70 and 430 and at separations of 35-55 mas ($0.7-1.2\ \lambda/D$ at 2.3 $\mu$m). These detections are particularly noteworthy since they represent the first time these M dwarf companions were directly detected, as the companions were previously only known from RV and/or astrometry. In the paper, we supplemented the VFN observations with interferometric observations from CHARA, highlighting the complementary nature of cross-aperture and long-baseline techniques. CHARA provided precise position measurements, along with the first flux ratio measurements for the companions, while KPIC provided the first spectra. I worked closely with another graduate student, Jerry Xuan, to select these targets and verify their validity using the SNR calculator I developed for the previous VFN paper. I then led the data analysis on the KPIC spectra to provide a preliminary glimpse at the characterization capabilities of VFN. These results lay the groundwork for a new observing campaign targeted at detecting companions around accelerating stars identified by Gaia. This interferometric campaign would complement existing direct imaging campaigns to extend the combined coverage of Gaia follow-up observations.

Chapter 8 served as a next-steps overview of work to improve the current KPIC VFN capabilities by adding a charge 1 mode. The chapter started with an investigation into scalar VFN, based on simulations executed by an undergraduate student under my supervision. It then proceeded with a break down of the design process that I led to procure a vector vortex mask, ensuring that the null contribution from the mask itself would not exceed $10^{-3}$. The chapter also explained the design requirements for the ADC, which were derived from my simulations on the effect of DAR on VFN. Finally, the chapter closed with a summary of work that I led to overhaul the tracking system. The tracking work was done in close coordination with a collaborator at JPL who designed the input Schroeder signal, analyzed the results, and designed the control law based on those results. I rewrote the control software, executed all the tests, and implemented the new controller. With the work presented in this chapter, KPIC VFN is ready for the charge 1 deployment in early 2024, which will unlock access to fainter targets at smaller separations.

## 9.2 Perspectives

This thesis showed that VFN works and can be readily implemented with few-to-no modifications to fiber-fed instruments. It also provided a glimpse into the kind of science that can be achieved. However, the VFN mode on KPIC is limited as it is primarily a demonstrator meant to test the VFN concept. VFN modes capable

of detecting Jupiter mass exoplanets have been baselined for two future ground-based instruments, HISPEC and MODHIS. Furthermore, a VFN mode on a future space telescope like the Habitable Worlds Observatory would push to even fainter targets and would extend the coverage of such a mission to smaller separations in the near-infrared.

***Ground-Based:*** The High-resolution Infrared Spectrograph for Exoplanet Characterization (HISPEC - Mawet, M. Fitzgerald, et al., 2019; Mawet, M. P. Fitzgerald, et al., 2022) is a new fiber-fed spectrograph operating from $1-2.5\ \mu$m with a spectral resolution of $R>100,000$ and a planned first-light date of 2026. This instrument is the direct successor to KPIC, inheriting many elements of its design but built from the bottom up for diffraction-limited fiber-fed operations behind an upgraded AO system at Keck. Based on the success of the KPIC VFN mode, HISPEC features a similar VFN mode to target faint exoplanets that would not be observable with the default direct or transit spectroscopy modes. As such, HISPEC achieves significantly better performance than KPIC but the similarities to its predecessor make it relatively straightforward to predict the VFN capabilities. In broad strokes, HISPEC is expected to have (based on internal communications with the HISPEC team): double the instrument throughput compared to KPIC, half the RMS wavefront error, three times the spectral resolution, four times the spectral coverage, and $1/20^{\text{th}}$ the thermal background. We can enter these values into Eq. 2.21, reproduced here for simplicity:

$$\tau = \frac{\eta_s}{\eta_p^2}\left[\frac{(\text{SNR})^2 R}{\epsilon^2 \Phi_s \lambda A q T}\right],$$

to predict the VFN improvement. The increased instrument throughput, $T$, will cut the integration time in half. Similarly, the reduced wavefront error will improve the null by a factor of four ($\eta \propto \omega^2$, see Eq. 2.25) and therefore cut the integration time by another factor of four. The increase in spectral resolution, $R$, will triple the integration time but the extended wavelength coverage should mitigate this effect since the SNR improves with the number of lines, $N$, in the spectrum ($\text{SNR} \propto \sqrt{N}$, see Birkby, 2018). Finally, the effect of the reduced background is harder to quantify in terms of requisite integration time but it will likely allow HISPEC to target fainter companions than KPIC, even with the increased spectral resolution. Overall, these improvements mean that HISPEC will require less than $1/8^{\text{th}}$ the integration time that KPIC does for a given SNR. In other words, a companion that would take KPIC a full night to detect would be detectable in just one hour with HISPEC.

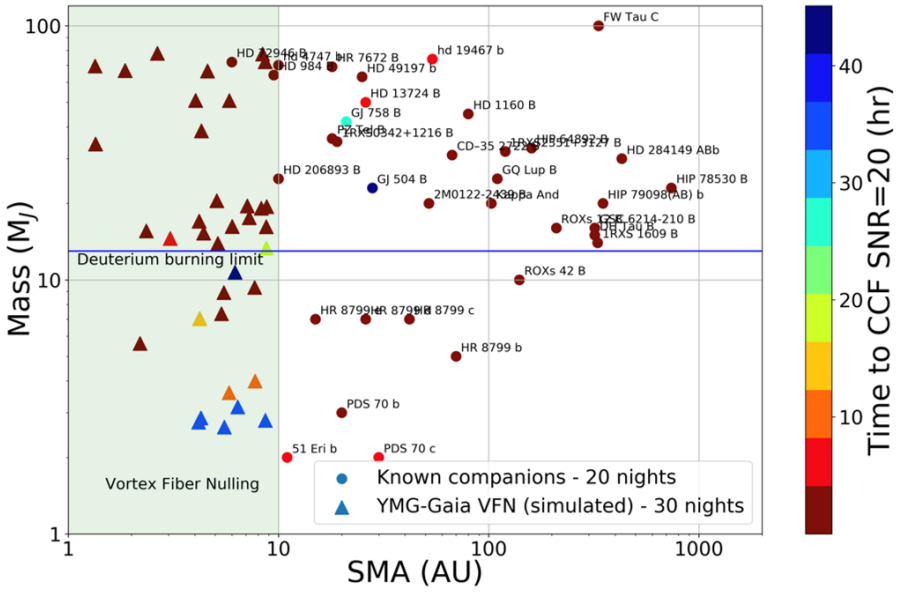


Figure 9.1: Yield and exposure time estimates for a HISPEC survey aimed at spectroscopically characterizing substellar companions. The circles denote known companions which would be accessible with the HISPEC DS mode. Meanwhile, the triangles are simulated Gaia detections of substellar companions within 2 $\lambda/D$ (100 mas at 100 pc in K band) in young moving groups (YMG), based on the occurrence rates from Rosenthal et al., 2021 and Gaia's astrometric sensitivity from Ranalli et al., 2018. The triangles are made accessible by the planned VFN mode. - Figure and caption adapted from the HISPEC proposal.

This order-of-magnitude improvement in performance from HISPEC starts to unlock the true capabilities of VFN. Figure 9.1 shows yield and exposure time estimates for HISPEC, based on simulations with the HISPEC exposure time calculator. The region in green on the left is the domain of the VFN mode, which spans the 1-10 AU region around stars within 100 pc. The calculator predicts that the HISPEC VFN mode will enable the direct spectroscopic characterization of around 35 Gaia-detected substellar companions, including several in the exoplanet-mass regime. Looking back at Fig. 1.5 from Chapter 1, these HISPEC VFN detections would drastically increase the number of spectroscopically-characterized companions in the intermediate regime between transit and direct spectroscopy.

As the first-light high-resolution spectrograph for the Thirty Meter Telescope, MODHIS (Multi-Objective Diffraction-limited High-Resolution Infrared Spectrograph) is the successor to HISPEC and has also baselined a VFN mode. However, with a first-light date in the 2030's, the predicted performance is still uncertain and it

is difficult to make extensive predictions about its VFN capabilities. The 30 m diameter of the primary mirror nevertheless provides two immediate improvements: a 10-fold increase in collecting area and a 3-fold decrease in inner working angle. If we conservatively assume that MODHIS is identical to HIPSEC and only the primary mirror changes, the increased area would cut the required integration time by a factor of 10. This would allow MODHIS VFN to reach exoplanets below 1 $M_{\mathrm{Jup}}$. Furthermore, assuming an inner working angle of about $\lambda/2D$ and an operating wavelength of $\lambda = 2.0$ $\mu$m, MODHIS VFN would be able to reach down to 8 mas and hence could access exoplanets at 0.5 AU around stars at 50 pc. However, the improved angular resolution would also make MODHIS VFN significantly more sensitive to pointing errors and geometric leakage from resolved stars, such that detailed simulations should be performed to get a better picture of the instrument's capabilities.

***Space-Based:*** The Astro 2020 Decadal Review recommended a dedicated high-contrast imaging space mission to launch in the 2040's. The so-called Habitable Worlds Observatory (HWO) has a goal of detecting and characterizing ~25 habitable Earth-like exoplanets (National Academies of Sciences, Engineering, and Medicine, 2021). Though HWO is still two decades away, the stability of the space environment and the extensive conceptual design work performed so far (see e.g., Gaudi et al., 2020; The LUVOIR Team, 2019) make it possible to predict the null and planet coupling for a putative VFN mode on the telescope.

The null with charge 1 VFN will most likely be limited by the angular size of the host stars. This is because the coronagraphic mode sets stringent wavefront residual requirements on the order of a few picometers and the corresponding null contribution in VFN will be $\lesssim 10^{-7}$. Meanwhile, a star with an angular diameter of 0.1 mas would contribute a geometric leakage of $\sim 4\times10^{-6}$ for charge 1. This sets the value for $\eta_s$. Given the negligible amount of wavefront error, the planet coupling should meet the theoretical limit which, for a LUVOIR-like aperture (The LUVOIR Team, 2019) would peak at 19%. The relative integration time reduction from the VFN mode would therefore be $\tau = \eta_s/\eta_p^2 = 2 \times 10^{-5}$. This is orders of magnitude deeper than VFN on ground-based instruments. In a more detailed analysis, Ruane et al. (2019) showed that a VFN mode on a LUVOIR-like mission would be able to detect a rocky exoplanet like Ross 128 b (Bonfils et al., 2017) in about 30 hours.

Such a VFN mode on HWO would serve multiple purposes. First, it would allow the mission to detect and characterize exoplanets at separations down to 10 mas

from their host star in the visible ($\lambda/2D$ assuming $\lambda$ = 500 nm and $D$ = 6 m). This extends the spatial coverage of the instrument which would be limited by the IWA of the coronagraph at the shortest wavelength. However, VFN would also extend the spectral coverage for the mission. If an exoplanet is detected at the coronagraphic IWA in the visible, it would normally be inaccessible in the near-infrared but with the VFN mode, the exoplanet would remain observable at longer wavelengths. VFN would therefore not only increase the number of exoplanets detected by HWO but would also improve the mission's characterization capabilities.

## References

Birkby, J. L. (2018). "Spectroscopic Direct Detection of Exoplanets". In: *Handbook of Exoplanets*. Ed. by H. J. Deeg and J. A. Belmonte. Cham: Springer International Publishing, pp. 1485–1508. ISBN: 978-3-319-55333-7. DOI: 10.1007/978-3-319-55333-7_16. URL: https://doi.org/10.1007/978-3-319-55333-7_16.

Bonfils, X. et al. (2017). "A temperate exo-Earth around a quiet M dwarf at 3.4 parsecs". In: *Astron. Astrophys.* 613, A25. DOI: 10.1051/0004-6361/201731973.

Gaudi, B. S. et al. (Jan. 2020). "The Habitable Exoplanet Observatory (HabEx) Mission Concept Study Final Report". In: *arXiv e-prints*, arXiv:2001.06683, arXiv:2001.06683. DOI: 10.48550/arXiv.2001.06683. arXiv: 2001.06683 [astro-ph.IM].

Mawet, D., M. Fitzgerald, et al. (Sept. 2019). "High-resolution Infrared Spectrograph for Exoplanet Characterization with the Keck and Thirty Meter Telescopes". In: *Bulletin of the American Astronomical Society*. Vol. 51, 134, p. 134. arXiv: 1908.03623 [astro-ph.IM].

Mawet, D., M. P. Fitzgerald, et al. (Aug. 2022). "Fiber-fed high-resolution infrared spectroscopy at the diffraction limit with Keck-HISPEC and TMT-MODHIS: status update". In: *Ground-based and Airborne Instrumentation for Astronomy IX*. Ed. by C. J. Evans, J. J. Bryant, and K. Motohara. Vol. 12184. Society of Photo-Optical Instrumentation Engineers (SPIE) Conference Series, 121841R, 121841R. DOI: 10.1117/12.2630142.

National Academies of Sciences, Engineering, and Medicine (2021). *Pathways to Discovery in Astronomy and Astrophysics for the 2020s*. The National Academies Press. ISBN: 978-0-309-46586-1. DOI: 10.17226/26141.

Ranalli, P., D. Hobbs, and L. Lindegren (June 2018). "Astrometry and exoplanets in the Gaia era: a Bayesian approach to detection and parameter recovery". In: *Astronomy & Astrophysics* 614, A30, A30. DOI: 10.1051/0004-6361/201730921. arXiv: 1704.02493 [astro-ph.EP].

Rosenthal, L. J. et al. (July 2021). "The California Legacy Survey. I. A Catalog of 178 Planets from Precision Radial Velocity Monitoring of 719 Nearby Stars over Three Decades". In: *The Astrophysical Journal Supplement Series* 255.1, 8, p. 8. DOI: 10.3847/1538-4365/abe23c. arXiv: 2105.11583 [astro-ph.EP].

Ruane, G. et al. (Sept. 2019). "Vortex fiber nulling for exoplanet observations: conceptual design, theoretical performance, and initial scientific yield predictions". In: *Society of Photo-Optical Instrumentation Engineers (SPIE) Conference Series*. Vol. 11117. Society of Photo-Optical Instrumentation Engineers (SPIE) Conference Series, 1111716, p. 1111716. DOI: 10.1117/12.2528555. arXiv: 1908.09780 [astro-ph.IM].

The LUVOIR Team (Dec. 2019). "The LUVOIR Mission Concept Study Final Report". In: *arXiv e-prints*, arXiv:1912.06219, arXiv:1912.06219. DOI: 10.48550/arXiv.1912.06219. arXiv: 1912.06219 [astro-ph.IM].